Design, Development, and Processing of Perovskite Nanocrystals for Optical Devices

Theodore Abraham Cohen

A dissertation

submitted in partial fulfillment of the

requirements for the degree of

Doctor of Philosophy

University of Washington

2022

Reading Committee:

Daniel R. Gamelin, Chair

Christine K. Luscombe

J. Devin MacKenzie

Program Authorized to Offer Degree:

Molecular Engineering

University of Washington

Abstract

Design, Development, and Processing of Perovskite Nanocrystals for Optical Devices

Theodore Abraham Cohen

Chair of the Supervisory Committee:
Professor Daniel R. Gamelin
Department of Chemistry

Perovskite nanocrystals (NCs) are an exciting new class of luminescent materials with impressive photoluminescence quantum yields, highly tunable properties, and remarkable defect tolerance. Such properties make them ideal candidates for applications in light emitting diodes, luminescent solar concentrators, and quantum photonic devices. However, more work is needed to understand their fundamental properties and leverage these properties in real-world devices. This thesis presents three use-inspired studies that draw on an understanding of fundamental perovskite NC material properties to develop these materials for working device platforms. Chapter 1 discusses fundamental perovskite NC properties and potential device considerations necessary to explore these materials in various applied research areas. Then, Chapter 2 discusses the potential of quantum-cutting Yb^{3+}-doped perovskite NCs for high-performance luminescent solar concentrators. This study produces design constraints for perovskite NC/polymer

composites that inform the development of modular polymers to suspend various perovskite NC compositions in the solid composites described in Chapter 3. Finally, this understanding of NC ligand chemistry and stability was leveraged to develop methods described in Chapter 4 to process perovskite NCs with electrohydrodynamic inkjet printing for photonic device integration. These studies are important steps towards translating perovskite NC research from fundamental innovations towards the numerous potential device applications of these materials.

TABLE OF CONTENTS

LIST OF FIGURES

LIST OF TABLES

ACKNOWLEDGEMENTS

It really does feel quite surreal and overwhelming to think about the many people in my life who helped me get here. To start, I cannot thank Daniel Gamelin enough for taking a chance on me in 2017 and inviting me to join his lab. The opportunity he and the MEM-C provided me was the best graduate research experience I could have imagined. You have an extraordinarily positive group environment and I hope to take many of the lessons from your group to my future mentorship work. I also must thank Devin MacKenzie for being one of the earliest supporters of my graduate studies. I'm so glad that you kept working with me and supporting me through such a broad array of projects. Finally, Christine Luscombe provided so many forms of support for me over the years, and I cannot thank her enough for that. I can't wait to visit you in Okinawa soon. The three of you made the perfect team to guide me through this adventure, and I will forever be grateful for your help and support.

Outside of my advisory team, I cannot thank Lilo Pozzo and Dave Beck enough for joining my committee. Lilo had excellent advice for me during my general exam, and Dave's support through the DIRECT program inspired a lot of the work in this thesis. I also very grateful for everyone in the Molecular Engineering and Science Institute, including Paul Neuber, Pat Stayton, and Doug Ballard for helping me join and navigate the Molecular Engineering PhD program. I've also really enjoyed working with the staff of the Materials Science and Engineering Department, the Chemistry Department, and the Clean Energy Institute.

I owe a lot of my success to the members of the Gamelin, Luscombe, and MacKenzie research labs that I've had the pleasure of meeting over the years. The older members of the group taught me so much about research and are exceptional models of what a future chemistry career can look like. I've enjoyed the fun lab moments, the group outings and events, and many other adventures over the years that we've gotten to do together. I can't wait to stay in touch with all of you and see where the world takes us. I'm also lucky that I've gotten to chat with and learn from plenty of other great people in other research labs and programs. These include students of John Berg, Lucien Brush, Jim Pfaendtner, Brandi Coissart, David Ginger, and especially Arka Majumdar. I will forever appreciate the opportunities to work with these great people, and the collaborative, encouraging environment here is one of the things I will forever appreciate about the University of Washington.

I also owe a lot of my success to my extracurricular work with the Washington Yacht Club, the DIRECT program, Global Renewable Infrastructure Development, the Clean Energy Institute, the Graduate Professional Student Senate, and the Services and Activity Fee Committee. I've made lifelong friends, had the most incredible adventures, and learned a ton of management and leadership skills from my work with these groups. The Washington Yacht Club was also a steppingstone to many more fun sailing adventures in the Seattle area. Additionally, I really appreciate the University of Washington for the excellent facilities, fun football games, and beautiful scenery that continually energized me to complete my studies.

Outside of UW, there are too many people to acknowledge and thank for me to list here. To start, there are plenty of great friends, coaches, and teachers from my elementary, middle, and high school years that helped me get to this point. I also learned from and worked with many incredible professors, colleagues, friends, and mentors at Washington University in St. Louis. In

particular, Rajan Chakrabarty, Jay Turner, Milorad Dudukovic, and especially Pratim Biswas were instrumental in teaching me everything I know about chemical engineering and convincing me to pursue graduate studies. I also had plenty of great sailing adventures through Washington University and found the school to be a great environment to make new friends, have lots of fun, and build a fruitful partnership with Anna Stebbins. I really appreciate her encouragement to move to Seattle and her help navigating the crazy pre/post grad world. Once I found my way to Seattle, I was lucky enough to make a ton of new friends through sailing, skiing, climbing, and all of the other amazing things this area has to offer. They were always there to support me, including during some of the hardest, most painful moments of my life, and show me new things. Among them, I am forever grateful to Molly Wright for her compassion, positive attitude, and immeasurable support through this process.

I also must thank my grandparents, cousins, uncles, and other family members that are here now and have passed on over the years. From ski trips, sailing outings, and extra fun family dinners, I've really appreciated spending quality time with all of you, and learning from your academic and other life experiences. In particular, I am so grateful that my grandmother Beverley Cohen was able to attend my defense in person; you are such an incredible inspiration. Finally, I owe so much of my success to my parents Steve Cohen and Karen Cohen and my sisters Allison and Lilly Cohen. You have been the most loving, supportive, and fun family to grow up with, and I will forever appreciate all the time we've spent together.

CHAPTER 1. INTRODUCTION

1.1 OVERVIEW

Semiconductor nanocrystals (NCs) have emerged as promising light manipulation materials for countless important applications. This is primarily because it was discovered that the band gap of these materials could be continuously tuned by changing the primary NC size,[1-2] a property that is not shared by ion-doped inorganic luminophores or organic dyes. Research of these materials eventually led to the development of a colloidal synthesis of a series of monodispersed II – VI NCs.[3] The CdSe NCs produced in this synthesis were easily tunable through the visible spectrum and have sufficiently narrow full width half maxima (FWHM) for applications as downconverting phosphors in light emitting diodes (LEDs).[4] Additionally, InP and other III – V, Cd^{2+}-free materials were developed as non-toxic alternatives to CdSe NCs,[5-8] an advancement that was important for their market deployment as color converters in televisions. Now, these materials are relevant for numerous technologies, including solar cells,[9] photodetectors,[10] biological labels[11] and catalysts.[12]

The discovery and deployment of light-emitting NCs relied on numerous research efforts and industrial developments that have yielded an impressive number of fundamental breakthroughs and advanced technologies. For instance, the initial discovery that a NC's band gap can be tuned by changing its size came from largely fundamental research efforts.[1-2] Conversely, the deployment of these materials in real-world devices relied on purely applied research innovations. Between these extremes, there were additional research thrusts that cannot be categorized as either purely fundamental or purely applied research. These efforts are best described as use-inspired fundamental research, a field of study that is critical for the deployment

of fundamental knowledge in real-world technologies.[13-14] For instance, the development of a colloidal synthesis that yielded monodispersed, size-tunable CdSe NCs is partly motivated by the goal of developing solution processable phosphors with narrow FWHMs that emit at specific wavelengths for LED applications.[3] However, these developments relied on fundamental innovations in colloidal inorganic chemistry that were directed to yield NC that met the use-inspired need of numerous applied technologies. The accumulation of these innovations over the course of 30 years was critical to move the discovery of band gap NC size tuneability from a fundamental idea to a critical component of numerous real-world technologies.

It is also useful to discuss the metric of technology readiness level (TRL). This system was initially developed by NASA in the 1980s to describe an innovation's readiness to be deployed in space flight[15] and was adapted by a number of other government agencies to describe the extent to which a technology has been validated and scaled for real world applications.[16-17] Early stages of technology readiness describe innovations that come from fundamental research, and later stages of technology readiness typically refer to products of applied research that aims to yield real world devices at scale. Between these extremes, TRLs 3 – 5 describe innovation steps that take fundamental concepts and translate them into prototype components and devices. These steps are motivated by particular end uses, but they still rely on the gathering of more fundamental understanding to truly advance a concept for use in real world devices. This TRL range is therefore an ideal area for use-inspired research

While II – VI and III – V NCs are the most thoroughly developed tunable luminescent NC materials system, perovskite NCs emerged in 2015 as promising alternatives to these chemistries.[18] These materials were found to have unusually high photoconductivity in 1958,[19] an observation that inspired investigation of these materials as absorbing and charge-separating

materials for dye-sensitized solar cells.[20-23] Since then, an extraordinary amount of research effort has been devoted to understanding these materials and using them in next-generation optical devices. There have been many successes with perovskite NCs over the years, but more research is needed to understand their fundamental properties and use these unique materials in real world devices.

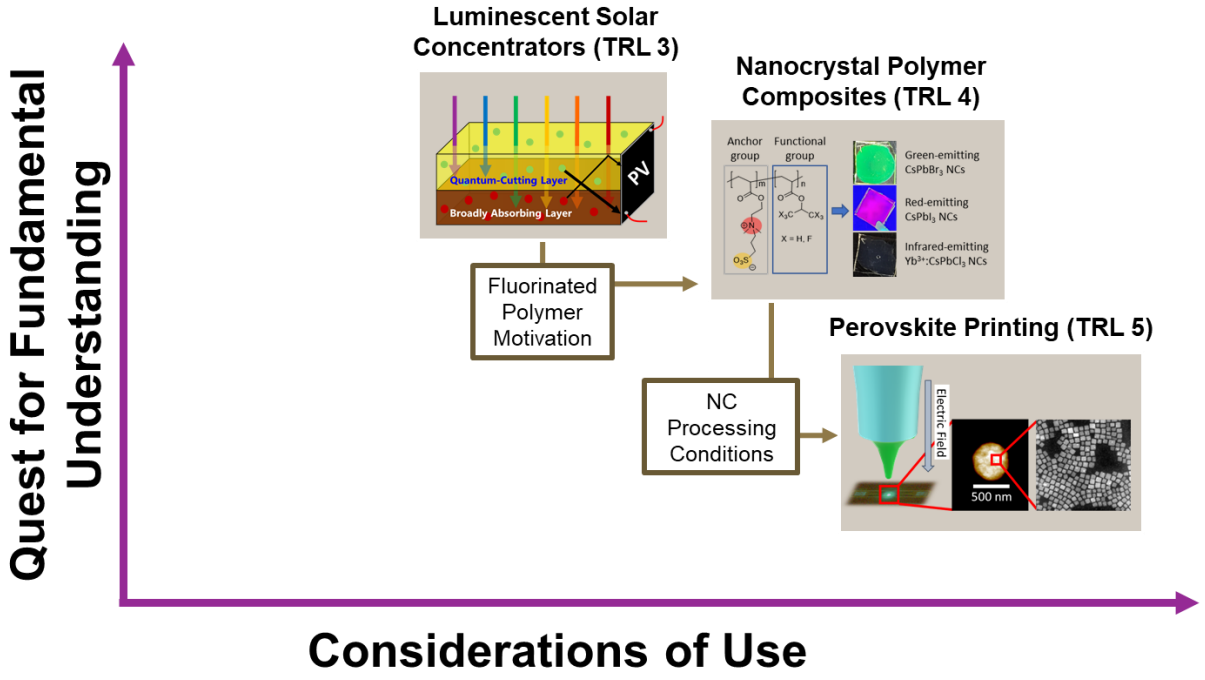

Figure 1.1. Summary of several use-inspired perovskite nanocrystal studies. An initial, largely fundamental study of novel monolithic bilayer LSCs motivates the development of custom modular zwitterionic polymer composites for various applications. The ligand chemistry understanding developed here is then used to investigate prospects for processing perovskite NCs with electrohydrodynamic inkjet printing for quantum photonic applications.

This thesis presents three use-inspired research efforts to improve understanding of perovskite NCs' fundamental properties and leverage those properties for numerous different applications. Within this category of use-inspired research, the three components of this thesis span a range of largely fundamental to largely applied research. To start, Chapter 2 presents a study that considers the use of near-infrared (NIR) emitting doped perovskite NCs in a solar

collection device called a luminescent solar concentrator (LSC). This work produces a proof-of-concept demonstration of the potential of quantum cutting in these devices, which moves the fundamental innovation to a TRL of 3. Chapter 3 then describes an investigation of perovskite NC surface chemistry to develop custom polymers tailored to stabilize these NCs in solid composites. This polymer composite component is a useful demonstration of a TRL 4 innovation. Finally, Chapter 4 presents a more applied study of a novel, high-resolution method of inkjet printing and its potential for processing perovskite NCs. This study yields a fully integrated laboratory device demonstration that can be classified as TRL 5, thereby completing the progression from largely fundamental use-inspired research to largely applied use-inspired research. The applications behind these topics are not inherently related to one another, but all of them leverage fundamental understanding of perovskite NC properties for various applications. However, such research provides excellent opportunities to understand what is necessary to develop these materials for real-world technologies.

1.2 Luminescent Solar Concentrators

LSCs[24-28] are an attractive class of light-concentrating devices typically composed of luminophores that absorb solar photons and a waveguide that directs re-emitted photons onto small solar cells coupled to the device's edges. LSCs can be tailored to a wide variety of applications ranging from semitransparent solar windows to space solar-power systems. Unlike optical concentrators, they can concentrate both direct and diffuse solar radiation with no theoretical concentration limit.[29-31] Figure 1.2 shows a schematic of a typical LSC. The luminophore in these devices should combine high solar absorbance with high photoluminescence quantum yields (PLQYs), while minimizing overlap between the two.

Furthermore, the waveguide should have an optimum refractive index for solar light collection and transmission and should be free of defects that scatter or absorb transmitted light.

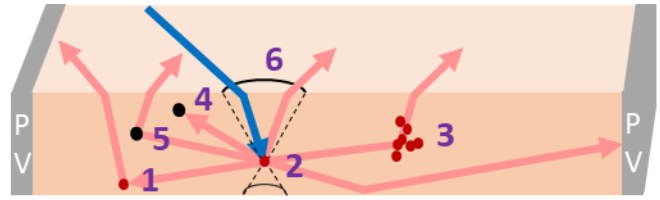

Luminophores
1. Limited absorption-emission overlap
2. High quantum yield
3. Well Dispersed

Polymer
4. High transmittance
5. Few defects
6. Optimized refractive index

Figure 1.2. Schematic of an LSC device and the various loss processes that can impede device performance. The list below the schematic presents the optimal luminophore and polymer properties that can eliminate the loss mechanisms shown here.

Over the years, various classes of luminophores, including organic dyes,[32-35] rare-earth ions doped into glasses,[24, 36-37] and inorganic coordination complexes,[38-40] have been explored in LSCs. Recently, colloidal semiconductor NCs have emerged as promising LSC luminophores because of their high PLQYs, large extinction coefficients, tunable energy gaps, and the ability to engineer small absorption/emission overlap.[27, 41-58] A particularly effective strategy for minimizing reabsorption involves using NC dopants as luminescence species,[44] thereby separating the tasks of solar absorption (by the NC) and emission (by the dilute dopant). To realize the applications of colloidal NCs in an LSC, the NCs must be suspended in a solid matrix with high solubility and stability. Because the transmission distances in full-scale LSCs can be as high as 1 m and transmittance decreases exponentially with increasing distance,[46-47] it is imperative that luminophores be well dispersed in a waveguiding medium with a low lateral attenuation coefficient (less than 0.01 cm^{-1}). This is below the level than can be seen by eye in thin samples or by most vertical transmittance measurements.[50] Therefore, Section 1.2.1

discusses methods to assess lateral transmission over large length scales. Section 1.2.2 then describes novel doped perovskite NCs and their potential as LSC luminophores.

1.2.1 *Attenuation Characterization with a 1D LSC*

As an initial assessment of NC/LSC compatibility, several lateral attenuation measurements have been developed. One involves comparing the emission of LSCs placed inside of an integrating sphere with blackened and non-blackened edges.[43] The difference in emitted light intensity from the integrating sphere can then be fit with a model to determine the reabsorption and scattering components of lateral attenuation.[53, 56, 59] Another method relies on direct measurement of the effect of changing the lateral distance between an excitation source and an optical detector mounted on the edge of an LSC. This has been done by fully illuminating different size samples,[60] covering varying facial areas of a single, fully-illuminated sample with an absorbing material,[44] or by moving a small excitation source laterally along the distance of a LSC sample.[50-51, 61-62] Unfortunately, these methods rely on the fabrication of a NC polymer composite slab, a process that can introduce optical impurities in the waveguide and reduce the PLQY of some NCs.[50, 52] This challenge can be circumvented by performing similar transmission measurements on solutions of NCs.

This liquid LSC measurement was first demonstrated by Bradshaw et al. in a device described as the 1D LSC.[46] In this work, a 120 x 0.1 x 0.1 cm^3 glass tube was fabricated and mounted so that it could be placed on a standard optics table. This tube was closed at one end and left open at the other so that a capillary tube could be threaded through the length of the glass tube. With this setup, one could use a syringe to carefully load a ~1 mL solution of NCs in their native solvents into the glass tube. From there, an excitation source is placed a set distance from the closed end of the tube so that light hits the sample perpendicular to the tube. Collection

optics are then placed near the closed end of the tube, and the distance between the closed end and the excitation source is varied. The spectra collected at each excitation distance are then analyzed so that the light transmission through a liquid media of NC solution can be evaluated.

This study by Bradshaw et al. made a number of important observations about lateral transmission of NC emission through a liquid medium of NCs.[46] First, it was found that even a small amount of absorption, emission overlap was sufficient to dramatically attenuate NC emission over length scales of 10 – 20 cm. This overlap is typical of "giant" CdSe/CdS core-shell NCs[43, 63] and dot-in-rod CdSe/CdS NCs,[42] and it will substantially limit the performance of large-area LSCs fabricated with these materials. This problem can circumvented using doped NCs such as Mn^{2+}-doped ZnSe NCs[44] and Mn^{2+}-doped $CsPbCl_3$ NCs,[49] as the Mn^{2+} $^4T_{1g} \rightarrow {}^6A_{1g}$ transition is sufficiently red-shifted from the host NC's band gap that very little reabsorption occurs. However, the second finding from Bradshaw et al. is that when NC reabsorption effects are eliminated, the composition of the solvent and ligands have a noticeable impact on the large scale attenuation characteristics of NC emission.[46] For instance, the C – H bonds in toluene have sufficiently high absorption that tetrachloroethylene was used as the primary solvent for most of the measurements in this study. Even when the solvent was replaced, attenuation was still observed for Mn^{2+}-doped $Cd_xZn_{1-x}Se$ emission, and this attention was attributed to C – H bonds on the NCs' ligands. These observations motivate the development of more doped NC systems for LSCs and establish the 1D LSC as a useful way to predict the performance of new LSC luminophore materials in various liquid media.

1.2.2 *Yb^{3+}-Doped Perovskites for LSCs*

Figure 1.3a describes the energy structures of an array of possible doped NC systems for LSCs. Mn^{2+}-doped materials have been discussed above, but Cu^+ emission received further

research attention because its characteristic emission can be lower in energy than Mn^{2+} emission. This permits the use of lower bandgap host semiconductors that can collect a larger fraction of the solar spectrum. Cu^{+}-doped CdSe[46, 51] and Cu^{+}-doped InP[58] have all been demonstrated as promising luminophores, but $CuInS_2$ NCs with high effective Stokes shifts and broad Cu^{+}-based PL were quickly identified as a promising luminophores for LSCs.[47-48, 50, 52, 64-65] Beyond these materials, Yb^{3+} emission was identified as an ideal candidate for LSCs because the $^2F_{5/2} \rightarrow {}^2F_{7/2}$ luminescent transition at roughly 985 nm is well-matched to the band gap of silicon and typically has a low FWHM.[66-67] NC-sensitized Yb^{3+} emission has been demonstrated for Yb^{3+}-doped CdSe NCs[68] and Yb^{3+}-doped $PbIn_2S_4$ NCs,[69] but neither of these materials have NIR PLQYs higher than 10%. Recently however, Yb^{3+}-doped $CsPbCl_3$ NC materials were successfully synthesized with NIR PLQYs greater than 100%.[70-71] This system was further characterized to demonstrate that this high PLQY can be explained by a quantum-cutting process that relies on concerted energy transfer from the NC excited state to two Yb^{3+}-ions that each release a photon for everyone one photon absorbed, as described in Figure 1.3b.[72]

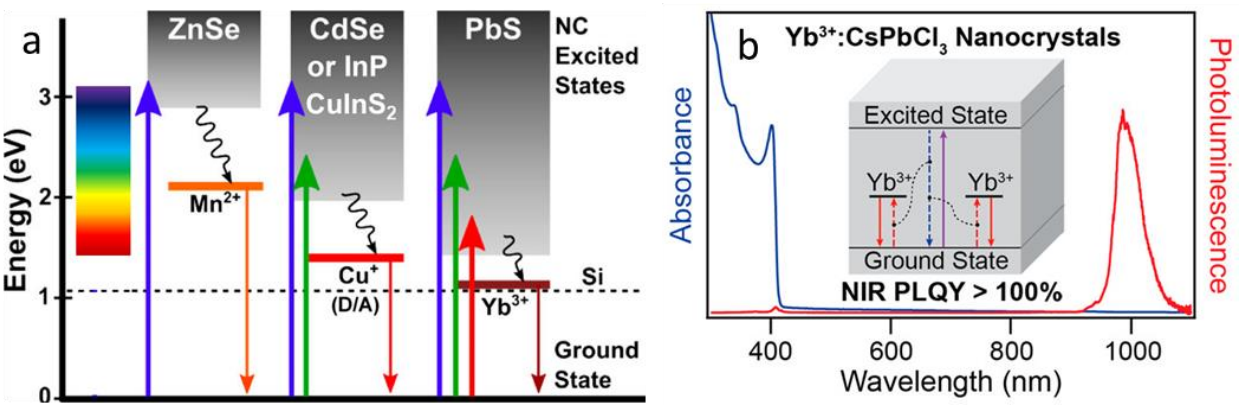

Figure 1.3. Energy structure of ideal doped NC systems for LSCs. **(a)** Band structure of possible material options for Mn^{2+}, Cu^{+}, and Yb^{3+}-doped systems. The photoluminescent transitions of these dopants are represented as orange, red, and maroon arrows, respectively, and possible host lattice conduction band structures are shown as shaded black areas. These energies are compared with the band gap of silicon, which is best matched to Yb^{3+} emission. **(b)** Absorption and photoluminescence spectra of Yb^{3+}:$CsPbCl_3$ NCs. The absorption-emission overlap is minimal, making them ideal for LSCs. The inset diagram describes the hypothesized quantum-cutting mechanism that explain measured PLQYs greater than 100% for these materials. Panel a Adapted with permission from ref. 44 Copywrite 2014 American Chemical Society. Panel b Reproduced with permission from ref. 72 Copywrite 2018 American Chemical Society.

Despite the exciting properties of these materials, there are two critical challenges that need to be addressed for their deployment in LSCs. First, the band gap of the host $CsPbCl_3$ material is too high to absorb a significant fraction of the solar spectrum. This could make Yb^{3+}:$CsPbCl_3$ materials ideal candidates for transparent solar window applications, and it's band gap can be slightly tuned with anion alloying.[73-74] Nevertheless, an additional approach must be developed to effectively use these quantum-cutting materials in high efficiency LSCs. One proven solution is to use a tandem architecture that provides an additional lower band gap component to the device architecture to collect light not absorbed by higher band gap materials.[38, 53, 63, 75-76] Unlike other tandems, this theoretical device would rely on quantum

cutting to enhance the photocurrent generated from voltage matched solar cells instead of relying on solar cells with different band gaps that require photocurrent matching to enhance overall voltage, vastly simplifying the device. Furthermore, since Yb^{3+} emission does not overlap with the bandgap of most possible LSC materials, both materials could be integrated in a layered monolithic device.

Second, as discussed in Section 1.2.1, C – H bonds common in most solvents and waveguiding materials are known to attenuate light due to a series of vibrational overtones in these bonds. These absorption features are relatively week in the visible regime,[77] but they have nevertheless been identified as a loss mechanism in some LSC configurations.[52, 65, 78] Additionally, the absorbance of these overtones increases with increasing wavelength, which suggests that NIR emission will be more severely attenuated than visible emission. It was predicted that the intensity of these vibration overtones could be substantially reduced by replacing hydrogens with other halogen atoms such as fluorine or chlorine.[77] This prediction was thoroughly explored within the fiber optics community to find that full replacement of all C – H bonds with C – F bonds in polymer materials nearly eliminates these overtone absorption features.[79] Furthermore, partial replacement of C – H bonds can mitigate the effect of these overtones while yielding materials that do not need to be processed with dangerous fluorinated solvents.[80-81] These possibilities are promising, but new methods of NC polymer composite fabrication would need to be developed to embed these NCs in a fluorinated polymer. Therefore, a solution state evaluation of the effect of these C – H bonds on the lateral transmission of NIR emission would be important to inform any future polymer composite work.

1.3 NANOCRYSTAL POLYMER COMPOSITES

The liquid cell measurement and LSC device design considerations discussed in Section 1.2 motivate a thorough investigation of methods to suspend perovskite NCs in various solid composites. This composite should have several key properties to be suitable for LSC and other applications. First, the NC/composite should be free of large NC aggregates that scatter light. Second, the composite should be solution processable under mild conditions with solvents that are non-toxic and that will not irreversibly degrade the perovskite NC structure. Third, as discussed in Chapter 2, the C – H bond content should be tunable for potential applications with NIR emitting NCs. Finally, the original NC properties should be preserved with high stability in the final composite.

A substantial amount of research effort has been dedicated to developing solid composites of CdSe and other III – V materials for LEDs. One informative example comes from Jun et al. and the Samsung Advanced Materials Research Division.[82] In this work, CdSe/CdS/ZnS NCs were stabilized in silica monolith structures for downconverting LEDs. They demonstrate that few CdSe aggregates form in these monoliths using UV-vis spectra that show minimal sub-bandgap scattering character for composites with high NC concentration. Additionally, they show that the original PLQY of the underlying NCs is well preserved through the fabrication of these solid composites. These successes can be explained by NC designs that insulate the emissive NC core from surface defects and by carefully considering NC surface chemistry when developing the silica condensation process. For instance, propylamine is used as a catalyst in this study because amine groups are known passivating groups for II – VI NC surfaces.[83-84]

While such observations are informative to the task of developing solid NC composites, there are a number of properties of this work that will not transfer well to perovskite NC/polymer composites for LSCs.[82] Firstly, silica monoliths typically form as large semi-crystalline domains that may scatter light in LSC applications. Second, the particular condensation reactions used to develop the solid composites in this study will likely require more water than perovskite NCs can tolerate. That said, the overall approaches here inform the polymer development study described in Chapter 3, along with several additional considerations. Firstly, this work is guided by a thorough understanding of perovskite NC surface chemistry discussed in Section 1.3.1. Then a number of polymer chemistry considerations are described in Section 1.3.2. Finally, to evaluate the overall stability of NCs within these solid polymer composites, Section 1.3.3 discusses methods to determine the viability of any potential NC/polymer composites.

1.3.1 *Perovskite Surface Chemistry*

Some sections adapted with permission from Huang, Y.; A. Cohen, T.; M. Sperry, B.; Larson, H.; A. Nguyen, H.; K. Homer, M.; Y. Dou, F.; M. Jacoby, L.; M. Cossairt, B.; R. Gamelin, D.; K. Luscombe, C. *Materials Horizons* **2022**, *9*, 61. Copywrite 2022 Royal Society of Chemistry.

In 1958, metal-halide perovskites were found to have unusually high and tunable photoconductivity.[19] In the earliest stages of the development of these materials, little was understood about the structure and chemistry of these materials. However, the high ionicity of the perovskite surface inspired the development of various cationic and anionic ligands to passivate charged surface defects. These efforts were critical for the fabrication of single-layer perovskite solar cells with power conversion efficiencies (PCEs) of 25.6%,[85] perovskite-perovskite tandem cells with a 24.8% PCE,[86] and perovskite-silicon tandem cells with a 29.15% PCE.[87] Such promising results inspired an expansion of perovskite research to colloidal

nanocrystalline versions of the materials[18, 88-92] that have now been used in applications such as LEDs,[93-95] lasers,[96-99] X-ray detectors,[100-101] and single-photon sources.[102-104] These applications are enabled by the high defect tolerance of perovskite NCs[105-108] and their broad spectral tunability with anion[109-111] and cation[70-72, 112-113] alloying. Many researchers have found that the high ionicity of metal-halide perovskites often leads to degradation of their favorable photoluminescence,[114-117] hindering their use in several important research areas. Fortunately, it has been shown that these NCs can be effectively stabilized and passivated by carefully considering their surface structure and designing anchor groups that accommodate their lattices.

The first reported synthesis of colloidally stable perovskite NCs used a combination of oleylamine and oleic acid.[18] Methylammonium is a key component of thin-film perovskites, and early reports demonstrate that longer chain alkylammonium molecules have high potential as defect passivating groups for perovskite solar cells.[118-119] These results suggest that ammonium ions are a critical anchor group for stabilizing the surfaces of perovskite NCs, a hypothesis that was confirmed by NMR studies to show that oleylammonium oleate groups are the main anchor groups that coordinate with perovskite NC surfaces, rather than oleylamine and oleic acid.[120] Figure 1.4a shows the ligand-NC binding equilibrium characteristics for these materials. Unlike the tight ligand binding characteristics typical of II – VI and III – V semiconductor NCs, perovskite NC-ligand interactions are far weaker[120-122] despite these materials having very high PLQYs. The high PLQYs are explained by density functional theory (DFT) studies demonstrating that most perovskite defect structures produce trap states that do not lie within the material's bandgap.[107-108] However, it was later shown experimentally[88] and with DFT[123] that undercoordinated lead sites at terminal surfaces or grain boundaries are critical defects that may be responsible for reduced NC PLQY. These studies inspired a large amount of synthetic and

ligand chemistry investigations to improve perovskite NC PLQY and increase overall NC stability by passivating such lead sites.

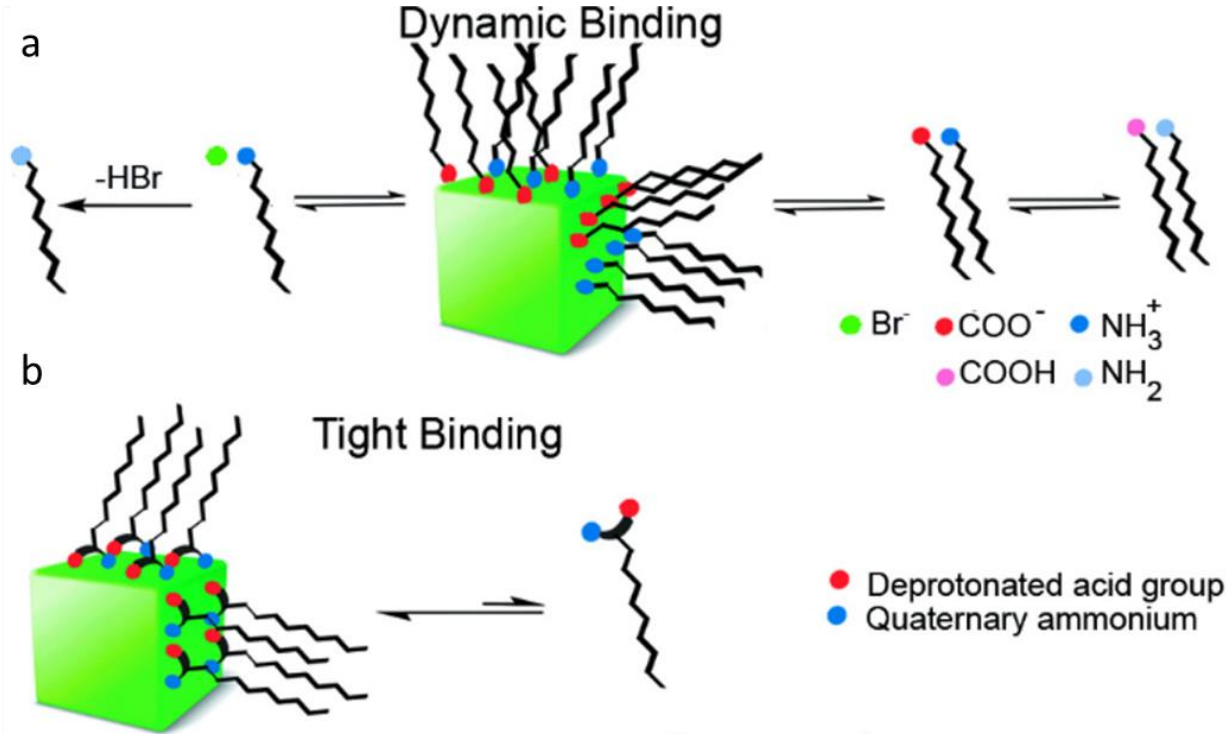

Figure 1.4. NC binding characteristics for various perovskite ligands. **(a)** Scheme demonstrating the dynamic ligand binding behavior observed when oleylamine and oleic acid ligands are used to stabilize perovskite NCs. **(b)** Scheme showing that zwitterionic groups containing soft Lewis bases (red) and quaternary ammonium ions (blue) exhibit tight binding with perovskite NC surfaces. Panels a,b reproduced with permission from ref. 124 Copywrite 2018 American Chemical Society.

This motivated the investigation of anionic groups that could passivate undercoordinated lead sites. Phosphonate and phosphines groups have exposed lone pair electrons that have shown high potential as passivating groups for thin-film perovskites.[125-126] Trioctylphosphine was occasionally used to help dissolve lead precursors for hot injection syntheses,[18] but was further explored to show that trioctylphosphine[127] and trioctylphosphine oxide[128] can be used to improve NC stability and PLQY. It was even shown that the PLQY of degraded NCs coordinated with traditional ligands could be recovered by simply treating with the NCs with a solution of

trioctylphosphine.[129-130] This recovery is presumably due to an association of electron pairs on phosphine or phosphine oxide moieties with the undercoordinated Pb^{2+} sites that are typically associated with low NC PLQY.[106, 131] The hypothesis was verified for perovskite thin films by studying the effect of film treatment with electron pair containing molecules such as thiophane and pyridine.[132] Perovskite NC defect passivation was investigated in a thorough study of DFT and experimental results from anionic ligand exchanges to show that softer Lewis base anions such as phosphonates, fluorinated carboxylates, and sulfonates are effective passivating groups for the soft Lewis acid character of undercoordinated lead.[106] Such results explain the high performance of phosphonate and sulfonate containing zwitterionic ligands described in Figure 1.4b.[124, 133]

1.3.2 *Polymer Composite Considerations*

This understanding of NC surface chemistry must then be paired with polymer science to develop a system that can suspend and stabilize perovskite NCs in a solid polymer composite. This can be done by designing a co-polymer system that contains NC binding groups and additional monomers that define the final polymer suspension medium. Of the possible NC binding groups described above, zwitterionic groups containing quaternary ammonium and sulfonate groups have been well validated through a number of NC ligand studies.[124, 133-134] Additionally, the distance between the ions on these groups can be tuned to accommodate the perovskite composition of interest by changing the number of methylene spacers between the ligand cationic and anionic groups,[124] providing an interesting route to tune these binding groups for a wide variety of perovskite materials. These groups are also commonly appended to polymer backbones for various applications,[135-136] including highly relevant demonstrations of their ability to stabilize perovskite solar cells.[137-138] Furthermore, tertiary amine groups can be

functionalized with zwitterionic groups post-polymerization, which increases the flexibility of zwitterionic polymer synthesis.[139-140]

Because of the inherent modularity of the co-polymer approach, various host matrix groups can be considered for this system. The broad use of acrylate polymer chemistry in LSCs[44, 49, 141] and their ease of processing led us to primarily investigated acrylate monomers for this work. Furthermore, as discussed in Section 1.2.2, partially fluorinate acrylate groups were investigated to limit NIR attenuation due to C – H bond absorption in LSCs. Prior studies of these polymers have established hexafluoroisopropyl methacrylate[80] and pentafluorophenyl methacrylate[81] as potential options for partially fluorinated host matrices. Of these two options, hexafluorisopropyl acrylate was chosen because this monomer and its non-fluorinated equivalent are both commercially available. Additionally, the branched nature of the isopropyl group is predicted to yield better solution processability and limit solid state aggregation when cast into thin films,[142-143] a property that is critical for its success in LSCs. Finally, in order to facilitate solution processability, chain transfer agents can be added during polymer synthesis to limit the molecular weight of the final polymers.[144] This yields polymers that are highly soluble, and by limiting the number of monomers in each polymer, the probability of forming a polymer that has two or more zwitterionic groups is reduced. This could limit NC crosslinking and aggregation in solid polymer composites.

1.3.3 *Methods of Evaluating NC/Polymer Stability*

Once a solid NC/polymer composite is successfully fabricated, it is important to evaluate the stability of the NCs within these composites under a variety of conditions. The simplest version of this measurement is to expose the sample to ambient atmospheric conditions for an extended period of time. Since oxygen and water are present in the atmosphere, this method of

stability characterization is particularly useful for evaluating the vulnerability of NC emission to oxygen and water exposure.[145-146] However, since most possible applications of these NCs rely on their stability under irradiation, it is critical that the photostability of any NC/polymer composite is thoroughly evaluated. This is because irradiation can catalyze several degradation reactions that have been shown to reduce the size of the cesium-based perovskite NCs with increased irradiation time, compromising their favorable optical properties.[103, 116-117] Furthermore, the thermalization of excited carriers to the perovskite band edge increases the internal temperature of the NCs, which can change the NC crystal structure in ways that compromises NC PLQY.[147-148]

Some previous reports have demonstrated impressive irradiation stability of perovskite NC/polymer composites. Meyns et al. made NC composites with poly(maleic anhydride-*alt*-1-octadecene) and demonstrate improved stability under 100 mW UV irradiation.[149] Raja et al. used polystyrene to stabilize NC composites that have high UV stability when analyzed by quantifying the number of photons absorbed per NCs before the samples fully degrade,[150] and He et al. used polymer micelles to stabilize NC solutions under 720 μW cm^{-2} UV irradiation.[151] Lu et al. stabilized perovskite NCs in a commercial, two component fluoropolymer called Hyflon AD 60, and demonstrated photostability under UV irradiation with a power intensity of 720 μW cm^{-2}.[152] These reports demonstrate qualitative improvements in photostability for a variety of NC/polymer composites, but the different sample preparation and irradiation quantification procedures makes it challenging to compare between these various studies. Furthermore, these measurements rely on single PL measurements taken with time intervals on the order of minutes or hours. This means that any decreases in PL intensity that occur on the timescales of seconds would be missed by these measurements.

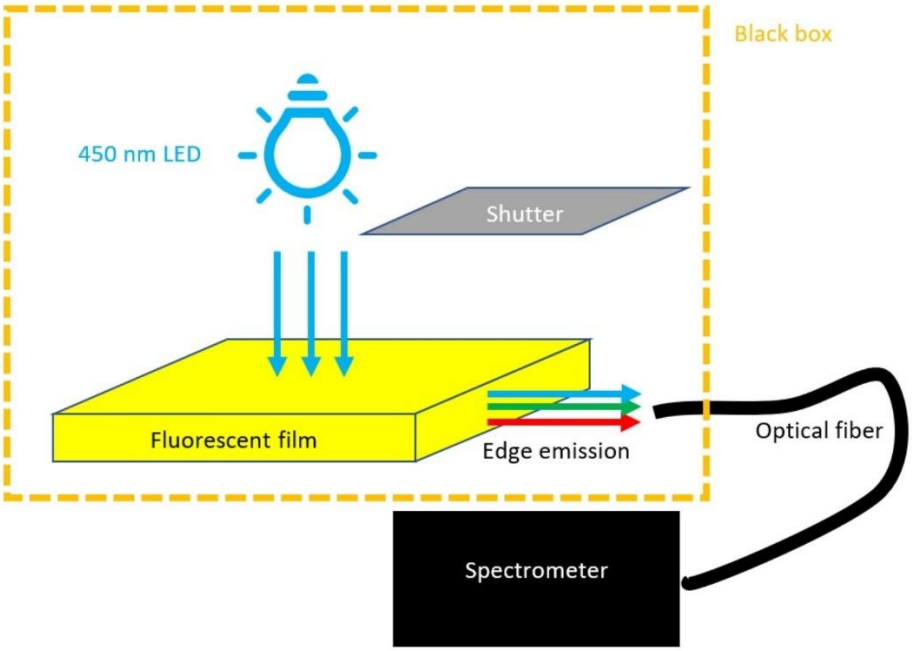

Figure 1.5. Diagram describing an irradiation stability measurement. A large-area, 50 W, 450 nm LED is mounted above a retractable shutter and the NC composite sample. Light emanating from the edge of the sample is collected through an optical fiber by a spectrometer. Once the shutter is retracted, continuous spectra can be collected at time intervals as small as seconds to observe early-time PL intensity dynamics. Reproduced with permission from ref. 153 Copywrite 2021 Royal Society of Chemistry.

Figure 1.5 describes an irradiation stability measurement appropriate for assessing a number of properties of perovskite NCs under high intensity illumination. This setup uses a 450 nm, large-area irradiation source to illuminate the full area of a NC sample. A shutter is placed between the irradiation source and the sample so that the initial LED intensity dynamics do not impact the stability measurement. A fiber coupled spectrometer is then used to collect full spectra from the sample with tunable collection intervals ranging from seconds to minutes. Additionally, the precise fluence incident on the entire facial area of the sample can be measured by replacing the sample with a calibrated photodiode. This eliminates the uncertainty regarding the translation of LED power to the actual fluence incident on the entire sample. Furthermore, full irradiation of the sample permits comparisons of the overall PLQY of the sample before and

after these measurements. Such data can be used to investigate whether the self-healing observed in methylammonium-based perovskite thin films is present in cesium-based perovskite NC/polymer composites.[154-155] Additionally, the use of a shutter and short collection intervals permits the detection and investigation of rapid changes in PL intensity under illumination that have been observed in formamidinium-based perovskite NCs.[156] Such changes are highly relevant for any potential application of NC/polymer composites.

1.4 Electrohydrodynamic Inkjet Processing of Perovskite Nanocrystals

The perovskite NC polymer stabilization approach described in Chapter 3 inspired a search for an interesting way to process these NCs for device applications. However, given the large amount of solvent and high cost required to fabricated perovskite NCs[157] and the development of methods to deposit large-area quantum-cutting scatter-free perovskite thin films via vapor deposition,[158] it was determined that a large-area NC-based LSCs were not the most ideal application for perovskite NCs. This inspired an exploration of methods to utilize NCs in applications that required smaller amounts of material than is needed to fabricate a full-scale LSC. On interesting opportunity is to use these NCs in emerging photonic device platforms that require coupling of NC emission to optical waveguides for quantum information and other applications. These devices require that NCs are deposited on solid structures while still maintaining their optical properties. These structures are several orders of magnitude smaller than typical LSCs, which reduces the amount of NC material required for these devices. In fact, some quantum photonic applications of these NCs requires the precise placement of single NCs on photonic devices.

The following section discusses the potential of electrohydrodynamic (EHD) inkjet printing as a method to process these NCs for photonic devices. Section 1.4.1 describes the relevant background of fluorescent NC patterning methods that motivates the development of this technique to process arrays of perovskite NCs, with the potential to place single NCs on quantum photonic devices. Section 1.4.2 describes the NC surface chemistry considerations necessary to formulate NC inks for EHD inkjet printing. These decisions are inspired by lessons learned in the polymer composite study described in Chapter 3. Finally, the necessary post-print characterization methods for these EHD inkjet-printed NCs are described in detail. This background is relevant to the use of EHD inkjet printing described in Chapter 4 to process $CsPbBr_3$ NCs for photonic device integration.

1.4.1 *Printing Motivations and Applications*

While the LSC applications of NCs discussed in Section 1.2 do not require precise materials patterning, LED and display technologies require that NCs structures are arranged on a device substrate with sub-micron precision. Within this effort to pattern luminescent materials, particular interest has been placed on the printing of single NCs to take advantage of their quantum coherence properties.[159-160] Early research in this area focused on III – V quantum wells fabricated with molecular beam epitaxy.[161-162] Tunable quantum dots of InAs fabricated with this method have been well characterized,[163] integrated with photonic circuits,[164] and optimized to yield single NCs with impressive optical coherence times.[165-167] However, the growth process cannot produce single, reproducible NCs on demand, which means that some post-synthesis NC selection is required to integrate these materials with photonic devices.[163-164, 168] This approach is promising for small investigations of single photonic devices, but would likely be incompatible with the complex architecture of a full integrate photonic circuit.[169] These substrate restricted

device designs can be addressed with atomic force microscope (AFM) based methods that either use electrostatics to “pick and place” emitters onto photonic devices[170-172] or heat an AFM tip to pick up and place NCs via hot-tip lithography.[173-175] Unfortunately, these approaches can be difficult to automate and may become impractical for large, complex device architectures. Transfer printing has also been used to deterministically place single NCs,[176] but this method still requires monitoring with an optical microscope to ensure precise NC placement on photonic devices.

When considering scalable materials patterning, most complex device structures are fabricated with lithography.[177] However, these methods have yet to be fully transferred to pattern luminescent NC materials. Early studies demonstrated that CdSe NCs could be patterned with optical lithography, but the NCs in these patterns typically had lower PLQYs and poor photostability.[178-179] More recently, optically-driven NC/ligand crosslinking reactions have been leveraged to produce high-resolution CdSe NC patterns with impressive electrical properties[180] and largely unchanged optical properties after patterning.[181-182] These methods are compatible with electron-beam lithography[183-184] and have evolved to be compatible with perovskite NCs.[185-187] Alternatives to optical and electron beam lithography include nanoimprint lithography[188-191] and other template-based techniques,[192-193] transfer printing,[194-197] and laser writing.[198-199] However, these inherently subtractive technique produces large amounts of material waste and either require a pre-fabricated mask or have long process times. They also cannot be used to pattern single NCs.

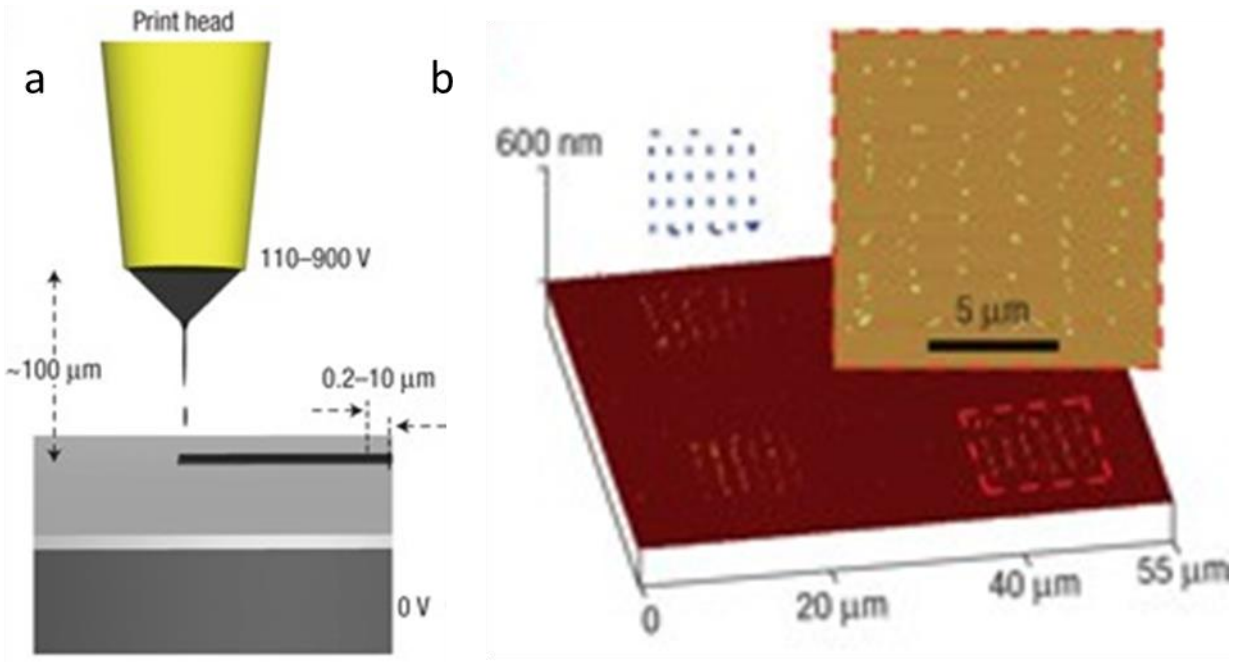

Figure 1.6. EHD inkjet-printing for materials processing. **(a)** Schematic describing the process of EHD inkjet printing. An electric field is applied from a print nozzle to a substrate, thereby creating a Taylor cone-shaped meniscus at the end of the print nozzle that generates far smaller droplets than is possible without an electric field **(b)** AFM images of EHD inkjet-printed polyurethane showing that sub-micron features can be generated with this method of printing. Reproduced with permission from ref. 200 Copywrite 2007 Springer Nature.

Inkjet printing is emerging as a promising method to pattern NCs for numerous applications,[201-203] because it is an additive, rapid, mask-free method of patterning colloidally stable materials with almost no material waste. Typical inkjet printing resolutions are limited to tens of microns, but it was discovered that an electric field could be used generate far smaller droplets and printed features than could be done previously.[200, 204] The sub-micron feature sizes demonstrated in Figure 1.6 suggests that this method of EHD inkjet printing is a highly promising method of patterning luminescent NCs. So far, EHD inkjet printing of luminescent NCs has been used to manufacture light emitting diodes,[205-206] photodetectors,[207] anti-counterfeit patterns,[208] and chip-integrated plasmonic lasers.[209-210] Additionally, EHD inkjet printing has been investigated as a potential method for patterning luminescent materials on integrated

photonic circuits. Early work in this area focused on integrating CdSe NCs with plasmonic structures,[211-212] and it was even shown that single CdSe NCs could be deterministically coupled to gold plasmonic wedge waveguides.[213] Organic dye molecules have also been coupled to photonic crystal cavities with EHD inkjet printing,[209] and a recent report demonstrates that quantum emitter behavior can be obtained from EHD printed terrylene dye molecules.[214] Since then, perovskite NCs have emerged as promising materials for photonic device integration due to their single photon emitter properties,[102-103] high optical coherence times,[104] and lifetime limited spin coherence.[215] Furthermore, it was shown that self-assembled perovskite NC superlattices have correlated quantum emission properties due to a superfluorescence-induced alignment of individual NC transition dipoles within these superlattices.[216] These NCs have been processed with EHD inkjet printing for LEDs[217] and radiative lifetime-encoded security tags,[208] but this method has not been used to deterministically place perovskite NCs on chip integrated photonic cavities.

1.4.2 *Perovskite NCs Ink Formulation and Print Characterization*

Some sections adapted with permission from Huang, Y.; A. Cohen, T.; M. Sperry, B.; Larson, H.; A. Nguyen, H.; K. Homer, M.; Y. Dou, F.; M. Jacoby, L.; M. Cossairt, B.; R. Gamelin, D.; K. Luscombe, C. *Materials Horizons* **2022**, *9*, 61. Copywrite 2022 Royal Society of Chemistry.

As discussed in Section 1.3, a careful consideration of NC surface chemistry is necessary to ensure that the NCs can be processed and stabilized for their intended application. Chapter 3 describes one example of a custom NC/polymer composite that excels at stabilizing perovskite NCs for various applications. However, prior studies of EHD inkjet printing of photoactive NCs demonstrated that NCs functionalized with typical organic ligands can be processed with EHD inkjet printing.[205, 218-219] Therefore, the library of typical perovskite NC ligands was considered

for the work described in **Error! Reference source not found.**. Amongst these options, we chose to investigate ligands that contain additional bromide. This is because in early work with perovskite NCs, it was noted that bromide ions play a critical role in ligand desorption reactions by coordinating with ammonium ions in solution.[120] This idea – along with the attribution of low NC PLQY to undercoordinated lead discussed in Section 1.3.1 – led researchers to explore routes to add additional halide anions to passivate these defects, considering that halides are native lead-coordinating components in perovskite lattices. Post-synthetic treatment with excess lead bromide,[220] and halide containing ligands such as didodecyl dimethylammonium bromide (DDABr) [221-223] and oleylammonium halide[224] also improve the PLQY and stability of perovskite NCs. This treatment with DDABr and other similar ligands has proven effective, and quaternary ammonium bromide-containing ligands has become a popular perovskite NC passivating group.[109, 116, 146, 208, 225-226] Therefore, we chose DDABr to develop EHD inkjet printable perovskite NC inks. Furthermore, the small droplets generated with this technique elevate the evaporation rate of NC solvents.[227] This motivates the use of high boiling point solvents such as tetradecane and 1,3,5-triethylbenzene for this technique. These solvents have relatively low polarizability, which suggests that the dielectric properties of the NCs will be most relevant to the printing process.

Previous studies of perovskite NC properties when placed high electric fields[228] and processed with EHD inkjet printing[208, 217] suggest that the original NC properties can be preserved after exposure to high electric fields. However, closed-packed perovskite NC structures can degrade in ways that cannot be detected by typical physical and spectroscopic characterization methods.[229] These changes can be seen by TEM, which motivates the development of methods to perform TEM of EHD inkjet-printed NCs. The carbon coated metal

TEM grids typically used for imaging non-printed NCs have been used in other reports of EHD inkjet printing,[230-232] but 6 – 12 kV of printing bias were required to print on these grids. Alternatively, silicon nitride membrane window TEM grids are silicon substrates that contain small windows of silicon nitride within the substrate facial area. These windows are ~30 nm thick, which is sufficiently transparent to electron beams that any material on top of them can be imaged with TEM. The silicon support structures of these grids are similar to the silicon substrates typically used for EHD inkjet printing, which suggests that similar print parameters to those used for silicon substrates can be used to print NCs onto these TEM grids. Upon imaging, given the high instability of perovskite NCs to electron beam exposure,[233] it is possible that the insulating nature of these grids will facilitate beam-induced degradation. This can be remedied by applying a small carbon coating to the silicon nitride membrane window TEM grid.

1.5 CONCLUSION

In summary, we've discussed three interesting use-inspired research areas of interest for perovskite NCs that can inform future device applications of these materials. These NCs have many impressive optical properties that can be utilized in numerous fundamental and applied studies. However, more work that leverages fundamental understanding in use-inspired work will be critical to develop these materials for their numerous potential applications. To this end, Section 1.2 discussed the considerations and experiments necessary to use quantum-cutting Yb^{3+}-doped perovskite NCs in LSCs. The implications of these studies regarding ideal polymer host matrices for LSCs motivate the development of modular NC/polymer composites, as discussed in Section 1.3. Finally, Section 1.4 explores ways to leverage fundamental knowledge of NC surface chemistry to process perovskite NCs with EHD inkjet printing. These discussions introduce several possible experimental and theoretical investigations of perovskite NCs that

range from more fundamental to more applied in nature. Such broad investigations should produce fundamental understanding while also yielding several use-inspired materials platforms and processes to help translate perovskite NCs from lab innovations to real-world products.

1.6 REFERENCES

1. Ekimov, A.; Onushchehko, A., Quantum Size Effect in Three-Dimensional Microscopic Semiconductor Crystals. *ZhETF Pis ma Redaktsiiu* **1981,** *34*, 363.
2. Rossetti, R.; Nakahara, S.; Brus, L. E., Quantum Size Effects in the Redox Potentials, Resonance Raman Spectra, and Electronic Spectra of Cds Crystallites in Aqueous Solution. *J. Chem. Phys.* **1983,** *79*, 1086-1088.
3. Murray, C. B.; Norris, D. J.; Bawendi, M. G., Synthesis and Characterization of Nearly Monodisperse Cde (E = Sulfur, Selenium, Tellurium) Semiconductor Nanocrystallites. *J. Am. Chem. Soc.* **1993,** *115*, 8706-8715.
4. Shimizu, K. T.; Böhmer, M.; Estrada, D.; Gangwal, S.; Grabowski, S.; Bechtel, H.; Kang, E.; Vampola, K. J.; Chamberlin, D.; Shchekin, O. B.; Bhardwaj, J., Toward Commercial Realization of Quantum Dot Based White Light-Emitting Diodes for General Illumination. *Photonics Res.* **2017,** *5*, A1-A6.
5. Gary, D. C.; Terban, M. W.; Billinge, S. J. L.; Cossairt, B. M., Two-Step Nucleation and Growth of Inp Quantum Dots Via Magic-Sized Cluster Intermediates. *Chem. Mater.* **2015,** *27*, 1432-1441.
6. Cossairt, B. M., Shining Light on Indium Phosphide Quantum Dots: Understanding the Interplay among Precursor Conversion, Nucleation, and Growth. *Chem. Mater.* **2016,** *28*, 7181-7189.
7. Li, Y.; Hou, X.; Dai, X.; Yao, Z.; Lv, L.; Jin, Y.; Peng, X., Stoichiometry-Controlled Inp-Based Quantum Dots: Synthesis, Photoluminescence, and Electroluminescence. *J. Am. Chem. Soc.* **2019,** *141*, 6448-6452.
8. Kim, Y.; Ham, S.; Jang, H.; Min, J. H.; Chung, H.; Lee, J.; Kim, D.; Jang, E., Bright and Uniform Green Light Emitting Inp/Znse/Zns Quantum Dots for Wide Color Gamut Displays. *ACS Appl. Nano Mater.* **2019,** *2*, 1496-1504.
9. Carey, G. H.; Abdelhady, A. L.; Ning, Z.; Thon, S. M.; Bakr, O. M.; Sargent, E. H., Colloidal Quantum Dot Solar Cells. *Chem. Rev.* **2015,** *115*, 12732-12763.
10. Sargent, E. H., Solar Cells, Photodetectors, and Optical Sources from Infrared Colloidal Quantum Dots. *Adv. Mater.* **2008,** *20*, 3958-3964.
11. Bruchez, M.; Moronne, M.; Gin, P.; Weiss, S.; Alivisatos, A. P., Semiconductor Nanocrystals as Fluorescent Biological Labels. *Science* **1998,** *281*, 2013-2016.
12. Amirav, L.; Alivisatos, A. P., Luminescence Studies of Individual Quantum Dot Photocatalysts. *J. Am. Chem. Soc.* **2013,** *135*, 13049-13053.
13. Stokes, D. E., *Pasteur's Quadrant: Basic Science and Technological Innovation*. Brookings Institution Press: 1997; p 204.
14. Amara, N.; Olmos-Peñuela, J.; Fernández-de-Lucio, I., Overcoming the "Lost before Translation" Problem: An Exploratory Study. *Research Policy* **2019,** *48*, 22-36.
15. Mankins, J. C.; others, Technology Readiness Levels. *White Paper, April* **1995,** *6*, 1995.

16. *Technology Readiness Assessment (Tra) Guidance*; Department of Defense: 2011/05/13/, 2011; p 21.
17. Engel, D. W.; Dalton, A. C.; Anderson, K. K.; Sivaramakrishnan, C.; Lansing, C. *Development of Technology Readiness Level (Trl) Metrics and Risk Measures*; PNNL-21737, 1067968; 2012/10/01/, 2012; pp PNNL-21737, 1067968.
18. Protesescu, L.; Yakunin, S.; Bodnarchuk, M. I.; Krieg, F.; Caputo, R.; Hendon, C. H.; Yang, R. X.; Walsh, A.; Kovalenko, M. V., Nanocrystals of Cesium Lead Halide Perovskites ($CsPbX_3$, X = Cl, Br, and I): Novel Optoelectronic Materials Showing Bright Emission with Wide Color Gamut. *Nano Lett.* **2015,** *15*, 3692-3696.
19. Møller, C. K., Crystal Structure and Photoconductivity of Cæsium Plumbohalides. *Nature* **1958,** *182*, 1436-1436.
20. Kojima, A.; Teshima, K.; Shirai, Y.; Miyasaka, T., Organometal Halide Perovskites as Visible-Light Sensitizers for Photovoltaic Cells. *J. Am. Chem. Soc.* **2009,** *131*, 6050-6051.
21. Etgar, L.; Gao, P.; Xue, Z.; Peng, Q.; Chandiran, A. K.; Liu, B.; Nazeeruddin, M. K.; Grätzel, M., Mesoscopic $CH_3NH_3PbI_3/TiO_2$ Heterojunction Solar Cells. *J. Am. Chem. Soc.* **2012,** *134*, 17396-17399.
22. Lee, M. M.; Teuscher, J.; Miyasaka, T.; Murakami, T. N.; Snaith, H. J., Efficient Hybrid Solar Cells Based on Meso-Superstructured Organometal Halide Perovskites. *Science* **2012,** *338*, 643-647.
23. Berry, J.; Buonassisi, T.; Egger, D. A.; Hodes, G.; Kronik, L.; Loo, Y.-L.; Lubomirsky, I.; Marder, S. R.; Mastai, Y.; Miller, J. S.; Mitzi, D. B.; Paz, Y.; Rappe, A. M.; Riess, I.; Rybtchinski, B.; Stafsudd, O.; Stevanovic, V.; Toney, M. F.; Zitoun, D.; Kahn, A.; Ginley, D.; Cahen, D., Hybrid Organic–Inorganic Perovskites (Hoips): Opportunities and Challenges. *Adv. Mater.* **2015,** *27*, 5102-5112.
24. Weber, W. H.; Lambe, J., Luminescent Greenhouse Collector for Solar Radiation. *Appl. Opt.* **1976,** *15*, 2299-2300.
25. Batchelder, J. S.; Zewail, A. H.; Cole, T., Luminescent Solar Concentrators .1. Theory of Operation and Techniques for Performance Evaluation. *Appl. Opt.* **1979,** *18*, 3090-3110.
26. Debije, M. G.; Verbunt, P. P. C., Thirty Years of Luminescent Solar Concentrator Research: Solar Energy for the Built Environment. *Adv. Energy Mater.* **2012,** *2*, 12-35.
27. Mazzaro, R.; Vomiero, A., The Renaissance of Luminescent Solar Concentrators: The Role of Inorganic Nanomaterials. *Adv. Energy Mater.* **2018,** *8*, 1801903.
28. Roncali, J., Luminescent Solar Collectors: Quo Vadis? *Adv. Energy Mater.* **2020**, 2001907.
29. Yablonovitch, E., Thermodynamics of the Fluorescent Planar Concentrator. *J. Opt. Soc. Am.* **1980,** *70*, 1362-1363.
30. Smestad, G.; Ries, H.; Winston, R.; Yablonovitch, E., The Thermodynamic Limits of Light Concentrators. *Sol. Energy Mater.* **1990,** *21*, 99-111.
31. Papakonstantinou, I.; Tummeltshammer, C., Fundamental Limits of Concentration in Luminescent Solar Concentrators Revised: The Effect of Reabsorption and Nonunity Quantum Yield. *Optica* **2015,** *2*, 841-849.
32. Slooff, L. H.; Bende, E. E.; Burgers, A. R.; Budel, T.; Pravettoni, M.; Kenny, R. P.; Dunlop, E. D.; Büchtemann, A., A Luminescent Solar Concentrator with 7.1% Power Conversion Efficiency. *Phys. Status Solidi Rapid Res. Lett.* **2008,** *2*, 257-259.

33. Zhang, J.; Wang, M.; Zhang, Y.; He, H.; Xie, W.; Yang, M.; Ding, J.; Bao, J.; Sun, S.; Gao, C., Optimization of Large-Size Glass Laminated Luminescent Solar Concentrators. *Sol. Energy* **2015,** *117*, 260-267.
34. Vossen, F. M.; Aarts, M. P. J.; Debije, M. G., Visual Performance of Red Luminescent Solar Concentrating Windows in an Office Environment. *Energ. Buildings* **2016,** *113*, 123-132.
35. Sark, W. v.; Moraitis, P.; Aalberts, C.; Drent, M.; Grasso, T.; L'Ortije, Y.; Visschers, M.; Westra, M.; Plas, R.; Planje, W., The "Electric Mondrian" as a Luminescent Solar Concentrator Demonstrator Case Study. *Sol. RRL* **2017,** *1*, 1600015.
36. Jeżowska-Trzebiatowska, B.; Łukowiak, E.; Stręk, W.; Buczkowski, A.; Patela, S.; Radojewski, J.; Sarzyński, J., Neodymium-Chromium Doped Phosphate Glasses as Luminescent Solar Concentrators. *Sol. Energy Mater* **1986,** *13*, 267-277.
37. Rufino Souza, A. K.; Langaro, A. P.; Silva, J. R.; Costa, F. B.; Yukimitu, K.; Silos Moraes, J. C.; Antonio de Oliveira Nunes, L.; Humberto da Cunha Andrade, L.; Lima, S. M., On the Efficient $Te^{4+} \rightarrow Yb^{3+}$ Cooperative Energy Transfer Mechanism in Tellurite Glasses: A Potential Material for Luminescent Solar Concentrators. *J. Alloys Compd.* **2019,** *781*, 1119-1126.
38. Currie, M. J.; Mapel, J. K.; Heidel, T. D.; Goffri, S.; Baldo, M. A., High-Efficiency Organic Solar Concentrators for Photovoltaics. *Science* **2008,** *321*, 226-228.
39. Wang, T.; Zhang, J.; Ma, W.; Luo, Y.; Wang, L.; Hu, Z.; Wu, W.; Wang, X.; Zou, G.; Zhang, Q., Luminescent Solar Concentrator Employing Rare Earth Complex with Zero Self-Absorption Loss. *Sol. Energy* **2011,** *85*, 2571-2579.
40. Sanguineti, A.; Monguzzi, A.; Vaccaro, G.; Meinardi, F.; Ronchi, E.; Moret, M.; Cosentino, U.; Moro, G.; Simonutti, R.; Mauri, M.; Tubino, R.; Beverina, L., Nir Emitting Ytterbium Chelates for Colourless Luminescent Solar Concentrators. *Phys. Chem. Chem. Phys.* **2012,** *14*, 6452-6455.
41. Purcell-Milton, F.; Gun'ko, Y. K., Quantum Dots for Luminescent Solar Concentrators. *J. Mater. Chem.* **2012,** *22*, 16687-16697.
42. Bronstein, N. D.; Li, L.; Xu, L.; Yao, Y.; Ferry, V. E.; Alivisatos, A. P.; Nuzzo, R. G., Luminescent Solar Concentration with Semiconductor Nanorods and Transfer-Printed Micro-Silicon Solar Cells. *ACS Nano* **2014,** *8*, 44-53.
43. Coropceanu, I.; Bawendi, M. G., Core/Shell Quantum Dot Based Luminescent Solar Concentrators with Reduced Reabsorption and Enhanced Efficiency. *Nano Lett.* **2014,** *14*, 4097-4101.
44. Erickson, C. S.; Bradshaw, L. R.; McDowall, S.; Gilbertson, J. D.; Gamelin, D. R.; Patrick, D. L., Zero-Reabsorption Doped-Nanocrystal Luminescent Solar Concentrators. *ACS Nano* **2014,** *8*, 3461-3467.
45. Meinardi, F.; Colombo, A.; Velizhanin, K. A.; Simonutti, R.; Lorenzon, M.; Beverina, L.; Viswanatha, R.; Klimov, V. I.; Brovelli, S., Large-Area Luminescent Solar Concentrators Based on 'Stokes-Shift-Engineered' Nanocrystals in a Mass-Polymerized Pmma Matrix. *Nat. Photonics* **2014,** *8*, 392-399.
46. Bradshaw, L. R.; Knowles, K. E.; McDowall, S.; Gamelin, D. R., Nanocrystals for Luminescent Solar Concentrators. *Nano Lett.* **2015,** *15*, 1315-1323.
47. Knowles, K. E.; Kilburn, T. B.; Alzate, D. G.; McDowall, S.; Gamelin, D. R., Bright $CuInS_2$/CdS Nanocrystal Phosphors for High-Gain Full-Spectrum Luminescent Solar Concentrators. *Chem. Commun.* **2015,** *51*, 9129-9132.

48. Meinardi, F.; McDaniel, H.; Carulli, F.; Colombo, A.; Velizhanin, K. A.; Makarov, N. S.; Simonutti, R.; Klimov, V. I.; Brovelli, S., Highly Efficient Large-Area Colourless Luminescent Solar Concentrators Using Heavy-Metal-Free Colloidal Quantum Dots. *Nat. Nanotechnol.* **2015,** *10*, 878-885.
49. Meinardi, F.; Akkerman, Q. A.; Bruni, F.; Park, S.; Mauri, M.; Dang, Z.; Manna, L.; Brovelli, S., Doped Halide Perovskite Nanocrystals for Reabsorption-Free Luminescent Solar Concentrators. *ACS Energy Lett.* **2017,** *2*, 2368-2377.
50. Sumner, R.; Eiselt, S.; Kilburn, T. B.; Erickson, C.; Carlson, B.; Gamelin, D. R.; McDowall, S.; Patrick, D. L., Analysis of Optical Losses in High-Efficiency $Cuins_2$-Based Nanocrystal Luminescent Solar Concentrators: Balancing Absorption Versus Scattering. *J. Phys. Chem. C* **2017,** *121*, 3252-3260.
51. Sharma, M.; Gungor, K.; Yeltik, A.; Olutas, M.; Guzelturk, B.; Kelestemur, Y.; Erdem, T.; Delikanli, S.; McBride, J. R.; Demir, H. V., Near-Unity Emitting Copper-Doped Colloidal Semiconductor Quantum Wells for Luminescent Solar Concentrators. *Adv. Mater.* **2017,** *29*, 1700821.
52. Bergren, M. R.; Makarov, N. S.; Ramasamy, K.; Jackson, A.; Guglielmetti, R.; McDaniel, H., High-Performance $CuInS_2$ Quantum Dot Laminated Glass Luminescent Solar Concentrators for Windows. *ACS Energy Lett.* **2018,** *3*, 520-525.
53. Wu, K.; Li, H.; Klimov, V. I., Tandem Luminescent Solar Concentrators Based on Engineered Quantum Dots. *Nat. Photonics* **2018,** *12*, 105-110.
54. Moraitis, P.; Schropp, R. E. I.; van Sark, W. G. J. H. M., Nanoparticles for Luminescent Solar Concentrators - a Review. *Opt. Mater.* **2018,** *84*, 636-645.
55. Zhou, Y.; Zhao, H.; Ma, D.; Rosei, F., Harnessing the Properties of Colloidal Quantum Dots in Luminescent Solar Concentrators. *Chem. Soc. Rev.* **2018,** *47*, 5866-5890.
56. Luo, X.; Ding, T.; Liu, X.; Liu, Y.; Wu, K., Quantum-Cutting Luminescent Solar Concentrators Using Ytterbium-Doped Perovskite Nanocrystals. *Nano Lett.* **2019,** *19*, 338-341.
57. Cohen, T. A.; Milstein, T. J.; Kroupa, D. M.; MacKenzie, J. D.; Luscombe, C. K.; Gamelin, D. R., Quantum-Cutting Yb^{3+}-Doped Perovskite Nanocrystals for Monolithic Bilayer Luminescent Solar Concentrators. *J. Mater. Chem. A* **2019,** *7*, 9279-9288.
58. Sadeghi, S.; Bahmani Jalali, H.; Srivastava, S. B.; Melikov, R.; Baylam, I.; Sennaroglu, A.; Nizamoglu, S., High-Performance, Large-Area, and Ecofriendly Luminescent Solar Concentrators Using Copper-Doped Inp Quantum Dots. *iScience* **2020,** *23*, 101272.
59. Li, H.; Wu, K.; Lim, J.; Song, H.-J.; Klimov, V. I., Doctor-Blade Deposition of Quantum Dots onto Standard Window Glass for Low-Loss Large-Area Luminescent Solar Concentrators. *Nat. Energy* **2016,** *1*, 16157.
60. Zhao, H.; Benetti, D.; Jin, L.; Zhou, Y.; Rosei, F.; Vomiero, A., Absorption Enhancement in "Giant" Core/Alloyed-Shell Quantum Dots for Luminescent Solar Concentrator. *Small* **2016,** *12*, 5354-5365.
61. Breukers, R. D.; Smith, G. J.; Stirrat, H. L.; Swanson, A. J.; Smith, T. A.; Ghiggino, K. P.; Raymond, S. G.; Winch, N. M.; Clarke, D. J.; Kay, A. J., Light Losses from Scattering in Luminescent Solar Concentrator Waveguides. *Appl. Opt.* **2017,** *56*, 2630-2635.
62. Yang, C.; Zhang, J.; Peng, W.-T.; Sheng, W.; Liu, D.; Kuttipillai, P. S.; Young, M.; Donahue, M. R.; Levine, B. G.; Borhan, B.; Lunt, R. R., Impact of Stokes Shift on the

Performance of near-Infrared Harvesting Transparent Luminescent Solar Concentrators. *Sci. Rep.* **2018,** *8*, 1-10.

63. Needell, D. R.; Ilic, O.; Bukowsky, C. R.; Nett, Z.; Xu, L.; He, J.; Bauser, H.; Lee, B. G.; Geisz, J. F.; Nuzzo, R. G.; Alivisatos, A. P.; Atwater, H. A., Design Criteria for Micro-Optical Tandem Luminescent Solar Concentrators. *IEEE J. Photovolt.* **2018,** *8*, 1-8.
64. Li, C.; Chen, W.; Wu, D.; Quan, D.; Zhou, Z.; Hao, J.; Qin, J.; Li, Y.; He, Z.; Wang, K., Large Stokes Shift and High Efficiency Luminescent Solar Concentrator Incorporated with $Cuins_2$/Zns Quantum Dots. *Sci. Rep.* **2015,** *5*, 17777.
65. Velarde, A. R. M.; Bartlett, E. R.; Makarov, N. S.; Castañeda, C.; Jackson, A.; Ramasamy, K.; Bergren, M. R.; McDaniel, H., Optimizing the Aesthetics of High-Performance $CuInS_2$/ZnS Quantum Dot Luminescent Solar Concentrator Windows. *ACS Appl. Energy Mater.* **2020**.
66. Tanner, P. A., Electronic Spectra of Yb^{3+} in Elpasolite Lattices. *Molecular Physics* **1986,** *58*, 317-328.
67. Acevedo, R.; Tanner, P. A.; Meruane, T.; Poblete, V., Vibronic Intensities in the Absorption Spectra of Yb^{3+}. *Phys. Rev. B* **1996,** *54*, 3976-3988.
68. Martín-Rodríguez, R.; Geitenbeek, R.; Meijerink, A., Incorporation and Luminescence of Yb^{3+} in CdSe Nanocrystals. *J. Am. Chem. Soc.* **2013,** *135*, 13668-13671.
69. Creutz, S. E.; Fainblat, R.; Kim, Y.; De Siena, M. C.; Gamelin, D. R., A Selective Cation Exchange Strategy for the Synthesis of Colloidal Yb3+-Doped Chalcogenide Nanocrystals with Strong Broadband Visible Absorption and Long-Lived near-Infrared Emission. *J. Am. Chem. Soc.* **2017,** *139*, 11814-11824.
70. Zhou, D.; Liu, D.; Pan, G.; Chen, X.; Li, D.; Xu, W.; Bai, X.; Song, H., Cerium and Ytterbium Codoped Halide Perovskite Quantum Dots: A Novel and Efficient Downconverter for Improving the Performance of Silicon Solar Cells. *Adv. Mater.* **2017,** *29*, 1704149.
71. Pan, G.; Bai, X.; Yang, D.; Chen, X.; Jing, P.; Qu, S.; Zhang, L.; Zhou, D.; Zhu, J.; Xu, W.; Dong, B.; Song, H., Doping Lanthanide into Perovskite Nanocrystals: Highly Improved and Expanded Optical Properties. *Nano Lett.* **2017,** *17*, 8005-8011.
72. Milstein, T. J.; Kroupa, D. M.; Gamelin, D. R., Picosecond Quantum Cutting Generates Photoluminescence Quantum Yields over 100% in Ytterbium-Doped $Cspbcl_3$ Nanocrystals. *Nano Lett.* **2018,** *18*, 3792–3799.
73. Kroupa, D. M.; Roh, J. Y. D.; Milstein, T. J.; Creutz, S. E.; Gamelin, D. R., Quantum-Cutting Ytterbium-Doped $CsPb(Cl_{1-x}Br_x)_3$ Perovskite Thin Films with Photoluminescence Quantum Yields over 190%. *ACS Energy Lett.* **2018,** *3*, 2390-2395.
74. Milstein, T. J.; Kluherz, K. T.; Kroupa, D. M.; Erickson, C. S.; De Yoreo, J. J.; Gamelin, D. R., Anion Exchange and the Quantum-Cutting Energy Threshold in Ytterbium-Doped $CsPb(Cl_{1-x}Br_x)_3$ Perovskite Nanocrystals. *Nano Lett.* **2019,** *19*, 1931-1937.
75. Earp, A. A.; Smith, G. B.; Franklin, J.; Swift, P., Optimisation of a Three-Colour Luminescent Solar Concentrator Daylighting System. *Sol. Energy Mater. Sol. Cells* **2004,** *84*, 411-426.
76. Zhao, H.; Benetti, D.; Tong, X.; Zhang, H.; Zhou, Y.; Liu, G.; Ma, D.; Sun, S.; Wang, Z. M.; Wang, Y.; Rosei, F., Efficient and Stable Tandem Luminescent Solar Concentrators Based on Carbon Dots and Perovskite Quantum Dots. *Nano Energy* **2018,** *50*, 756-765.
77. Groh, W., Overtone Absorption in Macromolecules for Polymer Optical Fibers. *Die Makromol. Chemie* **1988,** *189*, 2861-2874.

78. Meinardi, F.; Bruni, F.; Brovelli, S., Luminescent Solar Concentrators for Building-Integrated Photovoltaics. *Nat. Rev. Mater.* **2017,** *2*, 17072.
79. Ioannides, N.; Chunga, E. B.; Bachmatiuk, A.; Gonzalez-Martinez, I. G.; Trzebicka, B.; Adebimpe, D. B.; Kalymnios, D.; Rümmeli, M. H., Approaches to Mitigate Polymer-Core Loss in Plastic Optical Fibers: A Review. *Mater. Res. Express* **2014,** *1*, 032002.
80. Zhou, D.; Teng, H.; Koike, K.; Koike, Y.; Okamoto, Y., Copolymers of Methyl Methacrylate and Fluoroalkyl Methacrylates: Effects of Fluoroalkyl Groups on the Thermal and Optical Properties of the Copolymers. *J. Polym. Sci. Pol. Chem.* **2008,** *46*, 4748-4755.
81. Koike, K.; Kado, T.; Satoh, Z.; Okamoto, Y.; Koike, Y., Optical and Thermal Properties of Methyl Methacrylate and Pentafluorophenyl Methacrylate Copolymer: Design of Copolymers for Low-Loss Optical Fibers for Gigabit in-Home Communications. *Polymer* **2010,** *51*, 1377-1385.
82. Jun, S.; Lee, J.; Jang, E., Highly Luminescent and Photostable Quantum Dot–Silica Monolith and Its Application to Light-Emitting Diodes. *ACS Nano* **2013,** *7*, 1472-1477.
83. Boles, M. A.; Ling, D.; Hyeon, T.; Talapin, D. V., The Surface Science of Nanocrystals. *Nat. Mater.* **2016,** *15*, 141.
84. Zhou, J.; Zhu, M.; Meng, R.; Qin, H.; Peng, X., Ideal Cdse/Cds Core/Shell Nanocrystals Enabled by Entropic Ligands and Their Core Size-, Shell Thickness-, and Ligand-Dependent Photoluminescence Properties. *J. Am. Chem. Soc.* **2017,** *139*, 16556-16567.
85. Jeong, J.; Kim, M.; Seo, J.; Lu, H.; Ahlawat, P.; Mishra, A.; Yang, Y.; Hope, M. A.; Eickemeyer, F. T.; Kim, M.; Yoon, Y. J.; Choi, I. W.; Darwich, B. P.; Choi, S. J.; Jo, Y.; Lee, J. H.; Walker, B.; Zakeeruddin, S. M.; Emsley, L.; Rothlisberger, U.; Hagfeldt, A.; Kim, D. S.; Grätzel, M.; Kim, J. Y., Pseudo-Halide Anion Engineering for A-$FAPbI_3$ Perovskite Solar Cells. *Nature* **2021,** *592*, 381-385.
86. Lin, R.; Xiao, K.; Qin, Z.; Han, Q.; Zhang, C.; Wei, M.; Saidaminov, M. I.; Gao, Y.; Xu, J.; Xiao, M.; Li, A.; Zhu, J.; Sargent, E. H.; Tan, H., Monolithic All-Perovskite Tandem Solar Cells with 24.8% Efficiency Exploiting Comproportionation to Suppress Sn(II) Oxidation in Precursor Ink. *Nat. Energy* **2019,** *4*, 864-873.
87. Al-Ashouri, A.; Köhnen, E.; Li, B.; Magomedov, A.; Hempel, H.; Caprioglio, P.; Márquez, J. A.; Vilches, A. B. M.; Kasparavicius, E.; Smith, J. A.; Phung, N.; Menzel, D.; Grischek, M.; Kegelmann, L.; Skroblin, D.; Gollwitzer, C.; Malinauskas, T.; Jošt, M.; Matič, G.; Rech, B.; Schlatmann, R.; Topič, M.; Korte, L.; Abate, A.; Stannowski, B.; Neher, D.; Stolterfoht, M.; Unold, T.; Getautis, V.; Albrecht, S., Monolithic Perovskite/Silicon Tandem Solar Cell with <29% Efficiency by Enhanced Hole Extraction. *Science* **2020,** *370*, 1300-1309.
88. Koscher, B. A.; Swabeck, J. K.; Bronstein, N. D.; Alivisatos, A. P., Essentially Trap-Free $CsPbBr_3$ Colloidal Nanocrystals by Postsynthetic Thiocyanate Surface Treatment. *J. Am. Chem. Soc.* **2017,** *139*, 6566-6569.
89. Zhang, Y.; Siegler, T. D.; Thomas, C. J.; Abney, M. K.; Shah, T.; De Gorostiza, A.; Greene, R. M.; Korgel, B. A., A "Tips and Tricks" Practical Guide to the Synthesis of Metal Halide Perovskite Nanocrystals. *Chem. Mater.* **2020,** *32*, 5410–5423.
90. Pradhan, N., Tips and Twists in Making High Photoluminescence Quantum Yield Perovskite Nanocrystals. *ACS Energy Lett.* **2019,** *4*, 1634-1638.

91. Utzat, H.; Shulenberger, K. E.; Achorn, O. B.; Nasilowski, M.; Sinclair, T. S.; Bawendi, M. G., Probing Linewidths and Biexciton Quantum Yields of Single Cesium Lead Halide Nanocrystals in Solution. *Nano Lett.* **2017,** *17*, 6838-6846.
92. Chen, Z.; Li, H.; Tang, Y.; Huang, X.; Ho, D.; Lee, C.-S., Shape-Controlled Synthesis of Organolead Halide Perovskite Nanocrystals and Their Tunable Optical Absorption. *Mater. Res. Express* **2014,** *1*, 015034.
93. Li, G.; Tan, Z.-K.; Di, D.; Lai, M. L.; Jiang, L.; Lim, J. H.-W.; Friend, R. H.; Greenham, N. C., Efficient Light-Emitting Diodes Based on Nanocrystalline Perovskite in a Dielectric Polymer Matrix. *Nano Lett.* **2015,** *15*, 2640-2644.
94. Kim, Y.-H.; Kim, S.; Kakekhani, A.; Park, J.; Park, J.; Lee, Y.-H.; Xu, H.; Nagane, S.; Wexler, R. B.; Kim, D.-H.; Jo, S. H.; Martínez-Sarti, L.; Tan, P.; Sadhanala, A.; Park, G.-S.; Kim, Y.-W.; Hu, B.; Bolink, H. J.; Yoo, S.; Friend, R. H.; Rappe, A. M.; Lee, T.-W., Comprehensive Defect Suppression in Perovskite Nanocrystals for High-Efficiency Light-Emitting Diodes. *Nat. Photonics* **2021,** *15*, 148-155.
95. Zhao, Q.; Hazarika, A.; Schelhas, L. T.; Liu, J.; Gaulding, E. A.; Li, G.; Zhang, M.; Toney, M. F.; Sercel, P. C.; Luther, J. M., Size-Dependent Lattice Structure and Confinement Properties in Cspbi3 Perovskite Nanocrystals: Negative Surface Energy for Stabilization. *ACS Energy Lett.* **2020,** *5*, 238-247.
96. Yakunin, S.; Protesescu, L.; Krieg, F.; Bodnarchuk, M. I.; Nedelcu, G.; Humer, M.; Luca, G. D.; Fiebig, M.; Heiss, W.; Kovalenko, M. V., Low-Threshold Amplified Spontaneous Emission and Lasing from Colloidal Nanocrystals of Caesium Lead Halide Perovskites. *Nat. Commun.* **2015,** *6*, 8056.
97. Jia, Y.; Kerner, R. A.; Grede, A. J.; Brigeman, A. N.; Rand, B. P.; Giebink, N. C., Diode-Pumped Organo-Lead Halide Perovskite Lasing in a Metal-Clad Distributed Feedback Resonator. *Nano Lett.* **2016,** *16*, 4624-4629.
98. Jia, Y.; Kerner, R. A.; Grede, A. J.; Rand, B. P.; Giebink, N. C., Continuous-Wave Lasing in an Organic–Inorganic Lead Halide Perovskite Semiconductor. *Nat. Photonics* **2017,** *11*, 784-788.
99. Yoo, D.; Woo, J. Y.; Kim, Y.; Kim, S. W.; Wei, S.-H.; Jeong, S.; Kim, Y.-H., Origin of the Stability and Transition from Anionic to Cationic Surface Ligand Passivation of All-Inorganic Cesium Lead Halide Perovskite Nanocrystals. *J. Phys. Chem. Lett.* **2020,** *11*, 652-658.
100. Wei, H.; Fang, Y.; Mulligan, P.; Chuirazzi, W.; Fang, H.-H.; Wang, C.; Ecker, B. R.; Gao, Y.; Loi, M. A.; Cao, L.; Huang, J., Sensitive X-Ray Detectors Made of Methylammonium Lead Tribromide Perovskite Single Crystals. *Nat. Photonics* **2016,** *10*, 333-339.
101. Liu, J.; Shabbir, B.; Wang, C.; Wan, T.; Ou, Q.; Yu, P.; Tadich, A.; Jiao, X.; Chu, D.; Qi, D.; Li, D.; Kan, R.; Huang, Y.; Dong, Y.; Jasieniak, J.; Zhang, Y.; Bao, Q., Flexible, Printable Soft-X-Ray Detectors Based on All-Inorganic Perovskite Quantum Dots. *Adv. Mater.* **2019,** *31*, 1901644.
102. Rainò, G.; Nedelcu, G.; Protesescu, L.; Bodnarchuk, M. I.; Kovalenko, M. V.; Mahrt, R. F.; Stöferle, T., Single Cesium Lead Halide Perovskite Nanocrystals at Low Temperature: Fast Single-Photon Emission, Reduced Blinking, and Exciton Fine Structure. *ACS Nano* **2016,** *10*, 2485-2490.
103. Park, Y.-S.; Guo, S.; Makarov, N. S.; Klimov, V. I., Room Temperature Single-Photon Emission from Individual Perovskite Quantum Dots. *ACS Nano* **2015,** *9*, 10386-10393.

104. Utzat, H.; Sun, W.; Kaplan, A. E. K.; Krieg, F.; Ginterseder, M.; Spokoyny, B.; Klein, N. D.; Shulenberger, K. E.; Perkinson, C. F.; Kovalenko, M. V.; Bawendi, M. G., Coherent Single-Photon Emission from Colloidal Lead Halide Perovskite Quantum Dots. *Science* **2019,** *363*, 1068-1072.
105. Akkerman, Q. A.; Rainò, G.; Kovalenko, M. V.; Manna, L., Genesis, Challenges and Opportunities for Colloidal Lead Halide Perovskite Nanocrystals. *Nat. Mater.* **2018,** *17*, 394-405.
106. Nenon, D. P.; Pressler, K.; Kang, J.; Koscher, B. A.; Olshansky, J. H.; Osowiecki, W. T.; Koc, M. A.; Wang, L.-W.; Alivisatos, A. P., Design Principles for Trap-Free $CsPbX_3$ Nanocrystals: Enumerating and Eliminating Surface Halide Vacancies with Softer Lewis Bases. *J. Am. Chem. Soc.* **2018,** *140*, 17760-17772.
107. Kang, J.; Wang, L.-W., High Defect Tolerance in Lead Halide Perovskite $Cspbbr_3$. *J. Phys. Chem. Lett.* **2017,** *8*, 489-493.
108. ten Brinck, S.; Zaccaria, F.; Infante, I., Defects in Lead Halide Perovskite Nanocrystals: Analogies and (Many) Differences with the Bulk. *ACS Energy Lett.* **2019,** *4*, 2739-2747.
109. Creutz, S. E.; Crites, E. N.; De Siena, M. C.; Gamelin, D. R., Anion Exchange in Cesium Lead Halide Perovskite Nanocrystals and Thin Films Using Trimethylsilyl Halide Reagents. *Chem. Mater.* **2018,** *30*, 4887-4891.
110. Nedelcu, G.; Protesescu, L.; Yakunin, S.; Bodnarchuk, M. I.; Grotevent, M. J.; Kovalenko, M. V., Fast Anion-Exchange in Highly Luminescent Nanocrystals of Cesium Lead Halide Perovskites ($CsPbX_3$, X = Cl, Br, I). *Nano Lett.* **2015,** *15*, 5635-5640.
111. Imran, M.; Caligiuri, V.; Wang, M.; Goldoni, L.; Prato, M.; Krahne, R.; De Trizio, L.; Manna, L., Benzoyl Halides as Alternative Precursors for the Colloidal Synthesis of Lead-Based Halide Perovskite Nanocrystals. *J. Am. Chem. Soc.* **2018,** *140*, 2656-2664.
112. Liu, W.; Lin, Q.; Li, H.; Wu, K.; Robel, I.; Pietryga, J. M.; Klimov, V. I., Mn^{2+}-Doped Lead Halide Perovskite Nanocrystals with Dual-Color Emission Controlled by Halide Content. *J. Am. Chem. Soc.* **2016,** *138*, 14954-14961.
113. De Siena, M. C.; Sommer, D. E.; Creutz, S. E.; Dunham, S. T.; Gamelin, D. R., Spinodal Decomposition During Anion Exchange in Colloidal Mn^{2+}-Doped $CsPbX_3$ (X = Cl, Br) Perovskite Nanocrystals. *Chem. Mater.* **2019,** *31*, 7711-7722.
114. Conings, B.; Drijkoningen, J.; Gauquelin, N.; Babayigit, A.; D'Haen, J.; D'Olieslaeger, L.; Ethirajan, A.; Verbeeck, J.; Manca, J.; Mosconi, E.; Angelis, F. D.; Boyen, H.-G., Intrinsic Thermal Instability of Methylammonium Lead Trihalide Perovskite. *Adv. Energy Mater.* **2015,** *5*, n/a-n/a.
115. Manspeaker, C.; Venkatesan, S.; Zakhidov, A.; Martirosyan, K. S., Role of Interface in Stability of Perovskite Solar Cells. *Curr. Opin. Chem. Eng.* **2017,** *15*, 1-7.
116. Rainò, G.; Landuyt, A.; Krieg, F.; Bernasconi, C.; Ochsenbein, S. T.; Dirin, D. N.; Bodnarchuk, M. I.; Kovalenko, M. V., Underestimated Effect of a Polymer Matrix on the Light Emission of Single $CsPbBr_3$ Nanocrystals. *Nano Lett.* **2019,** *19*, 3648-3653.
117. Yuan, G.; Ritchie, C.; Ritter, M.; Murphy, S.; Gómez, D. E.; Mulvaney, P., The Degradation and Blinking of Single $Cspbi_3$ Perovskite Quantum Dots. *J. Phys. Chem. C* **2018,** *122*, 13407-13415.
118. Ogomi, Y.; Morita, A.; Tsukamoto, S.; Saitho, T.; Shen, Q.; Toyoda, T.; Yoshino, K.; Pandey, S. S.; Ma, T.; Hayase, S., All-Solid Perovskite Solar Cells with HOCO-R-$NG^{3+}I$– Anchor-Group Inserted between Porous Titania and Perovskite. *J. Phys. Chem. C* **2014,** *118*, 16651-16659.

119. Zuo, L.; Gu, Z.; Ye, T.; Fu, W.; Wu, G.; Li, H.; Chen, H., Enhanced Photovoltaic Performance of $CH_3NH_3PbI_3$ Perovskite Solar Cells through Interfacial Engineering Using Self-Assembling Monolayer. *J. Am. Chem. Soc.* **2015,** *137*, 2674-2679.
120. De Roo, J.; Ibáñez, M.; Geiregat, P.; Nedelcu, G.; Walravens, W.; Maes, J.; Martins, J. C.; Van Driessche, I.; Kovalenko, M. V.; Hens, Z., Highly Dynamic Ligand Binding and Light Absorption Coefficient of Cesium Lead Bromide Perovskite Nanocrystals. *ACS Nano* **2016,** *10*, 2071-2081.
121. Pan, A.; He, B.; Fan, X.; Liu, Z.; Urban, J. J.; Alivisatos, A. P.; He, L.; Liu, Y., Insight into the Ligand-Mediated Synthesis of Colloidal CsPbBr3 Perovskite Nanocrystals: The Role of Organic Acid, Base, and Cesium Precursors. *ACS Nano* **2016,** *10*, 7943-7954.
122. Ravi, V. K.; Santra, P. K.; Joshi, N.; Chugh, J.; Singh, S. K.; Rensmo, H.; Ghosh, P.; Nag, A., Origin of the Substitution Mechanism for the Binding of Organic Ligands on the Surface of $CsPbBr_3$ Perovskite Nanocubes. *J. Phys. Chem. Lett.* **2017,** *8*, 4988-4994.
123. ten Brinck, S.; Infante, I., Surface Termination, Morphology, and Bright Photoluminescence of Cesium Lead Halide Perovskite Nanocrystals. *ACS Energy Lett.* **2016,** *1*, 1266-1272.
124. Krieg, F.; Ochsenbein, S. T.; Yakunin, S.; ten Brinck, S.; Aellen, P.; Süess, A.; Clerc, B.; Guggisberg, D.; Nazarenko, O.; Shynkarenko, Y.; Kumar, S.; Shih, C.-J.; Infante, I.; Kovalenko, M. V., Colloidal $CsPbX_3$ (X = Cl, Br, I) Nanocrystals 2.0: Zwitterionic Capping Ligands for Improved Durability and Stability. *ACS Energy Lett.* **2018,** *3*, 641-646.
125. Li, X.; Ibrahim Dar, M.; Yi, C.; Luo, J.; Tschumi, M.; Zakeeruddin, S. M.; Nazeeruddin, M. K.; Han, H.; Grätzel, M., Improved Performance and Stability of Perovskite Solar Cells by Crystal Crosslinking with Alkylphosphonic Acid Ω-Ammonium Chlorides. *Nature Chemistry* **2015,** *7*, 703-711.
126. deQuilettes, D. W.; Koch, S.; Burke, S.; Paranji, R. K.; Shropshire, A. J.; Ziffer, M. E.; Ginger, D. S., Photoluminescence Lifetimes Exceeding 8 ms and Quantum Yields Exceeding 30% in Hybrid Perovskite Thin Films by Ligand Passivation. *ACS Energy Lett.* **2016,** *1*, 438-444.
127. Liu, F.; Zhang, Y.; Ding, C.; Kobayashi, S.; Izuishi, T.; Nakazawa, N.; Toyoda, T.; Ohta, T.; Hayase, S.; Minemoto, T.; Yoshino, K.; Dai, S.; Shen, Q., Highly Luminescent Phase-Stable $CsPbI_3$ Perovskite Quantum Dots Achieving near 100% Absolute Photoluminescence Quantum Yield. *ACS Nano* **2017,** *11*, 10373-10383.
128. Wu, L.; Zhong, Q.; Yang, D.; Chen, M.; Hu, H.; Pan, Q.; Liu, H.; Cao, M.; Xu, Y.; Sun, B.; Zhang, Q., Improving the Stability and Size Tunability of Cesium Lead Halide Perovskite Nanocrystals Using Trioctylphosphine Oxide as the Capping Ligand. *Langmuir* **2017,** *33*, 12689-12696.
129. Wang, H.; Sui, N.; Bai, X.; Zhang, Y.; Rice, Q.; Seo, F. J.; Zhang, Q.; Colvin, V. L.; Yu, W. W., Emission Recovery and Stability Enhancement of Inorganic Perovskite Quantum Dots. *J. Phys. Chem. Lett.* **2018,** *9*, 4166-4173.
130. Wang, H.; Zhang, X.; Sui, N.; Hu, Y.; Colvin, V. L.; Yu, W. W.; Zhang, Y., Photoluminescence Loss and Recovery of α-$CsPbI_3$ Quantum Dots Originated from Chemical Equilibrium Shift of Oleylammonium. *ACS Appl. Mater. Interfaces* **2020,** *12*, 11769-11777.
131. Tan, Y.; Zou, Y.; Wu, L.; Huang, Q.; Yang, D.; Chen, M.; Ban, M.; Wu, C.; Wu, T.; Bai, S.; Song, T.; Zhang, Q.; Sun, B., Highly Luminescent and Stable Perovskite Nanocrystals

with Octylphosphonic Acid as a Ligand for Efficient Light-Emitting Diodes. *ACS Appl. Mater. Interfaces* **2018,** *10*, 3784-3792.

132. Noel, N. K.; Abate, A.; Stranks, S. D.; Parrott, E. S.; Burlakov, V. M.; Goriely, A.; Snaith, H. J., Enhanced Photoluminescence and Solar Cell Performance Via Lewis Base Passivation of Organic–Inorganic Lead Halide Perovskites. *ACS Nano* **2014,** *8*, 9815-9821.
133. Krieg, F.; Ong, Q. K.; Burian, M.; Rainò, G.; Naumenko, D.; Amenitsch, H.; Süess, A.; Grotevent, M. J.; Krumeich, F.; Bodnarchuk, M. I.; Shorubalko, I.; Stellacci, F.; Kovalenko, M. V., Stable Ultraconcentrated and Ultradilute Colloids of $CsPbX_3$ (X = Cl, Br) Nanocrystals Using Natural Lecithin as a Capping Ligand. *J. Am. Chem. Soc.* **2019,** *141*, 19839-19849.
134. Krieg, F.; Sercel, P. C.; Burian, M.; Andrusiv, H.; Bodnarchuk, M. I.; Stöferle, T.; Mahrt, R. F.; Naumenko, D.; Amenitsch, H.; Rainò, G.; Kovalenko, M. V., Monodisperse Long-Chain Sulfobetaine-Capped CsPbBr3 Nanocrystals and Their Superfluorescent Assemblies. *ACS Cent. Sci.* **2021,** *7*, 135-144.
135. Starck, P.; Mosse, W. K. J.; Nicholas, N. J.; Spiniello, M.; Tyrrell, J.; Nelson, A.; Qiao, G. G.; Ducker, W. A., Surface Chemistry and Rheology of Polysulfobetaine-Coated Silica. *Langmuir* **2007,** *23*, 7587-7593.
136. Yang, Z.; Zhang, S.; Tarabara, V. V.; Bruening, M. L., Aqueous Swelling of Zwitterionic Poly(Sulfobetaine Methacrylate) Brushes in the Presence of Ionic Surfactants. *Macromolecules* **2018,** *51*, 1161-1171.
137. Chen, Q.; Yuan, L.; Duan, R.; Huang, P.; Fu, J.; Ma, H.; Wang, X.; Zhou, Y.; Song, B., Zwitterionic Polymer: A Facile Interfacial Material Works at Both Anode and Cathode in p-i-n Perovskite Solar Cells. *Sol. RRL* **2019,** *3*, 1900118.
138. Islam, A.; Li, J.; Pervaiz, M.; Lu, Z.-H.; Sain, M.; Chen, L.; Ouyang, X., Zwitterions for Organic/Perovskite Solar Cells, Light-Emitting Devices, and Lithium Ion Batteries: Recent Progress and Perspectives. *Adv. Energy Mater.* **2019,** *9*, 1803354.
139. Liu, Y.; Page, Z. A.; Russell, T. P.; Emrick, T., Finely Tuned Polymer Interlayers Enhance Solar Cell Efficiency. *Angew. Chem.* **2015,** *127*, 11647-11651.
140. Liu, Y.; Duzhko, V. V.; Page, Z. A.; Emrick, T.; Russell, T. P., Conjugated Polymer Zwitterions: Efficient Interlayer Materials in Organic Electronics. *Acc. Chem. Res.* **2016,** *49*, 2478-2488.
141. Li, Y.; Zhang, X.; Zhang, Y.; Dong, R.; Luscombe, C. K., Review on the Role of Polymers in Luminescent Solar Concentrators. *J. Polym. Sci. Pol. Chem.* **2019,** *57*, 201-215.
142. Lei, T.; Dou, J.-H.; Pei, J., Influence of Alkyl Chain Branching Positions on the Hole Mobilities of Polymer Thin-Film Transistors. *Adv. Mater.* **2012,** *24*, 6457-6461.
143. Shivhare, R.; Erdmann, T.; Hörmann, U.; Collado-Fregoso, E.; Zeiske, S.; Benduhn, J.; Ullbrich, S.; Hübner, R.; Hambsch, M.; Kiriy, A.; Voit, B.; Neher, D.; Vandewal, K.; Mannsfeld, S. C. B., Alkyl Branching Position in Diketopyrrolopyrrole Polymers: Interplay between Fibrillar Morphology and Crystallinity and Their Effect on Photogeneration and Recombination in Bulk-Heterojunction Solar Cells. *Chem. Mater.* **2018,** *30*, 6801-6809.
144. Çetinkaya, O.; Demirci, G.; Mergo, P., Effect of the Different Chain Transfer Agents on Molecular Weight and Optical Properties of Poly(Methyl Methacrylate). *Opt. Mater.* **2017,** *70*, 25-30.

145. Kim, Y.; Yassitepe, E.; Voznyy, O.; Comin, R.; Walters, G.; Gong, X.; Kanjanaboos, P.; Nogueira, A. F.; Sargent, E. H., Efficient Luminescence from Perovskite Quantum Dot Solids. *ACS Appl. Mater. Interfaces* **2015,** *7*, 25007-25013.
146. Cai, Y.; Wang, H.; Li, Y.; Wang, L.; Lv, Y.; Yang, X.; Xie, R.-J., Trimethylsilyl Iodine-Mediated Synthesis of Highly Bright Red-Emitting $Cspbi_3$ Perovskite Quantum Dots with Significantly Improved Stability. *Chem. Mater.* **2019,** *31*, 881-889.
147. Kirschner, M. S.; Diroll, B. T.; Guo, P.; Harvey, S. M.; Helweh, W.; Flanders, N. C.; Brumberg, A.; Watkins, N. E.; Leonard, A. A.; Evans, A. M.; Wasielewski, M. R.; Dichtel, W. R.; Zhang, X.; Chen, L. X.; Schaller, R. D., Photoinduced, Reversible Phase Transitions in All-Inorganic Perovskite Nanocrystals. *Nat. Commun.* **2019,** *10*, 504.
148. Liao, M.; Shan, B.; Li, M., In Situ Raman Spectroscopic Studies of Thermal Stability of All-Inorganic Cesium Lead Halide ($CsPbX_3$, X = Cl, Br, I) Perovskite Nanocrystals. *J. Phys. Chem. Lett.* **2019,** *10*, 1217-1225.
149. Meyns, M.; Perálvarez, M.; Heuer-Jungemann, A.; Hertog, W.; Ibáñez, M.; Nafria, R.; Genç, A.; Arbiol, J.; Kovalenko, M. V.; Carreras, J.; Cabot, A.; Kanaras, A. G., Polymer-Enhanced Stability of Inorganic Perovskite Nanocrystals and Their Application in Color Conversion Leds. *ACS Appl. Mater. Interfaces* **2016,** *8*, 19579-19586.
150. Raja, S. N.; Bekenstein, Y.; Koc, M. A.; Fischer, S.; Zhang, D.; Lin, L.; Ritchie, R. O.; Yang, P.; Alivisatos, A. P., Encapsulation of Perovskite Nanocrystals into Macroscale Polymer Matrices: Enhanced Stability and Polarization. *ACS Appl. Mater. Interfaces* **2016,** *8*, 35523-35533.
151. He, Y.; Yoon, Y. J.; Harn, Y. W.; Biesold-McGee, G. V.; Liang, S.; Lin, C. H.; Tsukruk, V. V.; Thadhani, N.; Kang, Z.; Lin, Z., Unconventional Route to Dual-Shelled Organolead Halide Perovskite Nanocrystals with Controlled Dimensions, Surface Chemistry, and Stabilities. *Sci. Adv.* **2019,** *5*, eaax4424.
152. Lu, Z.; Li, Y.; Qiu, W.; Rogach, A. L.; Nagl, S., Composite Films of $Cspbbr_3$ Perovskite Nanocrystals in a Hydrophobic Fluoropolymer for Temperature Imaging in Digital Microfluidics. *ACS Appl. Mater. Interfaces* **2020,** *12*, 19805-19812.
153. Huang, Y.; Cohen, T. A.; Sommerville, P. J. W.; Luscombe, C. K., Green Syntheses of Stable and Efficient Organic Dyes for Organic Hybrid Light-Emitting Diodes. *J. Mater. Chem. C* **2021,** *9*, 7274-7283.
154. Nie, W.; Blancon, J.-C.; Neukirch, A. J.; Appavoo, K.; Tsai, H.; Chhowalla, M.; Alam, M. A.; Sfeir, M. Y.; Katan, C.; Even, J.; Tretiak, S.; Crochet, J. J.; Gupta, G.; Mohite, A. D., Light-Activated Photocurrent Degradation and Self-Healing in Perovskite Solar Cells. *Nat. Commun.* **2016,** *7*, 1-9.
155. Ceratti, D. R.; Rakita, Y.; Cremonesi, L.; Tenne, R.; Kalchenko, V.; Elbaum, M.; Oron, D.; Potenza, M. A. C.; Hodes, G.; Cahen, D., Self-Healing inside $APbBr_3$ Halide Perovskite Crystals. *Adv. Mater.* **2018,** *30*, 1706273.
156. Ghosh, S.; Shi, Q.; Pradhan, B.; Mushtaq, A.; Acharya, S.; Karki, K. J.; Pullerits, T.; Pal, S. K., Light-Induced Defect Healing and Strong Many-Body Interactions in Formamidinium Lead Bromide Perovskite Nanocrystals. *J. Phys. Chem. Lett.* **2020,** *11*, 1239-1246.
157. Jean, J.; Xiao, J.; Nick, R.; Moody, N.; Nasilowski, M.; Bawendi, M.; Bulović, V., Synthesis Cost Dictates the Commercial Viability of Lead Sulfide and Perovskite Quantum Dot Photovoltaics. *Energy Environ. Sci.* **2018,** *11*, 2295-2305.

158. Crane, M. J.; Kroupa, D. M.; Roh, J. Y.; Anderson, R. T.; Smith, M. D.; Gamelin, D. R., Single-Source Vapor Deposition of Quantum-Cutting Yb^{3+}:$CsPb(Cl_{1-x}Br_x)_3$ and Other Complex Metal-Halide Perovskites. *ACS Appl. Energy Mater.* **2019,** *2*, 4560-4565.
159. Aharonovich, I.; Englund, D.; Toth, M., Solid-State Single-Photon Emitters. *Nat. Photonics* **2016,** *10*, 631-641.
160. Senellart, P.; Solomon, G.; White, A., High-Performance Semiconductor Quantum-Dot Single-Photon Sources. *Nat. Nanotechnol.* **2017,** *12*, 1026-1039.
161. Smith, J. S.; Derry, P. L.; Margalit, S.; Yariv, A., High Quality Molecular Beam Epitaxial Growth on Patterned Gaas Substrates. *Appl. Phys. Lett.* **1985,** *47*, 712-715.
162. Kash, K.; Scherer, A.; Worlock, J. M.; Craighead, H. G.; Tamargo, M. C., Optical Spectroscopy of Ultrasmall Structures Etched from Quantum Wells. *Appl. Phys. Lett.* **1986,** *49*, 1043-1045.
163. Alloing, B.; Zinoni, C.; Zwiller, V.; Li, L. H.; Monat, C.; Gobet, M.; Buchs, G.; Fiore, A.; Pelucchi, E.; Kapon, E., Growth and Characterization of Single Quantum Dots Emitting at 1300 Nm. *Appl. Phys. Lett.* **2005,** *86*, 101908.
164. Petruzzella, M.; Birindelli, S.; Pagliano, F. M.; Pellegrino, D.; Zobenica, Ž.; Li, L. H.; Linfield, E. H.; Fiore, A., Quantum Photonic Integrated Circuits Based on Tunable Dots and Tunable Cavities. *APL Photonics* **2018,** *3*, 106103.
165. Santori, C.; Fattal, D.; Vučković, J.; Solomon, G. S.; Yamamoto, Y., Indistinguishable Photons from a Single-Photon Device. *Nature* **2002,** *419*, 594-597.
166. Loredo, J. C.; Zakaria, N. A.; Somaschi, N.; Anton, C.; Santis, L. d.; Giesz, V.; Grange, T.; Broome, M. A.; Gazzano, O.; Coppola, G.; Sagnes, I.; Lemaitre, A.; Auffeves, A.; Senellart, P.; Almeida, M. P.; White, A. G., Scalable Performance in Solid-State Single-Photon Sources. *Optica* **2016,** *3*, 433-440.
167. Hummel, T.; Ouellet-Plamondon, C.; Ugur, E.; Kulkova, I.; Lund-Hansen, T.; Broome, M. A.; Uppu, R.; Lodahl, P., Efficient Demultiplexed Single-Photon Source with a Quantum Dot Coupled to a Nanophotonic Waveguide. *Appl. Phys. Lett.* **2019,** *115*, 021102.
168. Badolato, A.; Hennessy, K.; Atatüre, M.; Dreiser, J.; Hu, E.; Petroff, P. M.; Imamoğlu, A., Deterministic Coupling of Single Quantum Dots to Single Nanocavity Modes. *Science* **2005,** *308*, 1158-1161.
169. Wan, N. H.; Lu, T.-J.; Chen, K. C.; Walsh, M. P.; Trusheim, M. E.; De Santis, L.; Bersin, E. A.; Harris, I. B.; Mouradian, S. L.; Christen, I. R.; Bielejec, E. S.; Englund, D., Large-Scale Integration of Artificial Atoms in Hybrid Photonic Circuits. *Nature* **2020,** *583*, 226-231.
170. Junno, T.; Deppert, K.; Montelius, L.; Samuelson, L., Controlled Manipulation of Nanoparticles with an Atomic Force Microscope. *Appl. Phys. Lett.* **1995,** *66*, 3627-3629.
171. Zadeh, I. E.; Elshaari, A. W.; Jöns, K. D.; Fognini, A.; Dalacu, D.; Poole, P. J.; Reimer, M. E.; Zwiller, V., Deterministic Integration of Single Photon Sources in Silicon Based Photonic Circuits. *Nano Lett.* **2016,** *16*, 2289-2294.
172. Elshaari, A. W.; Zadeh, I. E.; Fognini, A.; Reimer, M. E.; Dalacu, D.; Poole, P. J.; Zwiller, V.; Jöns, K. D., On-Chip Single Photon Filtering and Multiplexing in Hybrid Quantum Photonic Circuits. *Nat. Commun.* **2017,** *8*, 379.
173. Lee, W. K.; Dai, Z.; King, W. P.; Sheehan, P. E., Maskless Nanoscale Writing of Nanoparticle−Polymer Composites and Nanoparticle Assemblies Using Thermal Nanoprobes. *Nano Lett.* **2010,** *10*, 129-133.

174. Bellido, E.; Domingo, N.; Ojea-Jiménez, I.; Ruiz-Molina, D., Structuration and Integration of Magnetic Nanoparticles on Surfaces and Devices. *Small* **2012,** *8*, 1465-1491.
175. Chen, J.; Sun, Y.; Zhong, L.; Shao, W.; Huang, J.; Liang, F.; Cui, Z.; Liang, Z.; Jiang, L.; Chi, L., Scalable Fabrication of Multiplexed Plasmonic Nanoparticle Structures Based on Afm Lithography. *Small* **2016,** *12*, 5818-5825.
176. Katsumi, R.; Ota, Y.; Osada, A.; Yamaguchi, T.; Tajiri, T.; Kakuda, M.; Iwamoto, S.; Akiyama, H.; Arakawa, Y., Quantum-Dot Single-Photon Source on a Cmos Silicon Photonic Chip Integrated Using Transfer Printing. *APL Photonics* **2019,** *4*, 036105.
177. Thompson, L. F., An Introduction to Lithography. In *Introduction to Microlithography*, American Chemical Society: 1983; Vol. 219, pp 1-13.
178. Wang, Y.; Tang, Z.; Correa-Duarte, M. A.; Liz-Marzán, L. M.; Kotov, N. A., Multicolor Luminescence Patterning by Photoactivation of Semiconductor Nanoparticle Films. *J. Am. Chem. Soc.* **2003,** *125*, 2830-2831.
179. Chen, X.; Rogach, A. L.; Talapin, D. V.; Fuchs, H.; Chi, L., Hierarchical Luminescence Patterning Based on Multiscaled Self-Assembly. *J. Am. Chem. Soc.* **2006,** *128*, 9592-9593.
180. Wang, Y.; Fedin, I.; Zhang, H.; Talapin, D. V., Direct Optical Lithography of Functional Inorganic Nanomaterials. *Science* **2017,** *357*, 385-388.
181. Cho, H.; Pan, J.-A.; Wu, H.; Lan, X.; Coropceanu, I.; Wang, Y.; Cho, W.; Hill, E. A.; Anderson, J. S.; Talapin, D. V., Direct Optical Patterning of Quantum Dot Light-Emitting Diodes Via in Situ Ligand Exchange. *Adv. Mater.* **2020,** *32*, 2003805.
182. Yang, J.; Hahm, D.; Kim, K.; Rhee, S.; Lee, M.; Kim, S.; Chang, J. H.; Park, H. W.; Lim, J.; Lee, M.; Kim, H.; Bang, J.; Ahn, H.; Cho, J. H.; Kwak, J.; Kim, B.; Lee, C.; Bae, W. K.; Kang, M. S., High-Resolution Patterning of Colloidal Quantum Dots Via Non-Destructive, Light-Driven Ligand Crosslinking. *Nat. Commun.* **2020,** *11*, 2874.
183. Wang, Y.; Pan, J.-A.; Wu, H.; Talapin, D. V., Direct Wavelength-Selective Optical and Electron-Beam Lithography of Functional Inorganic Nanomaterials. *ACS Nano* **2019,** *13*, 13917-13931.
184. Samadi Khoshkhoo, M.; Prudnikau, A.; Chashmejahanbin, M. R.; Helbig, R.; Lesnyak, V.; Cuniberti, G., Multicolor Patterning of 2D Semiconductor Nanoplatelets. *ACS Nano* **2021**.
185. Palazon, F.; Akkerman, Q. A.; Prato, M.; Manna, L., X-Ray Lithography on Perovskite Nanocrystals Films: From Patterning with Anion-Exchange Reactions to Enhanced Stability in Air and Water. *ACS Nano* **2016,** *10*, 1224-1230.
186. Minh, D. N.; Eom, S.; Nguyen, L. A. T.; Kim, J.; Sim, J. H.; Seo, C.; Nam, J.; Lee, S.; Suk, S.; Kim, J.; Kang, Y., Perovskite Nanoparticle Composite Films by Size Exclusion Lithography. *Adv. Mater.* **2018,** *30*, 1802555.
187. Pan, J.-A.; Ondry, J. C.; Talapin, D. V., Direct Optical Lithography of $CsPbX_3$ Nanocrystals *Via* Photoinduced Ligand Cleavage with Postpatterning Chemical Modification and Electronic Coupling. *Nano Lett.* **2021,** *21*, 7609-7616.
188. Wang, J.; Sun, X.; Chen, L.; Chou, S. Y., Direct Nanoimprint of Submicron Organic Light-Emitting Structures. *Appl. Phys. Lett.* **1999,** *75*, 2767-2769.
189. Cheng, Z. Y.; Wang, Z.; Xing, R. B.; Han, Y. C.; Lin, J., Patterning and Photoluminescent Properties of Perovskite-Type Organic/Inorganic Hybrid Luminescent Films by Soft Lithography. *Chemical Physics Letters* **2003,** *376*, 481-486.

190. Yu, M.; Lin, J.; Wang, Z.; Fu, J.; Wang, S.; Zhang, H. J.; Han, Y. C., Fabrication, Patterning, and Optical Properties of Nanocrystalline YVO_4:A (A = Eu^{3+}, Dy^{3+}, Sm^{3+}, Er^{3+}) Phosphor Films Via Sol−Gel Soft Lithography. *Chem. Mater.* **2002,** *14*, 2224-2231.
191. Tamborra, M.; Striccoli, M.; Curri, M. L.; Alducin, J. A.; Mecerreyes, D.; Pomposo, J. A.; Kehagias, N.; Reboud, V.; Sotomayor Torres, C. M.; Agostiano, A., Nanocrystal-Based Luminescent Composites for Nanoimprinting Lithography. *Small* **2007,** *3*, 822-828.
192. Kim, E.; Whitesides, G. M.; Freiler, M. B.; Levy, M.; Lin, J. L.; Osgood, R. M., Fabrication of Micrometer-Scale Structures on Gaas and Gaas/Algaas Quantum Well Material Using Microcontact Printing. **1996,** *7*, 266-269.
193. Li, X.; Hu, B.; Du, Z.; Wu, Y.; Jiang, L., Asymmetric Wettability Interfaces Induced a Large-Area Quantum Dot Microstructure toward High-Resolution Quantum Dot Light-Emitting Diodes. *ACS Appl. Mater. Interfaces* **2019,** *11*, 28520-28526.
194. Justice, J.; Bower, C.; Meitl, M.; Mooney, M. B.; Gubbins, M. A.; Corbett, B., Wafer-Scale Integration of Group III–V Lasers on Silicon Using Transfer Printing of Epitaxial Layers. *Nat. Photonics* **2012,** *6*, 610-614.
195. Yoon, J.; Lee, S.-M.; Kang, D.; Meitl, M. A.; Bower, C. A.; Rogers, J. A., Heterogeneously Integrated Optoelectronic Devices Enabled by Micro-Transfer Printing. *Adv. Opt. Mater.* **2015,** *3*, 1313-1335.
196. Groote, A. D.; Cardile, P.; Subramanian, A. Z.; Fecioru, A. M.; Bower, C.; Delbeke, D.; Baets, R.; Roelkens, G., Transfer-Printing-Based Integration of Single-Mode Waveguide-Coupled III-V-on-Silicon Broadband Light Emitters. *Opt. Express, OE* **2016,** *24*, 13754-13762.
197. Kim, B. H.; Nam, S.; Oh, N.; Cho, S.-Y.; Yu, K. J.; Lee, C. H.; Zhang, J.; Deshpande, K.; Trefonas, P.; Kim, J.-H.; Lee, J.; Shin, J. H.; Yu, Y.; Lim, J. B.; Won, S. M.; Cho, Y. K.; Kim, N. H.; Seo, K. J.; Lee, H.; Kim, T.-i.; Shim, M.; Rogers, J. A., Multilayer Transfer Printing for Pixelated, Multicolor Quantum Dot Light-Emitting Diodes. *ACS Nano* **2016,** *10*, 4920-4925.
198. Bertino, M. F.; Gadipalli, R. R.; Story, J. G.; Williams, C. G.; Zhang, G.; Sotiriou-Leventis, C.; Tokuhiro, A. T.; Guha, S.; Leventis, N., Laser Writing of Semiconductor Nanoparticles and Quantum Dots. *Appl. Phys. Lett.* **2004,** *85*, 6007-6009.
199. Shao, H.; Ying, G.; Lennon, S. A.; Brossard, F. S. F.; Griffiths, J. P.; Nuttall, L. P.; Osokin, V.; Clarke, E.; He, H.; Taylor, R. A., Purcell Enhancement of a Deterministically Coupled Quantum Dot in an Su-8 Laser Patterned Photonic Crystal Heterostructure. *Appl. Phys. Lett.* **2020,** *117*, 043103.
200. Park, J.-U.; Hardy, M.; Kang, S. J.; Barton, K.; Adair, K.; Mukhopadhyay, D. k.; Lee, C. Y.; Strano, M. S.; Alleyne, A. G.; Georgiadis, J. G.; Ferreira, P. M.; Rogers, J. A., High-Resolution Electrohydrodynamic Jet Printing. *Nat. Mater.* **2007,** *6*, 782-789.
201. Tekin, E.; Smith, P. J.; Hoeppener, S.; van den Berg, A. M. J.; Susha, A. S.; Rogach, A. L.; Feldmann, J.; Schubert, U. S., Inkjet Printing of Luminescent CdTe Nanocrystal–Polymer Composites. *Adv. Funct. Mater.* **2007,** *17*, 23-28.
202. Wood, V.; Panzer, M. J.; Chen, J.; Bradley, M. S.; Halpert, J. E.; Bawendi, M. G.; Bulović, V., Inkjet-Printed Quantum Dot–Polymer Composites for Full-Color AC-Driven Displays. *Adv. Mater.* **2009,** *21*, 2151-2155.

203. Lan, L.; Zou, J.; Jiang, C.; Liu, B.; Wang, L.; Peng, J., Inkjet Printing for Electroluminescent Devices: Emissive Materials, Film Formation, and Display Prototypes. *Front. Optoelectron.* **2017,** *10*, 329-352.
204. Nakao, H.; Murakami, T.; Hirahara, S.; Nagato, H.; Nomura, Y., Head Design for Novel Ink-Jet Printing Using Electrostatic Force. *NIP & Digital Fabrication Conference* **1999,** *1999*, 319-322.
205. Kim, B. H.; Onses, M. S.; Lim, J. B.; Nam, S.; Oh, N.; Kim, H.; Yu, K. J.; Lee, J. W.; Kim, J.-H.; Kang, S.-K.; Lee, C. H.; Lee, J.; Shin, J. H.; Kim, N. H.; Leal, C.; Shim, M.; Rogers, J. A., High-Resolution Patterns of Quantum Dots Formed by Electrohydrodynamic Jet Printing for Light-Emitting Diodes. *Nano Lett.* **2015,** *15*, 969-973.
206. Li, H.; Duan, Y.; Shao, Z.; Zhang, G.; Li, H.; Huang, Y.; Yin, Z., High-Resolution Pixelated Light Emitting Diodes Based on Electrohydrodynamic Printing and Coffee-Ring-Free Quantum Dot Film. *Adv. Mater. Technol.* **2020,** *5*, 2000401.
207. Grotevent, M. J.; Hail, C. U.; Yakunin, S.; Dirin, D. N.; Thodkar, K.; Borin Barin, G.; Guyot-Sionnest, P.; Calame, M.; Poulikakos, D.; Kovalenko, M. V.; Shorubalko, I., Nanoprinted Quantum Dot–Graphene Photodetectors. *Adv. Opt. Mater.* **2019,** *7*, 1900019.
208. Yakunin, S.; Chaaban, J.; Benin, B. M.; Cherniukh, I.; Bernasconi, C.; Landuyt, A.; Shynkarenko, Y.; Bolat, S.; Hofer, C.; Romanyuk, Y. E.; Cattaneo, S.; Pokutnyi, S. I.; Schaller, R. D.; Bodnarchuk, M. I.; Poulikakos, D.; Kovalenko, M. V., Radiative Lifetime-Encoded Unicolour Security Tags Using Perovskite Nanocrystals. *Nat. Commun.* **2021,** *12*, 981.
209. Brossard, F. S. F.; Pecunia, V.; Ramsay, A. J.; Griffiths, J. P.; Hugues, M.; Sirringhaus, H., Inkjet-Printed Nanocavities on a Photonic Crystal Template. *Adv. Mater.* **2017,** *29*, 1704425.
210. Aellen, M.; Rossinelli, A. A.; Keitel, R. C.; Brechbühler, R.; Antolinez, F. V.; Cui, J.; Norris, D. J., Reconsidering the Design of Planar Plasmonic Lasers: Gain, Gap Layers, and Mode Competition. *arXiv:2101.05881 [physics]* **2021**.
211. Kress, S. J. P.; Richner, P.; Jayanti, S. V.; Galliker, P.; Kim, D. K.; Poulikakos, D.; Norris, D. J., Near-Field Light Design with Colloidal Quantum Dots for Photonics and Plasmonics. *Nano Lett.* **2014,** *14*, 5827-5833.
212. Kress, S. J. P.; Cui, J.; Rohner, P.; Kim, D. K.; Antolinez, F. V.; Zaininger, K.-A.; Jayanti, S. V.; Richner, P.; McPeak, K. M.; Poulikakos, D.; Norris, D. J., A Customizable Class of Colloidal-Quantum-Dot Spasers and Plasmonic Amplifiers. *Sci. Adv.* **2017,** *3*, e1700688.
213. Kress, S. J. P.; Antolinez, F. V.; Richner, P.; Jayanti, S. V.; Kim, D. K.; Prins, F.; Riedinger, A.; Fischer, M. P. C.; Meyer, S.; McPeak, K. M.; Poulikakos, D.; Norris, D. J., Wedge Waveguides and Resonators for Quantum Plasmonics. *Nano Lett.* **2015,** *15*, 6267-6275.
214. Hail, C. U.; Höller, C.; Matsuzaki, K.; Rohner, P.; Renger, J.; Sandoghdar, V.; Poulikakos, D.; Eghlidi, H., Nanoprinting Organic Molecules at the Quantum Level. *Nat. Commun.* **2019,** *10*, 1880.
215. Crane, M. J.; Jacoby, L. M.; Cohen, T. A.; Huang, Y.; Luscombe, C. K.; Gamelin, D. R., Coherent Spin Precession and Lifetime-Limited Spin Dephasing in $CsPbBr_3$ Perovskite Nanocrystals. *Nano Lett.* **2020,** *20*, 8626-8633.

216. Rainò, G.; Becker, M. A.; Bodnarchuk, M. I.; Mahrt, R. F.; Kovalenko, M. V.; Stöferle, T., Superfluorescence from Lead Halide Perovskite Quantum Dot Superlattices. *Nature* **2018,** *563*, 671-675.
217. Altintas, Y.; Torun, I.; Yazici, A. F.; Beskazak, E.; Erdem, T.; Serdar Onses, M.; Mutlugun, E., Multiplexed Patterning of Cesium Lead Halide Perovskite Nanocrystals by Additive Jet Printing for Efficient White Light Generation. *Chem. Eng. J.* **2020,** *380*, 122493.
218. Galliker, P.; Schneider, J.; Eghlidi, H.; Kress, S.; Sandoghdar, V.; Poulikakos, D., Direct Printing of Nanostructures by Electrostatic Autofocussing of Ink Nanodroplets. *Nat. Commun.* **2012,** *3*, 890.
219. Richner, P.; Kress, S. J. P.; Norris, D. J.; Poulikakos, D., Charge Effects and Nanoparticle Pattern Formation in Electrohydrodynamic Nanodrip Printing of Colloids. *Nanoscale* **2016,** *8*, 6028-6034.
220. Di Stasio, F.; Christodoulou, S.; Huo, N.; Konstantatos, G., Near-Unity Photoluminescence Quantum Yield in $CsPbBr_3$ Nanocrystal Solid-State Films *Via* Postsynthesis Treatment with Lead Bromide. *Chem. Mater.* **2017,** *29*, 7663-7667.
221. Pan, J.; Quan, L. N.; Zhao, Y.; Peng, W.; Murali, B.; Sarmah, S. P.; Yuan, M.; Sinatra, L.; Alyami, N. M.; Liu, J.; Yassitepe, E.; Yang, Z.; Voznyy, O.; Comin, R.; Hedhili, M. N.; Mohammed, O. F.; Lu, Z. H.; Kim, D. H.; Sargent, E. H.; Bakr, O. M., Highly Efficient Perovskite-Quantum-Dot Light-Emitting Diodes by Surface Engineering. *Adv. Mater.* **2016,** *28*, 8718-8725.
222. Imran, M.; Ijaz, P.; Goldoni, L.; Maggioni, D.; Petralanda, U.; Prato, M.; Almeida, G.; Infante, I.; Manna, L., Simultaneous Cationic and Anionic Ligand Exchange for Colloidally Stable CsPbBr3 Nanocrystals. *ACS Energy Lett.* **2019,** *4*, 819-824.
223. Bodnarchuk, M. I.; Boehme, S. C.; ten Brinck, S.; Bernasconi, C.; Shynkarenko, Y.; Krieg, F.; Widmer, R.; Aeschlimann, B.; Günther, D.; Kovalenko, M. V.; Infante, I., Rationalizing and Controlling the Surface Structure and Electronic Passivation of Cesium Lead Halide Nanocrystals. *ACS Energy Lett.* **2019,** *4*, 63-74.
224. Dutta, A.; Behera, R. K.; Dutta, S. K.; Das Adhikari, S.; Pradhan, N., Annealing CsPbX3 (X = Cl and Br) Perovskite Nanocrystals at High Reaction Temperatures: Phase Change and Its Prevention. *The Journal of Physical Chemistry Letters* **2018,** *9*, 6599-6604.
225. Sun, H.; Yang, Z.; Wei, M.; Sun, W.; Li, X.; Ye, S.; Zhao, Y.; Tan, H.; Kynaston, E. L.; Schon, T. B.; Yan, H.; Lu, Z.-H.; Ozin, G. A.; Sargent, E. H.; Seferos, D. S., Chemically Addressable Perovskite Nanocrystals for Light-Emitting Applications. *Adv. Mater.* **2017,** *29*, 1701153.
226. Cherniukh, I.; Rainò, G.; Stöferle, T.; Burian, M.; Travesset, A.; Naumenko, D.; Amenitsch, H.; Erni, R.; Mahrt, R. F.; Bodnarchuk, M. I.; Kovalenko, M. V., Perovskite-Type Superlattices from Lead Halide Perovskite Nanocubes. *Nature* **2021,** *593*, 535-542.
227. Turns, S., *An Introduction to Combustion: Concepts and Applications*. 3 edition ed.; McGraw-Hill Education: New York, 2011; p 752.
228. Sharma, D. K.; Hirata, S.; Biju, V.; Vacha, M., Stark Effect and Environment-Induced Modulation of Emission in Single Halide Perovskite Nanocrystals. *ACS Nano* **2019,** *13*, 624-632.
229. Baranov, D.; Fieramosca, A.; Yang, R. X.; Polimeno, L.; Lerario, G.; Toso, S.; Giansante, C.; Giorgi, M. D.; Tan, L. Z.; Sanvitto, D.; Manna, L., Aging of Self-

Assembled Lead Halide Perovskite Nanocrystal Superlattices: Effects on Photoluminescence and Energy Transfer. *ACS Nano* **2021,** *15*, 650-664.

230. Jayasinghe, S. N.; Edirisinghe, M. J.; Wang, D. Z., Controlled Deposition of Nanoparticle Clusters by Electrohydrodynamic Atomization. *Nanotechnology* **2004,** *15*, 1519-1523.
231. Wang, D. Z.; Jayasinghe, S. N.; Edirisinghe, M. J., High Resolution Print-Patterning of a Nano-Suspension. *J. Nanopart. Res.* **2005,** *7*, 301-306.
232. Wang, D. Z.; Jayasinghe, S. N.; Edirisinghe, M. J.; Luklinska, Z. B., Coaxial Electrohydrodynamic Direct Writing of Nano-Suspensions. *J. Nanopart. Res.* **2007,** *9*, 825-831.
233. Dang, Z.; Shamsi, J.; Palazon, F.; Imran, M.; Akkerman, Q. A.; Park, S.; Bertoni, G.; Prato, M.; Brescia, R.; Manna, L., In Situ Transmission Electron Microscopy Study of Electron Beam-Induced Transformations in Colloidal Cesium Lead Halide Perovskite Nanocrystals. *ACS Nano* **2017,** *11*, 2124-2132.

CHAPTER 2. QUANTUM-CUTTING YB^{3+}-DOPED PEROVSKITE NANOCRYSTALS FOR MONOLITHIC BILAYER LUMINESCENT SOLAR CONCENTRATORS

Reproduced with permission from Cohen, T. A.; Milstein, T. J.; Kroupa, D. M.; MacKenzie, J. D.; Luscombe, C. K.; Gamelin, D. R. *J. Mater. Chem. A* **2019**, *7*, 9279.

2.1 OVERVIEW

Luminescent solar concentrators (LSCs) can concentrate direct and diffuse solar radiation spatially and energetically to help reduce the overall area of solar cells needed to meet current energy demands. LSCs require luminophores that absorb large fractions of the solar spectrum, emit photons into a light-capture medium with high photoluminescence quantum yields (PLQYs), and do not absorb their own photoluminescence. Luminescent nanocrystals (NCs) with near or above unity PLQYs and Stokes shifts large enough to avoid self-absorption losses are well-suited to meet these needs. In this work, we describe LSCs based on quantum-cutting Yb^{3+}:$CsPb(Cl_{1-x}Br_x)_3$ NCs that have documented PLQYs as high as ~200%. Through a combination of solution-phase 1D LSC measurements and modeling, we demonstrate that Yb^{3+}:$CsPbCl_3$ NC LSCs show negligible intrinsic reabsorption losses, and we use these data to model the performance of large-scale 2D LSCs based on these NCs. We further propose a new and unique *monolithic bilayer* LSC device architecture that contains a Yb^{3+}:$CsPb(Cl_{1-x}Br_x)_3$ NC top layer above a second narrower-gap LSC bottom layer (*e.g.*, based on $CuInS_2$ NCs), both within the same waveguide and interfaced with the same Si PV for conversion. We extend the modeling to predict the flux gains of such bilayer devices. Because of the exceptionally high

PLQYs of Yb^{3+}:$CsPb(Cl_{1-x}Br_x)_3$ NCs, the optimized bilayer device has a projected flux gain of 63 for dimensions of 70 x 70 x 0.1 cm^3, representing performance enhancement of at least 19% over the optimized $CuInS_2$ LSC alone.

2.2 INTRODUCTION

Luminescent solar concentrators (LSCs) are passive concentrating devices that use luminophores embedded in transparent waveguides to redirect solar radiation from large areas onto the smaller areas of optically coupled photovoltaic (PV) cells.[1-2] LSCs have been intensively researched for decades[3-7] because they can concentrate diffuse light with potentially unlimited flux gains[8-11] (ratio of photons converted by a given LSC-coupled PV to photons that would be converted by the same PV exposed directly to the same solar flux) using a collection waveguide fabricated from relatively low cost and low energy-to-manufacture per unit area materials. Recent models suggest that 100,000 square kilometers of conventional dense-cell solar-panel area would be required to meet current energy demands.[12] With an energy pay-back period for silicon PV that will likely remain on the order of several years,[13] LSCs are well suited to reduce the total area of silicon PV cells required to meet energy demands.[2]

Most early work with LSCs used organic dyes as luminophores, and these LSCs have now been implemented in a variety of large-scale installations.[14-17] Recently, several inorganic semiconductor nanocrystals (NCs) with high photoluminescence quantum yields (PLQYs) have been explored for LSC applications, including various simple luminescent NCs,[18-23] as well as more complicated NC structures such as core/shell NCs,[24-28] dot-in-rod NCs,[29] and a variety of impurity- or defect-activated NCs.[30-40] Such semiconductor NCs can be made with less reabsorption of their own emission, larger absorption cross-sections, greater photochemical stability, and broader solar absorption than organic dyes. A survey[31] of several leading NCs

showed that Mn^{2+}-doped[30-31, 36] and Cu^{+}-doped[37, 41] NCs have substantially less intrinsic reabsorption than heterostructured NCs. $CuInE_2$ (E = S, Se) NCs have similar PL characteristics as Cu^{+}-doped NCs[42-45] and can be made with higher PLQYs. Consequently, LSCs based on $CuInE_2$ NCs have been heavily investigated[32-35, 38-40] and are currently being commercialized by UbiQD. Beyond Mn^{2+} and Cu^{+}, Yb^{3+} has been targeted as a NC dopant of particular interest for LSCs because its $^2F_{5/2} \rightarrow {}^2F_{7/2}$ *f-f* transition combines a narrow PL lineshape with high PLQYs and low *f-f* oscillator strengths (low reabsorption) at energies only slightly above the silicon band gap.[30] Several LSC designs employing Yb^{3+} luminescence have already been reported,[46-50] but the luminophores used to date have lower absorption cross sections than organic dyes or inorganic NCs. Attempts at sensitizing Yb^{3+} luminescence using intermediate-gap semiconductor NCs have been moderately successful,[51-53] but none of these materials were sufficiently promising until the recent development of Yb^{3+}:$CsPbX_3$ perovskite NCs, which show highly efficient picosecond quantum cutting that generates PLQYs approaching the quantum-cutting limit of 200%.[54-56]

Although quantum-cutting Yb^{3+}-doped $CsPbX_3$ NCs have reabsorption-minimizing effective Stokes shifts and unprecedented PLQYs for doped NCs, the energy-conservation requirement of quantum cutting limits their solar absorption to $\lambda < \sim$500 nm.[55-56] This limitation mirrors the challenges faced by high-band-gap PV materials, which have therefore emerged as candidates for alternative configurations including tandem or multi-junction PV cells.[57-61] The tandem concept has already been explored in LSCs based on organic[62-64] or inorganic[18, 27, 40, 65-66] luminophores. Here, a top LSC coupled to a wider-gap PV is placed above a separate bottom LSC coupled to a lower-gap PV and the PV voltages are summed, allowing bluer photons to be converted with greater energy efficiency than in a single-layer LSC. Two-terminal tandem

devices require near-perfect photocurrent matching between the top and bottom cells under all operating conditions to prevent the closed-circuit current from being limited by the lowest performing PV cell, however. Photocurrent losses are observed even in state-of-the-art two-terminal tandem PV cells,[59-61] and this challenge has not been addressed in the tandem LSC literature.

In this work, we use a 120 cm 1D LSC[31-32] to demonstrate that Yb^{3+}:$CsPbCl_3$ NCs indeed behave as zero-reabsorption, high-efficiency luminophores suitable for application in large-scale LSCs. We show that Yb^{3+}:$CsPbCl_3$ NCs have negligible intrinsic attenuation losses over these large waveguide lengths, but also that severe attenuation is still observed when the waveguide contains C-H bonds (high-frequency vibrations). This result has important implications for future large-scale LSC work involving these materials, because it precludes the use of popular acrylics as waveguides. With these results in hand, we further propose and model a new monolithic-bilayer LSC device architecture integrating quantum cutting that offers an attractive alternative to traditional tandem LSCs. This new device concept is fundamentally different from tandem LSCs in that the concentrated photons from both luminophore layers are all directed *via* the same waveguide to the same PV, circumventing the expenses and technical challenges associated with current matching in normal tandem devices. For illustration, we model integration of a layer of band-gap-optimized Yb^{3+}:$CsPb(Cl_{1-x}Br_x)_3$ NCs on top of a state-of-the-art $CuInS_2$ NC LSC in a monolithic bilayer configuration and predict improvement of overall LSC performance by at least 19%. These results identify both practical guidelines and conceptual directions for future LSC development that can capitalize on the unique spectroscopic and photophysical properties of quantum-cutting Yb^{3+}:$CsPb(Cl_{1-x}Br_x)_3$ NCs.

2.3 METHODS

Materials. Lead acetate trihydrate [$Pb(OAc)_2 \cdot 3H_2O$] (99.9%, Baker Chemical), ytterbium acetate hydrate [$Yb(OAc)_3 \cdot xH_2O$] (99.9%, Strem Chemical), cesium acetate [CsOAc] (99.9%, Alfa Aesar), anhydrous ethanol (200 proof, Decon Laboratories, Inc.), chlorotrimethylsilane (TMS-Cl) (98%, Acros Organics), bromotrimethylsilane (TMS-Br) (97%, Sigma Aldirch), 1-octadecene (ODE) (90%, Sigma Aldrich), oleylamine (OAm) (70%, Sigma Aldrich), oleic acid (OA) (90%, Sigma Aldrich), hexanes (99%, Sigma Aldrich), tetrachloroethylene (TCE) (99%, Alfa Aesar), anhydrous ethyl acetate (99%, Sigma Aldrich), and 1/4" and 1/8" extruded poly(methyl methacylate) (PMMA) slabs (Evonik Cyro LLC) were used as received unless otherwise noted.

Nanocrystal synthesis and purification. Yb^{3+}:$CsPbCl_3$ NCs with the highest Yb^{3+} emission quantum yield were synthesized by hot-injection following procedures reported elsewhere.[55] Samples suspended in TCE were not filtered after washing and purification. To synthesize the mixed Yb^{3+}:$CsPb(Cl_{1-x}Br_x)_3$ NCs, a freshly synthesized Yb^{3+}:$CsPbCl_3$ NC sample in hexane was transferred into an N_2 filled glovebox. Small amounts of 1 M TMS-Br in hexane were titrated into the NC sample until the absorption onset reached 488 nm.[67]

Physical measurements. Optical absorption spectra in the visible regime that require a 1 cm cuvette were collected at room temperature using a Cary 60 spectrometer. All other optical absorption spectra were collected at room temperature using a Cary 5000 spectrometer. Wavelength independent absorption constants were added to the absorption spectra of hexanes and TCE to account for reflection losses. NC transmission electron microscopy (TEM) images were collected using a FEI TECNAI F20 microscope at 200 kV. TEM samples were prepared by drop casting NC suspensions onto carbon-coated copper grids from TED Pella, Inc. Powder X-

ray diffraction (XRD) spectra were collected using a Bruker D8 Advance diffractometer. Samples were prepared by drop-casting NC suspensions onto monocrystalline silicon wafer substrates. Samples were irradiated using Cu Kα radiation (50 W). Photoluminescence spectra for photoluminescence quantum yield (PLQY) and 1D LSC experiments were collected using a monochromator coupled to a spectrally corrected nitrogen-cooled CCD. PLQY measurements were performed according to the procedures described previously.[55] Elemental compositions were determined by inductively coupled plasma – atomic emission spectroscopy (ICP-AES, PerkinElmer 8300). Samples were prepared by digesting the NCs in concentrated nitric acid overnight with sonication. Yb^{3+} atomic concentrations are defined as $[Yb^{3+}]/([Yb^{3+}] + [Pb^{2+}])$.

1D LSC measurements. The apparatus for measuring LSC reabsorption losses used here is based on a 120 cm long hollow quartz waveguide (Friederick and Dimmock Co.) with a 1 mm x 1 mm square inner dimension and 1.65 mm x 1.65 mm outer dimension, suspended over a black aluminum channel. The quartz tube was filled with sample using a removable capillary tube. A 375 nm pulsed laser passed through an iris at its smallest setting was used as the excitation source. Emission from the 1D LSC is treated as a point source and was collected using our homebuilt CCD setup. The excitation source distance from the closed end of the tube was varied by moving the laser across the laser table and aligning the laser perpendicular to the tube to maximize signal.

2.4 Results and Analysis

2.4.1 *Nanocrystal Characterization and 1D LSC Measurement*

Figure 2.1a shows representative absorption and PL spectra of Yb^{3+}:$CsPbCl_3$ NCs dispersed in hexane, and compares these spectra with the external quantum efficiency (EQE) of a near infrared (NIR) enhanced Si HIT PV cell[61] and the AM 1.5 solar spectrum.[68] The analytical

atomic Yb^{3+} B-site concentration for these NCs was 5.4%, and the PLQY was measured to be 130% at a CW excitation rate ~ 350 s^{-1}. The NCs absorb UV light in a region where the Si PV EQE is poor, and they reemit this energy in a region where the Si PV EQE ~ 1. Figure 2.1b shows a representative TEM image of a sample of Yb^{3+}:$CsPbCl_3$ NCs. The NCs display the characteristic cube-like shapes of the parent $CsPbCl_3$ NCs. Figure 2.1c shows representative XRD data demonstrating that the perovskite crystal structure was indeed synthesized. The reproducibility of this synthesis was validated in our previous report.[55]

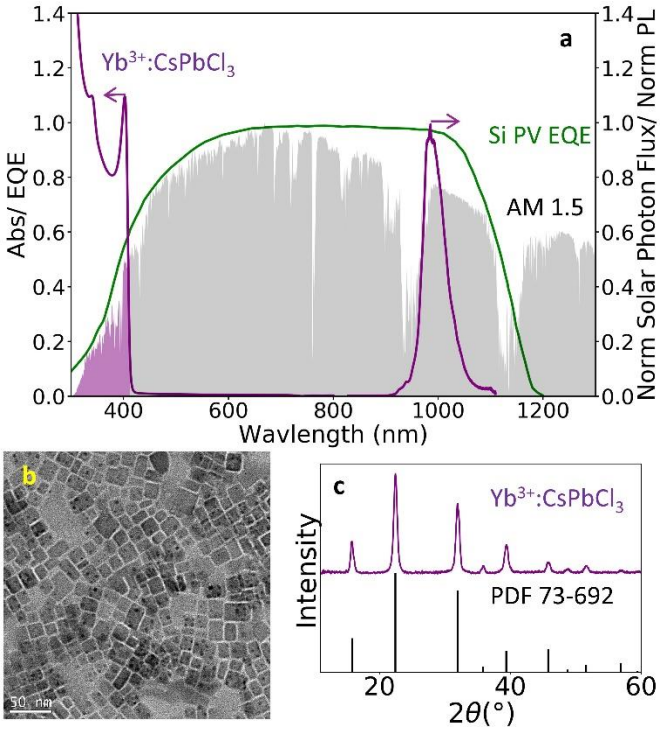

Figure 2.1. Yb^{3+}:$CsPbCl_3$ NCs characterization for 1D LSC measurement.**(a)** Absorption and normalized PL spectra of Yb^{3+}:$CsPbCl_3$ NCs (purple) plotted with the EQE of a NIR enhanced Si HIT PV (green) and the AM1.5 solar spectrum (shaded area). Spectra were collected at room temperature. **(b)** TEM and **(c)** XRD data for a representative sample of Yb^{3+}:$CsPbCl_3$ NCs.

Undoped perovskite NCs,[66, 69-70] thin films,[71] and Mn^{2+}-doped $CsPbCl_3$ NCs[36] have been used in LSCs previously. While this work was under preparation, a small-scale (5 cm x 5 cm) LSC using these same quantum-cutting Yb^{3+}:$CsPbCl_3$ NCs was also reported.[72] This report

supports the premise that Yb^{3+}:$CsPbCl_3$ NCs are attractive for LSCs, as anticipated from their spectroscopy, but it does not assess any of the fundamental loss mechanisms that *are* active within such LSCs, and it does not evaluate performance in waveguides beyond the 5 cm x 5 cm model LSC. Because the key attraction of LSCs is their ability to harvest photons over large LSC facial areas for concentration into small PV areas, it is important to evaluate the photon losses in larger waveguides, for example on the scale of a building's windows.[3-4, 39] To this end, measurements were performed here on Yb^{3+}:$CsPbCl_3$ NCs in a substantially larger waveguide than investigated previously.

Figure 2.2a plots normalized experimental PL spectra collected in a (120 cm) × $(1\ mm)^2$ 1D LSC at various excitation distances away from the LSC edge, where the photodetector is mounted (complete PL intensity data are provided in the Figure A.1). For these measurements, Yb^{3+}:$CsPbCl_3$ NCs were suspended in hexane with a transverse optical density (OD_t) of ~0.75 mm^{-1} at 375 nm (see Figure A.2 for complete visible absorption spectra). Figure 2.2b plots the integrated intensities of the raw PL traces as a function of excitation distance, normalized to the integrated PL intensity at the shortest excitation distance. These data show substantial attenuation of the PL as the distance traveled by emitted photons to the detector through the waveguide is increased. For comparison, Figure 2.2b also plots the experimentally determined waveguide attenuation over these extremely large waveguide lengths,[31] reflecting photon scattering and otherwise imperfect transmission even in the absence of NCs. The curve plotted here was obtained by fitting the 1D LSC attenuation data (see Figure A.3), which yielded a wavelength-independent attenuation coefficient of 0.002 cm^{-1}. This curve represents the performance limit of this particular 1D LSC waveguide, and it allows the intrinsic NC performance to be assessed. These results show that the experimental Yb^{3+} PL attenuation is not

due to waveguide losses. As independent confirmation, Figure 2.2b also plots analogous 1D LSC data collected for the same NCs diluted by a factor of 10. These LSC data are essentially indistinguishable from the higher-concentration data, indicating substantial attenuation that is *not* caused by the NCs themselves. Instead, this attenuation can be traced to absorption of the Yb^{3+} PL by vibrational bands of the organic medium containing the NCs in this 1D LSC. Figure 2.2a also plots the absorption spectrum of hexane in the wavelength region of the Yb^{3+} PL and reveals a series of weak but significant vibrational overtone bands characteristic of C-H stretching vibrations.[73] The data in Figure 2.2a show that the Yb^{3+} PL intensity is attenuated on its red and blue edges with increasing waveguide length, precisely where this PL overlaps with these vibrational overtone bands.

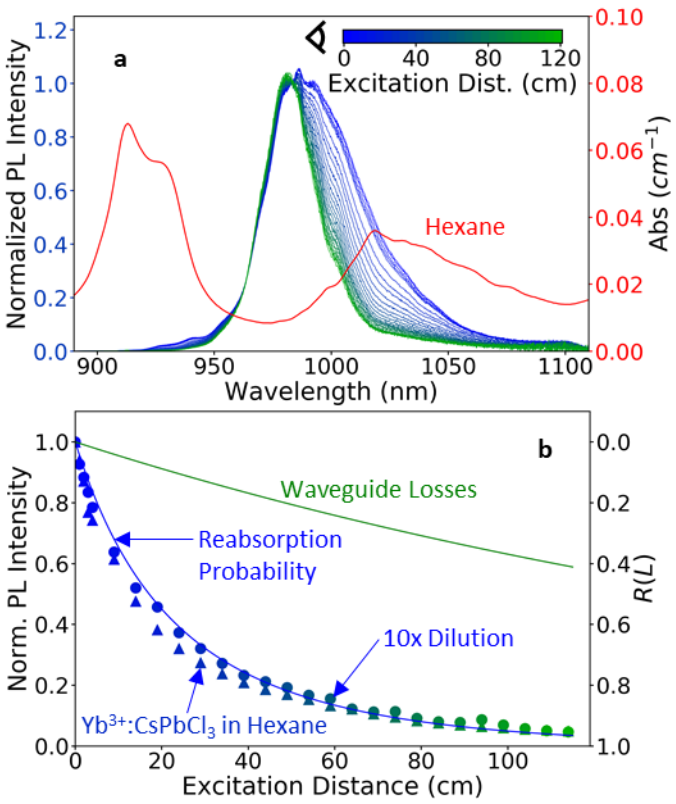

Figure 2.2. Spectral and integrated 1D LSC data from Yb^{3+}:$CsPbCl_3$ NCs in hexane. **(a)** Normalized PL spectra of Yb^{3+}:$CsPbCl_3$ NCs suspended in hexane with OD_t ~ 0.75 mm^{-1} at 375 nm, obtained from the 1D LSC experiment at various excitation distances relative to the edge-mounted photodetector (see inset). The red curve shows the absorption spectrum of the hexane solvent. **(b)** Integrated normalized Yb^{3+}:$CsPbCl_3$ NC PL intensity plotted as a function of excitation distance away from the photodetector, for NCs in hexane with OD_t ~ 0.75 mm^{-1} (triangles) and OD_t ~ 0.075 mm^{-1} (circles) at 375 nm. The blue trace is the reabsorption probability described in eq 1 modeled with hexane absorption from Figure 2a. The green line is the experimentally determined performance limit of the 1D LSC. All PL data were collected with excitation at 375 nm, and all data were collected at room temperature.

For quantitative data analysis, these 1D LSC data were modeled following methods adapted from our previous work.[31-32] Briefly, the PL reabsorption probability is described by eq 2.1,

$$R(L) = \int PL_{norm}(\lambda)\left(1 - 10^{\frac{-A_{norm}(\lambda) L\, OD_t}{t}}\right) d\lambda \qquad (2.1)$$

where $A_{norm}(\lambda)$ is the absorption spectrum of the NCs, solvent, and waveguide normalized at 375 nm, t is the thickness of the NC layer in the 1D LSC (t = 1.0 mm here), OD_t is the optical density over that thickness at the excitation wavelength of 375 nm, L is the excitation distance away from the LSC collection edge, and $PL_{norm}(\lambda)$ is the amplitude of the area-normalized NC PL spectrum measured at λ. Using eq 2.1, the hexane absorption spectrum, and the PL spectrum at L = 0 from Figure 2.2b, the attenuation of the integrated Yb^{3+} luminescence intensity as a function of L was simulated. The resulting curve is included in Figure 2.2b along with the experimental data, and good agreement between the two is observed. Overall, this analysis confirms that the PL attenuation in this experiment is not due to losses involving the NCs or the glass portion of the waveguide, but instead comes from absorption of emitted photons by C-H vibrations of the organic portion of the waveguide, and it allows quantitative description of these contributions to the overall LSC performance.

To eliminate the C-H absorption losses identified above, Yb^{3+}:$CsPbCl_3$ NCs were suspended in tetrachloroethylene (TCE), which lacks protons and is therefore transparent in the NIR window of interest. Figure 2.3a plots the Yb^{3+} PL intensity measured as a function of excitation distance for 1D LSC measurements with this solvent. For comparison, the corrected absorption spectrum of TCE is also included in Figure 2.3a. Because TCE has no C-H vibrational overtone bands in the NIR, the Yb^{3+} PL intensity decay is now independent of wavelength. For comparison, Figure 2.3b plots the integrated PL intensities *vs* excitation distance for the same NC concentration in both TCE and hexane (see Figure A.2 for absorption spectra). The PL intensity from the TCE solution is substantially greater at large excitation distances than that from the hexane solution under similar conditions. In fact, the integrated PL intensity from the TCE solution essentially follows the waveguide losses of the 1D LSC alone, indicating that

this decay now comes primarily from scattering within the glass waveguide. These NCs show reabsorption losses as low as any of the NCs measured previously over similar 120 cm waveguide lengths.[31-32]

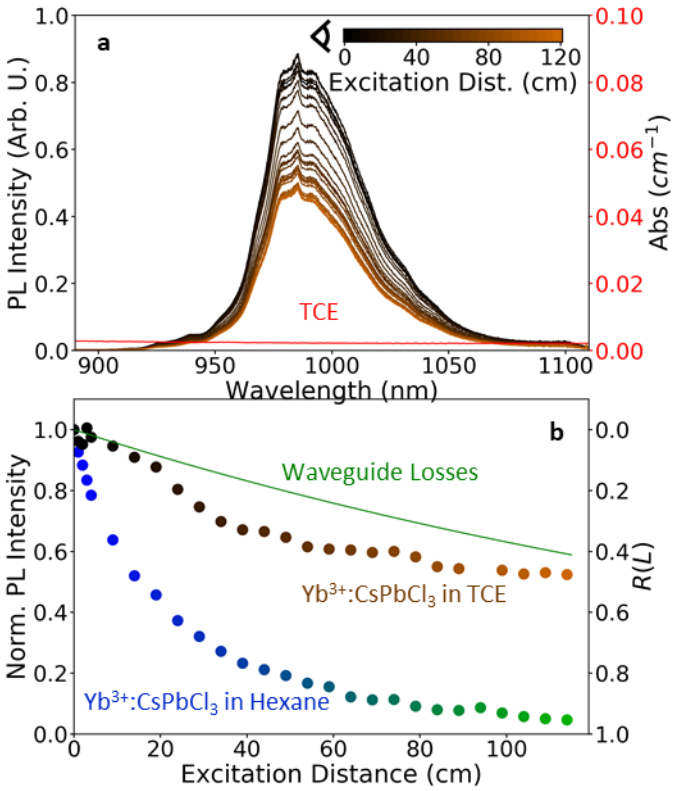

Figure 2.3. Spectral and integrated 1D LSC data from Yb^{3+}:$CsPbCl_3$ NCs in tetrachloroethylene (TCE) and hexane. **(a)** PL intensity of Yb^{3+}:$CsPbCl_3$ NCs suspended in tetrachloroethylene from the 1D LSC experiment plotted from low excitation distances to high excitation distance with the corrected absorption spectrum of TCE. **(b)** Integrated normalized PL intensity of Yb^{3+}:$CsPbCl_3$ NCs plotted as a function of excitation distance for solutions in hexane with an OD_t ~ 0.075 mm^{-1} (blue-green) and in TCE with an OD_t ~ 0.075 mm^{-1} (black-brown). The green line is the experimentally determined performance limit of the 1D LSC. The analytical atomic Yb^{3+} concentration for these NCs was 4.6% and the PLQY was 138% in hexane and 71% after transfer to TCE.

Figure 2.4a shows the absorption spectra of hexane and two potential waveguide materials (PMMA and Schott optical-quality glass) overlaid with the Yb^{3+} PL spectrum from these Yb^{3+}:$CsPbCl_3$ NCs. The PMMA spectrum is similar in magnitude and shape to those

reported previously,[73-74] and in particular, it shows C-H vibrational overtone absorption bands similar to those observed in hexane, shifted slightly to shorter wavelength and still overlapping the Yb^{3+} PL substantially. In contrast, the Schott glass shows little to no absorption in this region.

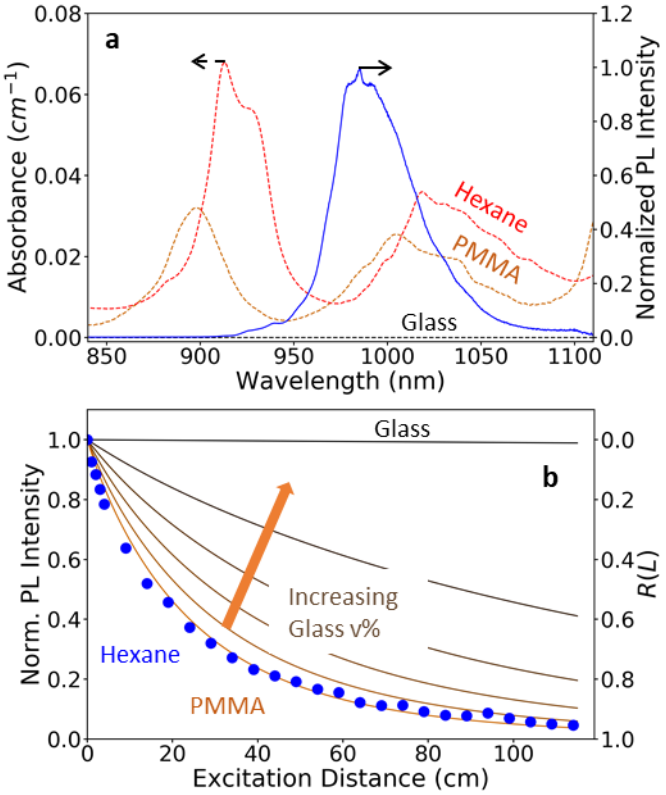

Figure 2.4. Spectral and integrated 1D LSC projection for the lateral attenuation of Yb^{3+} emission in various waveguiding media. **(a)** Absorption spectrum of hexane (red), a representative PMMA sample (orange), and Schott optical-quality glass (black) overlaid with the normalized PL spectrum of Yb^{3+}:$CsPbCl_3$ NCs (blue). The PMMA spectrum was obtained by subtracting experimental spectra measured for two samples with different thickness to eliminate surface reflection and scattering effects. **(b)** Normalized PL intensity of Yb^{3+}:$CsPbCl_3$ NCs in hexane as a function of excitation distance in a 120 cm-long 1D LSC (blue dots).

With these spectra, it is possible to simulate the anticipated performance of various acrylic and glass 1D LSCs, as well as of composite (or layered) waveguides involving different volume fractions of polymer and glass as per common 2D LSC configurations. An attenuation

coefficient of 4.14 x 10^{-5} cm^{-1} was used to model transmission through glass in these simulations.[75] Figure 2.4b plots the results of these calculations. From these simulations, the NC performance in a PMMA waveguide will likely be as poor as the experimental 1D LSC results in hexane reported in Figure 2.3b (and reproduced in Figure 2.4b for comparison). These results relate to the recent report of a small-scale LSC made from suspension of Yb^{3+}:$CsPbCl_3$ NCs in PMMA. The data from this device were fitted to conclude a wavelength-independent attenuation coefficient of 0.023 cm^{-1},[72] which the authors attributed to scattering and suggested could be eliminated through device optimization. The results in Figure 2.4a show, however, that the PMMA absorbance itself is ~0.02 cm^{-1} where it overlaps the Yb^{3+} PL, and this absorption is not wavelength independent. This analysis thus indicates that popular acrylics will likely not be suitable waveguide matrices for LSCs based on Yb^{3+} emission, including from quantum-cutting Yb^{3+}:$CsPb(Cl_{1-x}Br_x)_3$ NCs. In contrast, the performance of Yb^{3+}:$CsPb(Cl_{1-x}Br_x)_3$ NC LSCs using glass waveguides will likely be near the theoretical limit. Figure 2.4b further illustrates that a device configuration involving a thin PMMA film containing densely packed NCs on top of a glass waveguide falls between these two extremes, with LSC performance determined by the relative PMMA and glass waveguide volumes. Clearly, this layered PMMA/glass LSC configuration is only attractive with Yb^{3+}:$CsPb(Cl_{1-x}Br_x)_3$ NCs if the PMMA film is very thin relative to the glass waveguide (*e.g.*, <~5% PMMA by volume).

2.4.2 *2D LSCs*

Monolayer 2D LSCs. As detailed previously,[31-32] 1D LSC data and simulations of the type presented above provide all the necessary input to assess the 2D LSC performance of a given luminophore. The primary metric of interest is the LSC flux gain (*FG*), defined as the ratio of photons converted by a given LSC-coupled PV to photons that would be absorbed by the same

PV exposed directly to the same solar flux. The 2D LSC flux gain (FG_{2D}) is calculated using eq 2.2,

$$FG_{2D} = OQE(L)\frac{\eta_{pl}}{\eta_{AM}}\frac{A_{nc}}{A_{sol}}G(L) \tag{2.2}$$

where η_{nc} is the NC PLQY, η_{pl}/η_{AM} is the efficiency of a silicon PV exposed to the NC PL spectrum relative to the efficiency of the same PV exposed to AM 1.5 solar radiation. $G(L)$ is the LSC geometric gain, equal to $L/4t$, where L is the edge length and t is the waveguide thickness in a square 2D device. The optical quantum efficiency $OQE(L)$ is the ratio of photons that reach the LSC edge to solar photons absorbed by the LSC, A_{nc} is the solar flux absorbed by a particular NC LSC, and A_{sol} is the solar flux absorbed by the solar cells coupled to the edges of the device when directly exposed to the solar irradiation. A_{nc} and A_{sol} are calculated using eqs 2.3 and 2.4,

$$A_{nc} = \int \Phi_{AM1.5}(\lambda)\left(1 - 10^{-A_{abs}(\lambda)}\right)d\lambda \tag{2.3}$$

$$A_{sol} = \int \Phi_{AM1.5}(\lambda)EQE(\lambda)d\lambda \tag{2.4}$$

where $\Phi_{AM1.5}$ is the AM1.5 solar photon flux, $A_{abs}(\lambda)$ is the NC absorption spectrum, $EQE(\lambda)$ is the external quantum efficiency of the solar cell of interest. The 1D LSC results presented in Figure 2.3b suggest that there are no reabsorption losses for the Yb^{3+}:$CsPbCl_3$ layer. Therefore, $OQE(L)$ can be calculated using eq 2.5.

$$OQE(L) = \frac{\Phi}{4\pi L^2}\iint_{L\times L}\int_0^{2\pi}\int_{\varphi_{esc}}^{\pi-\varphi_{esc}} I_{PL}(l(x,y,\theta,\varphi))sin\varphi d\varphi d\theta dx dy \tag{2.5}$$

Here, $l(x,\ y,\ \theta,\varphi)$ is the distance a photon must travel from any point $x, y \in [0, L]$, any azimuthal angle $\theta \in [0, 2\pi]$, and any polar angle $\varphi \in [\varphi_{esc}, \varphi_{esc} - \pi]$, Φ is the NC PLQY,

$I_{PL}(L)$ is the normalized, integrated PL intensity as a function of excitation distance from a collection edge (obtained from the 1D LSC experimental data), and φ_{esc} is the polar angle that defines the photon escape cone, which equals $\arcsin(1/n)$, where n is the waveguide's refractive index.

The flux gain of an Yb^{3+}:$CsPbCl_3$ NC 2D LSC was calculated using eqs 2.2 – 2.5 using the experimental data from Figure 2.3b as input (or extrapolated from these data for waveguiding lengths exceeding 120 cm). In this simulation, a value of Φ = 170% was used, based on experiment,[55] and *n* was assumed to be 1.5, which is the approximate refractive index of glass or PMMA.[6] Si HIT PV cells provide the best spectral matching with these Yb^{3+}:$CsPbCl_3$ NCs, and these PV have $\eta_{pl}/\eta_{AM} \sim 1$ because of their high NIR EQE. $OQE(L)$ for the Yb^{3+}:$CsPbCl_3$ NCs was calculated using eq 2.5. As validation, average distances to the edge of a square calculated using $l(x, y, \theta, \varphi)$, along with 2D flux-gain predictions for $Zn_{0.87}Cd_{0.11}Mn_{0.02}Se$/ZnS NCs that match our previous report,[31] are provided as Figure A.4. Figure 2.5c (*vide infra*) summarizes the results of these simulations up to a geometric gain of 175. The initial slope of the flux gain trace for a Yb^{3+}:$CsPbCl_3$ NC 2D LSC is 0.06, and the maximum projected flux gain is 8 at *G* = 175. This value is substantially larger than the projected gain of 5 for a $Zn_{0.87}Cd_{0.11}Mn_{0.02}Se$/ZnS NC LSC simulated by the same methods,[30-31] despite the fact that Yb^{3+}:$CsPbCl_3$ NCs absorb 30% fewer AM1.5 solar photons than $Zn_{0.87}Cd_{0.11}Mn_{0.02}Se$/ZnS NCs do. These results demonstrate that even with their wide energy gap, Yb^{3+}:$CsPbCl_3$ NCs can excel as luminophores for 2D LSCs because of their exceptionally high PLQYs resulting from quantum cutting.

Bilayer 2D LSCs. (*i*) *Yb^{3+}:$CsPbCl_3$/$CuInS_2$ bilayers.* Although Yb^{3+}:$CsPbX_3$ NC LSCs themselves have inherent advantages over other LSCs arising from their unusual quantum-cutting capabilities, we propose that the greatest advantage can be taken of these materials if they

are paired with another set of narrower-gap NCs in the same waveguide to form a new type of monolithic bilayer LSC. Figure 2.5a illustrates the proposed device structure. In this configuration, high-energy light is absorbed by the quantum-cutting Yb^{3+}:$CsPbCl_3$ NCs. Lower-energy light is transmitted by the top layer and absorbed in the bottom layer, which may use any of several available broadband LSC luminophores. $CuInS_2$ and related NCs have emerged as particularly attractive materials for LSCs because of their high PLQYs, broadband absorption across the visible, and large effective PL Stokes shifts;[32, 35, 38-40] for illustrative purposes, we consider these for the bottom layer of the proposed device. Figure 2.5b plots relevant absorption and PL spectra for this device architecture. $CuInS_2$/ZnS NC absorption and PL spectra are reproduced from a recent report of high-performance NC LSCs.[39] Importantly, although the Yb^{3+}:$CsPbCl_3$ and $CuInS_2$/ZnS NCs are layered such that bluer photons are absorbed by the top-layer Yb^{3+}:$CsPbCl_3$ NCs, and transmitted redder photons are absorbed by the bottom-layer $CuInS_2$/ZnS NCs, both layers emit in the NIR at wavelengths that can be transmitted through *both* absorber layers of this waveguide. Like two-terminal tandem LSCs investigated previously,[18, 27, 40, 62-66] this bilayer device structure improves LSC efficiency by eliminating thermalization losses associated with the blue photons. Unlike two-terminal tandem LSCs, however, this structure has the distinct advantage that it avoids the use of two separate LSCs that use separate PV cells wired in series. For maximum efficiency, the tandem configuration would require current matching between the two LSC layers. In the monolithic bilayer configuration, it is the currents that are added at the fixed voltage of the single edge-mounted PV, vastly simplifying the device.

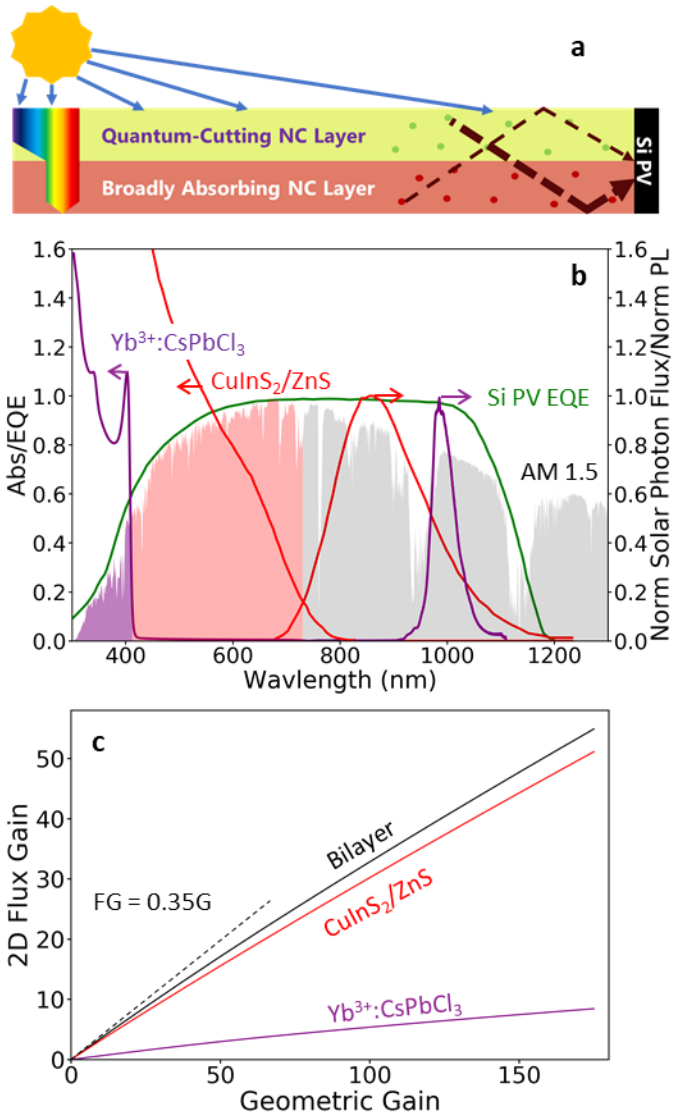

Figure 2.5. Diagram describing proposed quantum cutting-enhanced monolithic bilayer LSC. Spectra and performance projection for the various components of this device. **(a)** Schematic of the proposed monolithic bilayer LSC. The top layer contains quantum-cutting NCs (*e.g.*, Yb^{3+}:$CsPb(Cl_{1-x}Br_x)_3$ NCs) and the bottom layer contains broadly absorbing NCs (*e.g.*, $CuInS_2$ NCs). **(b)** Absorption and normalized PL spectra of Yb^{3+}:$CsPbCl_3$ NCs (purple) and $CuInS_2$/ZnS NCs (red) overlaid with the AM 1.5 solar spectrum (shaded area) and the external quantum efficiency (EQE) of a NIR enhanced Si HIT PV (green). **(c)** Projected 2D flux gain of a Yb^{3+}:$CsPbCl_3$ NC LSC (purple), a $CuInS_2$/ZnS NC LSC (red), and the monolithic, bilayer device shown in Figure 5a (black).

To explore the potential benefits that might be expected from such a quantum-cutting bilayer LSC, the experimental data described above were used to model the performance of 2D Yb^{3+}:$CsPbCl_3$ NC/$CuInS_2$ NC bilayer LSCs in the configuration illustrated in Figure 2.5a. The flux gains of Yb^{3+}:$CsPbCl_3$/$CuInS_2$ NC-based bilayer 2D LSCs were calculated using eqs 2.2 – 2.5. In these simulations, a value of Φ = 91% was used for the for $CuInS_2$ NCs, based on the highest reported literature value (obtained with $CuInS_2$/ZnS core/shell NCs).[39] η_{pl}/η_{AM} was again assumed to be ~1 due to the high NIR EQE of the Si HIT cells. For $CuInS_2$ NCs, an additional *OD* of 0.002 cm^{-1} was added to the attenuation spectrum to simulate the impact of waveguide losses on the projected flux gain (reabsorption probability simulations provided in Figure A.5). Because reabsorption losses will affect the performance of the $CuInS_2$ layer, the $OQE(L)$ of the $CuInS_2$ layer is computed using an advanced analytical model developed previously.[38] A detailed description of this model is provided in Section A.1.

To simulate the performance of the bilayer LSC of Figure 2.5a, the thickness of each waveguide layer was assumed to be 0.5 mm and the optical density of each layer was doubled compared to its single-layer analog. From here, the solar flux absorbed by the $CuInS_2$ NCs in the bilayer device is the difference between A_{CIS} and A_{CsPbCl_3}. Once this modification is made, the flux gain of the bilayer device is simply the sum of the Yb^{3+}:$CsPbCl_3$ NC LSC flux gain and the $CuInS_2$ NC LSC flux gain. Figure 2.5c summarizes the results of these simulations. The bilayer device reaches a flux gain of 55 for *G* = 175, which is a 7% improvement over the $CuInS_2$ NC LSC of similar dimensions. The initial slope of the bilayer device is 0.35, compared with 0.06 for the Yb^{3+}:$CsPbCl_3$ NC LSC or 0.32 for the $CuInS_2$ NC LSC alone.

(*ii*) *Yb^{3+}:$CsPb(Cl_{1-x}Br_x)_3$/$CuInS_2$ bilayers.* Improved solar absorption can be achieved by narrowing the top layer's energy gap through anion alloying. Figure 2.6a shows the absorption

and PL spectra of Yb^{3+}:$CsPb(Cl_{1-x}Br_x)_3$ NCs synthesized from Yb^{3+}:$CsPbCl_3$ NCs *via* anion exchange.[67, 76] Increasing x to ~0.75 decreases the NC energy gap to ~488 nm (~2.5 eV) and increases the fraction of the solar spectrum absorbed from ~2.6% (x = 0) to ~8.3% without impacting the PLQY of the Yb^{3+} emission.[67] Figure 2.6b plots the results of this model for three values of the perovskite absorption threshold, from 412 nm (x = 0) to 488 nm (x ~ 0.75), calculated by modifying $A_{CsPb(Cl_{1-x}Br_x)_3}$ in eq 2.3. Narrowing the perovskite energy gap increases the initial flux-gain slope of the stand-alone Yb^{3+}:$CsPb(Cl_{1-x}Br_x)_3$ NC LSC from 0.06 to 0.20 and increases the flux-gain to 27 at G = 175. The initial flux-gain slope of the bilayer device increases from 0.35 to 0.43 and the flux gain increases to 63 at G = 175. This means that for the modeled 70 x 70 cm^2 monolithic bilayer LSC, the 28 cm^2 of Si solar cells optically coupled to its edges are predicted to generate 63 times more current than when operating in non-concentrating conditions. These results represent a 19% performance increase compared with state-of-the-art $CuInS_2$ NC LSCs. The percentage improvement will be even greater if the PLQY of the $CuInS_2$ NC layer is not the record 91% but closer to the ~70% typically found for $CuInS_2$ NC/polymer composites.[38-40]

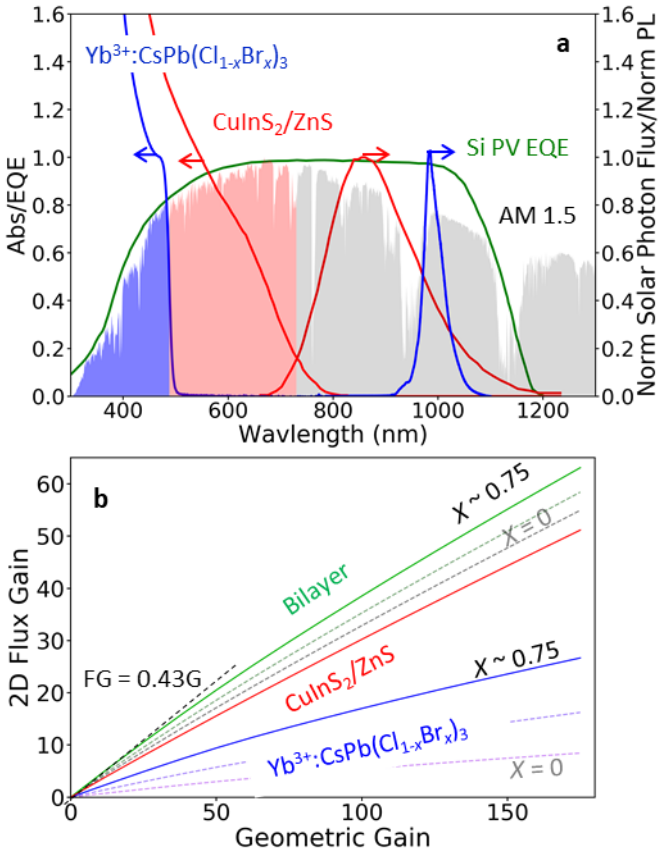

Figure 2.6. Spectra and flux gain projections for monolithic bilayer LSCs based on anion-alloyed quantum-cutting perovskite NCs. **(a)** Absorption and normalized PL spectra of Yb^{3+}:$CsPb(Cl_{1-x}Br_x)_3$ NCs with $x \sim 0.75$ (blue) and $CuInS_2$/ZnS NCs (red) overlaid with the AM 1.5 solar spectrum (shaded area) and the external quantum efficiency (EQE) of a NIR enhanced Si HIT PV (green). **(b)** Projected 2D flux gain of a Yb^{3+}:$CsPb(Cl_{1-x}Br_x)_3$ NC LSC (purple to blue gradient), a $CuInS_2$/ZnS NC LSC (red), and the monolithic, bilayer device shown in fig. 5a (black to green). The absorption onset of the Yb^{3+}:$CsPb(Cl_{1-x}Br_x)_3$ NCs is varied linearly from 412 nm to 488 nm for the three plotted traces.

We note that the $CuInS_2$ NCs used in ref. [39] and modeled above were likely optimized for a polycrystalline Si PV, whereas narrower-gap $CuIn(S_{1-y}Se_y)_2$ NCs may be more appropriate for the Si HIT PV simulated here. To assess the effect of increasing solar absorbance through this change, we modeled the performance of the same bilayer LSC but using the absorption and emission spectra of QD-950 from the Strem catalog[77] (absorption and PL spectra provided in Figure A.6a). Although the solar absorbance of the QD-950 NCs does increase from 26% to

38%, the flux gain of the Yb^{3+}:$CsPb(Cl_{1-x}Br_x)_3$ NC monolithic bilayer device *decreases*, *e.g.*, from 63 to 54 at G = 175 (see Figure A.6b), despite again assuming a PLQY of 91%. We attribute this lack of improvement to increased reabsorption losses in the QD-950 NCs because of their more pronounced absorption tail. Nonetheless, the flux gain of the monolithic bilayer LSC involving a QD-950 NC bottom layer is improved by 35% over the optimized QD-950 NC 2D LSC alone, again validating the bilayer LSC configuration as a simple and attractive opportunity for next-generation NC LSCs.

2.5 DISCUSSION

The experimental results described above demonstrate superb performance of Yb^{3+}-doped halo-perovskite NCs as zero-reabsorption luminophores for large-scale LSCs. Their experimental losses in a 1D LSC are almost completely negligible over extremely large waveguide lengths of up to 120 cm. Moreover, these Yb^{3+}:$CsPbCl_3$ NCs display the unusual and extremely attractive characteristic of quantum cutting, by which PLQYs vastly exceeding 100% have been measured. As demonstrated experimentally in Figure 2.2 – Figure 2.4, however, the PL of these quantum-cutting NCs is absorbed by overtones of high-frequency proton-stretching vibrations present in common LSC polymer matrices.[19-22, 25-30, 35-36, 38-40, 66, 69-70, 72] This works shows that to succeed, an LSC based on Yb^{3+}-doped NCs must use a waveguide matrix that contains very few protons in the form of C-H, O-H, or related bonds. Several proven possibilities already exist, although formation of NC LSCs out of such matrices has not yet been demonstrated, and costs may escalate too much for some of these options to be commercially attractive. Nonetheless, it is interesting to note that the amorphous fluorinated polymer Cytop[74] is already used in near-IR fiber optics and has a NIR attenuation coefficient that is close to those used in the glass simulations here. Additionally, organic-dye LSCs have been fabricated with

partially fluorinated polymers[78-79] that show reduced C-H overtone absorption. Some work has been done to incorporate PbSe and InAs NCs into a fluorinated, aromatic copolymer.[80] These results suggest that NC LSCs using fluorinated waveguides are indeed viable and should be developed further. Alternatively, all-inorganic waveguides such as the oxide matrices used for Nd^{3+} LSCs[1, 81] are also attractive; NC LSCs of this type have not yet been demonstrated, but a notable proof-of-concept is found in the examples of colored Schott glasses, which are composed of chalcogenide semiconductor NCs embedded within optical-quality borosilicate glass. High-efficiency Yb^{3+}-doped fiber lasers and amplifiers involving various oxide and fluoride glass compositions with low cavity losses have also been demonstrated.[82-83]

2.6 CONCLUSION

Through a combination of experimental and computational studies, we have shown that Yb^{3+}:$CsPb(Cl_{1-x}Br_x)_3$ NCs have high potential to serve as a unique LSC luminophore due to their large effective Stokes shift and extraordinarily high PLQY (approaching 200%), arising from their efficient quantum-cutting PL mechanism. These NCs have the lowest self-absorption of any NCs investigated to date, comparable to Mn^{2+}-doped II-VI NCs, but with overall LSC performance exceeding that of the Mn^{2+}-doped NCs because of their very high PLQYs. The experimental measurements presented here highlight the need for proton-free waveguide matrices in LSCs involving these luminophores, which motivates development of NC LSCs with waveguides based on inorganic glasses or fluorinated polymers. Finally, we propose and model a new monolithic bilayer LSC device architecture containing quantum-cutting Yb^{3+}:$CsPb(Cl_{1-x}Br_x)_3$ NCs in its top layer and, *e.g.*, $CuInS_2$/ZnS NCs in its bottom layer. This bilayer design is reminiscent of tandem PVs and LSCs, except that it uses quantum cutting to increase photocurrent rather than using multiple PV energy gaps to increase photovoltage. As such, this

bilayer device has the distinct advantage that PL from both the top (blue-absorbing) and bottom (red-absorbing) luminescent layers can be transported through the same waveguide to the same Si PV, obviating the need for multiple PV cells, interlayer wiring, and current matching as found in traditional tandem devices. Such advantages simplify device construction and operation. Modeling suggests that a bilayer LSC using Yb^{3+}:$CsPb(Cl_{0.25}Br_{0.75})_3$ NCs for the top layer could improve upon the performance of an idealized state-of-the-art $CuInS_2$/ZnS NC LSC bottom layer by at least 19%. It is possible that better inorganic or organic luminophores will be identified in the future to serve as partners with Yb^{3+}:$CsPb(Cl_{0.25}Br_{0.75})_3$ NCs in such bilayer configurations. Overall, these results and the new proposed device structure suggest promising avenues for the development of next-generation NC LSCs.

2.7 Acknowledgements

This research was supported by the National Science Foundation (NSF) through the UW Molecular Engineering Materials Center, a Materials Research Science and Engineering Center (DMR-1719797, to DRG and CKL), and through DMR-1807394 (to DRG). This work was also supported by the UW Clean Energy Institute and the Washington Research Foundation. Part of this work was conducted at the UW Molecular Analysis Facility, a National Nanotechnology Coordinated Infrastructure site supported in part by the NSF (ECC-1542101), the University of Washington, the Molecular Engineering and Sciences Institute, the Clean Energy Institute, and the National Institutes of Health. The authors gratefully acknowledge Kyle Kluherz for providing TEM images and Liam Bradshaw for providing 1D LSC attenuation data and for helpful discussion. We also acknowledge Prof. Gerd Bacher, Christian Erickson, and Matt Crane for helpful discussion.

2.8 REFERENCES

1. Weber, W. H.; Lambe, J., Luminescent Greenhouse Collector for Solar Radiation. *Appl. Opt.* **1976,** *15*, 2299-2300.
2. Goetzberger, A.; Greube, W., Solar Energy Conversion with Fluorescent Collectors. *Appl. Phys.* **1977,** *14*, 123-139.
3. Debije, M. G.; Verbunt, P. P. C., Thirty Years of Luminescent Solar Concentrator Research: Solar Energy for the Built Environment. *Adv. Energy Mater.* **2012,** *2*, 12-35.
4. Meinardi, F.; Bruni, F.; Brovelli, S., Luminescent Solar Concentrators for Building-Integrated Photovoltaics. *Nat. Rev. Mater.* **2017,** *2*, 17072.
5. McKenna, B.; Evans, R. C., Towards Efficient Spectral Converters through Materials Design for Luminescent Solar Devices. *Adv. Mater.* **2017,** *29*, n/a-n/a.
6. Moraitis, P.; Schropp, R. E. I.; van Sark, W. G. J. H. M., Nanoparticles for Luminescent Solar Concentrators - a Review. *Opt. Mater.* **2018,** *84*, 636-645.
7. Zhou, Y.; Zhao, H.; Ma, D.; Rosei, F., Harnessing the Properties of Colloidal Quantum Dots in Luminescent Solar Concentrators. *Chem. Soc. Rev.* **2018,** *47*, 5866-5890.
8. Yablonovitch, E., Thermodynamics of the Fluorescent Planar Concentrator. *J. Opt. Soc. Am.* **1980,** *70*, 1362-1363.
9. Smestad, G.; Ries, H.; Winston, R.; Yablonovitch, E., The Thermodynamic Limits of Light Concentrators. *Sol. Energy Mater.* **1990,** *21*, 99-111.
10. Song, H.-J.; Jeong, B. G.; Lim, J.; Lee, D. C.; Bae, W. K.; Klimov, V. I., Performance Limits of Luminescent Solar Concentrators Tested with Seed/Quantum-Well Quantum Dots in a Selective-Reflector-Based Optical Cavity. *Nano Lett.* **2018,** *18*, 395-404.
11. Klimov, V. I.; Baker, T. A.; Lim, J.; Velizhanin, K. A.; McDaniel, H., Quality Factor of Luminescent Solar Concentrators and Practical Concentration Limits Attainable with Semiconductor Quantum Dots. *ACS Photonics* **2016,** *3*, 1138-1148.
12. Cheng, Y.-B.; Pascoe, A.; Huang, F.; Peng, Y., Print Flexible Solar Cells. *Nat News* **2016,** *539*, 488.
13. Mazzio, K. A.; Luscombe, C. K., The Future of Organic Photovoltaics. *Chem. Soc. Rev.* **2014,** *44*, 78-90.
14. Zhang, J.; Wang, M.; Zhang, Y.; He, H.; Xie, W.; Yang, M.; Ding, J.; Bao, J.; Sun, S.; Gao, C., Optimization of Large-Size Glass Laminated Luminescent Solar Concentrators. *Sol. Energy* **2015,** *117*, 260-267.
15. Vossen, F. M.; Aarts, M. P. J.; Debije, M. G., Visual Performance of Red Luminescent Solar Concentrating Windows in an Office Environment. *Energ. Buildings* **2016,** *113*, 123-132.
16. Reinders, A.; Debije, M. G.; Rosemann, A., Measured Efficiency of a Luminescent Solar Concentrator Pv Module Called Leaf Roof. *IEEE J. Photovolt.* **2017,** *7*, 1663-1666.
17. Sark, W. v.; Moraitis, P.; Aalberts, C.; Drent, M.; Grasso, T.; L'Ortije, Y.; Visschers, M.; Westra, M.; Plas, R.; Planje, W., The “Electric Mondrian” as a Luminescent Solar Concentrator Demonstrator Case Study. *Sol. RRL* **2017,** *1*, 1600015.
18. Barnham, K.; Marques, J. L.; Hassard, J.; O’Brien, P., Quantum-Dot Concentrator and Thermodynamic Model for the Global Redshift. *Appl. Phys. Lett.* **2000,** *76*, 1197-1199.
19. Shcherbatyuk, G. V.; Inman, R. H.; Wang, C.; Winston, R.; Ghosh, S., Viability of Using near Infrared PbS Quantum Dots as Active Materials in Luminescent Solar Concentrators. *Appl. Phys. Lett.* **2010,** *96*, 191901.

20. Wilton, S. R.; Fetterman, M. R.; Low, J. J.; You, G.; Jiang, Z.; Xu, J., Monte Carlo Study of PbSe Quantum Dots as the Fluorescent Material in Luminescent Solar Concentrators. *Opt. Express, OE* **2014,** *22*, A35-A43.
21. Zhou, Y.; Benetti, D.; Fan, Z.; Zhao, H.; Ma, D.; Govorov, A. O.; Vomiero, A.; Rosei, F., Near Infrared, Highly Efficient Luminescent Solar Concentrators. *Adv. Energy Mater.* **2016,** *6*, 1501913.
22. Waldron, D. L.; Preske, A.; Zawodny, J. M.; Krauss, T. D.; Gupta, M. C., Pbse Quantum Dot Based Luminescent Solar Concentrators. *Nanotechnology* **2017,** *28*, 095205.
23. Meinardi, F.; Ehrenberg, S.; Dhamo, L.; Carulli, F.; Mauri, M.; Bruni, F.; Simonutti, R.; Kortshagen, U.; Brovelli, S., Highly Efficient Luminescent Solar Concentrators Based on Earth-Abundant Indirect-Bandgap Silicon Quantum Dots. *Nat. Photonics* **2017,** *11*, 177-185.
24. Krumer, Z.; Pera, S. J.; R. J.A. Dijk-Moes, V.; Zhao, Y.; A. F.P. Brouwer, D.; Groeneveld, E.; W. G.J.H.M. Sark, V.; Schropp, R. E. I.; C. Mello Donegá, D., Tackling Self-Absorption in Luminescent Solar Concentrators with Type-Ii Colloidal Quantum Dots. *Sol. Energy Mater. Sol. Cells* **2014,** *111*, 57-65.
25. Coropceanu, I.; Bawendi, M. G., Core/Shell Quantum Dot Based Luminescent Solar Concentrators with Reduced Reabsorption and Enhanced Efficiency. *Nano Lett.* **2014,** *14*, 4097-4101.
26. Meinardi, F.; Colombo, A.; Velizhanin, K. A.; Simonutti, R.; Lorenzon, M.; Beverina, L.; Viswanatha, R.; Klimov, V. I.; Brovelli, S., Large-Area Luminescent Solar Concentrators Based on 'Stokes-Shift-Engineered' Nanocrystals in a Mass-Polymerized Pmma Matrix. *Nat. Photonics* **2014,** *8*, 392-399.
27. Needell, D. R.; Ilic, O.; Bukowsky, C. R.; Nett, Z.; Xu, L.; He, J.; Bauser, H.; Lee, B. G.; Geisz, J. F.; Nuzzo, R. G.; Alivisatos, A. P.; Atwater, H. A., Design Criteria for Micro-Optical Tandem Luminescent Solar Concentrators. *IEEE J. Photovolt.* **2018,** *8*, 1-8.
28. Sadeghi, S.; Bahmani Jalali, H.; Melikov, R.; Ganesh Kumar, B.; Mohammadi Aria, M.; Ow-Yang, C. W.; Nizamoglu, S., Stokes-Shift-Engineered Indium Phosphide Quantum Dots for Efficient Luminescent Solar Concentrators. *ACS Appl. Mater. Interfaces* **2018,** *10*, 12975-12982.
29. Bronstein, N. D.; Li, L.; Xu, L.; Yao, Y.; Ferry, V. E.; Alivisatos, A. P.; Nuzzo, R. G., Luminescent Solar Concentration with Semiconductor Nanorods and Transfer-Printed Micro-Silicon Solar Cells. *ACS Nano* **2014,** *8*, 44-53.
30. Erickson, C. S.; Bradshaw, L. R.; McDowall, S.; Gilbertson, J. D.; Gamelin, D. R.; Patrick, D. L., Zero-Reabsorption Doped-Nanocrystal Luminescent Solar Concentrators. *ACS Nano* **2014,** *8*, 3461-3467.
31. Bradshaw, L. R.; Knowles, K. E.; McDowall, S.; Gamelin, D. R., Nanocrystals for Luminescent Solar Concentrators. *Nano Lett.* **2015,** *15*, 1315-1323.
32. Knowles, K. E.; Kilburn, T. B.; Alzate, D. G.; McDowall, S.; Gamelin, D. R., Bright $CuInS_2$/CdS Nanocrystal Phosphors for High-Gain Full-Spectrum Luminescent Solar Concentrators. *Chem. Commun.* **2015,** *51*, 9129-9132.
33. Hu, X.; Kang, R.; Zhang, Y.; Deng, L.; Zhong, H.; Zou, B.; Shi, L.-J., Ray-Trace Simulation of $CuInS(Se)_2$ Quantum Dot Based Luminescent Solar Concentrators. *Opt. Express* **2015,** *23*, A858-A867.
34. Meinardi, F.; McDaniel, H.; Carulli, F.; Colombo, A.; Velizhanin, K. A.; Makarov, N. S.; Simonutti, R.; Klimov, V. I.; Brovelli, S., Highly Efficient Large-Area Colourless

Luminescent Solar Concentrators Using Heavy-Metal-Free Colloidal Quantum Dots. *Nat. Nanotechnol.* **2015,** *10*, 878-885.

35. Li, C.; Chen, W.; Wu, D.; Quan, D.; Zhou, Z.; Hao, J.; Qin, J.; Li, Y.; He, Z.; Wang, K., Large Stokes Shift and High Efficiency Luminescent Solar Concentrator Incorporated with $CuInS_2$/ZnS Quantum Dots. *Sci. Rep.* **2015,** *5*, 17777.
36. Meinardi, F.; Akkerman, Q. A.; Bruni, F.; Park, S.; Mauri, M.; Dang, Z.; Manna, L.; Brovelli, S., Doped Halide Perovskite Nanocrystals for Reabsorption-Free Luminescent Solar Concentrators. *ACS Energy Lett.* **2017,** *2*, 2368-2377.
37. Sharma, M.; Gungor, K.; Yeltik, A.; Olutas, M.; Guzelturk, B.; Kelestemur, Y.; Erdem, T.; Delikanli, S.; McBride, J. R.; Demir, H. V., Near-Unity Emitting Copper-Doped Colloidal Semiconductor Quantum Wells for Luminescent Solar Concentrators. *Adv. Mater.* **2017,** *29*, 1700821.
38. Sumner, R.; Eiselt, S.; Kilburn, T. B.; Erickson, C.; Carlson, B.; Gamelin, D. R.; McDowall, S.; Patrick, D. L., Analysis of Optical Losses in High-Efficiency $CuInS_2$-Based Nanocrystal Luminescent Solar Concentrators: Balancing Absorption Versus Scattering. *J. Phys. Chem. C* **2017,** *121*, 3252-3260.
39. Bergren, M. R.; Makarov, N. S.; Ramasamy, K.; Jackson, A.; Guglielmetti, R.; McDaniel, H., High-Performance $CuInS_2$ Quantum Dot Laminated Glass Luminescent Solar Concentrators for Windows. *ACS Energy Lett.* **2018,** *3*, 520-525.
40. Wu, K.; Li, H.; Klimov, V. I., Tandem Luminescent Solar Concentrators Based on Engineered Quantum Dots. *Nat. Photonics* **2018,** *12*, 105-110.
41. Knowles, K. E.; Hartstein, K. H.; Kilburn, T. B.; Marchioro, A.; Nelson, H. D.; Whitham, P. J.; Gamelin, D. R., Luminescent Colloidal Semiconductor Nanocrystals Containing Copper: Synthesis, Photophysics, and Applications. *Chem. Rev.* **2016,** *116*, 10820-10851.
42. Marchioro, A.; Whitham, P. J.; Knowles, K. E.; Kilburn, T. B.; Reid, P. J.; Gamelin, D. R., Tunneling in the Delayed Luminescence of Colloidal CdSe, Cu^+-Doped CdSe, and $CuInS_2$ Semiconductor Nanocrystals and Relationship to Blinking. *J. Phys. Chem. C* **2016,** *120*, 27040-27049.
43. Nelson, H. D.; Li, X.; Gamelin, D. R., Computational Studies of the Electronic Structures of Copper-Doped CdSe Nanocrystals: Oxidation States, Jahn–Teller Distortions, Vibronic Bandshapes, and Singlet–Triplet Splittings. *J. Phys. Chem. C* **2016,** *120*, 5714-5723.
44. Hughes, K. E.; Hartstein, K. H.; Gamelin, D. R., Photodoping and Transient Spectroscopies of Copper-Doped CdSe/CdS Nanocrystals. *ACS Nano* **2018,** *12*, 718-728.
45. Nelson, H. D.; Gamelin, D. R., Valence-Band Electronic Structures of Cu^+-Doped ZnS, Alloyed Cu–In–Zn–S, and Ternary $CuInS_2$ Nanocrystals: A Unified Description of Photoluminescence across Compositions. *J. Phys. Chem. C* **2018,** *122*, 18124-18133.
46. Parent, C.; Lurin, C.; Le Flem, G.; Hagenmuller, P., $Nd^{3+} \rightarrow Yb^{3+}$ Energy Transfer in Glasses with Composition Close to $LiLnP_4O_{12}$ Metaphosphate (Ln = La, Nd, Yb). *J. Lumin.* **1986,** *36*, 49-55.
47. Sanguineti, A.; Monguzzi, A.; Vaccaro, G.; Meinardi, F.; Ronchi, E.; Moret, M.; Cosentino, U.; Moro, G.; Simonutti, R.; Mauri, M.; Tubino, R.; Beverina, L., Nir Emitting Ytterbium Chelates for Colourless Luminescent Solar Concentrators. *Phys. Chem. Chem. Phys.* **2012,** *14*, 6452-6455.

48. Liu, T.-C.; Zhang, G.; Qiao, X.; Wang, J.; Seo, H. J.; Tsai, D.-P.; Liu, R.-S., Near-Infrared Quantum Cutting Platform in Thermally Stable Phosphate Phosphors for Solar Cells. *Inorg. Chem.* **2013,** *52*, 7352-7357.
49. Liu, P.; Liu, J.; Zheng, X.; Luo, H.; Li, X.; Yao, Z.; Yu, X.; Shi, X.; Hou, B.; Xia, Y., An Efficient Light Converter YAB:Cr^{3+},Yb^{3+}/Nd^{3+} with Broadband Excitation and Strong Nir Emission for Harvesting C-Si-Based Solar Cells. *J. Mater. Chem. C* **2014,** *2*, 5769-5777.
50. Rufino Souza, A. K.; Langaro, A. P.; Silva, J. R.; Costa, F. B.; Yukimitu, K.; Silos Moraes, J. C.; Antonio de Oliveira Nunes, L.; Humberto da Cunha Andrade, L.; Lima, S. M., On the Efficient $Te^{4+}\rightarrow Yb^{3+}$ Cooperative Energy Transfer Mechanism in Tellurite Glasses: A Potential Material for Luminescent Solar Concentrators. *J. Alloys Compd.* **2019,** *781*, 1119-1126.
51. Martín-Rodríguez, R.; Geitenbeek, R.; Meijerink, A., Incorporation and Luminescence of Yb^{3+} in CdSe Nanocrystals. *J. Am. Chem. Soc.* **2013,** *135*, 13668-13671.
52. Creutz, S. E.; Fainblat, R.; Kim, Y.; De Siena, M. C.; Gamelin, D. R., A Selective Cation Exchange Strategy for the Synthesis of Colloidal Yb^{3+}-Doped Chalcogenide Nanocrystals with Strong Broadband Visible Absorption and Long-Lived near-Infrared Emission. *J. Am. Chem. Soc.* **2017,** *139*, 11814-11824.
53. Swabeck, J. K.; Fischer, S.; Bronstein, N. D.; Alivisatos, A. P., Broadband Sensitization of Lanthanide Emission with Indium Phosphide Quantum Dots for Visible to near-Infrared Downshifting. *J. Am. Chem. Soc.* **2018,** *140*, 9120-9126.
54. Zhou, D.; Liu, D.; Pan, G.; Chen, X.; Li, D.; Xu, W.; Bai, X.; Song, H., Cerium and Ytterbium Codoped Halide Perovskite Quantum Dots: A Novel and Efficient Downconverter for Improving the Performance of Silicon Solar Cells. *Adv. Mater.* **2017,** *29*, 1704149.
55. Milstein, T. J.; Kroupa, D. M.; Gamelin, D. R., Picosecond Quantum Cutting Generates Photoluminescence Quantum Yields over 100% in Ytterbium-Doped $Cspbcl_3$ Nanocrystals. *Nano Lett.* **2018,** *18*, 3792–3799.
56. Kroupa, D. M.; Roh, J. Y. D.; Milstein, T. J.; Creutz, S. E.; Gamelin, D. R., Quantum-Cutting Ytterbium-Doped $CsPb(Cl_{1-x}Br_x)_3$ Perovskite Thin Films with Photoluminescence Quantum Yields over 190%. *ACS Energy Lett.* **2018,** *3*, 2390-2395.
57. Vos, A. D., Detailed Balance Limit of the Efficiency of Tandem Solar Cells. *J. Phys. D: Appl. Phys.* **1980,** *13*, 839.
58. Bertness, K. A.; Kurtz, S. R.; Friedman, D. J.; Kibbler, A. E.; Kramer, C.; Olson, J. M., 29.5%-Efficient GaInP/GaAs Tandem Solar Cells. *Appl. Phys. Lett.* **1994,** *65*, 989-991.
59. Eperon, G. E.; Leijtens, T.; Bush, K. A.; Prasanna, R.; Green, T.; Wang, J. T.-W.; McMeekin, D. P.; Volonakis, G.; Milot, R. L.; May, R.; Palmstrom, A.; Slotcavage, D. J.; Belisle, R. A.; Patel, J. B.; Parrott, E. S.; Sutton, R. J.; Ma, W.; Moghadam, F.; Conings, B.; Babayigit, A.; Boyen, H.-G.; Bent, S.; Giustino, F.; Herz, L. M.; Johnston, M. B.; McGehee, M. D.; Snaith, H. J., Perovskite-Perovskite Tandem Photovoltaics with Optimized Band Gaps. *Science* **2016,** *354*, 861-865.
60. Bush, K. A.; Palmstrom, A. F.; Yu, Z. J.; Boccard, M.; Cheacharoen, R.; Mailoa, J. P.; McMeekin, D. P.; Hoye, R. L. Z.; Bailie, C. D.; Leijtens, T.; Peters, I. M.; Minichetti, M. C.; Rolston, N.; Prasanna, R.; Sofia, S.; Harwood, D.; Ma, W.; Moghadam, F.; Snaith, H. J.; Buonassisi, T.; Holman, Z. C.; Bent, S. F.; McGehee, M. D., 23.6%-Efficient

Monolithic Perovskite/Silicon Tandem Solar Cells with Improved Stability. *Nat. Energy* **2017,** *2*, 17009.

61. Essig, S.; Allebé, C.; Remo, T.; Geisz, J. F.; Steiner, M. A.; Horowitz, K.; Barraud, L.; Ward, J. S.; Schnabel, M.; Descoeudres, A.; Young, D. L.; Woodhouse, M.; Despeisse, M.; Ballif, C.; Tamboli, A., Raising the One-Sun Conversion Efficiency of III–V/Si Solar Cells to 32.8% for Two Junctions and 35.9% for Three Junctions. *Nat. Energy* **2017,** *2*, 17144.
62. Earp, A. A.; Smith, G. B.; Franklin, J.; Swift, P., Optimisation of a Three-Colour Luminescent Solar Concentrator Daylighting System. *Sol. Energy Mater. Sol. Cells* **2004,** *84*, 411-426.
63. Currie, M. J.; Mapel, J. K.; Heidel, T. D.; Goffri, S.; Baldo, M. A., High-Efficiency Organic Solar Concentrators for Photovoltaics. *Science* **2008,** *321*, 226-228.
64. Goldschmidt, J. C.; Peters, M.; Bösch, A.; Helmers, H.; Dimroth, F.; Glunz, S. W.; Willeke, G., Increasing the Efficiency of Fluorescent Concentrator Systems. *Sol. Energy Mater. Sol. Cells* **2009,** *93*, 176-182.
65. Ziegler, J. P.; Walker, H. W.; Griffey, R. H.; Wyeth, N. C. Luminescent Solar Concentrator. US8866001 B1, October 21, 2014, **2014**.
66. Zhao, H.; Benetti, D.; Tong, X.; Zhang, H.; Zhou, Y.; Liu, G.; Ma, D.; Sun, S.; Wang, Z. M.; Wang, Y.; Rosei, F., Efficient and Stable Tandem Luminescent Solar Concentrators Based on Carbon Dots and Perovskite Quantum Dots. *Nano Energy* **2018,** *50*, 756-765.
67. Milstein, T. J.; Kluherz, K. T.; Kroupa, D. M.; Erickson, C. S.; De Yoreo, J. J.; Gamelin, D. R., Anion Exchange and the Quantum-Cutting Energy Threshold in Ytterbium-Doped $CsPb(Cl_{1-x}Br_x)_3$ Perovskite Nanocrystals. *Nano Lett.* **2019,** *19*, 1931-1937.
68. Reference Air Mass 1.5 Spectra | Grid Modernization | Nrel. https://www.nrel.gov/grid/solar-resource/spectra-am1.5.html.
69. Zhao, H.; Zhou, Y.; Benetti, D.; Ma, D.; Rosei, F., Perovskite Quantum Dots Integrated in Large-Area Luminescent Solar Concentrators. *Nano Energy* **2017,** *37*, 214-223.
70. Shu, J.; Zhang, X.; Wang, P.; Chen, R.; Zhang, H.; Li, D.; Zhang, P.; Xu, J., Monte-Carlo Simulations of Optical Efficiency in Luminescent Solar Concentrators Based on All-Inorganic Perovskite Quantum Dots. *Physica B* **2018,** *548*, 53-57.
71. Nikolaidou, K.; Sarang, S.; Hoffman, C.; Mendewala, B.; Ishihara, H.; Lu, J. Q.; Ilan, B.; Tung, V.; Ghosh, S., Hybrid Perovskite Thin Films as Highly Efficient Luminescent Solar Concentrators. *Adv. Opt. Mater.* **2016,** *4*, 2126-2132.
72. Luo, X.; Ding, T.; Liu, X.; Liu, Y.; Wu, K., Quantum-Cutting Luminescent Solar Concentrators Using Ytterbium-Doped Perovskite Nanocrystals. *Nano Lett.* **2019,** *19*, 338-341.
73. Groh, W., Overtone Absorption in Macromolecules for Polymer Optical Fibers. *Die Makromol. Chemie* **1988,** *189*, 2861-2874.
74. Lee, S. C. J. Discrete Multitone Modulation for Short-Range Optical Communications. Eindhoven University of Technology, 2009.
75. Schott Optical Glass Collection Datasheet. https://www.us.schott.com/advanced_optics.
76. Creutz, S. E.; Crites, E. N.; De Siena, M. C.; Gamelin, D. R., Anion Exchange in Cesium Lead Halide Perovskite Nanocrystals and Thin Films Using Trimethylsilyl Halide Reagents. *Chem. Mater.* **2018,** *30*, 4887-4891.
77. Copper Indium Disulfide/Zinc Sulfide Quantum Dots. https://www.strem.com/ubiqd.

78. Griffini, G.; Levi, M.; Turri, S., Novel Crosslinked Host Matrices Based on Fluorinated Polymers for Long-Term Durability in Thin-Film Luminescent Solar Concentrators. *Sol. Energy Mater Sol. Cells* **2013,** *118,* 36-42.
79. Pintossi, D.; Turri, S.; Griffini, G.; Colombo, A.; Dragonetti, C. In *Crosslinking Uv-Curable Polymers with Organic Dyes for Highly Stable, Multifunctional, Light-Harvesting Luminescent Solar Concentrators*, 2017 IEEE International Conference on Environment and Electrical Engineering and 2017 IEEE Industrial and Commercial Power Systems Europe, June 2017; 2017; pp 1-5.
80. Olsson, Y. K.; Chen, G.; Rapaport, R.; Fuchs, D. T.; Sundar, V. C.; Steckel, J. S.; Bawendi, M. G.; Aharoni, A.; Banin, U., Fabrication and Optical Properties of Polymeric Waveguides Containing Nanocrystalline Quantum Dots. *Appl. Phys. Lett.* **2004,** *85,* 4469-4471.
81. Jeżowska-Trzebiatowska, B.; Łukowiak, E.; Stręk, W.; Buczkowski, A.; Patela, S.; Radojewski, J.; Sarzyński, J., Neodymium-Chromium Doped Phosphate Glasses as Luminescent Solar Concentrators. *Sol. Energy Mater* **1986,** *13,* 267-277.
82. Goldberg, L.; Koplow, J. P.; Kliner, D. A. V., Highly Efficient 4-W Yb-Doped Fiber Amplifier Pumped by a Broad-Stripe Laser Diode. *Opt. Lett., OL* **1999,** *24,* 673-675.
83. Paschotta, R.; Nilsson, J.; Tropper, A. C.; Hanna, D. C., Ytterbium-Doped Fiber Amplifiers. *IEEE Journal of Quantum Electronics* **1997,** *33,* 1049-1056.

CHAPTER 3. MODULAR ZWITTERION-FUNCTIONALIZED POLY(ISOPROPYL METHACRYLATE) POLYMERS FOR HOSTING LUMINESCENT LEAD-HALIDE PEROVSKITE NANOCRYSTALS

Reproduced with permission from Cohen, T. A.; Huang, Y.; Bricker, N. A.; Juhl, C. S.; Milstein, T. J.; MacKenzie, J. D.; Luscombe, C. K.; Gamelin, D. R. *Chem. Mater*. **2021**, *33*, 3779.

3.1 OVERVIEW

Inorganic lead-halide perovskite nanocrystals (NCs) are an exciting class of luminescent materials with high defect tolerance and broad spectral tunability, but such NCs are vulnerable to degradation under ambient conditions. Here, we report a class of modular zwitterion-functionalized isopropyl methacrylate polymers designed to stabilize a wide variety of perovskite NCs of different compositions, while also enabling processing in green solvents. Specifically, we report polymers in which the zwitterion spacing is tuned to accommodate the different lattice parameters of $CsPb(Cl_{1-x}Br_x)_3$ and $CsPbI_3$ NCs, and we report partially fluorinated polymers prepared to accommodate the needs of infrared-emitting NCs. We show that as-synthesized $CsPbBr_3$, $CsPbI_3$, and Yb^{3+}:$CsPbCl_3$ NCs are easily transferred into these zwitterionic polymers *via* a simple ligand-exchange procedure. These NC/polymer composites were then cast into thin films that showed substantially improved photoluminescence (PL) and stability compared with more conventional NC/polymer films. Specifically, $CsPbBr_3$ and $CsPbI_3$ NCs in films of their appropriately designed polymers had PL quantum yields of ~90% and ~80%, respectively. PL

quantum yields decreased under continuous illumination, but self-healed completely after dark storage. We also found that all the NC compositions studied here maintain their PL quantum yields in NC/polymer composite films even after 1 year of ambient storage. These encouraging results demonstrate the utility of such modular zwitterion-functionalized polymers for hosting specific perovskite NCs, potentially opening avenues for robust new photonic applications of this important class of NCs.

3.2 INTRODUCTION

Lead-halide perovskite nanocrystals (NCs) have been heavily investigated for their intriguing properties,[1-5] including broad spectral tunability with anion[6-8] and cation[9-13] replacement, unique electronic structure,[14-16] and high defect tolerance.[17-20] These properties have made such NCs a popular emitter for application in light-emitting diodes (LEDs),[21-22] lasers,[23-26] single-photon sources,[27-29] and luminescent solar concentrators.[30-33] Unfortunately, these NCs are sensitive to degradation in the presence of oxygen and water.[34-35] To bridge the gap between laboratory research and commercial application, NC stability needs to be improved without sacrificing optoelectronic properties or processability. Furthermore, the broad range of potential applications means that different functional polymer matrices may be required for different uses. For instance, whereas as-synthesized NCs can be supported in various apolar polymers,[30, 36-40] some applications require that NCs are suspended in silicone,[21, 41-43] aqueous,[44] fluorinated,[32, 45-47] or semiconducting[48-50] matrices to enable the desired functionalities. Because these host matrices have limited chemical compatibility with the aliphatic ligands often used to stabilize perovskite NCs, additional interface modifiers must be introduced to improve compatibility between the native NC surface ligands and the polymer. Alternatively, these

ligands must be replaced with novel ligands tailored to be compatible with the host polymer of interest.

The interface modifier approach has been demonstrated by direct synthesis of perovskite NCs in a hydrophobically stabilized micelle of lauryl methacrylate[40] and by using custom polymers that form micelles to stabilize the NCs in different hosts,[44, 51-54] with varying levels of success. Novel-ligand approaches have mostly focused on ammonium,[21, 48-49, 55-57] carboxylate,[58] and poly(vinylidene difluoride)[22, 59] NC coordination. These binding groups have limited affinity for perovskite NC surfaces,[60] however, and some are consumed during subsequent polymerization reactions in making the NC/polymer composites.[61] Consequently, most of these polymer-suspension protocols yield samples with poor dispersion and reduced NC photoluminescence quantum yields (PLQYs). Alternatively, strongly binding phosphonate,[62-66] sulfonate,[18] and zwitterionic[67-68] ligands have recently been used to synthesize perovskite NCs with improved PLQYs and stability. The covalently tethered positive and negative ions on zwitterionic ligands are well matched to the highly ionic surface of the NCs. These ligands are mostly aliphatic, however, which limits their ability to solvate NCs in many non-aliphatic functional polymers, complicating device fabrication and ultimately limiting the application range of perovskite NCs. Zwitterionic polymers have been used to passivate perovskite thin films,[69-70] and while this manuscript was in preparation, zwitterionic polymers were reported to stabilize $CsPbBr_3$ NCs in solution and in the solid state.[71-72] Ref. 71 reported random copolymers of *n*-butyl methacrylate and phosphorylcholine or sulfobetaine zwitterion groups to yield zwitterion-functionalized polymers that can bind and enhance the stability of $CsPbBr_3$ NCs, focusing primarily on development of solid NC/polymer composites. Ref. 72 reported that incorporation of sulfobetaine zwitterion groups into poly(isobutylene-*alt*-maleic anhydride),

along with solubilizing alkyl chains, yielded high-affinity coatings that stabilize colloidal $CsPbBr_3$ NCs in both non-polar and polar solvents and that allow facile phase transfer between nonpolar and polar media. These works solidify the idea that zwitterionic polymers have high potential as perovskite NC host matrices.

Here, we describe a set of modular zwitterion-functionalized poly(isopropyl methacrylate) polymers developed to match the specific needs of various colloidal lead-halide perovskite NCs. In general, polymers with appended alkyl chains have high solubility in organic solvents,[73-75] but branched alkyl structures can also improve polymer solubility in green solvents that are sufficiently apolar to prevent NC degradation[76] and inhibit the formation of crystalline scattering structures in a solid composite.[77-78] Consequently, isopropyl methacrylate was used instead of commonly used long-chain alkyl acrylates; the increased solubility from the isopropyl side chain facilitates solution processing with green solvents such as butyl acetate that are still sufficiently apolar to prevent NC degradation. Within these polymers, the distances between positive quaternary ammonium moieties and negative sulfonate moieties are tuned using either 3- or 4-methylene spacers. This tunability allows the zwitterion separation to be matched with the relevant NC lattice spacings when the NC anions are changed from Cl^-/Br^- to I^-.[68] We show that the native NC ligands are easily replaced by these zwitterionic polymers, and the resulting polymers are shown to stabilize lead-halide perovskite NCs across the entire composition and luminescence-color range. For Yb^{3+}-doped NCs with near-infrared emission, we further utilize a fluorinated version of poly(isopropyl methacrylate) that reduces absorption from C–H vibrational overtones at Yb^{3+} emission at infrared wavelengths.[32, 79] The modularity of these polymers provides access to a variety of perovskite NC/polymer composites with attractive solution

processability, optical properties, and long-term stability, making these polymers appealing hosts for use of colloidal lead-halide perovskite NCs in various photonic applications.

3.3 METHODS

3.3.1 *Materials*

Lead acetate trihydrate [$Pb(OAc)_2 \cdot 3H_2O$] (99.9%, Baker Chemical), cesium carbonate [Cs_2CO_3] (99.9%, Sigma Aldrich), cesium acetate [CsOAc] (99.9%, Alfa Aesar), ytterbium acetate hydrate [$Yb(OAc)_3 \cdot xH_2O$] (99.9% Strem Chemical), anhydrous ethanol (200 proof, Decon Laboratories), chlorotrimethylsilane [TMS-Cl] (98%, Acros Organic), bromotrimethylsilane [TMS-Br] (97%, Sigma Aldirch), iodotrimethylsilane [TMS-I] (97%, Sigma Aldirch), 1-octadecene [ODE] (90%, Sigma Aldrich), oleylamine [OAm] (70%, Sigma Aldrich), oleic acid [OA] (90%, Sigma Aldrich), 3-(N,N-Dimethyloctadecylammonio)-propanesulfonate [ZW-lig] (≥99.0% TLC, Sigma Aldrich), hexanes (99%, mixture of isomers, Sigma Aldrich), toluene (HPLC, Fischer Chemical), anhydrous ethyl acetate (99%, Sigma Aldrich), anhydrous butyl acetate (99%, Sigma Aldrich), anhydrous tetrahydrofuran [THF] (Optima®, Fischer Chemical), methanol (ACS, EMD Millipore), acetone (ACS, Fischer Chemical), 2-propanol (ACS, Fischer Chemical), methanol-d_4 (>99.8 atom % D, Sigma Aldrich), acetone-d_6 (99.9 atom % D, Sigma Aldrich), poly(methyl methacrylate) [PMMA] (~120,000 MW Sigma Aldrich), *tert*-Nonyl mercaptan (>97.0%, mixture of isomers, TCI), 2,2'-azobis(2-methylpropionitrile) (98%, Sigma Aldrich) 2-(dimethylamino)ethyl acrylate (>98.0%, stabilized with MEHQ, TCI), isopropyl methacrylate (>98.0%, stabilized with MEHQ, TCI), 1,1,1,3,3,3-hexafluoroisopropyl methacrylate (99%, stab., Alfa Aesar), 1,4-butanesultone (99%, TCI), 1,3-propanesultone (99%, TCI), Poly(ethylene-*co*-vinyl acetate) [EVA] (MSL Solar Company), and Spectra/Por® 6 dialysis tubing (MWCO 1000) were used as received unless otherwise noted.

3.3.2 *Polymer Syntheses and Purification*

Amine precursor polymer syntheses. The polymer synthesis process is outlined in Scheme 1. 2-(Dimethylamino)ethyl acrylate (143 mg, 1 mmol) and either isopropyl methacrylate (1152 mg, 9 mmol) or 1,1,1,3,3,3-hexafluoroisopropyl methacrylate (2124 mg, 9 mmol) was added to a vial that was pre-dried overnight in a 120 °C oven. 2,2'-azobis(2-methylpropionitrile) (8 mg, 0.5 mmol) and *tert*-nonyl mercaptan (8 μL, 0.5 mmol) – a chain transfer agent to reduce molecular weight[61] – were added subsequently. The vial was then degassed and sealed. The reaction was heated at 60 °C for one day, and at 80 °C for another two days. After cooling down to room temperature, 2 mL of THF was added to dissolve the polymer, followed by precipitation with 50 mL of deionized water. The precipitate was later washed with methanol and dried under vacuum overnight.

Zwitterion-functionalized polymer syntheses. Amine precursor polymer (400 mg, 0.18-0.30 mmol of amine group depending on the polymer) was dissolved in 8 mL THF and heated to 60 °C. After 30 min, an excess of sultone (1,4-butanesultone (400 mg, 2.94 mmol) or 1,3-propanesultone (400 mg, 3.28 mmol)) was added dropwise. 3 mL of methanol was added after 1 hour and another 3 mL of methanol was added after 24 hrs. The reaction was further heated at 60 °C for another day before cooling down to room temperature. The solution was transferred into a dialysis tube (molecular weight cut-off = 1000) and stirred in 1000 mL of methanol for 2 hrs and 1000 mL ethyl acetate for an additional 2 hrs. After dialysis, the solution inside the dialysis tube was transferred to a round-bottom flask and concentrated under vacuum. Clear transparent solids were obtained and dried under vacuum to remove residual solvents. The zwitterionic polymers are soluble in most common organic solvents, including green organic

solvents such as ethyl and butyl acetate[80] that are common antisolvents for perovskite NC purification.[1, 3, 68] ^{1}H-NMR spectra of the polymers synthesized here are provided in Appendix B.

3.3.3 *Nanocrystal Synthesis and Purification*

Preparation of Pb^{2+}-oleate solution. $Pb(OAc)_2 \cdot 3H_2O$ (1152 mg, 3 mmol), OA (1720 mg, ~6 mmol), and ODE (3280 mg, 4.15 mL) were combined in a 100 mL three neck flask. The temperature of the flask was slowly elevated and was held at 120 ^oC for 1 hr on a Schlenk line under vacuum. The solution was then heated under N_2 at 150 ^oC for 1 hr to ensure that all reactants were well dissolved. The resulting ~0.5 M Pb^{2+} oleate solution ($Pb(OA)_2$) was transferred into a N_2-filled glovebox and became a waxy solid when cooled to room temperature.

Preparation of Cs^+-oleate solution. Cs_2CO_3 (1628 mg, 10 mmol of Cs^+ ions), OA (4500 mg, ~15 mmol), and ODE (15 g, 20 mL) were combined in a 100 mL three neck flask. The solution was initially degassed on a Schlenk line at room temperature to remove highly volatile compounds. The temperature was then slowly elevated and held at 120 ^oC for 1 hr under vacuum. The solution was then heated under N_2 to 150 ^oC for 1 hr to ensure that all reactants were well dissolved. The resulting ~0.5 M Cs^+ oleate solution (CsOA) was transferred into a N_2-filled glovebox and became a highly viscous, turbid liquid when cooled to room temperature.

$CsPb(Br_{1-x}I_x)_3$ NC synthesis. Perovskite NCs were prepared using a procedure adapted from the literature.[68, 81] CsOA and $Pb(OA)_2$ precursor solutions were heated to 130 ^oC in a N_2 filled glovebox to fully dissolve all of their components. Once dissolved, CsOA (0.8 mL, ~0.4 mmol Cs^+) and $Pb(OA)_2$ (1 mL, ~0.5 mmol Pb^{2+}) were loaded into a 100 mL three neck flask. The flask was removed from the glovebox and ODE (6650 mg, 8.5 mL) and OAm (420 mg, ~1.5 mmol) were loaded into the flask. The resulting metal oleate solution was degassed on a Schlenk line at 120 ^oC until the base pressure of the line was reached (typically 1-2 hrs). A solution

containing TMS-Br (180 µL, 1.4 mmol) (or TMS-I (200 µL, 1.4 mmol)) and 400 µL of ODE was prepared and sealed with a septum in a pear-shaped flask in a N_2-filled glovebox. The metal oleate solution on the Schlenk line was heated under N_2 to 180 °C. Once the injection temperature was reached, the TMS-Br (or TMS-I) solution was swiftly injected into the flask. The reaction was quenched after ~5 s with an ice bath and the resulting $CsPb(Br_{1-x}I_x)_3$ NCs were centrifuged from the crude reaction solution at 1318 gx for 10 min. The precipitate was resuspended in hexanes and the resulting solution was precipitated with an excess of anhydrous ethyl acetate. This turbid solution was centrifuged at 1318 gx for 15 min and the precipitate was resuspended in hexanes. The hexanes solution was again centrifuged at 1318 gx for 5 min and the supernatant was dried under N_2 gas flow and transferred into a N_2-filled glovebox. Once in the glovebox, the $CsPb(Br_{1-x}I_x)_3$ NC pellet was resuspended in hexanes and the solution was filtered through a 0.22 µm polytetrafluoroethylene (PTFE) syringe filter. Anion-alloyed $CsPb(Br_{1-x}I_x)_3$ NCs were synthesized by mixing solutions of $CsPbBr_3$ NCs and $CsPbI_3$ NCs in appropriate amounts to obtain a solution with a PL max of ~660 nm. Solution-state absorption spectra of the undoped NCs synthesized here are provided in Appendix B.

Yb^{3+}:$CsPbCl_3$ NC synthesis. NCs exchanged into ZFP3 were prepared using methods reported previously.[9] Zwitterion-capped Yb^{3+}:$CsPbCl_3$ NCs were synthesized according to the same procedure, but OAm was replaced with 100 mg ZW-lig and the washed NCs were suspended in toluene rather than hexanes.

3.3.4 *General Aspects of NC/Polymer Composite Film Preparation*

Glass substrates were cut and sonicated for 15 min sequentially in deionized water with 2% detergent, deionized water, acetone, and 2-propanol; after which each substrate was dried with compressed air. To transfer perovskite NCs into a zwitterionic polymer matrix, the desired

quantities of polymer were added to 0.75 mL of ethyl acetate in a N_2-filled glovebox and stirred overnight. Then, a small volume of NC solution in hexanes was added to the solution of zwitterionic polymer in ethyl acetate. NC concentrations were determined using literature perovskite NC extinction coefficients,[60] and the volume of NC solution added was determined such that the equivalents (Eq) of zwitterionic groups per NC was kept between 10 and 300 kEq. This solution was then removed from the glovebox and sonicated for 5 min. The resulting NC/zwitterionic polymer composites were precipitated out of solution by adding an excess of hexanes and centrifuging the resulting turbid solution at 1318 gx for 10 min. Very few NCs remained in the resulting supernatant (see Figure B.7), indicating that the native aliphatic ligands were successfully exchanged for the zwitterionic polymer ligands. This final pellet was then dispersed in 0.5 mL of butyl acetate. To investigate the effect of aggregates on the observed PL red shifts, we diluted a representative solution of $CsPbBr_3$ NC/ZP3 composite by a factor of 50 with butyl acetate and drop cast an aliquot of this solution and all subsequent solutions onto clean glass substrates. After casting the first film, the remaining dilute NC/ZP3 solution was centrifuged at 16,060 gx for 10 minutes and the precipitate was discarded. Finally, the remaining centrifuged solution was filtered through a 0.22 μm PTFE syringe filter. This process yielded a total of three solid samples for future characterization.

PMMA films were fabricated from dispersions prepared in the following manner: 120 mg of PMMA was capped and stirred in 0.45 mL of toluene overnight in an N_2-filled glovebox. NCs were then added to the 25 wt% PMMA solution and stirred into the solution for several hours until a uniform dispersion was obtained. This solution was then drop cast onto a glass substrate in the N_2-filled glovebox and allowed to dry for several hours before the resulting solid sample was exposed to ambient conditions. EVA lamination was performed with a Bent River

SPL2828PIN laminator as follows: After a zwitterionic polymer or PMMA sample was drop cast and dried, a piece of EVA was placed between the dried sample and second clean glass substrate. This stack was placed on the laminator bed and was vacuum laminated at 80 °C for 10 min using a time-varying pressure profile with 10.4 psi of maximum applied pressure. The edges of the final samples were trimmed with a razor blade.

3.4 Results and Analysis

3.4.1 *Preparation of Zwitterion-Functionalized Polymers*

Figure 3.1 summarizes the approach used to synthesize modular zwitterion-functionalized polymers. We used 2,2'-azobis(2-methylpropionitrile) (AIBN) to initiate the radical copolymerization of two commercial acrylate monomers, 2-(dimethylamino)ethyl acrylate and isopropyl methacrylate (or fluorinated isopropyl methacrylate) in a 1:9 ratio, to obtain amine-precursor polymers. This approach allows adaptation for many other functional groups simply by replacing isopropyl methacrylate with other acrylate or methacrylate monomers. Thiol, a chain transfer agent, was added to the polymerization reaction to prevent formation of high-molecular-weight polymers with reduced solubility. These amine-precursor polymers were then reacted with the corresponding sultones to yield the desired zwitterion-functionalized polymers. This flexible chemistry allows integration of zwitterions with different anion-cation separations (3 or 4 methylene spacers). For this work, we successfully synthesized 3-carbon-separated zwitterion-functionalized polymers (ZP3) and their fluorinated analogs (ZFP3), as well as 4-carbon-separated zwitterion-functionalized polymers (ZP4) and their fluorinated analogs (ZFP4). ^{1}H-nuclear magnetic resonance (NMR) spectra of all four polymers are provided in Appendix B. These data show that the four polymers all have degrees of polymerization around 10 and molecular weights (MW) around 2 kDa, which are anticipated values considering that 0.05

equivalents of radical initiator and 0.05 equivalents of chain transfer agent were added to the polymerization reaction to limit the formation of high-MW polymers. We observe that the chemical structures of the polymers impact their solubility; the non-fluorinated polymers are soluble in most organic solvents except hexane, whereas the fluorinated polymers are less soluble in aprotic solvents.

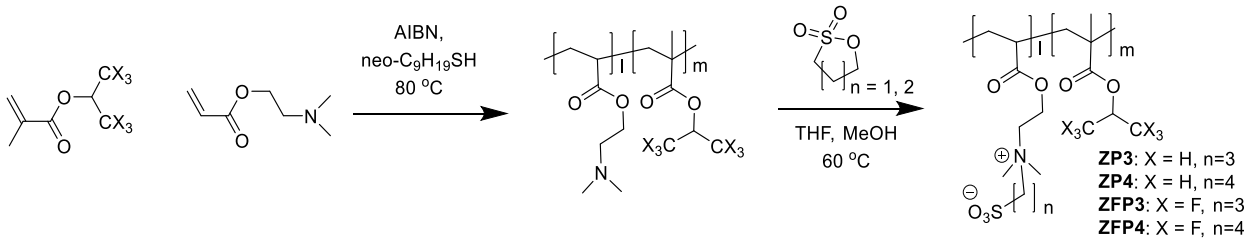

Figure 3.1. Summary of the synthesis of a series of zwitterion-functionalized polymers. The ratio l:m is 1:9 for all polymers reported here.

Three of these polymers were then used for hosting three different categories of perovskite NCs, as summarized in Table 3.1: undoped NCs with small lattice parameters (*e.g.*, $CsPbBr_3$ NCs), large lattice parameters (*e.g.*, $CsPbI_3$ NCs), and doped NCs showing NIR emission (*e.g.*, Yb^{3+}:$CsPbCl_3$ NCs).

Table 3.1. Summary of the zwitterionic polymers developed in this work and the perovskite NC/polymer composites prepared from each. The fluorinated polymer with 4-carbon zwitterion spacing was successfully synthesized but was not soluble in ethyl acetate.

Abbreviation	Zwitterion separation	Fluorinated	NCs used	Amt. ZP used per 3 pico-mol NC
ZP3	3 carbons	No	$CsPbBr_3$	77 mg
ZP4	4 carbons	No	$CsPbI_3$, $CsPb(Br_{1-x}I_x)_3$	7 mg
ZFP3	3 carbons	Yes	$CsPbBr_3$, Yb^{3+}:$CsPbCl_3$	120 mg

3.4.2 *$CsPbBr_3$ NC/Polymer Composites*

Figure 3.2a shows ^{1}H-NMR spectra of ZP3 before and after the $CsPbBr_3$ NC ligand exchange from native ligands to zwitterionic polymers. There is no signal at 5.5-6.0 ppm attributing to the C=C bond of OA or OAm in the pre-ligand-exchanged sample.[6] This result

indicates that the original NC ligands are fully removed in the ligand exchange. In the ligand-exchanged sample, we do notice a singlet centered at 0.12 ppm, which is assigned to TMS-acetate,[82] indicating incomplete removal of acetate groups during NC preparation. No signals from TMS-Br (0.36 ppm) or TMS-sulfonate (0.40 ppm, the product after TMS-Br reacts with sulfonate groups) were detected. This result indicates that the TMS-halide precursors were all consumed during synthesis and converted to TMS-acetate, a molecule that is likely a spectator in subsequent procedures. NMR signals associated with the polymer backbone appear between 0.7 and 2.5 ppm. The additional peaks between 2.7 and 5.2 ppm are assigned according to the color-coded diagram in the inset of Figure 3.2a. Most NMR peaks remain essentially unchanged upon NC addition, but the reduced electron density of the sulfonate anion upon association with NC surface cations leads to a shift of the adjacent methylene protons from 2.93 to 3.05 ppm (highlighted magenta).[83-87] For the quaternary ammonium ion, the NMR data show that only one methylene group is closely associated with the NC surfaces (highlighted green), while the other methyl/methylenes are not. The NMR signal of the H atoms on this closely interacting methylene group have the highest frequency of all the methyl/methylene groups on the quaternary ammonium ion. This result indicates that those H atoms have the lowest electron density and thus are more likely to interact with halide anions of the NC surfaces. These NC polymer composites were soluble in butyl acetate, a green solvent that is a common antisolvent for perovskite NCs.[80] Furthermore, the solution-state NC PLQY in a given zwitterionic polymer did not increase as the NC concentration was increased (see Figure B.6), indicating that the zwitterionic polymers are strongly bound to the NCs.[18, 65] The NCs in a zwitterionic polymer solution had a maximum PLQY of 84 ± 5% compared with 59 ± 5% for the same as-synthesized

NCs, indicating that surface defects are effectively passivated by the zwitterions on these polymers.

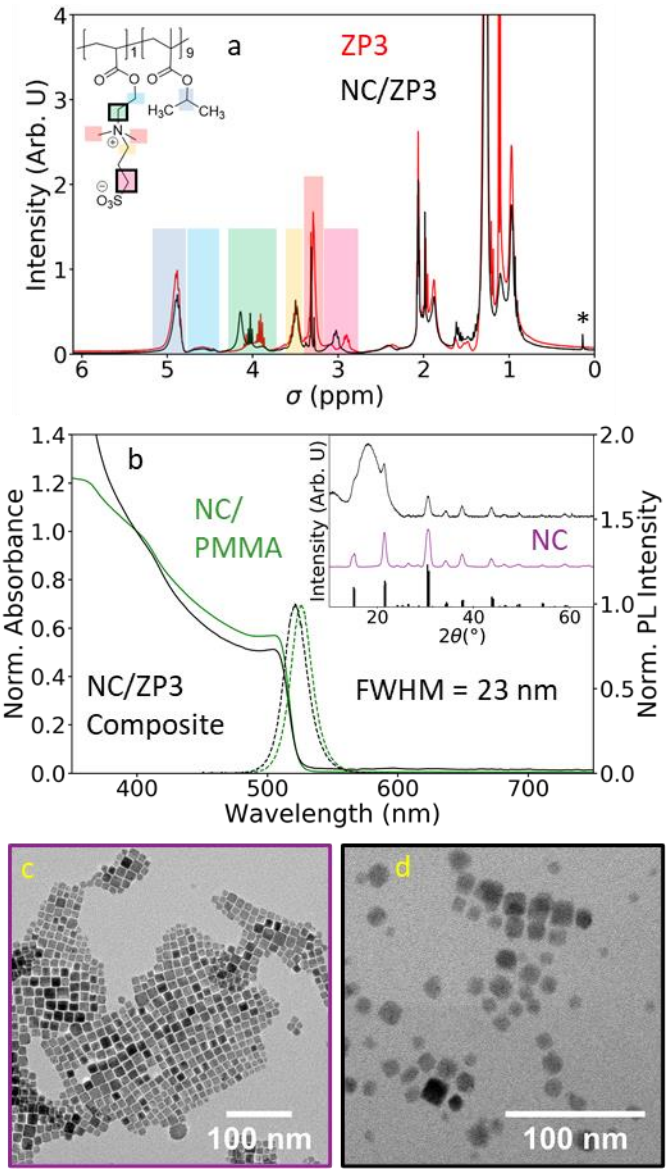

Figure 3.2. Characterization of $CsPbBr_3$ NCs as synthesized and in a ZP3 composite. **(a)** ^{1}H-NMR spectra of ZP3 in acetone-d_6 before and after binding to $CsPbBr_3$ NCs. The peaks around 3 and 4 ppm are substantially shifted after NC binding, indicating that the protons associated with these peaks (bolded boxes) are confined near NC surfaces. * indicates the peak associated with TMS-acetate. **(b)** Absorption and PL spectra of $CsPbBr_3$ NC/polymer composites drop cast from a solution of NCs and ZP3 in butyl acetate and a solution of NCs and PMMA in toluene. *Inset*: XRD data collected before and after transfer of NCs to ZP3. The broad peaks from ~10 to ~17° are attributed to scattering by the amorphous polymer. TEM images of $CsPbBr_3$ NCs **(c)** drop cast from hexanes solution and **(d)** drop cast from a solution of NC/ZP3 composite in butyl acetate.

Once purified, the $CsPbBr_3$ NC/ZP3 solution was drop cast onto clean glass slides to form composite thin films. Figure 3.2b shows absorption and photoluminescence (PL) spectra of $CsPbBr_3$ NCs in a ZP3 film and, for comparison, the same NCs in a high-molecular-weight poly(methyl methacrylate) (PMMA) composite (see Figure B.7). Apart from small reabsorption- and aggregation-induced shifts in the PL (see Figure B.8), the UV/vis and PL spectra are nearly unchanged after the NCs are transferred into a ZP3 composite and the full width at half-maximum (FWHM) of the NC PL is sufficiently small for applications in LEDs with precise green color rendering.[88] The NC/ZP3 composite has no detectable sub-bandgap scattering, indicating that it has few NC aggregates.[89]

The inset of Figure 3.2b shows X-ray diffraction (XRD) data collected from as-synthesized $CsPbBr_3$ NCs and the same NCs in a ZP3 composite. Apart from additional amorphous scattering signals, the diffraction peaks are the same for both samples. Because each peak in the XRD consists of multiple Bragg reflections derived from the orthorhombic $CsPbBr_3$ crystal structure, we could not perform a precise Scherrer analysis. That said, although the XRD FWHM for the NC diffraction peak at 44° increases by ~0.006° (0.7%) in the ZP3 composite, this difference is likely within experimental uncertainty. Furthermore, the transmission electron microscope (TEM) images in Figure 3.2c,d show that the $CsPbBr_3$ NCs maintain their cube-like shapes in a ZP3 composite. The dark spots in both images are attributed to Pb^0 nanoparticles formed during TEM imaging. The average NC edge lengths before and after binding by ZP3 are 10.6 ± 2.1 nm and 10.4 ± 2.4 nm, respectively (see Figure B.9). Importantly, the solid-state PLQYs of the $CsPbBr_3$ NCs in PMMA and ZP3 composites were measured to be 55 ± 5% and 90 ± 5%, respectively. These PLQYs suggest that non-radiative recombination sites are effectively passivated when the NCs are transferred into ZP3.

The stabilities of the NC composites were assessed in ambient atmosphere both in the dark and under illumination (room temperature and relative humidity ranging from 50 to 80%[90]). In initial experiments, we note that $CsPbBr_3$ NC/zwitterionic polymer solutions in butyl acetate stored in ambient conditions maintained ~95% of their initial PLQY after 5 months of dark storage (see Figure B.6), whereas as-synthesized NCs in hexanes generally precipitate from solution after several days of ambient dark storage. To understand how these observations might translate to solid-state samples, we performed systematic stability measurements on various solid composites. To probe the PL stability of these NC composites, Figure 3.3a plots PLQYs of solid $CsPbBr_3$ NC/ZP3 and NC/PMMA composites measured as a function of ambient dark storage time. The NCs showed similar long-term dark storage stability in ZP3 as in PMMA, but the PLQY of the NC/ZP3 composite was ~2 times greater, indicating the efficacy of these zwitterionic polymers as a ligating matrix. XRD data (Figure B.11) show that $CsPbBr_3$ NCs in solid zwitterionic polymer composites maintain their crystal structure after 9 months of dark storage and the PLQY decreased slightly from 90 ± 5% to 85 ± 5% after 1 year of dark storage. Both results are indications of the resilience of these NCs in zwitterionic polymer composites.

Figure 3.3b plots PLQYs of various NC/polymer composites measured as a function of illumination time under ambient atmosphere, using ~90 mW cm^{-2} of full-area, 450 nm irradiation. The NC/ZP3 sample loses about 20% of its absolute PLQY in the first 12 hrs of illumination, but the NC PL intensity remains constant through the remaining 75 hrs of the experiment. Furthermore, the PLQYs of the NC/ZP3 samples recover over multiple time scales. For example, Figure B.13 shows an initial PLQY loss (5-10 sec) that fully recovers after ~10 min of dark storage, and Figure 3.3b shows that both the rapid PLQY loss and the slower PLQY decrease (~12 hrs) recover to ~90% of the initial PLQY after 6 days of dark storage. In contrast,

the NC/PMMA sample loses almost all of its PLQY after 24 hrs of irradiation, and this PLQY does not recover with dark storage. We also investigated the stability of drop-cast films of $CsPbBr_3$ NCs, but we found that these NCs had PLQYs of only ~20% and were far less stable than either the ZP3-passivated NCs or the PMMA-encapsulated NCs (see Figure B.12). These results are consistent with the observation that drop-cast perovskite NCs and NC/PMMA composites cannot withstand the high fluences (>100 W cm^{-2}) of single-particle spectroscopic measurements in ambient conditions.[91] Most reports of related NC/polymer composites do not perform irradiation stability measurements on the timescale needed to observe the rapid PLQY loss observed in Figure B.13, so it is unclear whether this drop is even more general among perovskite NCs.

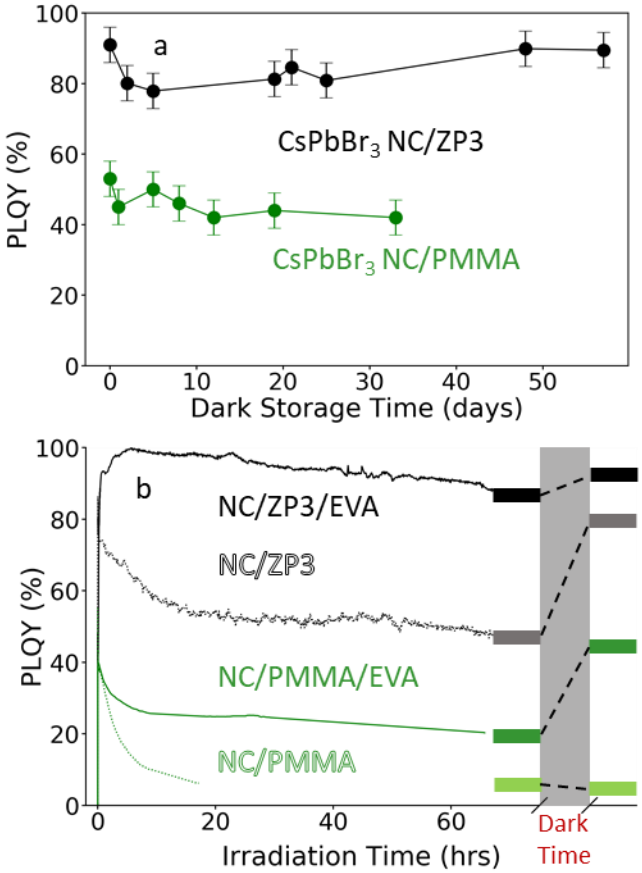

Figure 3.3. Stability assessment of various $CsPbBr_3$ NC/polymer composites. **(a)** PLQYs as a function of dark storage time under ambient atmosphere for drop-cast $CsPbBr_3$ NCs in PMMA and ZP3 composites. The NCs in ZP3 preserve all their original PLQY over 2 months while NCs in PMMA lose 20% of their PLQY over the first 15 days of dark storage. **(b)** PLQYs plotted as a function of 450 nm irradiation time for $CsPbBr_3$ NC/ZP3 and NC/PMMA composites with and without EVA encapsulation. The PLQYs were measured again after each sample was stored in the dark for several days following the irradiation experiment, and the values measured before and after dark storage are indicated as horizontal bars.

To better evaluate the potential of these NC/polymer composite in commercial applications, we laminated $CsPbBr_3$ NC/ZP3 and NC/PMMA samples between two layers of glass with poly(ethylene-*co*-vinyl acetate) (EVA) to reduce exposure of the NCs to air. Remarkably, the PLQY of the EVA-laminated NC/ZP3 sample increases to nearly 100% within the first few hours of illumination and stays constant at this value for the remaining 75 hrs of the

experiment. *Ex situ* integrating-sphere measurements verify that after 75 hrs of irradiation, the PLQY of the EVA-laminated sample increased from 48 ± 5% to 93 ± 5%; this PLQY is among the highest reported to date for any inorganic or hybrid bromo-perovskite NC/polymer solids.[22, 51, 58, 92] We also note that the PL spectra of both samples do not change substantially over the course of this measurement (see Figure B.12), suggesting that this photo-brightening is not attributable to irreversible etching of the NCs.[27, 37] In contrast, the PLQY of the EVA-laminated NC/PMMA sample decreased under illumination, recovering again after dark storage. These irradiation results indicate that the photostability of $CsPbBr_3$ NCs can be substantially enhanced by limiting air exposure. Additionally, when these NCs are hosted in a ZP3 composite, the high density of zwitterionic passivating groups in this polymer improves photostability in ambient conditions and increases PLQY in inert conditions relative to the same NCs in PMMA.

3.4.3 *$CsPb(Br_{1-x}I_x)_3$ NC/Polymer Composites*

We now turn our attention to polymer composites that stabilize red-emitting $CsPbI_3$ NCs. The $CsPbI_3$ NCs were found to be noticeably less stable than $CsPbBr_3$ NCs upon mixing with the zwitterionic polymers. For example, to prevent NC dissolution during mixing, it was necessary to use ~10x less polymer per of NC. Even when NC/polymer solutions were deposited onto substrates immediately after ligand exchange, XRD data (see Figure B.14) show a larger increase in the FWHM of the 28° peak of the γ-cubic phase $CsPbI_3$ NCs in ZP4 than was noted for $CsPbBr_3$ NCs in ZP3, suggesting that the $CsPbI_3$ NCs are etched during polymer binding. Additionally, although $CsPbBr_3$ NC/ZP3 composites in butyl acetate were stable under ambient conditions for up to 5 months, $CsPbI_3$ NC/ZP4 composites in butyl acetate were only stable for ~24 hrs in similar storage conditions.

Fortunately, the $CsPbI_3$ NCs in ZP4 show significantly improved PL compared to the same NCs either drop cast without polymer or embedded in PMMA composites. Figure 3.4a plots absorption and PL spectra of a $CsPbI_3$ NC/ZP4 composite and, for comparison, also of a $CsPbI_3$ NC/PMMA composite. The absorption and PL spectra for NCs in ZP4 and PMMA are nearly identical, apart from greater sub-bandgap scattering and a slight PL blue shift in the NC/ZP4 sample. The PL decay of the NCs in ZP4 is nearly monoexponential, whereas that of the NCs in PMMA appears biexponential (see Figure B.15). The PLQYs of the NCs in ZP4 and PMMA composites are 85 ± 5% and 45 ± 5%, respectively, suggesting that the additional PL decay component of the NCs in a PMMA composite can be attributed to non-radiative recombination at non-passivated surface traps. We also successfully stabilized $CsPb(Br_{1-x}I_x)_3$ NCs in ZP4 composites, but observed a 50 nm PL blue shift after polymer binding. The PLQY of $CsPb(Br_{1-x}I_x)_3$ NC/ZP4 composite was only ~30% (see Figure B.17).

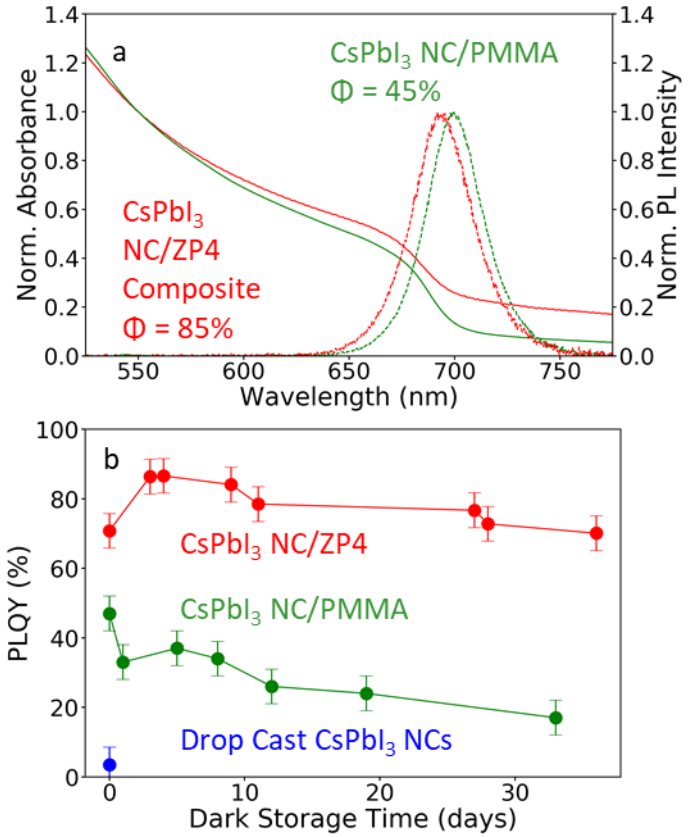

Figure 3.4. Characterization and stability assessment of various $CsPbI_3$ NC/polymer composites. **(a)** Absorption and PL spectra of $CsPbI_3$ NCs in ZP4 and PMMA composites. Absorption spectra are normalized at 550 nm and PL spectra are normalized to the PL maximum. The PLQYs of these samples are also indicated. **(b)** $CsPbI_3$ NC PLQYs plotted as a function of dark storage time in ambient atmosphere, measured for $CsPbI_3$ NC/ZP4 and NC/PMMA composites and the same NCs drop cast from hexane solution.

Figure 3.4b plots PLQYs of $CsPbI_3$ NCs drop cast onto a glass substrate along with $CsPbI_3$ NC/ZP4 and $CsPbI_3$ NC/PMMA composites, measured as a function of dark storage time under ambient atmosphere. The drop-cast $CsPbI_3$ NCs degraded almost as soon as they were exposed to air, and the NCs in PMMA lost two thirds of their PLQY over the course of ~32 days, dropping to 18 ± 5%. In contrast, the NCs in ZP4 maintain their PLQY well over the entire 36-day experiment, indicating improved long-term stability of $CsPbI_3$ NCs embedded within the ZP4 polymer matrix. Additionally, XRD data (Figure B.14) show that the same $CsPbI_3$ NC

crystal structure is maintained after 9 months of dark storage and the PLQY decreased from 85 ± 5% to 60 ± 5% after 1 year of dark storage in ambient conditions. We also found that the PLQYs of NC/ZP4 and NC/PMMA composites decrease under 450 nm, full area irradiation, but the NC/PMMA composite fully degrades within the first 5 hrs of irradiation, while the NC/ZP4 composite retains some luminescence through the full 100 hrs of irradiation (see Figure B.16). Furthermore, NC/ZP4 composites recover most of their PLQY after dark storage time, while the PLQY of the NC/PMMA composites remain low after dark storage time. These observations demonstrate that, like the $CsPbBr_3$ NC/ZP3 composites, $CsPbI_3$ NCs in ZP4 show *reversible* PL degradation when irradiated in the presence of air whereas the same NCs in PMMA show irreversible PL degradation.

3.4.4 *Yb^{3+}-Doped $CsPbCl_3$ NC/Polymer Composites*

Figure 3.5a shows the absorption spectrum of Yb^{3+}:$CsPbCl_3$ NCs in a ZFP3 composite thin film. The corresponding fluorinated polymer without zwitterions is insoluble in the apolar solvents used to process as-synthesized NCs. When zwitterionic groups are added, however, the zwitterionic fluorinated polymer is soluble in butyl acetate and can be used to stabilize as-synthesized Yb^{3+}:$CsPbCl_3$ NCs *via* the ligand exchange procedure described here. The absorption spectrum of the NC/ZFP3 film shows minimal sub-bandgap scattering, indicating that high concentrations of NCs can be well dispersed in ZFP3. The inset of Figure 3.5a shows a TEM image of the Yb^{3+}:$CsPbCl_3$ NCs in ZFP3. This image shows that the NC structure is similar to those reported previously for colloidal Yb^{3+}:$CsPbCl_3$ NCs.[9] Figure 3.5b plots PL spectra of zwitterionic ligand-capped Yb^{3+}:$CsPbCl_3$ NCs drop cast from solution and of oleylamine-capped NCs after incorporation into a ZFP3 composite, measured such that relative intensities can be compared quantitatively. The PLQY of the NC/ZFP3 film is slightly greater

than that of drop-cast NCs, owing to effective surface passivation by zwitterions in ZFP3. Additionally, the NC/ZFP3 film retains nearly the same PLQY for over 1.8 years of dark storage, an indication that the Yb^{3+}:$CsPbCl_3$ NCs are highly stable in this polymer.

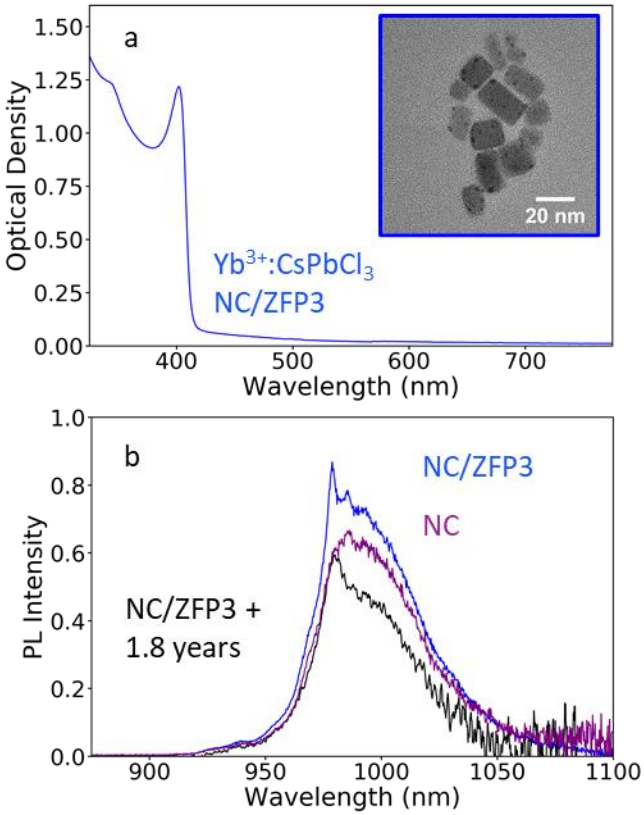

Figure 3.5. Characterization of Yb^{3+}:$CsPbCl_3$ NC/ZFP3 composite films. **(a)** Absorption spectra of a Yb^{3+}:$CsPbCl_3$ NC/ZPF3 composite film drop cast from butyl acetate. *Inset*: TEM image of these NCs in the NC/ZFP3 composite. **(b)** NIR PL spectra of the Yb^{3+}:$CsPbCl_3$ NC/polymer composite shown in panel (a). The PL spectra of the NC/ZFP3 composite after 1.8 years of dark, ambient storage and of the drop-cast zwitterionic-ligand capped NCs without polymer are also provided for reference. These PL spectra were measured quantitatively such that relative integrated intensities are proportional to relative PLQYs.

3.5 Discussion

We have developed a series of modular zwitterion-functionalized poly(isopropyl methacrylate) polymers with tailored inter-ion spacings and C–H bond densities, and have

demonstrated the use of these polymers to host highly luminescent $CsPbBr_3$, $CsPbI_3$, and Yb^{3+}:$CsPbCl_3$ NCs in green organic solvents without sacrificing their attractive PL characteristics. For all the NCs investigated here, the PLQYs increased upon incorporation into the zwitterion-functionalized polymers, an observation attributed to effective NC surface passivation by the zwitterionic functional groups. These NC/polymer composites could be cast into stable thin films, forming high-optical-quality solids with well-dispersed NCs in most cases. The NCs in these polymers show dark recovery of their PLQYs following extended irradiation in ambient atmosphere, likely aided by the high local concentrations of unbound zwitterion groups in these polymers, which may help to passivate surface defects formed through continuous NC irradiation. Collectively, this work and the two previously reported studies of zwitterionic polymers[71-72] represent the emergence of a new family of functionalized polymers specifically designed to support a multitude of applications of metal-halide perovskite NCs.

Although many studies have addressed the stability of $CsPbBr_3$ NCs in polymer matrices,[21-22, 36, 40, 49, 51, 55, 58, 67, 71-72] $CsPbI_3$ NCs have proven especially challenging to stabilize in polymers.[27, 34, 93] $CsPbI_3$ NCs have been stabilized in solution with near-unity PLQYs,[18, 62, 81] but only one recent report claims to have stabilized $CsPbI_3$ NCs in a polymer with ~99% PLQY, obtaining this high PLQY with phosphine additives.[66] The two prior studies of zwitterionic-polymer-stabilized perovskite NCs only demonstrated stabilization of $CsPbBr_3$ NCs, one focusing on solid composites[71] and the other on NCs in solution[72]; the latter polymers were additionally reported to be ineffective for stabilizing $CsPbI_3$ NCs.[72] Here, we have demonstrated the use of zwitterion-functionalized polymers to stabilize $CsPbI_3$ NCs with ~80% PLQY. The polymer was tailored to accommodate the lattice parameters of $CsPbI_3$ NCs[68] using zwitterionic functional groups having 4-methylene spacers between sulfonate and quaternary ammonium

ions. Furthermore, because $CsPbI_3$ NCs are less stable against dissolution in polar solvents than their bromide analogues, the branched isopropyl groups of the zwitterion-functionalized polymers introduced here play an important role by enhancing polymer solubility in aprotic solvents. This solubility is likely improved relative to previously reported zwitterionic polymers by the lack of non-coordinating carboxylate groups in the polymer structure.[72] This enables formation of NC/polymer composites in most organic solvents, including green solvents like butyl acetate that prevent $CsPbI_3$ NC dissolution over a modest, but acceptable processing window.

In addition to these attributes, the chemistry of the polymers developed here also makes them attractive for hosting perovskite NCs in various contexts. The synthetic strategy described in Scheme 1 is sufficiently modular that both the NC-coordinating and functional groups are interchangeable with little modification of reaction procedures. Proof-of-concept results have been demonstrated by swapping the isopropyl methacrylate with fluorinated isopropyl methacrylate. The high NIR transparencies of resultant fluorinated polymers[94-95] combined with the high solubility and stability of Yb^{3+}:$CsPbCl_3$ NCs in this fluorinated polymer offers an attractive solution to the problem of rapidly attenuated Yb^{3+} NIR emission in optical waveguides made from C-H-bond rich polymers that suffer from intense infrared absorption, for example in quantum-cutting luminescent solar concentrators or optical cavities.[32] In addition to fluorinated isopropyl methacrylate, the modularity of this polymer synthesis suggests that a wide variety of acrylate/methacrylate monomers with various functional groups can be included to modify the physical and chemical properties of these NC composites. For example, poly(ethylene glycol) offers water solubility[96] and benzophenone has been demonstrated as an effective crosslinking group for $CsPbBr_3$ NC/zwitterionic polymer composites.[71] Similarly, although proof-of-concept

results have been presented demonstrating stable red-emitting $CsPb(Br_{1-x}I_x)_3$ NC/polymer composite thin films relevant to LEDs,[88] prior work has suggested that phosphonate-based zwitterionic groups may better stabilize such anion-alloyed perovskite NCs,[68] and the synthesis methods described here are also amenable to swapping these functional groups. Moreover, because the NC/polymer composites are highly soluble in different organic solvents/mediums, they should also be easily blended and crosslinked with commercial resins without impacting their ability to stabilize perovskite NCs. Such an approach could be used to prepare fully crosslinked NC/polymer composites with various mechanical properties (*e.g.*, flexibility and stretchability) to further expand the functionalities of these NC/polymer composite for most commercial or experimental applications. This class of polymers thus offers broadly attractive chemical flexibility.

3.6 CONCLUSION

In summary, we demonstrate a straightforward method to synthesize a full series of novel, modular zwitterion-functionalized poly(isopropyl methacrylate) polymers that can be specifically tailored to host different types of luminescent perovskite NCs. These polymers use tunable zwitterionic anchor groups to stabilize the perovskite NCs, and they use fluorinated or non-fluorinated moieties to tune other optical characteristics, making them useful for hosting a broad array of doped and undoped perovskite NCs. As-prepared perovskite NCs could be easily transferred into these polymers *via* simple ligand exchange and precipitation, and the resulting perovskite NC/polymer composites show good NC solubility in most solvents, including green solvents like ethyl and butyl acetate. These solvated composites could be easily cast into high-optical-quality solid thin films for further optical interrogation or application. The NC PLQYs and ambient stabilities in these polymers are substantially enhanced relative to those in more

conventional PMMA polymer matrices. Overall, these findings establish this class of zwitterion-functionalized polymers as a flexible platform for advancing fundamental research involving perovskite NC/polymer composites and may help to advance the commercialization potential of perovskite NCs by facilitating full-scale manufacturing of luminescent NC-based composites *via* solution processing with green solvents.

3.7 ACKNOWLEDGEMENT

This research was primarily supported by the National Science Foundation (NSF) through the UW Molecular Engineering Materials Center, a Materials Research Science and Engineering Center (DMR-1719797 to DRG and CKL). This work was also supported by the State of Washington through the Washington Research Foundation (to JDM) and the Clean Energy Institute (to TAC and JDM). Part of this work was conducted at the Washington Clean Energy Testbeds and the Photonic Research Center, facilities operated by the University of Washington Clean Energy Institute. Part of this work was conducted at the Molecular Analysis Facility, a National Nanotechnology Coordinated Infrastructure site at the University of Washington that is supported in part by the National Science Foundation (ECC-1542101), the University of Washington, the Molecular Engineering & Sciences Institute, and the Clean Energy Institute. YH thanks the Data Intensive Research Enabling Clean Technology (DIRECT) NSF National Research Traineeship (DGE-1633216) for support. We gratefully acknowledge the assistance of K. Kluherz and E. Lavoie in collecting TEM images, S. Young for assistance collecting XRD data, and D. Kroupa for assistance collecting NIR PL data. We also acknowledge C. Krajewska for providing Yb^{3+}:$CsPbCl_3$ NCs that were used in early iterations of this work.

3.8 REFERENCES

1. Protesescu, L.; Yakunin, S.; Bodnarchuk, M. I.; Krieg, F.; Caputo, R.; Hendon, C. H.; Yang, R. X.; Walsh, A.; Kovalenko, M. V., Nanocrystals of Cesium Lead Halide Perovskites ($CsPbX_3$, X = Cl, Br, and I): Novel Optoelectronic Materials Showing Bright Emission with Wide Color Gamut. *Nano Lett.* **2015,** *15*, 3692-3696.
2. Koscher, B. A.; Swabeck, J. K.; Bronstein, N. D.; Alivisatos, A. P., Essentially Trap-Free $CsPbBr_3$ Colloidal Nanocrystals by Postsynthetic Thiocyanate Surface Treatment. *J. Am. Chem. Soc.* **2017,** *139*, 6566-6569.
3. Zhang, Y.; Siegler, T. D.; Thomas, C. J.; Abney, M. K.; Shah, T.; De Gorostiza, A.; Greene, R. M.; Korgel, B. A., A "Tips and Tricks" Practical Guide to the Synthesis of Metal Halide Perovskite Nanocrystals. *Chem. Mater.* **2020,** *32*, 5410–5423.
4. Pradhan, N., Tips and Twists in Making High Photoluminescence Quantum Yield Perovskite Nanocrystals. *ACS Energy Lett.* **2019,** *4*, 1634-1638.
5. Utzat, H.; Shulenberger, K. E.; Achorn, O. B.; Nasilowski, M.; Sinclair, T. S.; Bawendi, M. G., Probing Linewidths and Biexciton Quantum Yields of Single Cesium Lead Halide Nanocrystals in Solution. *Nano Lett.* **2017,** *17*, 6838-6846.
6. Creutz, S. E.; Crites, E. N.; De Siena, M. C.; Gamelin, D. R., Anion Exchange in Cesium Lead Halide Perovskite Nanocrystals and Thin Films Using Trimethylsilyl Halide Reagents. *Chem. Mater.* **2018,** *30*, 4887-4891.
7. Nedelcu, G.; Protesescu, L.; Yakunin, S.; Bodnarchuk, M. I.; Grotevent, M. J.; Kovalenko, M. V., Fast Anion-Exchange in Highly Luminescent Nanocrystals of Cesium Lead Halide Perovskites ($CsPbX_3$, X = Cl, Br, I). *Nano Lett.* **2015,** *15*, 5635-5640.
8. Imran, M.; Caligiuri, V.; Wang, M.; Goldoni, L.; Prato, M.; Krahne, R.; De Trizio, L.; Manna, L., Benzoyl Halides as Alternative Precursors for the Colloidal Synthesis of Lead-Based Halide Perovskite Nanocrystals. *J. Am. Chem. Soc.* **2018,** *140*, 2656-2664.
9. Milstein, T. J.; Kroupa, D. M.; Gamelin, D. R., Picosecond Quantum Cutting Generates Photoluminescence Quantum Yields over 100% in Ytterbium-Doped $Cspbcl_3$ Nanocrystals. *Nano Lett.* **2018,** *18*, 3792–3799.
10. Liu, W.; Lin, Q.; Li, H.; Wu, K.; Robel, I.; Pietryga, J. M.; Klimov, V. I., Mn^{2+}-Doped Lead Halide Perovskite Nanocrystals with Dual-Color Emission Controlled by Halide Content. *J. Am. Chem. Soc.* **2016,** *138*, 14954-14961.
11. Pan, G.; Bai, X.; Yang, D.; Chen, X.; Jing, P.; Qu, S.; Zhang, L.; Zhou, D.; Zhu, J.; Xu, W.; Dong, B.; Song, H., Doping Lanthanide into Perovskite Nanocrystals: Highly Improved and Expanded Optical Properties. *Nano Lett.* **2017,** *17*, 8005-8011.
12. Zhou, D.; Liu, D.; Pan, G.; Chen, X.; Li, D.; Xu, W.; Bai, X.; Song, H., Cerium and Ytterbium Codoped Halide Perovskite Quantum Dots: A Novel and Efficient Downconverter for Improving the Performance of Silicon Solar Cells. *Adv. Mater.* **2017,** *29*, 1704149.
13. De Siena, M. C.; Sommer, D. E.; Creutz, S. E.; Dunham, S. T.; Gamelin, D. R., Spinodal Decomposition During Anion Exchange in Colloidal Mn^{2+}-Doped $CsPbX_3$ (X = Cl, Br) Perovskite Nanocrystals. *Chem. Mater.* **2019,** *31*, 7711-7722.
14. Becker, M. A.; Vaxenburg, R.; Nedelcu, G.; Sercel, P. C.; Shabaev, A.; Mehl, M. J.; Michopoulos, J. G.; Lambrakos, S. G.; Bernstein, N.; Lyons, J. L.; Stöferle, T.; Mahrt, R. F.; Kovalenko, M. V.; Norris, D. J.; Rainò, G.; Efros, A. L., Bright Triplet Excitons in Caesium Lead Halide Perovskites. *Nature* **2018,** *553*, 189-193.

15. Isarov, M.; Tan, L. Z.; Bodnarchuk, M. I.; Kovalenko, M. V.; Rappe, A. M.; Lifshitz, E., Rashba Effect in a Single Colloidal $CsPbBr_3$ Perovskite Nanocrystal Detected by Magneto-Optical Measurements. *Nano Lett.* **2017,** *17*, 5020-5026.
16. Liu, Z.; Vaswani, C.; Yang, X.; Zhao, X.; Yao, Y.; Song, Z.; Cheng, D.; Shi, Y.; Luo, L.; Mudiyanselage, D. H.; Huang, C.; Park, J. M.; Kim, R. H. J.; Zhao, J.; Yan, Y.; Ho, K. M.; Wang, J., Ultrafast Control of Excitonic Rashba Fine Structure by Phonon Coherence in the Metal Halide Perovskite $Ch_3nh_3pbi_3$. *Phys. Rev. Lett.* **2020,** *124*, 157401.
17. Akkerman, Q. A.; Rainò, G.; Kovalenko, M. V.; Manna, L., Genesis, Challenges and Opportunities for Colloidal Lead Halide Perovskite Nanocrystals. *Nat. Mater.* **2018,** *17*, 394-405.
18. Nenon, D. P.; Pressler, K.; Kang, J.; Koscher, B. A.; Olshansky, J. H.; Osowiecki, W. T.; Koc, M. A.; Wang, L.-W.; Alivisatos, A. P., Design Principles for Trap-Free $CsPbX_3$ Nanocrystals: Enumerating and Eliminating Surface Halide Vacancies with Softer Lewis Bases. *J. Am. Chem. Soc.* **2018,** *140*, 17760-17772.
19. Kang, J.; Wang, L.-W., High Defect Tolerance in Lead Halide Perovskite $Cspbbr_3$. *J. Phys. Chem. Lett.* **2017,** *8*, 489-493.
20. ten Brinck, S.; Zaccaria, F.; Infante, I., Defects in Lead Halide Perovskite Nanocrystals: Analogies and (Many) Differences with the Bulk. *ACS Energy Lett.* **2019,** *4*, 2739-2747.
21. Sun, C.; Zhang, Y.; Ruan, C.; Yin, C.; Wang, X.; Wang, Y.; Yu, W. W., Efficient and Stable White Leds with Silica-Coated Inorganic Perovskite Quantum Dots. *Adv. Mater.* **2016,** *28*, 10088-10094.
22. Zhou, Q.; Bai, Z.; Lu, W.-g.; Wang, Y.; Zou, B.; Zhong, H., *In Situ* Fabrication of Halide Perovskite Nanocrystal-Embedded Polymer Composite Films with Enhanced Photoluminescence for Display Backlights. *Adv. Mater.* **2016,** *28*, 9163-9168.
23. Yakunin, S.; Protesescu, L.; Krieg, F.; Bodnarchuk, M. I.; Nedelcu, G.; Humer, M.; Luca, G. D.; Fiebig, M.; Heiss, W.; Kovalenko, M. V., Low-Threshold Amplified Spontaneous Emission and Lasing from Colloidal Nanocrystals of Caesium Lead Halide Perovskites. *Nat. Commun.* **2015,** *6*, 8056.
24. Makarov, N. S.; Guo, S.; Isaienko, O.; Liu, W.; Robel, I.; Klimov, V. I., Spectral and Dynamical Properties of Single Excitons, Biexcitons, and Trions in Cesium–Lead-Halide Perovskite Quantum Dots. *Nano Lett.* **2016,** *16*, 2349-2362.
25. Huang, C.-Y.; Zou, C.; Mao, C.; Corp, K. L.; Yao, Y.-C.; Lee, Y.-J.; Schlenker, C. W.; Jen, A. K. Y.; Lin, L. Y., $CsPbBr_3$ Perovskite Quantum Dot Vertical Cavity Lasers with Low Threshold and High Stability. *ACS Photonics* **2017,** *4*, 2281-2289.
26. Wang, Y.; Zhi, M.; Chang, Y.-Q.; Zhang, J.-P.; Chan, Y., Stable, Ultralow Threshold Amplified Spontaneous Emission from $CsPbBr_3$ Nanoparticles Exhibiting Trion Gain. *Nano Lett.* **2018,** *18*, 4976-4984.
27. Park, Y.-S.; Guo, S.; Makarov, N. S.; Klimov, V. I., Room Temperature Single-Photon Emission from Individual Perovskite Quantum Dots. *ACS Nano* **2015,** *9*, 10386-10393.
28. Rainò, G.; Nedelcu, G.; Protesescu, L.; Bodnarchuk, M. I.; Kovalenko, M. V.; Mahrt, R. F.; Stöferle, T., Single Cesium Lead Halide Perovskite Nanocrystals at Low Temperature: Fast Single-Photon Emission, Reduced Blinking, and Exciton Fine Structure. *ACS Nano* **2016,** *10*, 2485-2490.
29. Utzat, H.; Sun, W.; Kaplan, A. E. K.; Krieg, F.; Ginterseder, M.; Spokoyny, B.; Klein, N. D.; Shulenberger, K. E.; Perkinson, C. F.; Kovalenko, M. V.; Bawendi, M. G., Coherent

Single-Photon Emission from Colloidal Lead Halide Perovskite Quantum Dots. *Science* **2019,** *363*, 1068-1072.

30. Meinardi, F.; Akkerman, Q. A.; Bruni, F.; Park, S.; Mauri, M.; Dang, Z.; Manna, L.; Brovelli, S., Doped Halide Perovskite Nanocrystals for Reabsorption-Free Luminescent Solar Concentrators. *ACS Energy Lett.* **2017,** *2*, 2368-2377.
31. Zhao, H.; Benetti, D.; Tong, X.; Zhang, H.; Zhou, Y.; Liu, G.; Ma, D.; Sun, S.; Wang, Z. M.; Wang, Y.; Rosei, F., Efficient and Stable Tandem Luminescent Solar Concentrators Based on Carbon Dots and Perovskite Quantum Dots. *Nano Energy* **2018,** *50*, 756-765.
32. Cohen, T. A.; Milstein, T. J.; Kroupa, D. M.; MacKenzie, J. D.; Luscombe, C. K.; Gamelin, D. R., Quantum-Cutting Yb^{3+}-Doped Perovskite Nanocrystals for Monolithic Bilayer Luminescent Solar Concentrators. *J. Mater. Chem. A* **2019,** *7*, 9279-9288.
33. Wei, M.; Arquer, F. P. G. d.; Walters, G.; Yang, Z.; Quan, L. N.; Kim, Y.; Sabatini, R.; Quintero-Bermudez, R.; Gao, L.; Fan, J. Z.; Fan, F.; Gold-Parker, A.; Toney, M. F.; Sargent, E. H., Ultrafast Narrowband Exciton Routing within Layered Perovskite Nanoplatelets Enables Low-Loss Luminescent Solar Concentrators. *Nat. Energy* **2019,** *4*, 197-205.
34. Yuan, G.; Ritchie, C.; Ritter, M.; Murphy, S.; Gómez, D. E.; Mulvaney, P., The Degradation and Blinking of Single $CsPbI_3$ Perovskite Quantum Dots. *J. Phys. Chem. C* **2018,** *122*, 13407-13415.
35. Vicente, J. R.; Rafiei Miandashti, A.; Sy Piecco, K. W. E.; Pyle, J. R.; Kordesch, M. E.; Chen, J., Single-Particle Organolead Halide Perovskite Photoluminescence as a Probe for Surface Reaction Kinetics. *ACS Appl. Mater. Interfaces* **2019,** *11*, 18034-18043.
36. Meyns, M.; Perálvarez, M.; Heuer-Jungemann, A.; Hertog, W.; Ibáñez, M.; Nafria, R.; Genç, A.; Arbiol, J.; Kovalenko, M. V.; Carreras, J.; Cabot, A.; Kanaras, A. G., Polymer-Enhanced Stability of Inorganic Perovskite Nanocrystals and Their Application in Color Conversion Leds. *ACS Appl. Mater. Interfaces* **2016,** *8*, 19579-19586.
37. Raja, S. N.; Bekenstein, Y.; Koc, M. A.; Fischer, S.; Zhang, D.; Lin, L.; Ritchie, R. O.; Yang, P.; Alivisatos, A. P., Encapsulation of Perovskite Nanocrystals into Macroscale Polymer Matrices: Enhanced Stability and Polarization. *ACS Appl. Mater. Interfaces* **2016,** *8*, 35523-35533.
38. Wu, H.; Wang, S.; Cao, F.; Zhou, J.; Wu, Q.; Wang, H.; Li, X.; Yin, L.; Yang, X., Ultrastable Inorganic Perovskite Nanocrystals Coated with a Thick Long-Chain Polymer for Efficient White Light-Emitting Diodes. *Chem. Mater.* **2019,** *31*, 1936-1940.
39. Wei, S.; Zhu, H.; Zhang, J.; Wang, L.; An, M.; Wang, Y.; Zhang, X.; Liu, Y., Luminescent Perovskite Nanocrystal-Epoxy Resin Composite with High Stability against Water and Air. *J. Alloys Compd.* **2019,** *789*, 209-214.
40. Tong, J.; Wu, J.; Shen, W.; Zhang, Y.; Liu, Y.; Zhang, T.; Nie, S.; Deng, Z., Direct Hot-Injection Synthesis of Lead Halide Perovskite Nanocubes in Acrylic Monomers for Ultrastable and Bright Nanocrystal–Polymer Composite Films. *ACS Appl. Mater. Interfaces* **2019,** *11*, 9317-9325.
41. Wang, H.-C.; Lin, S.-Y.; Tang, A.-C.; Singh, B. P.; Tong, H.-C.; Chen, C.-Y.; Lee, Y.-C.; Tsai, T.-L.; Liu, R.-S., Mesoporous Silica Particles Integrated with All-Inorganic $CsPbBr_3$ Perovskite Quantum-Dot Nanocomposites (Mp-PQDs) with High Stability and Wide Color Gamut Used for Backlight Display. *Angew. Chem. Int. Ed.* **2016,** *55*, 7924-7929.

42. Chen, D.; Fang, G.; Chen, X., Silica-Coated Mn-Doped $CsPb(Cl/Br)_3$ Inorganic Perovskite Quantum Dots: Exciton-to-Mn Energy Transfer and Blue-Excitable Solid-State Lighting. *ACS Appl. Mater. Interfaces* **2017,** *9*, 40477-40487.
43. Li, Z.; Kong, L.; Huang, S.; Li, L., Highly Luminescent and Ultrastable $Cspbbr_3$ Perovskite Quantum Dots Incorporated into a Silica/Alumina Monolith. *Angew. Chem.* **2017,** *129*, 8246-8250.
44. Pramanik, A.; Gates, K.; Patibandla, S.; Davis, D.; Begum, S.; Iftekhar, R.; Alamgir, S.; Paige, S.; Porter, M. M.; Ray, P. C., Water-Soluble and Bright Luminescent Cesium–Lead–Bromide Perovskite Quantum Dot–Polymer Composites for Tumor-Derived Exosome Imaging. *ACS Appl. Bio Mater.* **2019,** *2*, 5872-5879.
45. Lu, Z.; Li, Y.; Qiu, W.; Rogach, A. L.; Nagl, S., Composite Films of $Cspbbr_3$ Perovskite Nanocrystals in a Hydrophobic Fluoropolymer for Temperature Imaging in Digital Microfluidics. *ACS Appl. Mater. Interfaces* **2020,** *12*, 19805-19812.
46. Ahmed, T.; Seth, S.; Samanta, A., Boosting the Photoluminescence of $CsPbX_3$ (X = Cl, Br, I) Perovskite Nanocrystals Covering a Wide Wavelength Range by Postsynthetic Treatment with Tetrafluoroborate Salts. *Chem. Mater.* **2018,** *30*, 3633-3637.
47. Zhang, Q.; Li, Z.; Liu, M.; Kong, L.; Zheng, W.; Wang, B.; Li, L., Bifunctional Passivation Strategy to Achieve Stable $CsPbBr_3$ Nanocrystals with Drastically Reduced Thermal-Quenching. *J. Phys. Chem. Lett.* **2020,** *11*, 993-999.
48. Sun, H.; Yang, Z.; Wei, M.; Sun, W.; Li, X.; Ye, S.; Zhao, Y.; Tan, H.; Kynaston, E. L.; Schon, T. B.; Yan, H.; Lu, Z.-H.; Ozin, G. A.; Sargent, E. H.; Seferos, D. S., Chemically Addressable Perovskite Nanocrystals for Light-Emitting Applications. *Adv. Mater.* **2017,** *29*, 1701153.
49. Kim, H.; So, S.; Ribbe, A.; Liu, Y.; Hu, W.; Duzhko, V. V.; Hayward, R. C.; Emrick, T., Functional Polymers for Growth and Stabilization of $CsPbBr_3$ Perovskite Nanoparticles. *Chem. Commun.* **2019,** *55*, 1833-1836.
50. Suh, Y.-H.; Kim, T.; Choi, J. W.; Lee, C.-L.; Park, J., High-Performance $Cspbx_3$ Perovskite Quantum-Dot Light-Emitting Devices *via* Solid-State Ligand Exchange. *ACS Appl. Nano Mater.* **2018,** *1*, 488-496.
51. He, Y.; Yoon, Y. J.; Harn, Y. W.; Biesold-McGee, G. V.; Liang, S.; Lin, C. H.; Tsukruk, V. V.; Thadhani, N.; Kang, Z.; Lin, Z., Unconventional Route to Dual-Shelled Organolead Halide Perovskite Nanocrystals with Controlled Dimensions, Surface Chemistry, and Stabilities. *Sci. Adv.* **2019,** *5*, eaax4424.
52. Hou, S.; Guo, Y.; Tang, Y.; Quan, Q., Synthesis and Stabilization of Colloidal Perovskite Nanocrystals by Multidentate Polymer Micelles. *ACS Appl. Mater. Interfaces* **2017,** *9*, 18417-18422.
53. Hui, L. S.; Beswick, C.; Getachew, A.; Heilbrunner, H.; Liang, K.; Hanta, G.; Arbi, R.; Munir, M.; Dawood, H.; Isik Goktas, N.; LaPierre, R.; Scharber, M. C.; Sariciftci, N. S.; Turak, A., Reverse Micelle Templating Route to Ordered Monodispersed Spherical Organo-Lead Halide Perovskite Nanoparticles for Light Emission. *ACS Appl. Nano Mater.* **2019,** *2*, 4121-4132.
54. Liu, Y.; Wang, Z.; Liang, S.; Li, Z.; Zhang, M.; Li, H.; Lin, Z., Polar Organic Solvent-Tolerant Perovskite Nanocrystals Permanently Ligated with Polymer Hairs *via* Star-Like Molecular Bottlebrush Trilobe Nanoreactors. *Nano Lett.* **2019,** *19*, 9019-9028.

55. Xin, Y.; Shen, W.; Deng, Z.; Zhang, J., Highly Emissive and Color-Tunable Perovskite Cross-Linkers for Luminescent Polymer Networks. *ACS Appl. Mater. Interfaces* **2018,** *10*, 28971-28978.
56. Guan, H.; Zhao, S.; Wang, H.; Yan, D.; Wang, M.; Zang, Z., Room Temperature Synthesis of Stable Single Silica-Coated $CsPbBr_3$ Quantum Dots Combining Tunable Red Emission of Ag–In–Zn–S for High-CRI White Light-Emitting Diodes. *Nano Energy* **2020,** *67*, 104279.
57. Jancik Prochazkova, A.; Demchyshyn, S.; Yumusak, C.; Másilko, J.; Brüggemann, O.; Weiter, M.; Kaltenbrunner, M.; Sariciftci, N. S.; Krajcovic, J.; Salinas, Y.; Kovalenko, A., Proteinogenic Amino Acid Assisted Preparation of Highly Luminescent Hybrid Perovskite Nanoparticles. *ACS Appl. Nano Mater.* **2019,** *2*, 4267-4274.
58. Pan, A.; Wang, J.; Jurow, M. J.; Jia, M.; Liu, Y.; Wu, Y.; Zhang, Y.; He, L.; Liu, Y., General Strategy for the Preparation of Stable Luminous Nanocomposite Inks Using Chemically Addressable $CsPbX_3$ Peroskite Nanocrystals. *Chem. Mater.* **2018,** *30*, 2771-2780.
59. Liang, P.; Zhang, P.; Pan, A.; Yan, K.; Zhu, Y.; Yang, M.; He, L., Unusual Stability and Temperature-Dependent Properties of Highly Emissive $CsPbBr_3$ Perovskite Nanocrystals Obtained from *in Situ* Crystallization in Poly(Vinylidene Difluoride). *ACS Appl. Mater. Interfaces* **2019,** *11*, 22786-22793.
60. De Roo, J.; Ibáñez, M.; Geiregat, P.; Nedelcu, G.; Walravens, W.; Maes, J.; Martins, J. C.; Van Driessche, I.; Kovalenko, M. V.; Hens, Z., Highly Dynamic Ligand Binding and Light Absorption Coefficient of Cesium Lead Bromide Perovskite Nanocrystals. *ACS Nano* **2016,** *10*, 2071-2081.
61. Çetinkaya, O.; Demirci, G.; Mergo, P., Effect of the Different Chain Transfer Agents on Molecular Weight and Optical Properties of Poly(Methyl Methacrylate). *Opt. Mater.* **2017,** *70*, 25-30.
62. Liu, F.; Zhang, Y.; Ding, C.; Kobayashi, S.; Izuishi, T.; Nakazawa, N.; Toyoda, T.; Ohta, T.; Hayase, S.; Minemoto, T.; Yoshino, K.; Dai, S.; Shen, Q., Highly Luminescent Phase-Stable $CsPbI_3$ Perovskite Quantum Dots Achieving near 100% Absolute Photoluminescence Quantum Yield. *ACS Nano* **2017,** *11*, 10373-10383.
63. Wu, L.; Zhong, Q.; Yang, D.; Chen, M.; Hu, H.; Pan, Q.; Liu, H.; Cao, M.; Xu, Y.; Sun, B.; Zhang, Q., Improving the Stability and Size Tunability of Cesium Lead Halide Perovskite Nanocrystals Using Trioctylphosphine Oxide as the Capping Ligand. *Langmuir* **2017,** *33*, 12689-12696.
64. Tan, Y.; Zou, Y.; Wu, L.; Huang, Q.; Yang, D.; Chen, M.; Ban, M.; Wu, C.; Wu, T.; Bai, S.; Song, T.; Zhang, Q.; Sun, B., Highly Luminescent and Stable Perovskite Nanocrystals with Octylphosphonic Acid as a Ligand for Efficient Light-Emitting Diodes. *ACS Appl. Mater. Interfaces* **2018,** *10*, 3784-3792.
65. Zhang, B.; Goldoni, L.; Zito, J.; Dang, Z.; Almeida, G.; Zaccaria, F.; de Wit, J.; Infante, I.; De Trizio, L.; Manna, L., Alkyl Phosphonic Acids Deliver $CsPbBr_3$ Nanocrystals with High Photoluminescence Quantum Yield and Truncated Octahedron Shape. *Chem. Mater.* **2019,** *31*, 9140-9147.
66. Wu, J.; Tong, J.; Gao, Y.; Wang, A.; Zhang, T.; Tan, H.; Nie, S.; Deng, Z., Efficient and Stable Thin-Film Luminescent Solar Concentrators Enabled by near-Infrared Emission Perovskite Nanocrystals. *Angew. Chem. Int. Ed.* **2020,** *59*, 7738-7742.

67. Krieg, F.; Ong, Q. K.; Burian, M.; Rainò, G.; Naumenko, D.; Amenitsch, H.; Süess, A.; Grotevent, M. J.; Krumeich, F.; Bodnarchuk, M. I.; Shorubalko, I.; Stellacci, F.; Kovalenko, M. V., Stable Ultraconcentrated and Ultradilute Colloids of $CsPbX_3$ (X = Cl, Br) Nanocrystals Using Natural Lecithin as a Capping Ligand. *J. Am. Chem. Soc.* **2019,** *141*, 19839-19849.
68. Krieg, F.; Ochsenbein, S. T.; Yakunin, S.; ten Brinck, S.; Aellen, P.; Süess, A.; Clerc, B.; Guggisberg, D.; Nazarenko, O.; Shynkarenko, Y.; Kumar, S.; Shih, C.-J.; Infante, I.; Kovalenko, M. V., Colloidal $CsPbX_3$ (X = Cl, Br, I) Nanocrystals 2.0: Zwitterionic Capping Ligands for Improved Durability and Stability. *ACS Energy Lett.* **2018,** *3*, 641-646.
69. Chen, Q.; Yuan, L.; Duan, R.; Huang, P.; Fu, J.; Ma, H.; Wang, X.; Zhou, Y.; Song, B., Zwitterionic Polymer: A Facile Interfacial Material Works at Both Anode and Cathode in p-i-n Perovskite Solar Cells. *Sol. RRL* **2019,** *3*, 1900118.
70. Zhou, S.; Zhu, T.; Zheng, L.; Zhang, D.; Xu, W.; Liu, L.; Cheng, G.; Zheng, J.; Gong, X., A Zwitterionic Polymer as an Interfacial Layer for Efficient and Stable Perovskite Solar Cells. *RSC Advances* **2019,** *9*, 30317-30324.
71. Kim, H.; Hight-Huf, N.; Kang, J.-H.; Bisnoff, P.; Sundararajan, S.; Thompson, T.; Barnes, M.; Hayward, R. C.; Emrick, T., Polymer Zwitterions for Stabilization of $CsPbBr_3$ Perovskite Nanoparticles and Nanocomposite Films. *Angew. Chem. Int. Ed.* **2020,** *59*, 10802-10806.
72. Wang, S.; Du, L.; Jin, Z.; Xin, Y.; Mattoussi, H., Enhanced Stabilization and Easy Phase Transfer of $CsPbBr_3$ Perovskite Quantum Dots Promoted by High Affinity Polyzwitterionic Ligands. *J. Am. Chem. Soc.* **2020,** *142*, 12669-12680.
73. Cabanetos, C.; El Labban, A.; Bartelt, J. A.; Douglas, J. D.; Mateker, W. R.; Fréchet, J. M. J.; McGehee, M. D.; Beaujuge, P. M., Linear Side Chains in Benzo[1,2-B:4,5-B′]dithiophene–thieno[3,4-C]pyrrole-4,6-dione Polymers Direct Self-Assembly and Solar Cell Performance. *J. Am. Chem. Soc.* **2013,** *135*, 4656-4659.
74. Gadisa, A.; Oosterbaan, W. D.; Vandewal, K.; Bolsée, J.-C.; Bertho, S.; D'Haen, J.; Lutsen, L.; Vanderzande, D.; Manca, J. V., Effect of Alkyl Side-Chain Length on Photovoltaic Properties of Poly(3-Alkylthiophene)/PCBM Bulk Heterojunctions. *Adv. Funct. Mater.* **2009,** *19*, 3300-3306.
75. Xie, R.; Chen, Z.; Zhong, W.; Zhang, G.; Huang, Y.; Ying, L.; Huang, F.; Cao, Y., Synthesis and Characterization of π-Conjugated Copolymers Based on Alkyltriazolyl Substituted Benzodithiophene. *New J. Chem.* **2016,** *40*, 4727-4734.
76. Meager, I.; Ashraf, R. S.; Mollinger, S.; Schroeder, B. C.; Bronstein, H.; Beatrup, D.; Vezie, M. S.; Kirchartz, T.; Salleo, A.; Nelson, J.; McCulloch, I., Photocurrent Enhancement from Diketopyrrolopyrrole Polymer Solar Cells through Alkyl-Chain Branching Point Manipulation. *J. Am. Chem. Soc.* **2013,** *135*, 11537-11540.
77. Shivhare, R.; Erdmann, T.; Hörmann, U.; Collado-Fregoso, E.; Zeiske, S.; Benduhn, J.; Ullbrich, S.; Hübner, R.; Hambsch, M.; Kiriy, A.; Voit, B.; Neher, D.; Vandewal, K.; Mannsfeld, S. C. B., Alkyl Branching Position in Diketopyrrolopyrrole Polymers: Interplay between Fibrillar Morphology and Crystallinity and Their Effect on Photogeneration and Recombination in Bulk-Heterojunction Solar Cells. *Chem. Mater.* **2018,** *30*, 6801-6809.
78. Lei, T.; Dou, J.-H.; Pei, J., Influence of Alkyl Chain Branching Positions on the Hole Mobilities of Polymer Thin-Film Transistors. *Adv. Mater.* **2012,** *24*, 6457-6461.

79. Groh, W., Overtone Absorption in Macromolecules for Polymer Optical Fibers. *Die Makromol. Chemie* **1988,** *189*, 2861-2874.
80. Prat, D.; Wells, A.; Hayler, J.; Sneddon, H.; McElroy, C. R.; Abou-Shehada, S.; Dunn, P. J., Chem21 Selection Guide of Classical- and Less Classical-Solvents. *Green Chem.* **2015,** *18*, 288-296.
81. Cai, Y.; Wang, H.; Li, Y.; Wang, L.; Lv, Y.; Yang, X.; Xie, R.-J., Trimethylsilyl Iodine-Mediated Synthesis of Highly Bright Red-Emitting $CsPbI_3$ Perovskite Quantum Dots with Significantly Improved Stability. *Chem. Mater.* **2019,** *31*, 881-889.
82. Obrezkova, M. A.; Kalinina, A. A.; Pavlichenko, I. V.; Vasilenko, N. G.; Mironova, M. V.; Semakov, A. V.; Kulichikhin, V. G.; Buzin, M. I.; Muzafarov, A. M., Comb-Like Polymethylsiloxanes. Synthesis, Structure and Properties. *Silicon* **2015,** *7*, 177-189.
83. Knauf, R. R.; Lennox, J. C.; Dempsey, J. L., Quantifying Ligand Exchange Reactions at CdSe Nanocrystal Surfaces. *Chem. Mater.* **2016,** *28*, 4762-4770.
84. Dierick, R.; Van den Broeck, F.; De Nolf, K.; Zhao, Q.; Vantomme, A.; Martins, J. C.; Hens, Z., Surface Chemistry of $CuInS_2$ Colloidal Nanocrystals, Tight Binding of L-Type Ligands. *Chem. Mater.* **2014,** *26*, 5950-5957.
85. Hens, Z.; Martins, J. C., A Solution Nmr Toolbox for Characterizing the Surface Chemistry of Colloidal Nanocrystals. *Chem. Mater.* **2013,** *25*, 1211-1221.
86. Imran, M.; Ijaz, P.; Goldoni, L.; Maggioni, D.; Petralanda, U.; Prato, M.; Almeida, G.; Infante, I.; Manna, L., Simultaneous Cationic and Anionic Ligand Exchange for Colloidally Stable $CsPbBr_3$ Nanocrystals. *ACS Energy Lett.* **2019,** *4*, 819-824.
87. Quarta, D.; Imran, M.; Capodilupo, A.-L.; Petralanda, U.; van Beek, B.; De Angelis, F.; Manna, L.; Infante, I.; De Trizio, L.; Giansante, C., Stable Ligand Coordination at the Surface of Colloidal $CsPbBr_3$ Nanocrystals. *J. Phys. Chem. Lett.* **2019,** *10*, 3715-3726.
88. Shimizu, K. T.; Böhmer, M.; Estrada, D.; Gangwal, S.; Grabowski, S.; Bechtel, H.; Kang, E.; Vampola, K. J.; Chamberlin, D.; Shchekin, O. B.; Bhardwaj, J., Toward Commercial Realization of Quantum Dot Based White Light-Emitting Diodes for General Illumination. *Photonics Res.* **2017,** *5*, A1-A6.
89. Sorensen, C. M., Light Scattering by Fractal Aggregates: A Review. *Aerosol Sci. Tech.* **2001,** *35*, 648-687.
90. Tillman, J. E.; Johnson, N. C., Department of Atmospheric Sciences, University of Washington; Supported by Iita Program, Office of Aeronautics; in Collaboration with Pathfinder Project, NASA JPL, Office Space Sciences. 2021.
91. Rainò, G.; Landuyt, A.; Krieg, F.; Bernasconi, C.; Ochsenbein, S. T.; Dirin, D. N.; Bodnarchuk, M. I.; Kovalenko, M. V., Underestimated Effect of a Polymer Matrix on the Light Emission of Single $CsPbBr_3$ Nanocrystals. *Nano Lett.* **2019,** *19*, 3648-3653.
92. Di Stasio, F.; Christodoulou, S.; Huo, N.; Konstantatos, G., Near-Unity Photoluminescence Quantum Yield in $CsPbBr_3$ Nanocrystal Solid-State Films *Via* Postsynthesis Treatment with Lead Bromide. *Chem. Mater.* **2017,** *29*, 7663-7667.
93. Dutta, A.; Pradhan, N., Phase-Stable Red-Emitting $CsPbI_3$ Nanocrystals: Successes and Challenges. *ACS Energy Lett.* **2019,** *4*, 709-719.
94. Zhou, D.; Teng, H.; Koike, K.; Koike, Y.; Okamoto, Y., Copolymers of Methyl Methacrylate and Fluoroalkyl Methacrylates: Effects of Fluoroalkyl Groups on the Thermal and Optical Properties of the Copolymers. *J. Polym. Sci. Pol. Chem.* **2008,** *46*, 4748-4755.

95. Koike, K.; Kado, T.; Satoh, Z.; Okamoto, Y.; Koike, Y., Optical and Thermal Properties of Methyl Methacrylate and Pentafluorophenyl Methacrylate Copolymer: Design of Copolymers for Low-Loss Optical Fibers for Gigabit in-Home Communications. *Polymer* **2010,** *51*, 1377-1385.
96. Moquin, A.; Hanna, R.; Liang, T.; Erguven, H.; Gran, E. R.; Arndtsen, B. A.; Maysinger, D.; Kakkar, A., Peg-Conjugated Pyrrole-Based Polymers: One-Pot Multicomponent Synthesis and Self-Assembly into Soft Nanoparticles for Drug Delivery. *Chem. Commun.* **2019,** *55*, 9829-9832.

CHAPTER 4. DIRECT PATTERNING OF PEROVSKITE NANOCRYSTALS ON NANOPHOTONIC CAVITIES WITH ELECTROHYDRODYNAMIC INKJET PRINTING

Reproduced with permission from Cohen, T. A; Sharp, D; Kluherz, K. T; Chen, Y; Munley, C; Anderson, R. T; Swanson, C. S; De Yoreo, J. J; Luscombe, C. K; Majumdar, A; Gamelin, D. R; MacKenzie, J. D. *Nano Letters* **2022**, *Submitted.*

4.1 OVERVIEW

Overcoming the challenges of patterning luminescent materials will unlock additive and more sustainable paths for manufacturing of next generation on chip photonic devices. Electrohydrodynamic (EHD) inkjet printing is a promising method for deterministically placing emitters on photonic devices. However, the use of this technique to pattern luminescent lead-halide perovskite nanocrystals (NCs), notable for their defect tolerance and impressive optical and spin coherence properties, for integration with optoelectronic devices remains unexplored. In this work, we additively deposit nanoscale $CsPbBr_3$ NC features on photonic structures via EHD inkjet printing. We perform transmission electron microscopy of EHD inkjet-printed NCs to demonstrate that the NCs' structural integrity is maintained throughout the printing process. Lastly, NCs are deposited with submicron control on an array of parallel silicon nitride nanophotonic cavities and demonstrate cavity-emitter coupling via photoluminescence spectroscopy. These results demonstrate EHD inkjet printing as a scalable, precise method to pattern luminescent nanomaterials for photonic applications.

4.2 INTRODUCTION

Nanoscale patterning of materials has been critical for the rapid advancement of electronic information processing technologies.[1-2] The patterning of luminescent materials attracted early research interest,[3] and this capability has become critical for many emerging photonic device platforms where precise heterointegration of emitters and other materials on nanophotonic structures is needed.[4-5] Inkjet printing has emerged as a promising method for patterning photoactive nanocrystals (NCs) because it is a rapid, mask free method of placing on-demand droplets of material into any arbitrary pattern with almost no material waste.[6-8] Typical inkjet-printing resolutions are limited to tens of microns, which is less precise than needed for integrated photonics. Smaller printed features can be generated using electrohydrodynamic (EHD) inkjet printing, a process that uses an electric field applied from the print nozzle to overcome surface energetics and viscous kinetics that limit mechanical droplet formation to generate droplets far smaller than those obtained with traditional inkjet printing.[9-10] Perovskite NCs are promising materials for quantum photonics due to superior single-photon emission,[11-12] high optical coherence times,[13] and lifetime-limited excited-state spin coherence.[14] These NCs have been processed with EHD inkjet printing for LEDs[15] and radiative lifetime-encoded security tags,[16] but this method has not been used to deterministically place perovskite NCs on nano-photonic cavities, an advancement that is necessary to develop next-generation chip-integrated quantum photonic devices. Furthermore, given the many documented structural instabilities of perovskite NCs,[17-18] a thorough analysis after EHD inkjet printing is necessary to evaluate whether the high voltages used during processing are compatible with these notoriously unstable materials.

In this work, we use EHD inkjet printing to deterministically position $CsPbBr_3$ NCs on nanophotonic structures. Atomic force microscopy (AFM) images and photoluminescence (PL) studies of printed NCs show that tunable NC features with diameters of 500 nm and heights of 50 nm could be reproducibly fabricated without compromising the NCs' PL properties. Additionally, we use silicon nitride membrane transmission electron microscopy (TEM) grids to collect the first high resolution TEM images of EHD printed NCs to date. Finally, we demonstrate that this printing method can be used to deterministically place these NCs onto silicon nitride nanobeam cavities[19-20] with NC emission successfully coupled to the cavity modes. These results show that perovskite NCs can be effectively processed with EHD inkjet printing with high precision and at scale for photonic device integration.

4.3 METHODS

Materials. Lead acetate trihydrate [$Pb(OAc)_2 \cdot 3H_2O$] (99.9%, Baker Chemical), cesium carbonate [Cs_2CO_3] (99.9%, Sigma Aldrich), bromotrimethylsilane [TMS-Br] (97%, Sigma Aldirch), 1-octadecene [ODE] (90%, Sigma Aldrich), oleylamine [OAm] (70%, Sigma Aldrich), oleic acid [OA] (90%, Sigma Aldrich), didodecyldimethylammonium bromide [DDABr] (98%, Sigma Aldrich), hexanes (99%, mixture of isomers, Sigma Aldrich), ethyl acetate (99%, Sigma Aldrich), toluene (HPLC, Fischer Chemical), octane (99%, Sigma Aldrich), hexadecane (99%, Sigma Aldrich), nitric acid (20%, EMD), trichloro(1*H*,1*H*,2*H*,2*H*-perfluorooctyl)silane (97%, Sigma Aldrich), anisole (99.7%, Sigma Aldrich), and poly(methyl methacrylate) [PMMA] (~120,000 MW, Sigma Aldrich) were used as received unless otherwise noted.

Nanocrystal Synthesis and Solution Preparation. $CsPbBr_3$ NCs were synthesized according to methods reported previously.[21] Once purified, the NCs were treated with DDABr according to methods reported previously.[17] Briefly, 600 µL of stock NC solution in hexanes was

combined with 600 μL of toluene, 160 μL of 0.05 M DDABr solution in toluene, and 30 μL of oleic acid in an N_2-filled glovebox. The resulting NCs were precipitated with ethyl acetate in air and centrifuged at 16,060 gx for 10 minutes. The precipitated NCs were resuspended in hexanes and stored in an N_2-filled glovebox for future use. NC inks were prepared by removing a 100 μL aliquot of hexanes NC solution from the glovebox and drying the NCs under N_2 flow. Once dried, 500 μL of octane and hexadecane were added, and the resulting solution was filtered through a 220 nm PTFE syringe filter to yield a solution with a NC concentration of ~10^{-7} M. Hexadecane was chosen for its high boiling point to prevent drying and nozzle clogging during the printing process, but additional octane was necessary to facilitate suspension of these NCs in solution. All NC inks were used within one day of preparation. PMMA solutions were prepared by stirring 80 mg mL^{-1} of PMMA in anisole overnight and filtering through a 460 nm PTFE syringe filter.

Electrohydrodynamic Inkjet Printing. Printing was performed with the SIJ Technologies, S050 EHD inkjet printer. Substrates were cleaned with concentrated nitric acid overnight and washed with DI water. Clean substrates were then coated with a low surface energy fluorinated SAM by placing the substrate on a 160 °C hotplate under a petri dish with 10 μL of trichloro(1*H*,1*H*,2*H*,2*H*-perfluorooctyl)silane for 1 hr prior to mounting on the EHD inkjet printer stage. A fresh super-fine EHD inkjet print nozzle with a ~2 μm inner diameter was then loaded with 10 μL of NC ink using a custom-designed narrow pipet tip, and the print nozzle was magnetically mounted to the EHD inkjet printer. The nozzle tip was lowered ~10 μm above the substrate and printing was performed in bump mode with a 75% square waveform between 200 V and 600 V operating at a frequency of 1 kHz. The bed speed and bump hold time were tuned to the desired droplet spacing and print consistency (see Figure C.3). To print droplets aligned to

pre-fabricated device substrates, E-beam etched marks on the device substrate were found with the printer's built-in alignment camera, and the associated stage location is saved in the software. A nozzle alignment mark was then printed on the substrate and found with the alignment camera, and the associated alignment camera location was saved in the software. This information, along with the spacing between nanobeam cavity devices on the substrate, was used to calibrate the coordinate plane of the stage and the alignment camera to the movement of the nozzle, thereby enabling the placement of NC droplets onto the center of Si_3N_4 nanobeam cavities with micron-scale precision (see Figure C.7). If necessary, 100 μL of PMMA solution in anisole was spin coated onto the printed substrate at 2000 RPM for 1 minute. The substrate was then annealed at 70 °C for 10 min.

4.4 Results and Analysis

$CsPbBr_3$ NCs were synthesized and ligand treated according to methods reported previously.[17, 21] This synthesis yields orthorhombic perovskite NCs with an average edge length of 9.7 ± 2.1 nm and narrow ~520 nm PL with a PL quantum yield of ~80% (see Figure C.1). The NCs were then dispersed in a 1:1 mixture of octane and hexadecane at a NC concentration of ~10^{-7} M for the formulation of a stable EHD printing ink dispersion. Figure 1a shows a schematic of the EHD inkjet printing setup used in this work. Printing is performed by applying a voltage between the electrode within the print nozzle and the substrate ground plane. This voltage polarizes the printing solution, creating an electric field that overcomes the intrinsic surface energy controlling the meniscus curvature of the EHD ink at the nozzle orifice, i.e. creating a Taylor cone at the tip of the print nozzle, as illustrated in the inset of Figure 4.1a. Computer control of the voltage parameters associated with this electric field allows droplet formation and acceleration towards the substrate, and the controlled movement of the substrate

stage enables the printing of very high-resolution patterns. Silicon and glass substrates coated with a fluorinated self-assembled monolayer (SAM) were used to prevent droplet spreading that could increase printed feature sizes. Printing was performed with 'bump mode' waveform control, a method of printing where the control software stops the print nozzle at discrete points and applies an AC potential for a set time to dispense femtoliter-scale NC ink droplets at each point (see Figure C.2). This approach allows fine and arbitrary tuning of the NC drop spacing in any desired pattern.

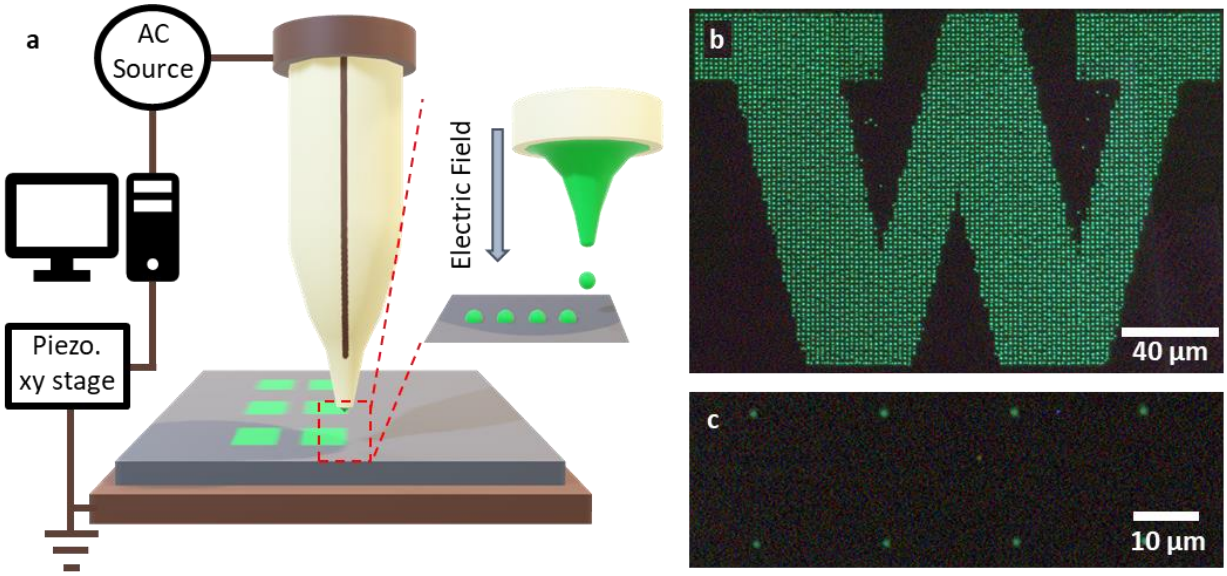

Figure 4.1. EHD inkjet printing for high-resolution patterning of perovskite NCs. **(a)** Scheme describing the EHD inkjet printing setup. A computer-controlled AC source creates an alternating voltage profile between the print nozzle and the printer bed via a small electrode embedded in the print nozzle. This voltage generates an electric field between the print nozzle and the print substrate that drives printing. *Inset:* Diagram showing the effect of an electric field on the meniscus at the tip of an EHD inkjet print nozzle. Partial polarization of the NC ink overcomes the ink's surface energy and draws a convex Taylor cone out of the EHD nozzle to produce small droplets that form the final print pattern. PL microscope images of printed $CsPbBr_3$ NCs on a fluorinated SAM-treated silicon substrate with **(b)** 2 µm feature spacing and **(c)** 20 µm feature spacing.

4.4.1 *NC Print Characterization*

Figure 4.1b-c shows PL microscope images of EHD inkjet-printed $CsPbBr_3$ NCs under 450 nm excitation. The 210 µm print pattern in Figure 4.1b consists of 2 µm spaced NC features printed with a 70 ms hold time. Figure 4.1c shows a section of a 500 µm pattern composed of 20 µm spaced features printed with 40 ms hold time. The hold times were selected based on an optimization to maximize the ratio of on-target to off-target printed features, as exemplified in Figure C.3. Green PL is observed from each printed NC feature, and the 2 and 20 µm grid patterns are well maintained across the entire printed pattern with few defects. To test whether EHD inkjet printing impacts the optoelectronic properties of the $CsPbBr_3$ NCs, steady-state PL studies of NCs before and after printing were conducted. Figure 4.2a shows PL spectra of an individual printed feature and an ensemble of the same NCs drop cast onto a silicon substrate. The NC PL blue-shifts when printing biases of 750 – 1250 V are used (see Figure C.4), but it remains largely unchanged under the typical printing conditions used here (200 – 600 V). Furthermore, the inset of Figure 4.2a shows that when NC print patterns are excited with 450 nm light, visible NC PL can be observed by eye and imaged with a cell phone camera. The NCs thus remain bright following the EHD inkjet printing process.

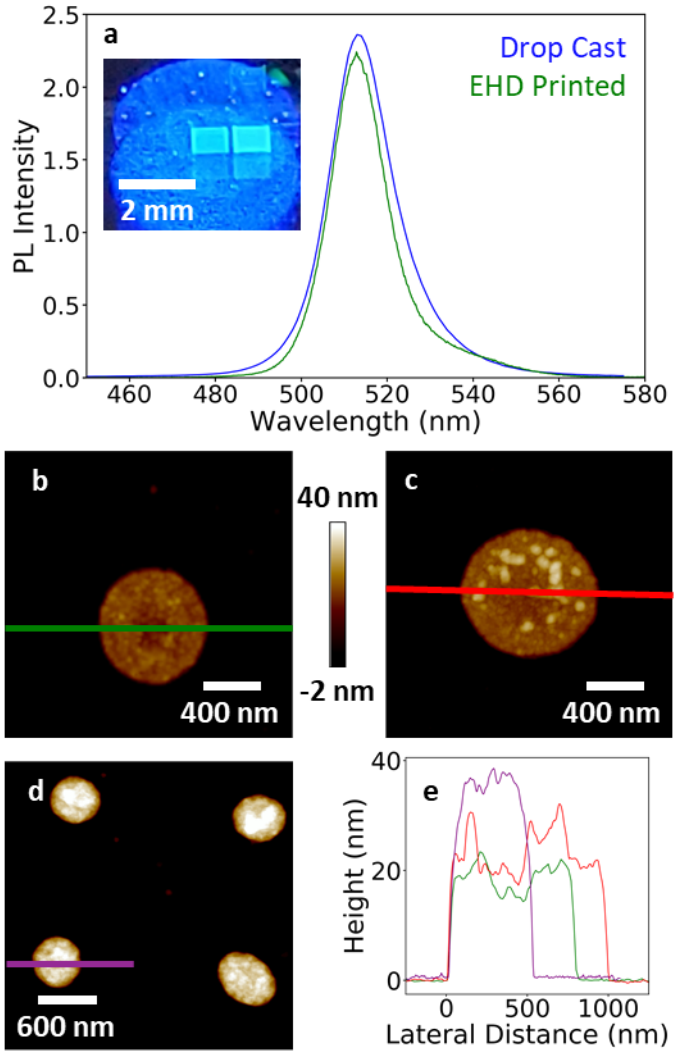

Figure 4.2. Optical and structural characterization of EHD inkjet-printed NCs. **(a)** Normalized PL spectra of $CsPbBr_3$ NCs drop cast from hexanes solvent and EHD inkjet printed on a silicon substrate. *Inset*: Photograph of printed patterns on a glass substrate, under 450 nm illumination. The 1 mm^2 print patterns visible here have different brightness because they were printed with different parameters and different numbers of print passes. AFM images of NCs printed with 20 µm feature spacing and bump hold times of **(b)** 40 ms and **(c)** 70 ms. **(d)** AFM image of NCs printed with 2 µm feature spacing. **(e)** Height profiles from the color-coded lines in the AFM images in panels b-d show controllable, sub-micron NC feature sizes.

Figure 4.2b-d shows AFM images of EHD inkjet-printed $CsPbBr_3$ NCs, and Figure 4.2e shows height profiles collected along the color-coded lines shown in Figure 4.2b-d. These printed features are less than 1 µm in diameter, which highlights high-resolution patterning

capability of EHD inkjet printing. Figure 4.2d and the additional AFM image in Figure C.5 show that remarkably consistent feature spacings of 2 μm can be readily achieved with this technique. The height profiles in Figure 4.2e further demonstrate that printed features can be reduced to diameters as small as 500 nm by optimizing print parameters. These liquid ink-derived features show minimal 'coffee ring' character, which demonstrates that the fluorinated SAM-coated silicon substrates provide the surface energy mismatch necessary for effective dewetting to yield high-resolution print features.[22-23] Additionally, while 500 nm diameter on-target features could be reproducibly formed, further AFM analysis in Figure C.5 shows that some off-target droplets form features with diameters below 300 nm, which suggests that further optimization of print parameters could yield even smaller on-target EHD printed NC features. Finally, the step heights observed for the prints shown here are all multiples of the NC edge length of ~10 nm, demonstrating that these print features are composed of only 2 – 4 layers of $CsPbBr_3$ NCs.

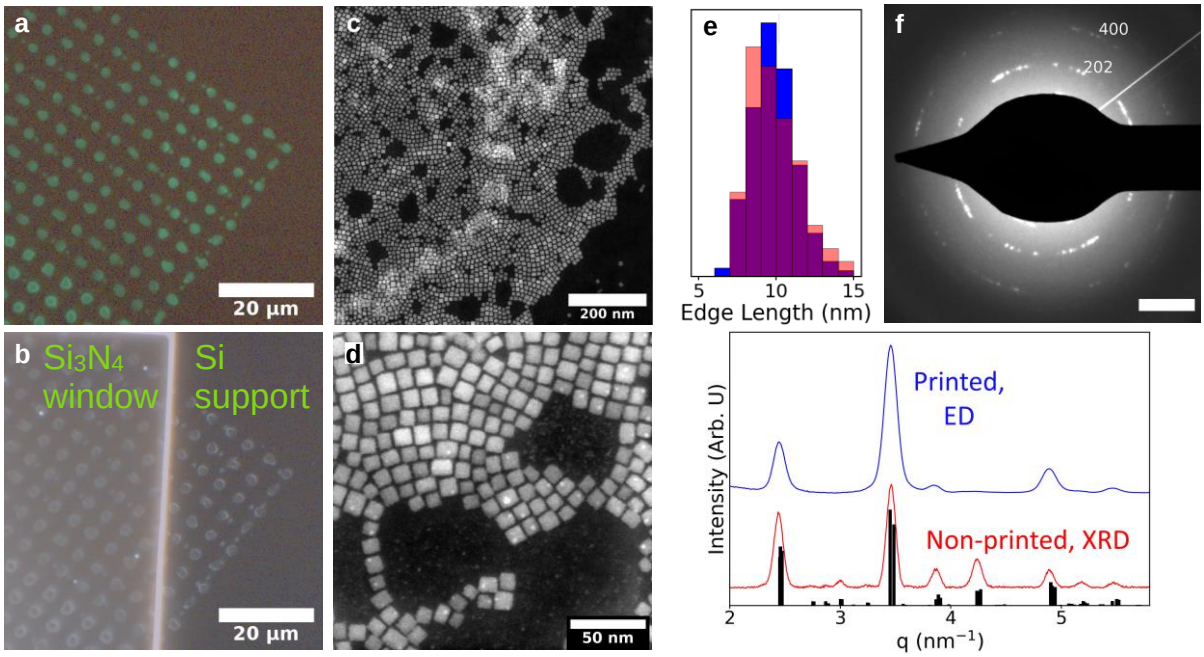

Figure 4.3. Transmission electron microscopy of EHD inkjet-printed perovskite NCs. **(a)** PL microscope image of EHD inkjet-printed $CsPbBr_3$ NCs on a carbon-coated Si_3N_4 membrane window TEM grid under 450 nm irradiation. **(b)** Dark field optical microscope image of the same area shown in panel a. The bright white line is the edge of the Si_3N_4 TEM window. **(c,d)** HAADF-STEM images of $CsPbBr_3$ NCs within an EHD inkjet-printed droplet. **(e)** Edge length distribution of EHD inkjet-printed NCs (blue) and non-printed NCs (red). **(f)** Electron diffraction (ED) image of a selected area showing a spot diffraction pattern which indexes to the $CsPbBr_3$ Pnma lattice planes. **(g)** ED pattern ring integration of printed $CsPbBr_3$ NCs (blue) compared with the XRD pattern of non-printed NCs (red) and a standard reference (black). The differing peak intensities are attributed to differences in preferential NC orientation when prepared for XRD and ED analysis. *Inset:* Large area ED image used to acquire the integrated pattern in panel g. Scale bars in panels f and g are 2 nm^{-1}.

Ideally, the NC crystal phase, size distribution, and cubic shape would all be preserved after printing. These characteristics can be measured by TEM, but EHD inkjet-printed NCs have not been characterized with high resolution TEM to date. The few reported TEM images of EHD-printed structures were collected from silica structures on copper TEM grids generated

with printing biases between 6 and 12 kV,[24-25] or from gold nanostructures printed on molybdenum half grids for STEM imaging.[26] The voltages used for silica printing would likely be too high to adequately preserve perovskite NC PL properties, as discussed above, and we were unable to successfully print $CsPbBr_3$ NCs onto carbon coated copper or nickel TEM grids at lower voltages due to the grids' high conductivity. Furthermore, the molybdenum half grid approach cannot be used to collect high resolution images or electron diffraction (ED) patterns of printed structures, which are important for assessing NC morphological and structural properties after printing. Therefore, we used carbon-coated Si_3N_4 membrane TEM grids for imaging our EHD inkjet-printed NCs. Figure 4.3a,b shows optical microscope images of $CsPbBr_3$ NCs collected in PL and dark field modes, respectively. Similar printing voltages (200 – 600 V) to those employed in Figure 4.1 – Figure 4.2 were used to print on Si_3N_4 membrane TEM grids, and NC PL is clearly visible in regions both above the Si_3N_4 window and on the surrounding silicon support. We did not apply the same fluorinated SAM treatment to the Si_3N_4 TEM grids as was used on the silicon substrates discussed previously, which results in the printing of larger droplets in Figure 4.3a,b. Nevertheless, the high angle annular dark field scanning transmission electron microscopy (HAADF-STEM) images in Figure 4.3c,d show that each printed feature comprises clusters of individually resolvable $CsPbBr_3$ NCs. Additionally, ordered NC superlattice domains are visible in these and other printed NC STEM images shown in Figure C.6. Figure 4.3e shows edge length distributions from NCs printed on Si_3N_4 TEM grids and drop cast from hexanes onto a carbon coated copper TEM grid. The average NC edge lengths before and after printing are 9.7 ± 2.1 nm and 9.8 ± 1.6 nm respectively, which demonstrates that the NC size distribution is largely unchanged by the EHD inkjet printing process. Figure 4.3f shows the ED obtained from a small-area of the EHD inkjet-printed NCs. The spot patterns in this

image index to the orthorhombic $CsPbBr_3$ crystal lattice, and the alignment of the diffraction spots reinforces the observation that the printed NCs form self-assembled superlattice domains under these printing conditions. Finally, the radially integrated, large-area ED pattern in Figure 4.3g can be directly indexed to the orthorhombic $CsPbBr_3$ powder XRD reference pattern and the XRD data obtained for non-printed $CsPbBr_3$ NCs, with no additional detectable crystal phases. Notably, the ED peak intensities differ from the powder XRD intensities, reflecting the preferred orientation of the printed NCs.

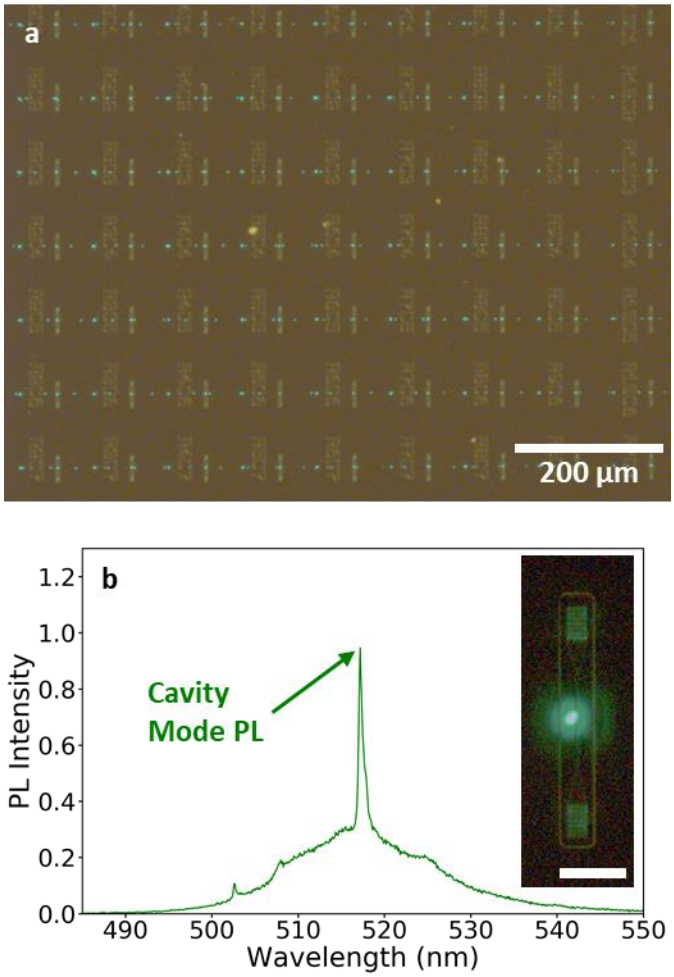

Figure 4.4. Optical coupling of EHD inkjet-printed NCs to nanophotonic cavities. **(a)** PL microscope image of EHD inkjet-printed $CsPbBr_3$ NCs on an array of pre-fabricated monolithic Si_3N_4 nanobeam cavities. NC features were printed with 50 µm spacing, and several off-target features are present. Visible PL can be seen emanating from the grating couplers at the top and bottom of each cavity. **(b)** PL spectra collected through the nanobeam cavity grating coupler. In addition to broad background $CsPbBr_3$ NC emission, a sharp peak is observed at ~517 nm, associated with NC PL coupled to the nanobeam cavity mode (Q ~ 1000). *Inset:* PL microscope image of the nanobeam cavity characterized in panel b. Scale bar is 10 µm.

The patterns analyzed above were all printed on blank silicon substrates. To print NCs onto pre-fabricated Si_3N_4 nanobeam cavities,[19, 27] we use an EHD inkjet printing alignment process to ensure that printed droplets are placed directly on the centers of the nanobeam

cavities, as described in Figure C.7. Aligned print patterns were then coated with poly(methyl methacrylate) (PMMA) to encapsulate the NCs against environmental degradation during optical characterization and to preserve the inversion symmetry of the refractive index surrounding the cavity without impacting NC PL (see Figure C.8). The nanobeam cavities are designed to maintain a high quality factor even when they are encapsulated in polymer.[28] Figure 4.4a shows a PL microscope image of EHD inkjet-printed NCs on a large array of nanobeam cavities. The inset of Figure 4.4b shows a magnified image of one individual nanobeam cavity. The green emission of the printed $CsPbBr_3$ NCs is clearly visible at the centers and at the grating couplers found at both ends of each nanobeam cavity waveguide. This result shows that the printed NC emission is successfully coupled into the nanobeam cavity and that EHD inkjet printing successfully placed NCs onto all the devices. Figure 4.4b shows the spectrum of emission emanating from the grating coupler of the nanobeam cavity in the inset of Figure 4.4b with additional images in Figure C.9. In addition to the broad background PL of non-cavity coupled NCs, a sharp peak at ~517 nm is observed. This peak can be assigned to NC emission that is coupled to the cavity mode of this nanobeam cavity. Lorentzian fitting of this peak reveals a Q-factor of ~1,000 for this cavity-coupled emission, which is in good agreement with the expected Q-factors for this nanobeam cavity structure.[19] We also note an additional higher order cavity peak at ~503 nm. We attribute this mode to slight out-of-plane inversion symmetry breaking of the refractive index by the printed NCs.[27]

4.5 DISCUSSION

There are several important advancements in this work that demonstrate the potential of EHD inkjet printing for integration of perovskite NCs with photonic devices. First, despite the promising structural characterization in prior reports of EHD inkjet-printed CdSe[29-30] or

perovskite[16,17] NCs, the TEM data presented here provide unique and comprehensive evidence of NC structure preservation and self-assembly during the printing process. This result is particularly important for perovskites because of their well-documented environmental instability and the potential of both single perovskite NCs as single photon sources[11, 13] and self-assembled superlattices as superfluorescent correlated photon sources[31-32] for chip-integrated quantum photonics. Secondly, while CdSe NCs have been EHD inkjet-printed on plasmonic devices with near micron precision,[33-34] and reports of EHD printed perovskite NCs demonstrate ink co-alignment with a precision of ~10 μm,[16] this report demonstrates sufficient feature alignment precision to place perovskites on a ~10 mm^2 array of dielectric photonic crystal cavities with unmatched, submicron precision. The co-alignment imprecision here is greater than one micron, but it can be improved by using a more precise print stage and alignment setup. Similarly, the Q-factor of ~1000 demonstrated here can be improved through improved cavity design.[20]

4.6 CONCLUSION

In summary, we've shown that $CsPbBr_3$ NCs can be deterministically patterned over large areas and with sub-micron precision using EHD inkjet printing. Additionally, we collected the first high-resolution STEM images of EHD inkjet-printed structures, showing that the original NC structure is preserved post printing and that NCs within these printed structures self-assemble into superlattices. We also used micron-scale alignment to place printed NC droplets onto the centers of a ~10 mm^2 array of prefabricated Si_3N_4 nanobeam cavities. This demonstration will motivate the further exploration of this printing method to process perovskite NCs for photonic devices, with the potential to leverage quantum emission from single printed perovskite NCs or self-assembled NC superlattices with monolayer thickness control. It also

motivates the exploration of EHD inkjet printing of other novel luminescent materials for photonic device integration.

4.7 ACKNOWLEDGEMENT

This research was primarily supported by the National Science Foundation (NSF) through the UW Molecular Engineering Materials Center, a Materials Research Science and Engineering Center (DMR-1719797 to DRG and CKL). This work was also supported by the State of Washington through the Washington Research Foundation and the Joint Center for Deployment and Research in Earth Abundant Materials (to JDM). Part of this work was conducted at the Washington Clean Energy Testbeds and the Photonic Research Center, facilities operated by the University of Washington Clean Energy Institute. Part of this work was conducted at the Molecular Analysis Facility, a National Nanotechnology Coordinated Infrastructure site at the University of Washington that is supported in part by the National Science Foundation (ECC-1542101), the University of Washington, the Molecular Engineering & Sciences Institute, and the Clean Energy Institute. We gratefully acknowledge the assistance of Kelly Walsh for collecting XRD data. We also acknowledge Yunping Huang for helpful discussion.

4.8 REFERENCES

1. Thompson, L. F., An Introduction to Lithography. In *Introduction to Microlithography*, American Chemical Society: 1983; Vol. 219, pp 1-13.
2. Xia, Y.; Rogers, J. A.; Paul, K. E.; Whitesides, G. M., Unconventional Methods for Fabricating and Patterning Nanostructures. *Chem. Rev.* **1999,** *99*, 1823-1848.
3. Kash, K.; Scherer, A.; Worlock, J. M.; Craighead, H. G.; Tamargo, M. C., Optical Spectroscopy of Ultrasmall Structures Etched from Quantum Wells. *Appl. Phys. Lett.* **1986,** *49*, 1043-1045.
4. Senellart, P.; Solomon, G.; White, A., High-Performance Semiconductor Quantum-Dot Single-Photon Sources. *Nat. Nanotechnol.* **2017,** *12*, 1026-1039.

5. Suh, Y.-H.; Shin, D.-W.; Chun, Y. T., Micro-to-Nanometer Patterning of Solution-Based Materials for Electronics and Optoelectronics. *RSC Advances* **2019,** *9*, 38085-38104.
6. Tekin, E.; Smith, P. J.; Hoeppener, S.; van den Berg, A. M. J.; Susha, A. S.; Rogach, A. L.; Feldmann, J.; Schubert, U. S., Inkjet Printing of Luminescent CdTe Nanocrystal–Polymer Composites. *Adv. Funct. Mater.* **2007,** *17*, 23-28.
7. Wood, V.; Panzer, M. J.; Chen, J.; Bradley, M. S.; Halpert, J. E.; Bawendi, M. G.; Bulović, V., Inkjet-Printed Quantum Dot–Polymer Composites for Full-Color AC-Driven Displays. *Adv. Mater.* **2009,** *21*, 2151-2155.
8. Lan, L.; Zou, J.; Jiang, C.; Liu, B.; Wang, L.; Peng, J., Inkjet Printing for Electroluminescent Devices: Emissive Materials, Film Formation, and Display Prototypes. *Front. Optoelectron.* **2017,** *10*, 329-352.
9. Nakao, H.; Murakami, T.; Hirahara, S.; Nagato, H.; Nomura, Y., Head Design for Novel Ink-Jet Printing Using Electrostatic Force. *NIP & Digital Fabrication Conference* **1999,** *1999*, 319-322.
10. Park, J.-U.; Hardy, M.; Kang, S. J.; Barton, K.; Adair, K.; Mukhopadhyay, D. k.; Lee, C. Y.; Strano, M. S.; Alleyne, A. G.; Georgiadis, J. G.; Ferreira, P. M.; Rogers, J. A., High-Resolution Electrohydrodynamic Jet Printing. *Nat. Mater.* **2007,** *6*, 782-789.
11. Park, Y.-S.; Guo, S.; Makarov, N. S.; Klimov, V. I., Room Temperature Single-Photon Emission from Individual Perovskite Quantum Dots. *ACS Nano* **2015,** *9*, 10386-10393.
12. Rainò, G.; Nedelcu, G.; Protesescu, L.; Bodnarchuk, M. I.; Kovalenko, M. V.; Mahrt, R. F.; Stöferle, T., Single Cesium Lead Halide Perovskite Nanocrystals at Low Temperature: Fast Single-Photon Emission, Reduced Blinking, and Exciton Fine Structure. *ACS Nano* **2016,** *10*, 2485-2490.
13. Utzat, H.; Sun, W.; Kaplan, A. E. K.; Krieg, F.; Ginterseder, M.; Spokoyny, B.; Klein, N. D.; Shulenberger, K. E.; Perkinson, C. F.; Kovalenko, M. V.; Bawendi, M. G., Coherent Single-Photon Emission from Colloidal Lead Halide Perovskite Quantum Dots. *Science* **2019,** *363*, 1068-1072.
14. Crane, M. J.; Jacoby, L. M.; Cohen, T. A.; Huang, Y.; Luscombe, C. K.; Gamelin, D. R., Coherent Spin Precession and Lifetime-Limited Spin Dephasing in $CsPbBr_3$ Perovskite Nanocrystals. *Nano Lett.* **2020,** *20*, 8626-8633.
15. Altintas, Y.; Torun, I.; Yazici, A. F.; Beskazak, E.; Erdem, T.; Serdar Onses, M.; Mutlugun, E., Multiplexed Patterning of Cesium Lead Halide Perovskite Nanocrystals by Additive Jet Printing for Efficient White Light Generation. *Chem. Eng. J.* **2020,** *380*, 122493.
16. Yakunin, S.; Chaaban, J.; Benin, B. M.; Cherniukh, I.; Bernasconi, C.; Landuyt, A.; Shynkarenko, Y.; Bolat, S.; Hofer, C.; Romanyuk, Y. E.; Cattaneo, S.; Pokutnyi, S. I.; Schaller, R. D.; Bodnarchuk, M. I.; Poulikakos, D.; Kovalenko, M. V., Radiative Lifetime-Encoded Unicolour Security Tags Using Perovskite Nanocrystals. *Nat. Commun.* **2021,** *12*, 981.
17. Rainò, G.; Landuyt, A.; Krieg, F.; Bernasconi, C.; Ochsenbein, S. T.; Dirin, D. N.; Bodnarchuk, M. I.; Kovalenko, M. V., Underestimated Effect of a Polymer Matrix on the Light Emission of Single $CsPbBr_3$ Nanocrystals. *Nano Lett.* **2019,** *19*, 3648-3653.
18. Baranov, D.; Fieramosca, A.; Yang, R. X.; Polimeno, L.; Lerario, G.; Toso, S.; Giansante, C.; Giorgi, M. D.; Tan, L. Z.; Sanvitto, D.; Manna, L., Aging of Self-Assembled Lead Halide Perovskite Nanocrystal Superlattices: Effects on Photoluminescence and Energy Transfer. *ACS Nano* **2021,** *15*, 650-664.

19. Fong, C. F.; Yin, Y.; Chen, Y.; Rosser, D.; Xing, J.; Majumdar, A.; Xiong, Q., Silicon Nitride Nanobeam Enhanced Emission from All-Inorganic Perovskite Nanocrystals. *Opt. Express, OE* **2019,** *27*, 18673-18682.
20. He, Z.; Chen, B.; Hua, Y.; Liu, Z.; Wei, Y.; Liu, S.; Hu, A.; Shen, X.; Zhang, Y.; Gao, Y.; Liu, J., CMOS Compatible High-Performance Nanolasing Based on Perovskite–Sin Hybrid Integration. *Adv. Opt. Mater.* **2020,** *8*, 2000453.
21. Cohen, T. A.; Huang, Y.; Bricker, N. A.; Juhl, C. S.; Milstein, T. J.; MacKenzie, J. D.; Luscombe, C. K.; Gamelin, D. R., Modular Zwitterion-Functionalized Poly(Isopropyl Methacrylate) Polymers for Hosting Luminescent Lead Halide Perovskite Nanocrystals. *Chem. Mater.* **2021,** *33*, 3779-3790.
22. Schlisske, S.; Held, M.; Rödlmeier, T.; Menghi, S.; Fuchs, K.; Ruscello, M.; Morfa, A. J.; Lemmer, U.; Hernandez-Sosa, G., Substrate-Independent Surface Energy Tuning Via Siloxane Treatment for Printed Electronics. *Langmuir* **2018,** *34*, 5964-5970.
23. Klein, T.; Yan, S.; Cui, J.; Magee, J. W.; Kroenlein, K.; Rausch, M. H.; Koller, T. M.; Fröba, A. P., Liquid Viscosity and Surface Tension of n-hexane, n-octane, n-decane, and n-hexadecane up to 573 K by Surface Light Scattering. *J. Chem. Eng. Data* **2019,** *64*, 4116-4131.
24. Wang, D. Z.; Jayasinghe, S. N.; Edirisinghe, M. J., High Resolution Print-Patterning of a Nano-Suspension. *Journal of Nanoparticle Research* **2005,** *7*, 301-306.
25. Wang, D. Z.; Jayasinghe, S. N.; Edirisinghe, M. J.; Luklinska, Z. B., Coaxial Electrohydrodynamic Direct Writing of Nano-Suspensions. *Journal of Nanoparticle Research* **2007,** *9*, 825-831.
26. Rohner, P.; Reiser, A.; Rabouw, F. T.; Sologubenko, A. S.; Norris, D. J.; Spolenak, R.; Poulikakos, D., 3d Electrohydrodynamic Printing and Characterisation of Highly Conductive Gold Nanowalls. *Nanoscale* **2020,** *12*, 20158-20164.
27. Chen, Y.; Ryou, A.; Friedfeld, M. R.; Fryett, T.; Whitehead, J.; Cossairt, B. M.; Majumdar, A., Deterministic Positioning of Colloidal Quantum Dots on Silicon Nitride Nanobeam Cavities. *Nano Lett.* **2018,** *18*, 6404-6410.
28. Fryett, T. K.; Chen, Y.; Whitehead, J.; Peycke, Z. M.; Xu, X.; Majumdar, A., Encapsulated Silicon Nitride Nanobeam Cavity for Hybrid Nanophotonics. *ACS Photonics* **2018,** *5*, 2176-2181.
29. Kim, B. H.; Onses, M. S.; Lim, J. B.; Nam, S.; Oh, N.; Kim, H.; Yu, K. J.; Lee, J. W.; Kim, J.-H.; Kang, S.-K.; Lee, C. H.; Lee, J.; Shin, J. H.; Kim, N. H.; Leal, C.; Shim, M.; Rogers, J. A., High-Resolution Patterns of Quantum Dots Formed by Electrohydrodynamic Jet Printing for Light-Emitting Diodes. *Nano Lett.* **2015,** *15*, 969-973.
30. Kress, S. J. P.; Richner, P.; Jayanti, S. V.; Galliker, P.; Kim, D. K.; Poulikakos, D.; Norris, D. J., Near-Field Light Design with Colloidal Quantum Dots for Photonics and Plasmonics. *Nano Lett.* **2014,** *14*, 5827-5833.
31. Rainò, G.; Becker, M. A.; Bodnarchuk, M. I.; Mahrt, R. F.; Kovalenko, M. V.; Stöferle, T., Superfluorescence from Lead Halide Perovskite Quantum Dot Superlattices. *Nature* **2018,** *563*, 671-675.
32. Cherniukh, I.; Rainò, G.; Stöferle, T.; Burian, M.; Travesset, A.; Naumenko, D.; Amenitsch, H.; Erni, R.; Mahrt, R. F.; Bodnarchuk, M. I.; Kovalenko, M. V., Perovskite-Type Superlattices from Lead Halide Perovskite Nanocubes. *Nature* **2021,** *593*, 535-542.

33. Kress, S. J. P.; Antolinez, F. V.; Richner, P.; Jayanti, S. V.; Kim, D. K.; Prins, F.; Riedinger, A.; Fischer, M. P. C.; Meyer, S.; McPeak, K. M.; Poulikakos, D.; Norris, D. J., Wedge Waveguides and Resonators for Quantum Plasmonics. *Nano Lett.* **2015,** *15*, 6267-6275.
34. Kress, S. J. P.; Cui, J.; Rohner, P.; Kim, D. K.; Antolinez, F. V.; Zaininger, K.-A.; Jayanti, S. V.; Richner, P.; McPeak, K. M.; Poulikakos, D.; Norris, D. J., A Customizable Class of Colloidal-Quantum-Dot Spasers and Plasmonic Amplifiers. *Sci. Adv.* **2017,** *3*, e1700688.

APPENDIX A. SUPPORTING INFORMATION FOR QUANTUM-CUTTING YB^{3+}-DOPED PEROVSKITE NANOCRYSTALS FOR MONOLITHIC BILAYER LUMINESCENT SOLAR CONCENTRATORS

A.1 $CuInS_2$ LSC Layer Modeling

The model described here was developed and validated in a previous report.[1] In this model, the fraction of absorbed photons attenuated by the waveguide, re-absorbed once by the NCs, and emitted into the escape cone are calculated separately using equations A.1, A.2, and A.3, respectively.

$$\mathcal{F} = \frac{1}{4\pi L^2} \iint_{L\times L} \int_0^{2\pi} \int_{\varphi_{esc}}^{\pi-\varphi_{esc}} \int PL_{norm}(\lambda) \frac{\alpha}{\alpha + A_{abs}(\lambda)} (1 - e^{-(\alpha - A_{abs}(\lambda))l(x,y,\theta,\varphi)}) \sin\varphi \, d\lambda d\varphi d\theta dx dy \tag{A.1}$$

$$\mathcal{R} = \frac{1}{4\pi L^2} \iint_{L\times L} \int_0^{2\pi} \int_{\varphi_{esc}}^{\pi-\varphi_{esc}} \int PL_{norm}(\lambda) \frac{A_{abs}(\lambda)}{\alpha + A_{abs}(\lambda)} (1 - e^{-(\alpha - A_{abs}(\lambda))l(x,y,\theta,\varphi)}) \sin\varphi \, d\lambda d\varphi d\theta dx dy \tag{A.2}$$

$$\mathcal{E} = 1 - \sqrt{1 - \frac{1}{n^2}} \tag{A.3}$$

Here, α is the attenuation of the waveguide (0.002 cm^{-1}). From here, the proportion of emitted photons that reach the edge of the LSC without being re-absorbed, attenuated, or emitted through the escape cone is $\mathcal{L} = 1 - \mathcal{F} - \mathcal{R} - \mathcal{E}$. To account for multiple cycles of re-absorption

and emission, the $OQE(L)$ of the $CuInS_2$ NC layer is calculated using an infinite series as follows:

$$OQE(L) = \mathcal{L}\Phi \sum_{i=0}^{\infty} (\mathcal{R}\Phi)^i = \frac{\mathcal{L}\Phi}{1 - \mathcal{R}\Phi} \tag{A.4}$$

A.2 SUPPORTING FIGURES

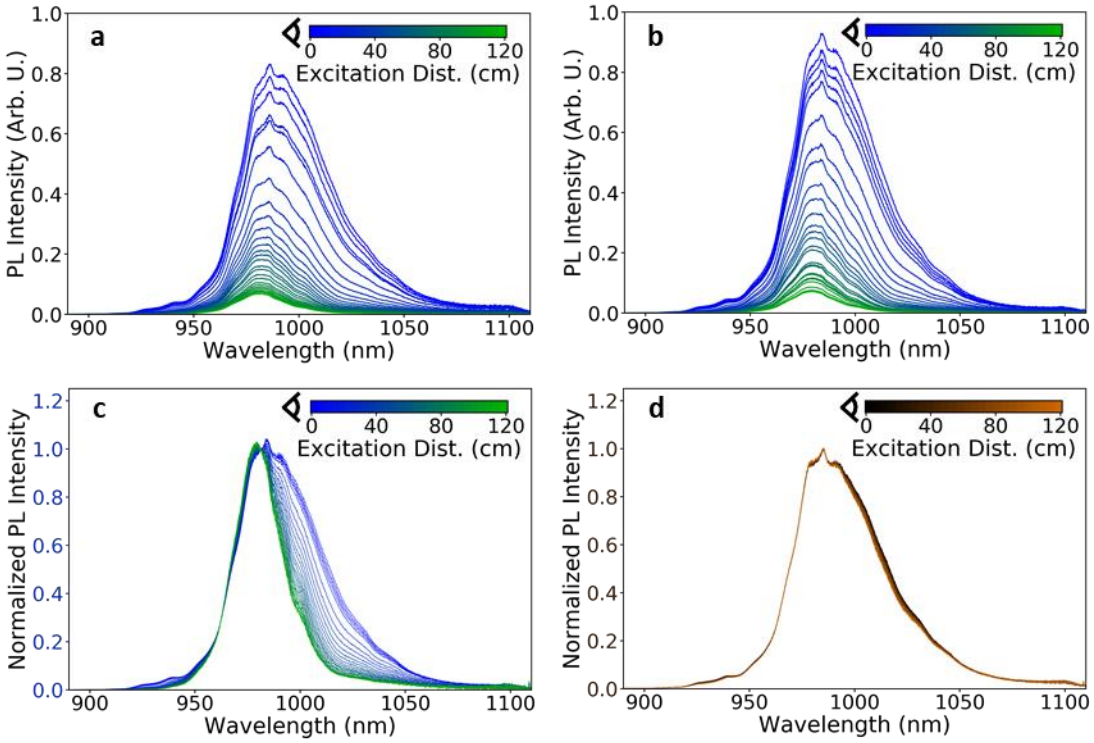

Figure A.1. Additional 1D LSC spectral data. **(a, b)** PL spectra of Yb^{3+}:$CsPbCl_3$ NCs with **(a)** OD_t ~ 0.75 mm^{-1} at 375 nm and **(b)** OD_t ~ 0.075 mm^{-1} at 375 nm, suspended in hexane. Spectra were collected at various excitation distances in the 120 cm 1D LSC. **(c, d)** Normalized PL spectra of Yb^{3+}:$CsPbCl_3$ NCs with OD_t ~ 0.075 mm^{-1} at 375 nm suspended in **(c)** hexane and **(d)** TCE, collected at different excitation distances in the 1D LSC. The insets show the color coding with distance.

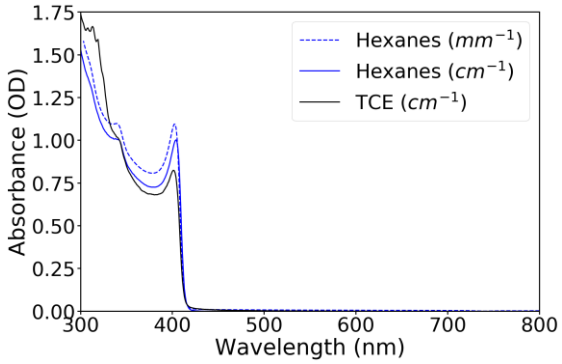

Figure A.2. Absorption spectra of the Yb^{3+}:$CsPbCl_3$ nanocrystals used in the 1D LSC experiment. The blue dashed trace corresponds to the triangles reported in Figure 2.2b, the blue solid trace corresponds to the circles reported in Figure 2.2b, and the solid black trace corresponds to the NCs in TCE shown in Figure 2.3.

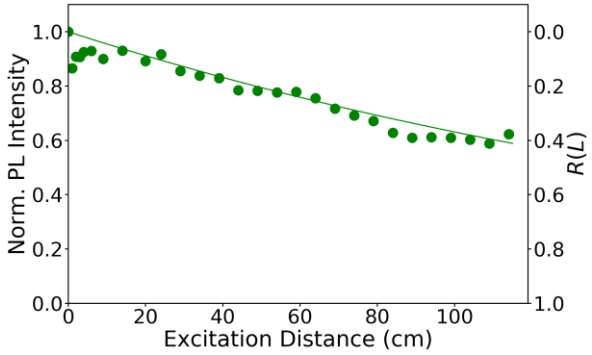

Figure A.3. Waveguide attenuation data plotted as PL intensity *vs* excitation distance. The green curve shows the result of fitting the data using eq 2.1, with a wavelength independent extinction coefficient of 0.002 cm^{-1}.

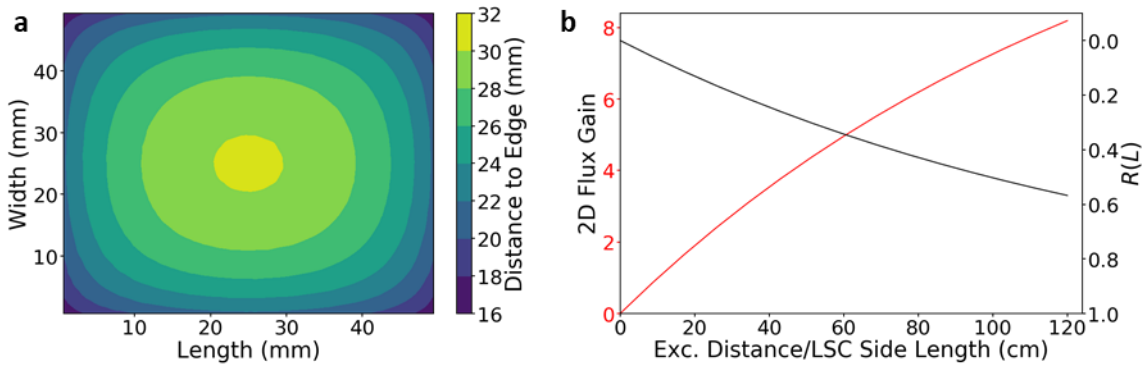

Figure A.4. 1D LSC model validation data. **(a)** Average distance to the edge of a 50 x 50 x 1 mm square from any point in the square. Averaging was performed over polar angles from 42° to 138° and over all azimuthal angles. **(b)** Reabsorption probability and 2D flux gain simulation of an LSC containing $Zn_{0.87}Cd_{0.11}Mn_{0.02}Se/ZnS$ NCs obtained using the same methods developed for the models presented in 0. Both curves are in good agreement with our previous report.[2]

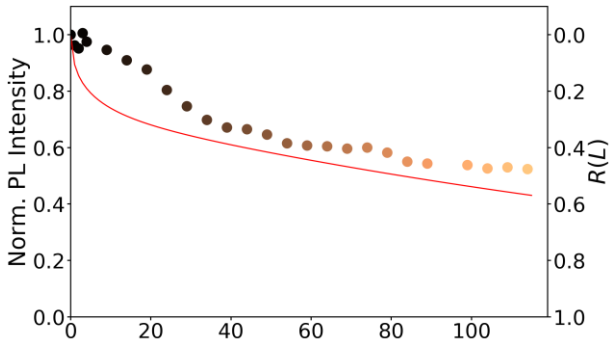

Figure A.5. Integrated PL intensity and reabsorption probability traces for various monolithic LSC materials. Integrated normalized PL intensity of Yb^{3+}:$CsPbCl_3$ NCs plotted as a function of excitation distance in the 1D LSC for solutions in TCE with an OD_t ~ 0.075 mm^{-1} (black-brown). The red trace shows the reabsorption probability as a function of excitation distance for the $CuInS_2/ZnS$ NCs used in modeling, obtained from the absorption and PL spectra shown in Figure 2.5b.

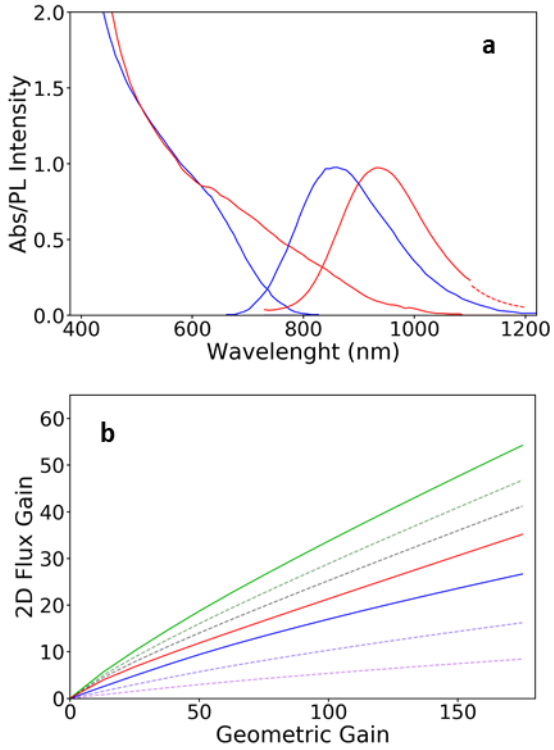

Figure A.6. 2D LSC model comparison for different CuInS2-based materials. Absorption and normalized PL spectra of high-quality CuInS2/ZnS NCs from literature[3] (blue traces) and of QD-950 NCs from the Strem catalog[4] (red traces). PL data above 1100 nm were not provided in ref 4, so the PL intensity below 1100 nm was extrapolated by plotting the PL on an energy x-axis and fitting the available PL data to a gaussian curve. Data extrapolated from the gaussian fit is shown as a dashed red curve. (b) Projected 2D flux gain of an Yb^{3+}:$CsPb(Cl_{1-x}Br_x)_3$ NC LSC (purple to blue gradient), a QD-950 NC LSC with a PLQY of 91% (red), and the monolithic bilayer device shown in Figure 2.5a (black to green gradient), using the QD-950 absorbance and PL intensity data shown in panel (a). The absorption onset of the Yb^{3+}:$CsPb(Cl_{1-x}Br_x)_3$ NCs is varied linearly from 412 to 488 nm for the three plotted traces.

A.3 REFERENCES

1. Sumner, R.; Eiselt, S.; Kilburn, T. B.; Erickson, C.; Carlson, B.; Gamelin, D. R.; McDowall, S.; Patrick, D. L., Analysis of Optical Losses in High-Efficiency $CuInS_2$-Based Nanocrystal Luminescent Solar Concentrators: Balancing Absorption Versus Scattering. *J. Phys. Chem. C* **2017,** *121*, 3252-3260.
2. Bradshaw, L. R.; Knowles, K. E.; McDowall, S.; Gamelin, D. R., Nanocrystals for Luminescent Solar Concentrators. *Nano Lett.* **2015,** *15*, 1315-1323.

3. Bergren, M. R.; Makarov, N. S.; Ramasamy, K.; Jackson, A.; Guglielmetti, R.; McDaniel, H., High-Performance $CuInS_2$ Quantum Dot Laminated Glass Luminescent Solar Concentrators for Windows. *ACS Energy Lett.* **2018,** *3*, 520-525.
4. Copper Indium Disulfide/Zinc Sulfide Quantum Dots. https://www.strem.com/ubiqd.

APPENDIX B. SUPPORTING INFORMATION FOR MODULAR ZWITTERION-FUNCTIONALIZED POLY(ISOPROPYL METHACRYLATE) POLYMERS FOR HOSTING LUMINESCENT LEAD-HALIDE PEROVSKITE NANOCRYSTALS

B.1 PHYSICAL MEASUREMENTS

Nanocrystal (NC) transmission electron microscopy (TEM) images were collected using a FEI TECNAI F20 microscope operated at 200 kV. TEM samples were prepared by drop casting NC suspensions onto carbon-coated copper grids obtained from TED Pella, Inc. Edge length distribution data were collected with ImageJ and uncertainties associated with TEM size distributions are reported as standard deviations. Powder X-ray diffraction (XRD) data were collected using a Bruker D8 Discover diffractometer. Samples were prepared by drop-casting NC suspensions onto monocrystalline silicon wafer substrates. Samples were then irradiated using a high-efficiency IμS microfocus X-ray source for Cu Kα radiation (50 kV, 1 mA) to obtain the reported data. Crystal structures were identified using reference patterns from the Inorganic Crystal Structure Database. Samples for ^{1}H-nuclear magnetic resonance (NMR) measurements were prepared by dissolving zwitterionic polymers in ~0.5 mL acetone-d_6 or methanol-d_4. For the NC/ZP3 NMR sample, a NC/polymer composite was prepared according to

the hexane precipitation procedure described in Section 3.3.4. Once prepared, the sample was dried under vacuum to remove residual solvent and was dispersed in acetone-d_6. Spectra were collected with an AV-300 NMR system operating at a ^{1}H frequency of 300.13 MHz. Raw data from the spectrometer were processed with the SpinWorks v4.2.8 software.

B.2 Spectroscopic Measurements

Absorption spectra of solutions and solid samples were collected at room temperature using Cary 60 and Cary 500 spectrometers, respectively. Photoluminescence (PL) spectra were collected using a homebuilt setup with 365 nm diode excitation and an Ocean Optics 2000+ USB photodetector. Spectra were calibrated with an Ocean Optics deuterium-tungsten halogen light source. Time-resolved PL (TRPL) measurements were collected at room temperature using an Edinburgh FLS1000 spectrometer and pulsed excitation was provided by a 405 nm Edinburgh picosecond laser. Emission from the samples was collected through a monochromator-coupled PMT detector. PLQY measurements in the visible regime were performed with a Hamamatsu integrating sphere quantum-yield measurement system with 450-nm excitation. Solution-state PLQYs were collected at various concentrations due to the dependence of PLQY on ligand concentration.[1] These concentrations are summarized by an absorption percentage, which is calculated by comparing the integrated excitation light intensity for a given NC concentration with the integrated excitation light intensity for a blank cuvette filled with solvent. For as-synthesized NCs and solvated NC/ZFP3 samples, Chapter 3 reports PLQYs of the highest and lowest concentration samples, respectively. Yb^{3+} PL was collected through an integrating sphere using a monochromator coupled to a spectrally corrected nitrogen-cooled CCD. Relative PL calibration was performed according to procedures described previously.[2] PL microscope images were collected with a Nikon Eclipse LV150N digital microscope. A 450 nm excitation source

was focused onto the sample with a 50x objective lens, and the resultant PL was imaged with a CCD camera.

B.3 PL Lifetime Analysis

Raw PL decay curves were first normalized at their maxima and were then fit to the following model:[3-4]

$$I(t) = \sum_{i=0}^{n} A_i e^{-\frac{t}{\tau_i}} \tag{B.1}$$

where $I(t)$ is the number of photon counts as a function of pulse delay time, A_i is the amplitude of a decay component with a lifetime of τ_i, and *n* is the number of exponents used in the fit. The data were fit using a custom Python scrip employing the SciPy software package. Once fit, the average weighted lifetime was calculated using the following equation:[5-6]

$$\tau_{avg} = \frac{\sum_{i=0}^{n} A_i {\tau_i}^2}{\sum_{i=0}^{n} A_i \tau_i} \tag{B.2}$$

B.4 Stability Under Illumination

NC stabilities under illumination were measured using a Chanzon, 50 W, 450 nm LED light source attached to a heat sink and cooled with a 12V DC fan. The LED warmed up for 15 min before use and was separated from the sample by a large shutter to ensure that the entire sample was uniformly illuminated. The LED power was adjusted to provide an irradiance of ~90 mW cm^{-2}, which was measured with a Coherent energy meter through a 1 mm diameter pinhole. PL data for these stability measurements were collected using a fiber-coupled ASEQ instruments LR1-T spectrometer. The spectrometer was operated in continuous mode with spectra collected every 3 s for the first 20 min and every 5 min for the remainder of the experiment. Spectra were

integrated from 525 to 550 nm and 600 to 800 nm for $CsPbBr_3$ and $CsPbI_3$ NCs, respectively, to determine PL intensity as a function of illumination time.

B.5 SUPPORTING FIGURES

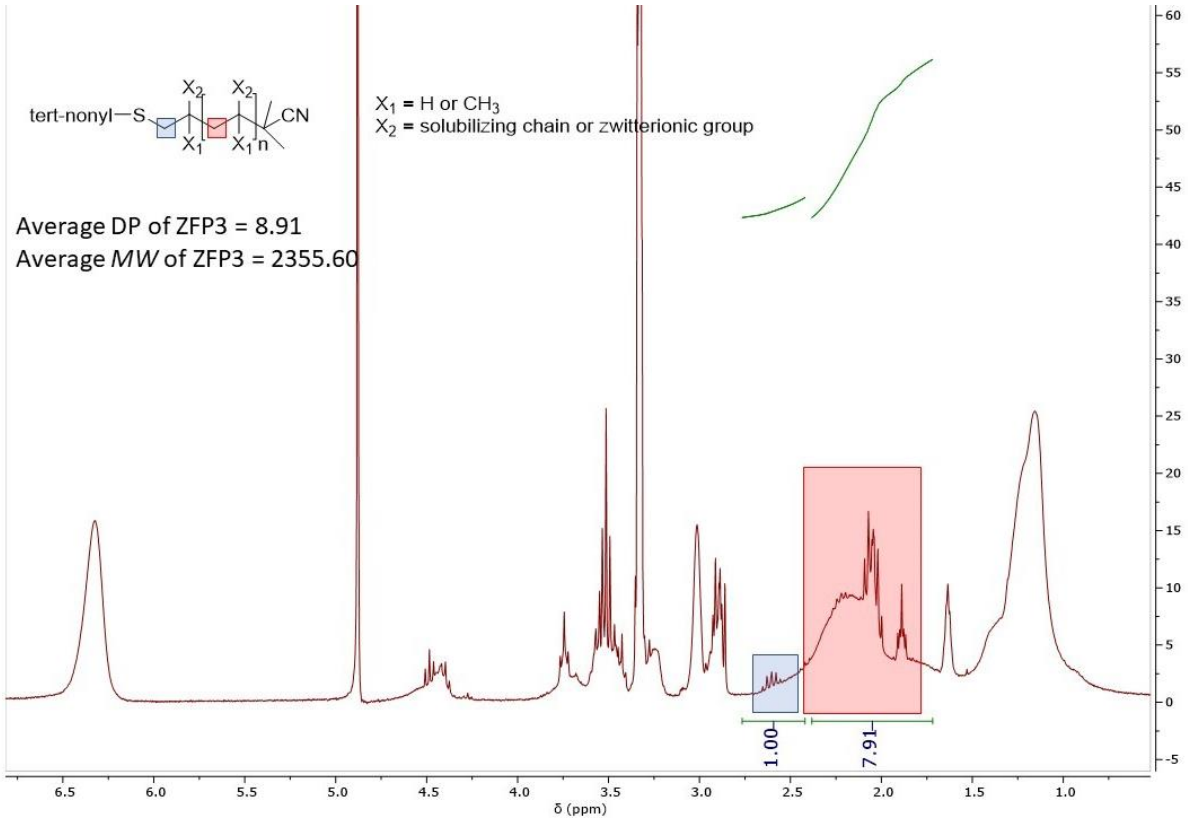

Figure B.1. NMR spectrum of ZFP3 in methanol-d_4 measured at room temperature. The NMR peaks used to calculate degree of polymerization (DP) and molecular weight (MW) are highlighted.

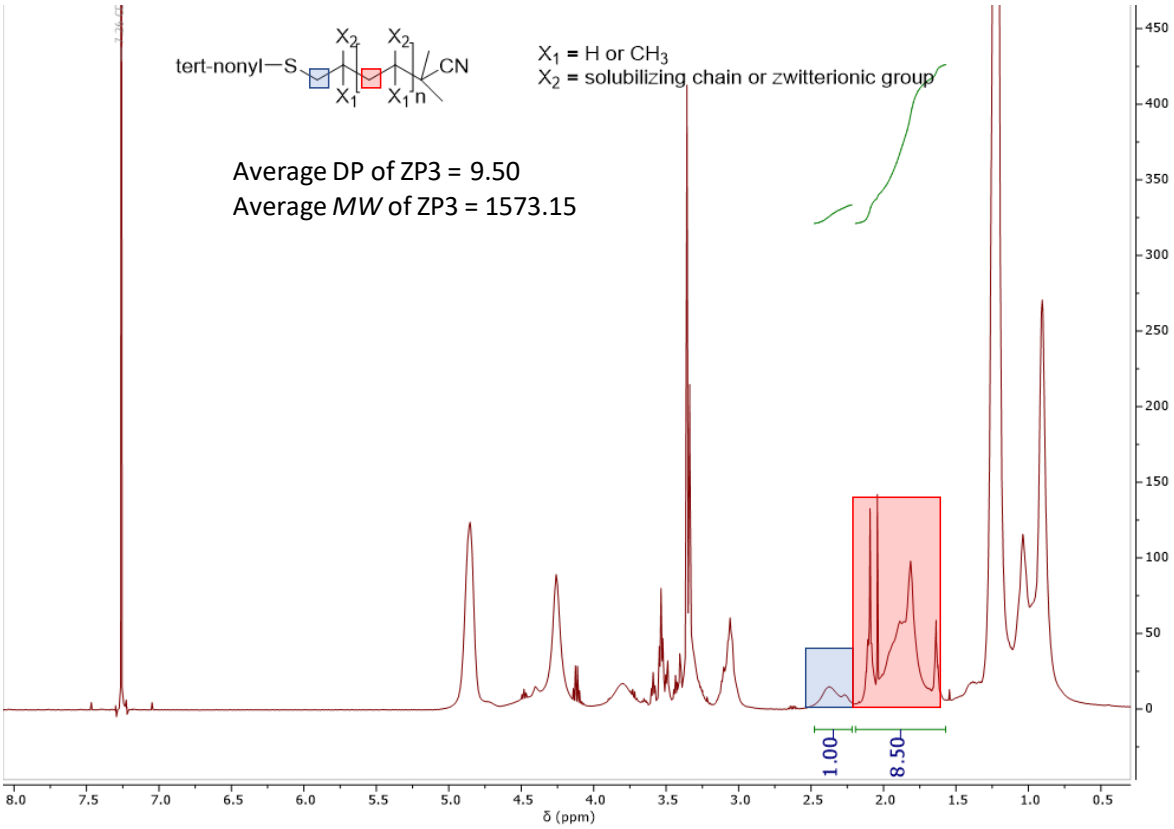

Figure B.2. NMR spectrum of ZP3 in methanol-d_4 measured at room temperature. The NMR peaks used to calculate degree of polymerization (DP) and molecular weight (MW) are highlighted.

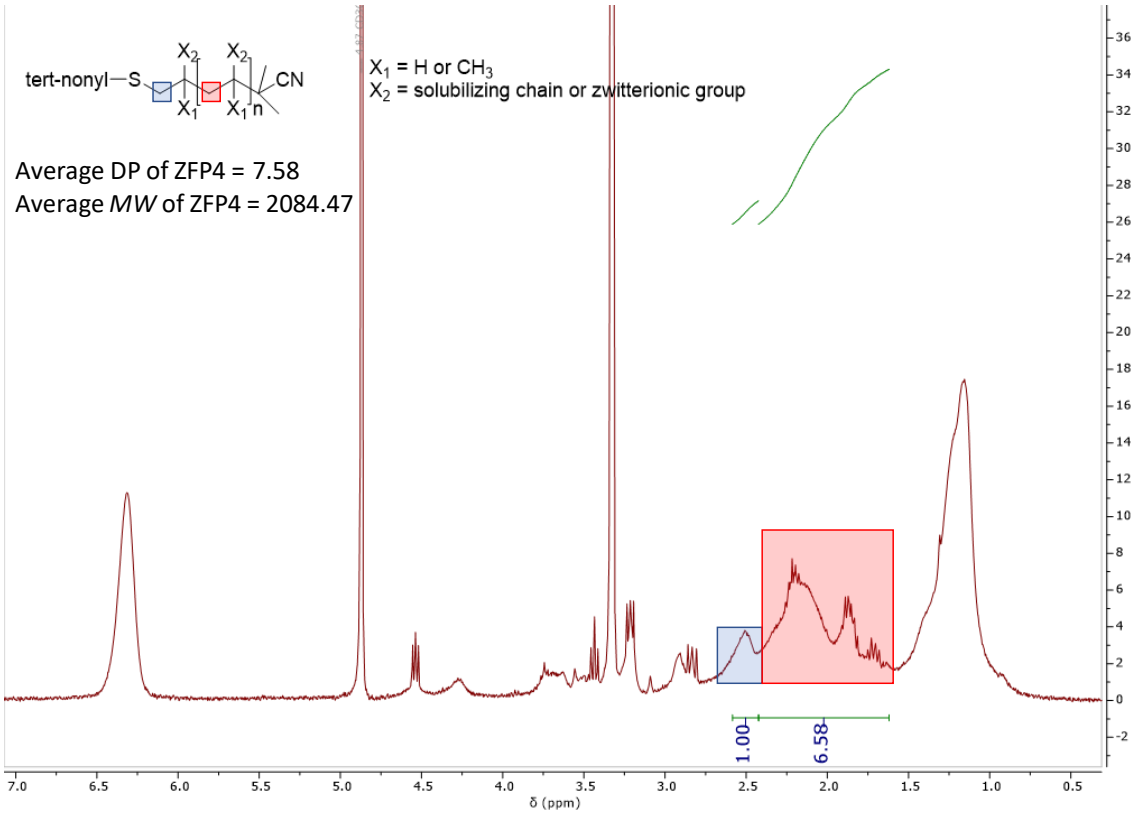

Figure B.3. NMR spectrum of ZFP4 in methanol-d_4 measured at room temperature. The NMR peaks used to calculate degree of polymerization (DP) and molecular weight (MW) are highlighted. This polymer was not used in this work because it was not soluble in ethyl or butyl acetate.

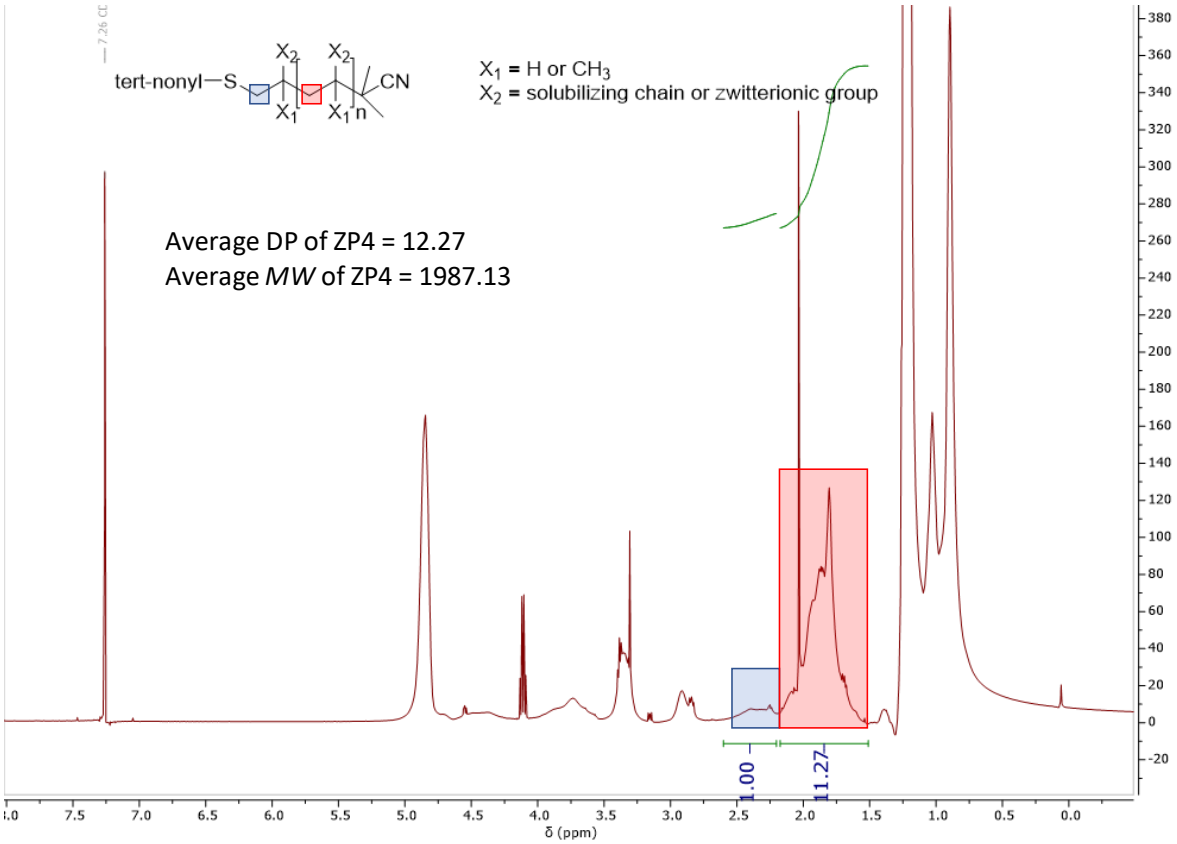

Figure B.4. NMR spectrum of ZP4 in methanol-d_4 measured at room temperature. The NMR peaks used to calculate degree of polymerization (DP) and molecular weight (MW) are highlighted.

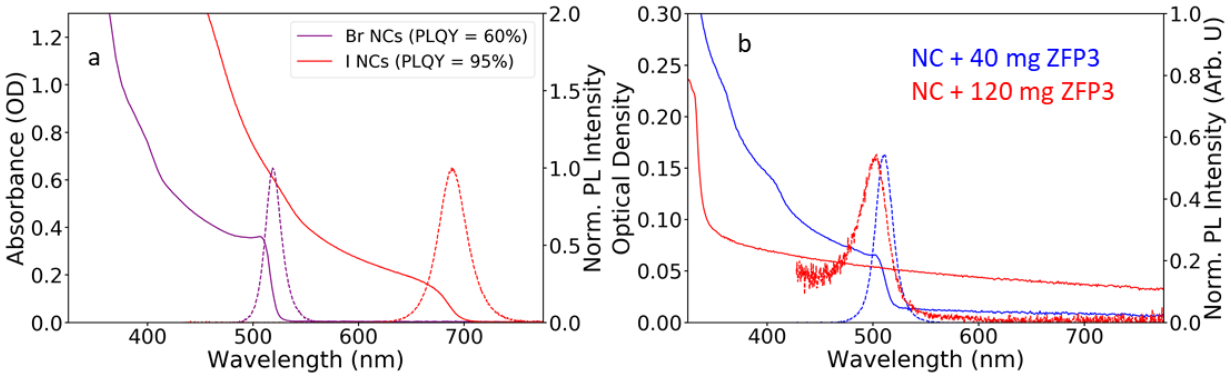

Figure B.5. Initial characterization of perovskite NCs for zwitterionic polymer studies. **(a)** Absorption and PL spectra of as-synthesized $CsPbBr_3$ and $CsPbI_3$ NCs. Solution-state PLQY values are provided in the legend. **(b)** Absorption spectra of $CsPbBr_3$ NCs in the hexane supernatant after purification of the NC/ZFP3 composite from ethyl acetate. When less ZFP3 is used, a small amount of NCs are present in the supernatant, and the majority of the NCs precipitate as a NC/ZFP3 composite. When more ZFP3 is used, almost all NCs are transferred into the composite.

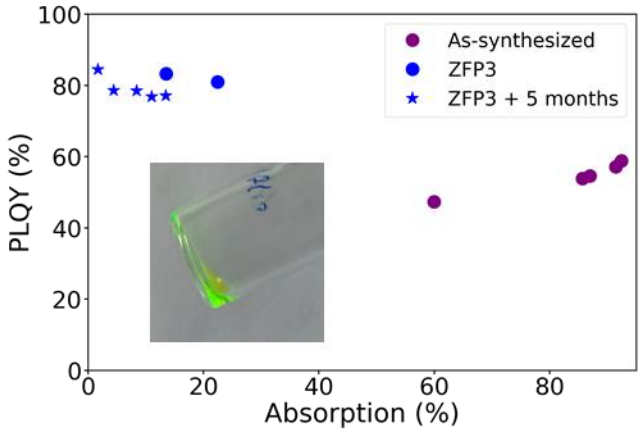

Figure B.6. PLQY as a function of absorption percentage of as-synthesized $CsPbBr_3$ NCs in hexanes and after transfer into a ZFP3 composite in butyl acetate at room temperature. As-synthesized NC solutions needed to be stored in a N_2-filled glovebox, while NC/ZFP3 solutions did not. *Inset:* Photograph of $CsPbBr_3$ NC/ZFP3 solution after 5 months of dark, ambient storage.

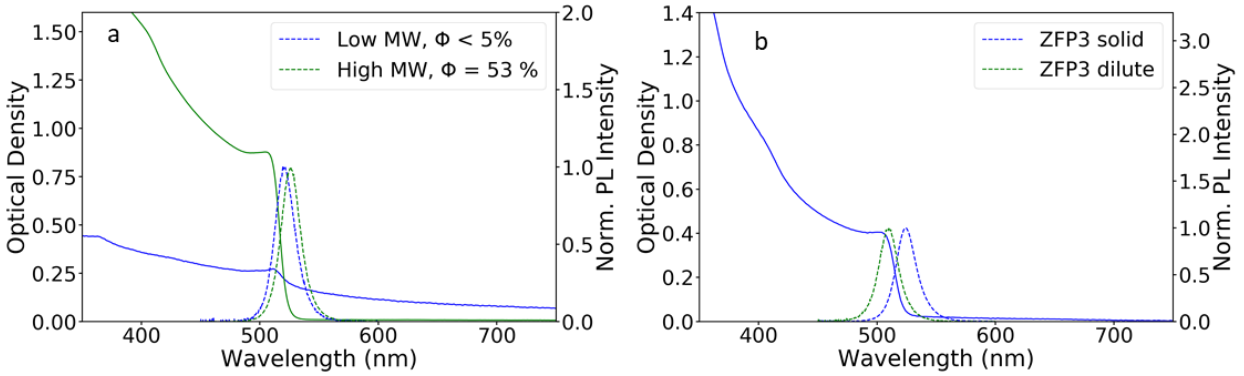

Figure B.7. Polymer dependent characterization of perovskite NCs. **(a)** Absorption and PL spectra of $CsPbBr_3$ NC/PMMA composites. Aggregation was observed when the toluene evaporated from a drop-cast solution of NCs and low-molecular-weight (MW) PMMA, but aggregation was not observed when high-MW PMMA was used. **(b)** Absorption spectrum of a representative high-concentration NC/ZFP3 composite and PL spectra of a representative NC/ZFP3 composite drop cast from high- and low-concentration solutions of butyl acetate. Reabsorption-induced red-shifts were observed for all samples analyzed in this work.

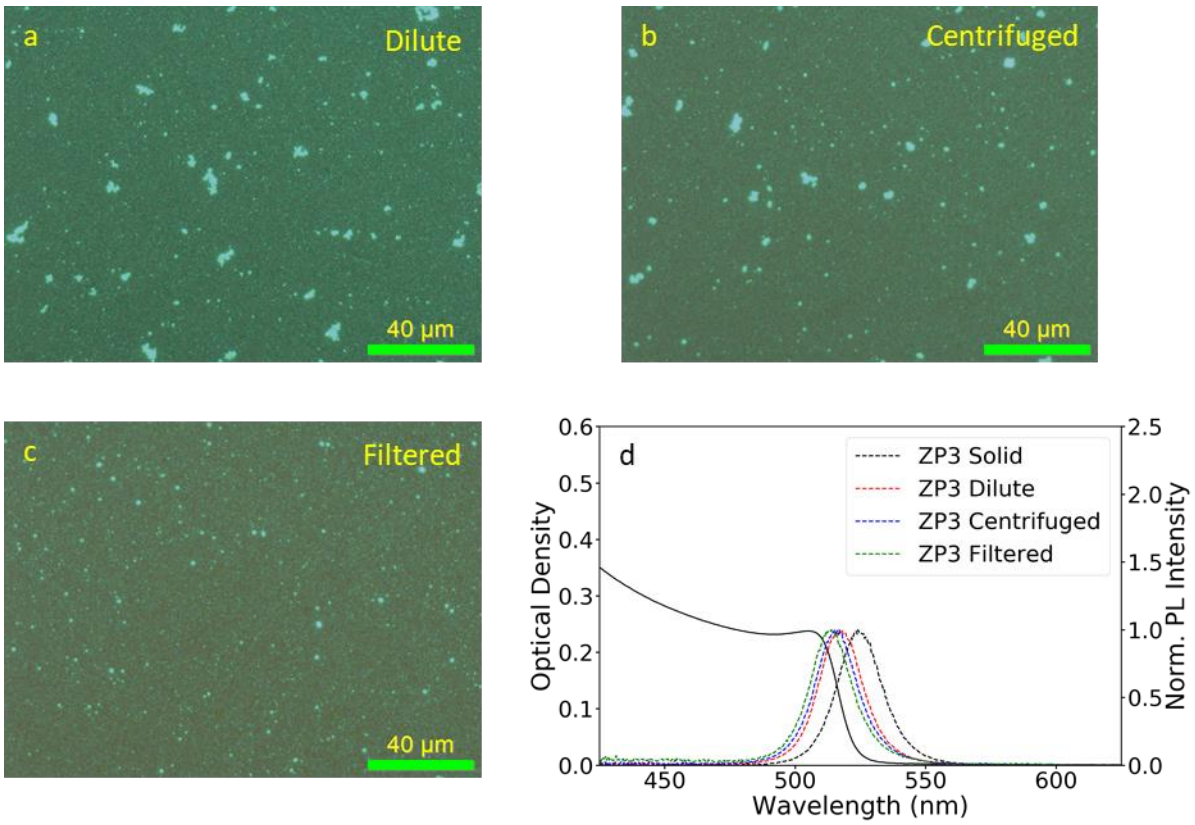

Figure B.8. PL microscope and PL characterization of $CsPbBr_3$ NC/ZP3 composites. PL microscope images of representative solid-state $CsPbBr_3$ NC/ZP3 composites after **(a)** dilution of the original NC/ZP3 butyl acetate solution by a factor of 50, **(b)** centrifugation of the diluted NC/ZP3 solution, and **(c)** filtering of the centrifuged, diluted NC/ZP3 solution through a 0.22 μm PTFE syringe filter prior to drop casting. The processes of centrifugation and filtering successfully removed large aggregates from these composites. **(d)** Absorption and PL spectra of a high-optical density $CsPbBr_3$ NC/ZP3 composite film plotted with the PL spectra of the three low-optical density films shown in panels a-c. The slight blue shift observed after centrifugation and filtration suggests that a small fraction of the PL redshifts observed in these samples can be attributed to aggregation, but reabsorption is the main contributor to the observed PL redshifts for high-optical density samples.

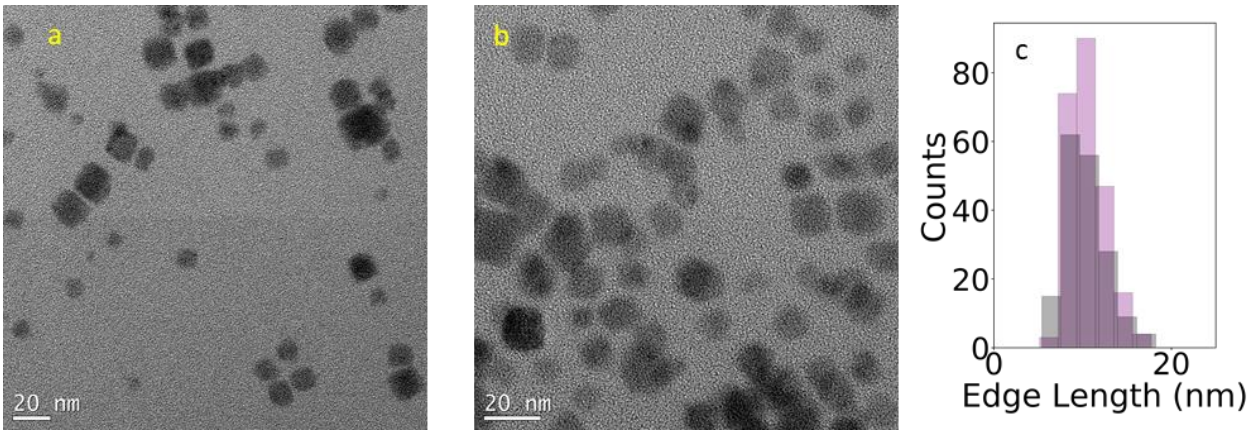

Figure B.9. Additional TEM characterization of $CsPbBr_3$ NC/ZP3 composites. **(a,b)** TEM images of $CsPbBr_3$ NCs drop cast from a butyl acetate solution of NC/ZP3 composite. These images were used to acquire additional data for analysis of particle size distributions. **(c)** Histogram of edge lengths from the TEM images shown in panels a,b and Figure 3.2c,d.

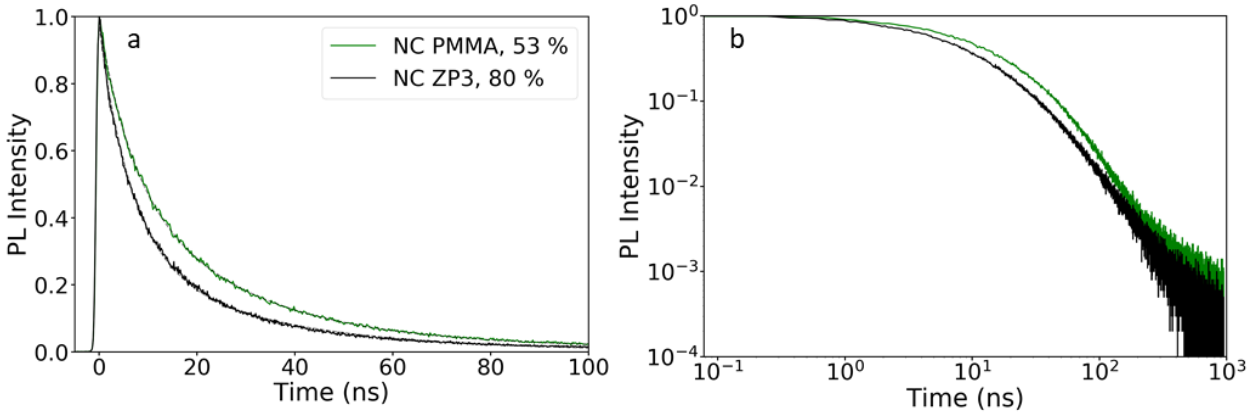

Figure B.10. PL lifetime analysis of various $CsPbBr_3$ NC composites. **(a)** PL decay curves measured in ambient conditions with 405 nm excitation for $CsPbBr_3$ NCs in a PMMA and a ZP3 composite, normalized at $t = 0$. Gray dashed traces correspond to the result of biexponential and triexponential decay fits for NCs in ZP3 and PMMA composites, respectively. **(b)** Log – log plot of the PL decay data shown in panel (a). These data appear to follow a power-law relationship at long times after the excitation pulse, suggesting the presence of delayed exciton luminescence due to reversible trapping.[4, 6-9]

Table B.2. Fitting parameters from fits to the PL lifetime data shown in Figure B.10a.

parameter	PMMA	ZP3
τ_1	6.3 ns	6.8 ns
$\%\tau_1$	42.1 %	70.9 %
τ_2	23.7 ns	31.1 ns
$\%\tau_2$	54.3 %	29.1 %
τ_3	111 ns	
$\%\tau_3$	3.5 %	
τ_{avg}	39.3 ns	22.7 ns

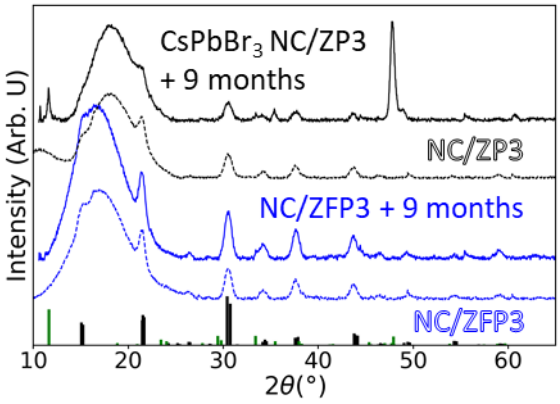

Figure B.11. XRD data for $CsPbBr_3$ NCs in ZFP3 and ZP3 composites collected after preparation and after 9 months of dark storage. The additional peaks that appear in the NC/ZP3 data after 9 months index to the $CsPb_2Br_5$ crystal structure (PDF-254290, green bars) rather than the $CsPbBr_3$ crystal structure (PDF-97851, black bars). Despite the appearance of $CsPb_2Br_5$, the PLQYs of the NCs in ZFP3 and ZP3 remained constant at 59 and 85%, respectively after 1 year of dark storage.

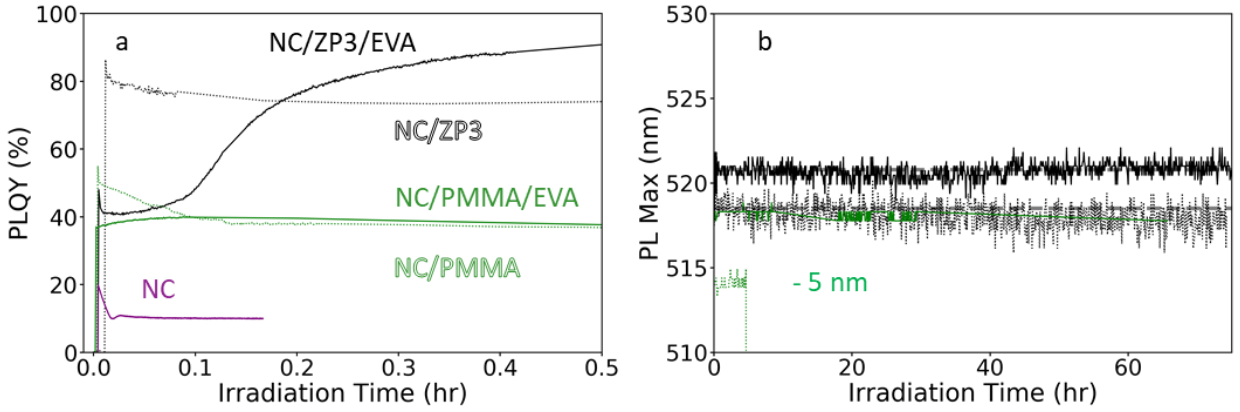

Figure B.12. Additional characterization from $CsPbBr_3$ NC irradiation stability measurements. **(a)** PLQYs measured during illumination of the $CsPbBr_3$ NC/ZP3 and NC/PMMA composites with and without EVA encapsulation from Figure 3.3d and of unencapsulated, drop-cast films of NCs, plotted over the first half hour. Photobrightening is observed in encapsulated samples over the first 40 min of irradiation. **(b)** PL maximum as a function of illumination time for laminated and non-laminated samples from panel (a). There is very little shift in the PL maxima in all cases. The PL maximum for the NCs in PMMA without EVA encapsulation has been artificially shifted down by 5 nm for ease of viewing.

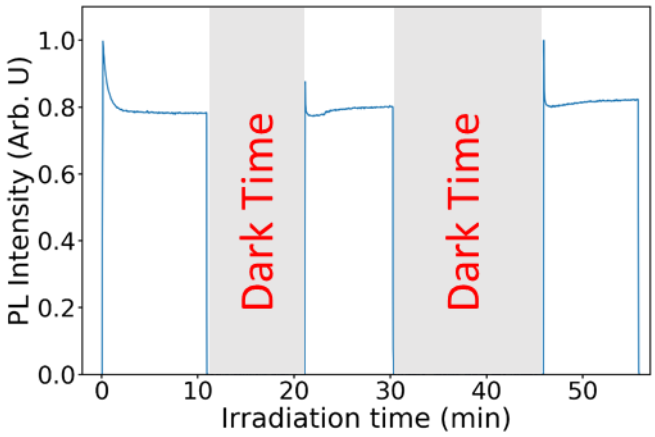

Figure B.13. PL intensity of a $CsPbBr_3$ NC/ZP3 composite plotted as a function of illumination time. The LED shutter was periodically opened and closed to demonstrate that the PL intensities can fully recover after a short amount of dark recovery time but then decay again with continued illumination.

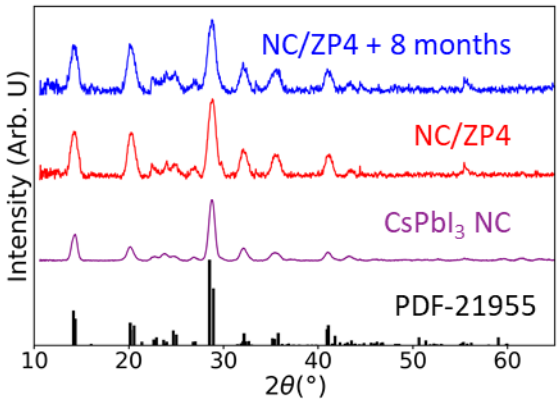

Figure B.14. XRD data for $CsPbI_3$ NCs in their as-synthesized and NC/ZP4 composite forms. XRD data were collected for the same NC/ZP4 composite following preparation and again after 8 months of dark storage. Both measurements show peaks that are consistent with the γ-cubic $CsPbI_3$ phase. The FWHM of the peak at 28° increases by about 0.155° (from 0.742° to 0.897°) upon formation of the NC/ZP4 composite, suggesting that the nanocrystals may be slightly etched by the polymer transfer process. Neither the crystal structure nor the FWHM appears to change substantially after 8 months of dark storage. The PLQY of the NC/ZP4 composite was 60% after 1 year of dark storage.

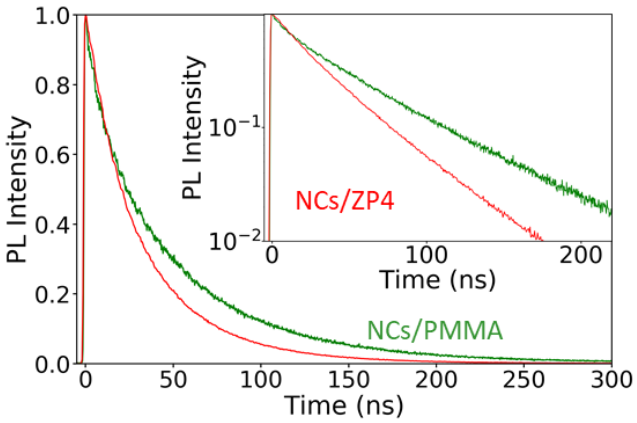

Figure B.15. PL lifetime comparisons of $CsPbI_3$ NC/polymer composites. PL decay curves measured in ambient conditions with 405 nm excitation for $CsPbI_3$ NCs in ZP4 and PMMA composites shown in Figure 3.4, normalized at $t = 0$. *Inset*: PL decay curves plotted on a log scale.

Table B.3. Fitting parameters from various fits to the PL decay data shown in Figure B.15.

parameter	PMMA	ZP4
τ_1	12.5 ns	32.3 ns
$\%\tau_1$	29.8 %	100 %
τ_2	58.8 ns	
$\%\tau_2$	70.1 %	
τ_{avg}	55.0 ns	32.3 ns

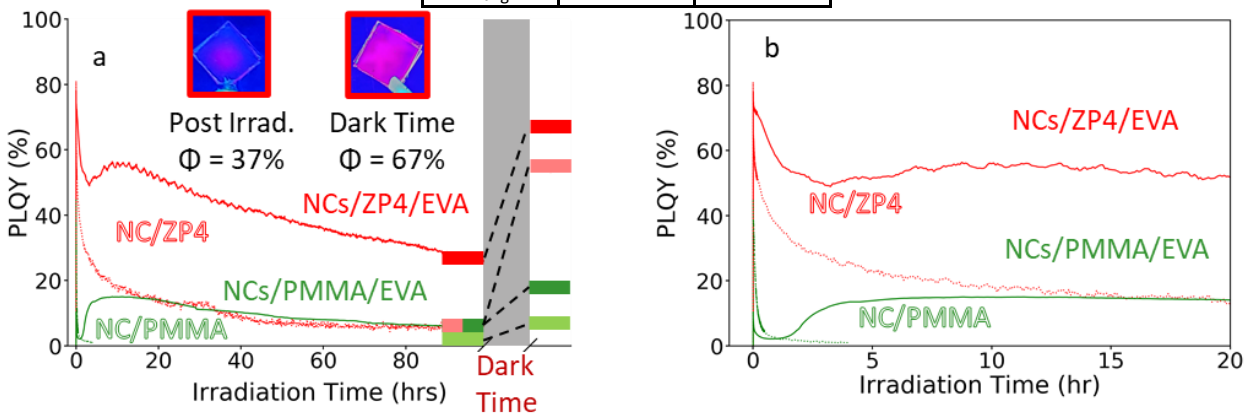

Figure B.16. Irradiation stability measurements of $CsPbI_3$ NC/polymer composites. **(a)** PLQY as a function of 450 nm, ambient irradiation time for $CsPbI_3$ NC/ZP4 and NC/PMMA composites with and without EVA encapsulation. The PLQY values measured before and after dark storage are indicated as horizontal bars. *Inset*: Photographs of an EVA-laminated $CsPbI_3$ NC/ZP4 composite taken immediately after irradiation and after 2 months of dark storage under ambient conditions. PLQYs are provided below each image**. (b)** PLQY as a function of 450 nm, ambient irradiation time for NC/ZP4 and NC/PMMA composites with and without EVA, plotted over the first 20 hrs of irradiation.

Figure B.16a,b show that the PLQY of the $CsPbI_3$ NC/ZP4 composite is better preserved under irradiation than the PLQY of the NC/PMMA composite. Furthermore, the PLQY of the NC/ZP4 composite recovers to 67% of its original value after 14 days of dark storage, whereas that of the NC/PMMA sample only recovers to 16% of its original value after dark storage. To understand the role of air in the NC photodegradation, we also laminated $CsPbI_3$ NC/ZP4 and $CsPbI_3$ NC/PMMA composites with EVA, and PL results from these laminated composites under irradiation are included in Figure B.16a,b. The PLQY of the NC/ZP4 composite remains

high (~80%) immediately following lamination, whereas that of the NC/PMMA composite drops to only ~10% after lamination. Under illumination, the PLQYs of both composites are better preserved when encapsulated in EVA, suggesting that exposure to a combination of air and light is responsible for the decreases in PLQY observed here. The photographs in Figure S16a show that the NCs at the edges of the EVA-laminated $CsPbI_3$ NC/ZP4 composite degrade first, confirming that water and/or oxygen diffuses inward from the edges of the laminated composite to degrade the NCs while they are irradiated. A PLQY of 37% was measured 1 day after irradiation. Interestingly, we found that even these edge NCs recover their luminescence, returning the PLQY of the entire $CsPbI_3$ NC/ZP4/EVA composite to 52% after 10 days of dark storage and 67% after 50 days of dark storage. These results suggest that NC PLQY recovery requires both dark storage time *and* air exposure. The $CsPbI_3$ NC/PMMA/EVA composite recovers some PLQY within the first few hours of irradiation and recovers its PLQY after dark storage, but its absolute PLQY remains low.

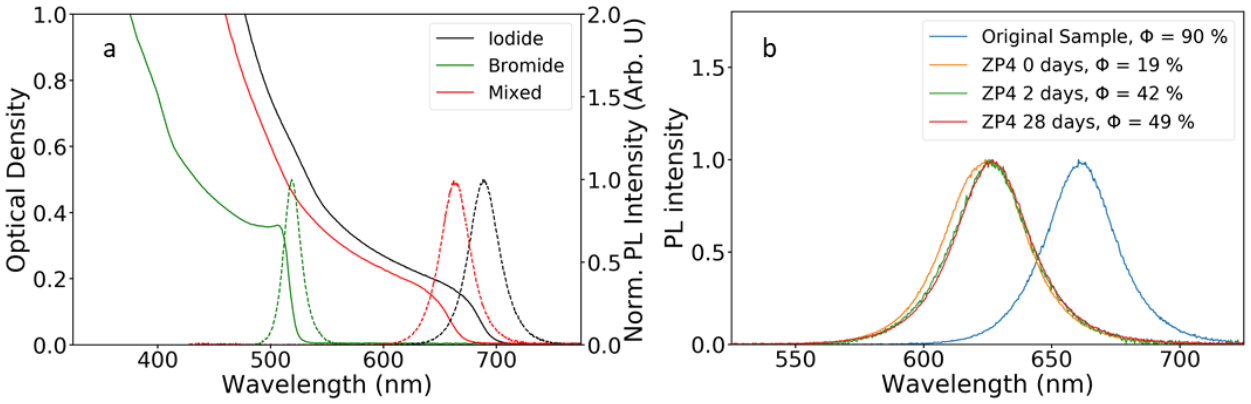

Figure B.17. Mixed iodide-bromide NC characterization. **(a)** Absorption and PL spectra of $CsPbI_3$ (black) and $CsPbBr_3$ (green) NCs in hexanes solutions. Aliquots of these solutions were combined to yield mixed $CsPb(Br_{1-x}I_x)_3$ NCs (red). **(b)** PL spectra of the as-synthesized $CsPb(Br_{1-x}I_x)_3$ NCs and the same NCs in a ZP4 composite. Transfer into ZP4 was accompanied by a 50 nm blue shift, but the PLQY remained high after nearly a month of dark storage.

Table B.4. Summary of publications that report successful stabilization of $CsPbI_3$ or $CsPb(Br_{1-x}I_x)_3$ NCs in solid composites. The solid-state PLQYs of these composites are also provided.

ref.	Matrix description	Used for $CsPbI_3$ NCs (x = 1)	PLQY (%)
Di Stasio et al.[10]	$PbBr_2$ treated, anion exchanged film	yes	31
Li et al.[11]	silica microsphere bound	no	35
Cai et al.[12]	poly(2-ethyl-2-oxazoline)	no	45
Xuan et al.[13]	porous organic polymer network	yes	37
Wei et al.[14]	epoxy resin composite	yes	17
Zhang et al.[15]	polymer microsphere precipitation	no	40
Chen et al.[16]	PMMA	yes	48
Zhang et al.[17]	$CsPbI_3$:$CsPbCl_3$ NC glass	yes	45
Wu et al.[18]	Triphenyl phosphine treated film	yes	99

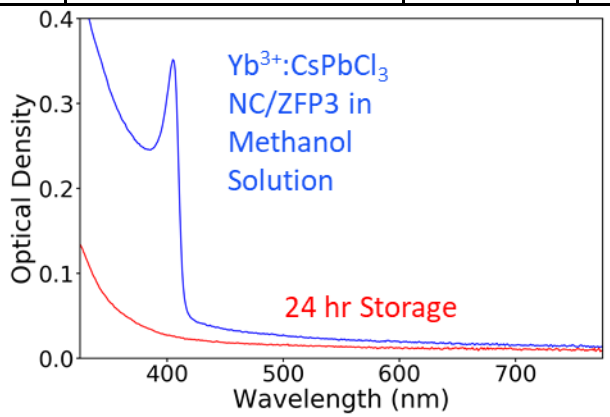

Figure B.18. Solvent stability assessment of ZFP3-stabilized NCs. Absorption spectra of Yb^{3+}:$CsPbCl_3$ NC/ZFP3 composites suspended in methanol initially and after 24 hours of dark ambient storage. The NCs degraded in the presence of methanol. No comparable degradation is observed when butyl acetate is used as the solvent instead of methanol.

B.6 References

1. Nenon, D. P.; Pressler, K.; Kang, J.; Koscher, B. A.; Olshansky, J. H.; Osowiecki, W. T.; Koc, M. A.; Wang, L.-W.; Alivisatos, A. P., Design Principles for Trap-Free $CsPbX_3$

Nanocrystals: Enumerating and Eliminating Surface Halide Vacancies with Softer Lewis Bases. *J. Am. Chem. Soc.* **2018,** *140*, 17760-17772.

2. Milstein, T. J.; Kroupa, D. M.; Gamelin, D. R., Picosecond Quantum Cutting Generates Photoluminescence Quantum Yields over 100% in Ytterbium-Doped $CsPbCl_3$ Nanocrystals. *Nano Lett.* **2018,** *18*, 3792–3799.
3. Makarov, N. S.; Guo, S.; Isaienko, O.; Liu, W.; Robel, I.; Klimov, V. I., Spectral and Dynamical Properties of Single Excitons, Biexcitons, and Trions in Cesium–Lead-Halide Perovskite Quantum Dots. *Nano Lett.* **2016,** *16*, 2349-2362.
4. Utzat, H.; Shulenberger, K. E.; Achorn, O. B.; Nasilowski, M.; Sinclair, T. S.; Bawendi, M. G., Probing Linewidths and Biexciton Quantum Yields of Single Cesium Lead Halide Nanocrystals in Solution. *Nano Lett.* **2017,** *17*, 6838-6846.
5. Sillen, A.; Engelborghs, Y., The Correct Use of "Average" Fluorescence Parameters. *Photochem.* **1998,** *67*, 475-486.
6. Chirvony, V. S.; González-Carrero, S.; Suárez, I.; Galian, R. E.; Sessolo, M.; Bolink, H. J.; Martínez-Pastor, J. P.; Pérez-Prieto, J., Delayed Luminescence in Lead Halide Perovskite Nanocrystals. *J. Phys. Chem. C* **2017,** *121*, 13381-13390.
7. Rabouw, F. T.; van der Bok, J. C.; Spinicelli, P.; Mahler, B.; Nasilowski, M.; Pedetti, S.; Dubertret, B.; Vanmaekelbergh, D., Temporary Charge Carrier Separation Dominates the Photoluminescence Decay Dynamics of Colloidal CdSe Nanoplatelets. *Nano Lett.* **2016,** *16*, 2047-2053.
8. Marchioro, A.; Whitham, P. J.; Knowles, K. E.; Kilburn, T. B.; Reid, P. J.; Gamelin, D. R., Tunneling in the Delayed Luminescence of Colloidal CdSe, Cu^+-doped CdSe, and $CuInS_2$ Semiconductor Nanocrystals and Relationship to Blinking. *J. Phys. Chem. C* **2016,** *120*, 27040-27049.
9. Rabouw, F. T.; Kamp, M.; van Dijk-Moes, R. J. A.; Gamelin, D. R.; Koenderink, A. F.; Meijerink, A.; Vanmaekelbergh, D., Delayed Exciton Emission and Its Relation to Blinking in CdSe Quantum Dots. *Nano Lett.* **2015,** *15*, 7718-7725.
10. Di Stasio, F.; Christodoulou, S.; Huo, N.; Konstantatos, G., Near-Unity Photoluminescence Quantum Yield in $CsPbBr_3$ Nanocrystal Solid-State Films *via* Postsynthesis Treatment with Lead Bromide. *Chem. Mater.* **2017,** *29*, 7663-7667.
11. Li, X.; Wang, Y.; Sun, H.; Zeng, H., Amino-Mediated Anchoring Perovskite Quantum Dots for Stable and Low-Threshold Random Lasing. *Adv. Mater.* **2017,** *29*, 1701185.
12. Cai, W.; Chen, Z.; Li, Z.; Yan, L.; Zhang, D.; Liu, L.; Xu, Q.-h.; Ma, Y.; Huang, F.; Yip, H.-L.; Cao, Y., Polymer-Assisted *in situ* Growth of All-Inorganic Perovskite Nanocrystal Film for Efficient and Stable Pure-Red Light-Emitting Devices. *ACS Appl. Mater. Interfaces* **2018,** *10*, 42564-42572.
13. Xuan, T.; Huang, J.; Liu, H.; Lou, S.; Cao, L.; Gan, W.; Liu, R.-S.; Wang, J., Super-Hydrophobic Cesium Lead Halide Perovskite Quantum Dot-Polymer Composites with High Stability and Luminescent Efficiency for Wide Color Gamut White Light-Emitting Diodes. *Chem. Mater.* **2019,** *31*, 1042-1047.
14. Wei, S.; Zhu, H.; Zhang, J.; Wang, L.; An, M.; Wang, Y.; Zhang, X.; Liu, Y., Luminescent Perovskite Nanocrystal-Epoxy Resin Composite with High Stability against Water and Air. *J. Alloys Compd.* **2019,** *789*, 209-214.
15. Zhang, C.; He, Z.; Chen, H.; Zhou, L.; Tan, G.; Wu, S.-T.; Dong, Y., Light Diffusing, Down-Converting Perovskite-on-Polymer Microspheres. *J. Mater. Chem. C* **2019,** *7*, 6527-6533.

16. Chen, C.; Li, D.; Wu, Y.; Chen, C.; Zhu, Z.-G.; Shih, W. Y.; Shih, W.-H., Flexible Inorganic $CsPbI_3$ Perovskite Nanocrystal-PMMA Composite Films with Enhanced Stability in Air and Water for White Light-Emitting Diodes. *Nanotechnology* **2020,** *31*, 225602.
17. Zhang, Z.; Shen, L.; Zhao, Y.; Zhang, Y.; Yang, H.; Xiang, W.; Liang, X.; Chen, G.; Yu, H., Coexisting $CsPbCl_3$:$CsPbI_3$ Perovskite Nanocrystal Glasses with High Luminescence and Stability. *Chem. Eng. J.* **2020,** *385*, 123415.
18. Wu, J.; Tong, J.; Gao, Y.; Wang, A.; Zhang, T.; Tan, H.; Nie, S.; Deng, Z., Efficient and Stable Thin-Film Luminescent Solar Concentrators Enabled by near-Infrared Emission Perovskite Nanocrystals. *Angew. Chem. Int. Ed.* **2020,** *59*, 7738-7742.

APPENDIX C. SUPPORTING INFORMATION FOR DIRECT PATTERNING OF PEROVSKITE NANOCRYSTALS ON NANOPHOTONIC CAVITIES WITH ELECTROHYDRODYNAMIC INKJET PRINTING

Reproduced with permission from Cohen, T. A; Sharp, D; Kluherz, K. T; Chen, Y; Munley, C; Anderson, R. T; Swanson, C. S; De Yoreo, J. J; Luscombe, C. K; Majumdar, A; Gamelin, D. R; MacKenzie, J. D. *Nano Letters* **2022**, *Submitted.*

C.1 SPECTROSCOPIC MEASUREMENTS

All measurements were collected at room temperature in ambient conditions, unless otherwise noted. Solution-state nanocrystal (NC) absorption spectra were collected from dilute hexanes NC suspensions using a Cary 60 spectrometer. NC concentrations were determined from absorption spectra using previously published NC extinction coefficients.[1] Solution-state photoluminescence (PL) measurements were performed with a homebuilt setup using filtered 365 nm excitation and an Ocean Optics 2000+ USB photodetector calibrated with an Ocean Optics deuterium-tungsten halogen light source. Drop cast NC PL spectra were collected with an Edinburgh FLS1000 fluorimeter. Samples were prepared by casting and drying 50 µL of purified NC solution in hexanes onto a cleaned monocrystalline silicon substrate in a N_2 filled glovebox. Spectra were collected with 420 nm excitation generated by a monochromator-coupled xenon lamp, and the resultant PL was collected with a monochromator-coupled PMT. PL quantum yields were collected with a Hamamatsu integrating sphere measurement system with 450 nm excitation generated by a monochromator-coupled xenon lamp. PL and dark-field microscope

images were acquired with a Nikon Eclipse LV150N digital microscope. A 450 nm or broadband excitation source was focused onto the sample for PL or dark-field imaging, respectively, and the resulting images were collected through long-pass filters with a CCD camera.

C.2 Physical Measurements

Powder X-ray diffraction (XRD) data were collected with a Bruker D8 Discover diffractometer. NCs in hexanes were drop cast and dried on a monocrystalline silicon substrate. Samples were irradiated with a high-efficiency IμS microfocus X-ray source for Cu Kα radiation (50 kV, 1 mA) and the diffracted X-rays were collected with a Pilatus 100K large-area 2D detector. The resultant 2D diffraction patterns were radially integrated and the backgrounds subtracted to obtain the reported data. Crystal structures were identified according to reference patterns in the Inorganic Crystal Structure Database. Atomic force microscopy (AFM) images were collected with a Bruker Icon AFM operated in tapping mode with an OTESPA-R3 probe. Images were processed and line profiles were extracted using the NanoScopic Analysis software. Optical Profilometry images were collected with an Olympus OLS4100 optical profilometer with a 100x objective lens. Height profiles from images at scratched PMMA edges were used to determine the PMMA layer thickness.

C.3 TEM Image Collection and Analysis

NC scanning transmission electron microscope (STEM) images were obtained using an FEI TECNAI G2 F20 SuperTwin microscope operated at 200 kV. A C2 aperture size of 70 μm was used to reduce the electron dose. Non-printed samples for TEM were prepared by drop casting NCs onto UC-A 400 mesh Cu grids from Ted Pella, Inc. The sample grids were then dried under vacuum overnight. For imaging printed nanocrystals, Si_3N_4 Membrane Window

TEM grids (Ted Pella, 21569-10) were coated with an 11 nm carbon layer using a Leica ACE600 coater. The resulting TEM grids were then placed on top of a secondary silicon substrate that was mounted on the printer bed. Several 100 × 100 μm^2 NC print patterns with 5 μm drop spacing were printed onto the Si_3N_4 window according to the procedures described in the main text. Approximately 1300 individual NCs per sample were sized from STEM images using ImageJ's Analyze Particles tool with a threshold corrected image to obtain the mean NC sizes reported here. Image thresholding was manually checked before applying the particle counting tool.

Electron diffraction patterns were integrated using the Radial Integration Package in ImageJ. A baseline was subtracted from this integrated trace prior to plotting in the main text. XRD data from non-printed NCs and the XRD reference pattern were converted to q space using the following equation:

$$q_{XRD} = \frac{2A}{\lambda_{Cu\ k\alpha}} \sin\theta_{XRD} \tag{C.1}$$

where A is a constant chosen to align the XRD pattern with the electron diffraction pattern.

C.4 Si_3N_4 Nanobeam Cavity Design, Fabrication, and Characterization

Nanobeam cavities were designed and fabricated according to the methods reported previously.[2-3] The Si_3N_4 nanobeam cavity design used here consists of 20 tapered elliptical holes with a period of 157 nm and major and minor diameters of 202 nm and 100 nm, respectively, to form a Bragg region on both sides of the nanobeam. The period and major axis of 10 holes from each side are linearly tapered to the center of the nanobeam, with the innermost elliptical holes having a minimum period and major diameter of 146 nm and 150.4 nm, respectively, with an

edge-to-edge gap of the two innermost holes of 78.3 nm. The nanobeam is 220 nm thick and 450 nm wide. This design generates a fundamental mode at ~520 nm, where $CsPbBr_3$ NCs exhibit the highest PL intensity. This cavity mode has a theoretical Q-factor of ~9,000 and a mode volume of $3(\lambda/n)^3$, where λ is the fundamental cavity mode and n is the cavity cladding refractive index (~1.5 for PMMA and SiO_2).

Cavity-coupled PL was measured with a confocal microscopy set-up. A 405 nm continuous-wave laser (Thorlabs CPS405) was focused on the center of the nanobeam cavity (red circle in Figure 4a) using a 40x (NA 0.6) objective lens to excite the ~517 nm PL. A 450 nm long pass filter was used to filter the pump laser, and a pinhole was used to spatially select the PL from the grating coupler. The PL was detected using a Princeton Instruments Isoplane 160 spectrometer with a 600 lines/mm grating coupled to a Pixis 400 CCD.

C.5 SUPPORTING FIGURES

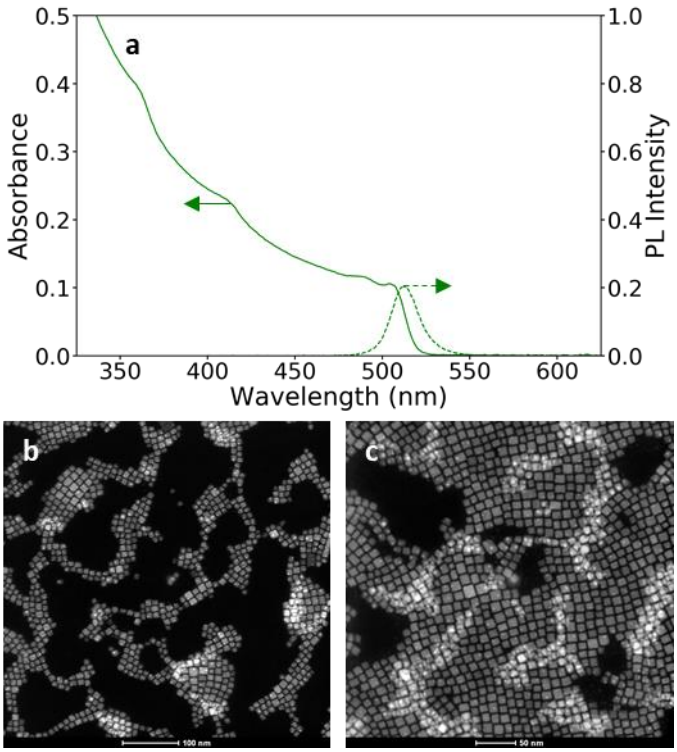

Figure C.1. Optical and structural characterization of as-prepared NCs. **(a)** Solution-state absorption and PL spectra of $CsPbBr_3$ NCs. Solutions were made from a 3000x dilution of the NC ink in hexanes. **(b,c)** TEM images of $CsPbBr_3$ NCs drop cast from hexanes solvent. NC size distributions were obtained from the image in panel c.

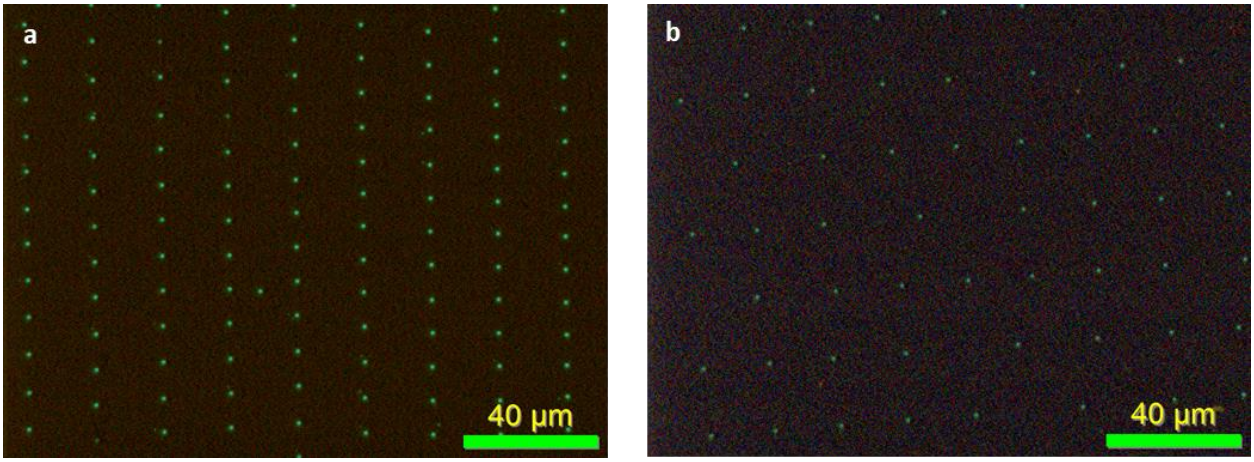

Figure C.2. EHD inkjet printing continuous and ‘bump’ mode comparison. PL microscope images of EHD inkjet-printed NCs printed in **(a)** continuous print mode and **(b)** ‘bump’ mode. Continuous print mode creates droplets that are spaced by a constant distance, whereas ‘bump’ mode produces droplets that are spaced by a predefined distance.

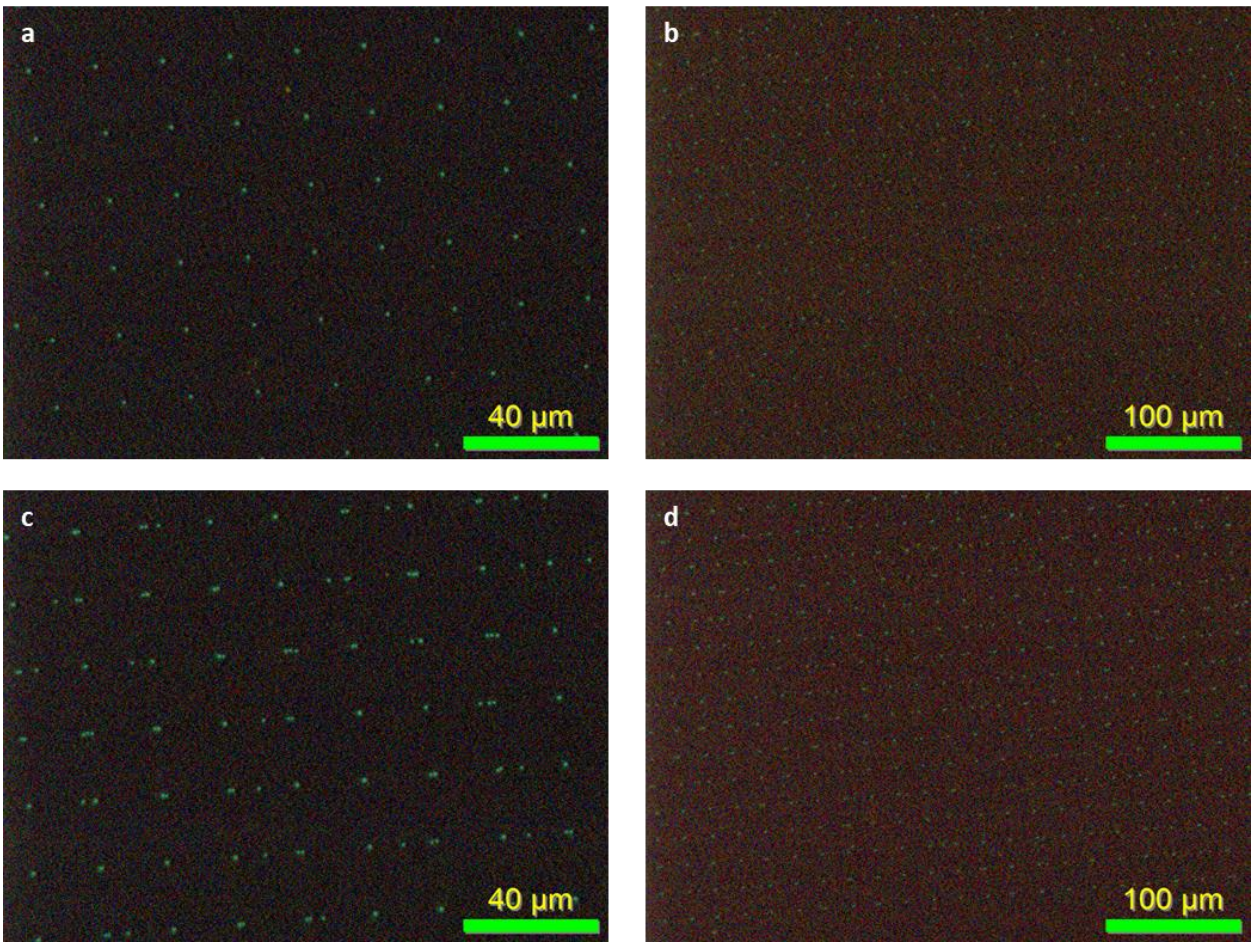

Figure C.3. Parameter optimization for high precision printing. PL microscope images of EHD inkjet-printed NCs spaced by 20 µm and printed with print hold times of **(a,b)** 40 ms and **(c,d)** 70 ms. Low print hold times ensure that fewer off-target droplets are printed, but high print hold times ensure that each on-target print location has a droplet of printed NCs with nearly 100% fidelity. This tradeoff was considered and accounted for in the print patterns presented in Chapter 4.

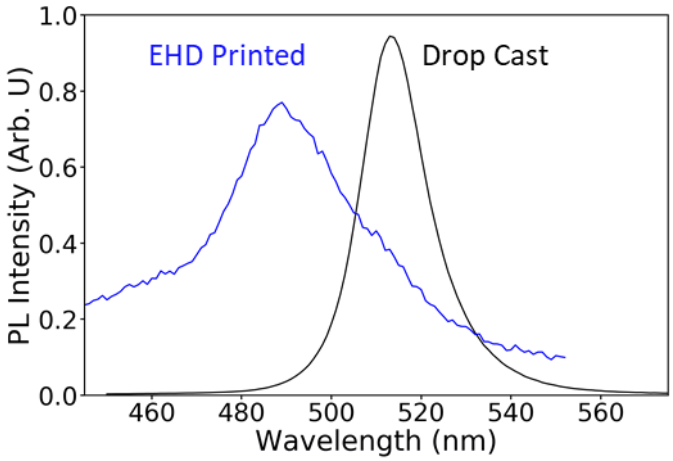

Figure C.4. PL characterization of NCs printed at high voltages. Ensemble PL spectra of $CsPbBr_3$ NCs drop cast from hexanes and EHD inkjet printed at high voltages (750 – 1250 V). A clear blue-shift in the PL maximum is noted when such high voltages are used to drive printing.

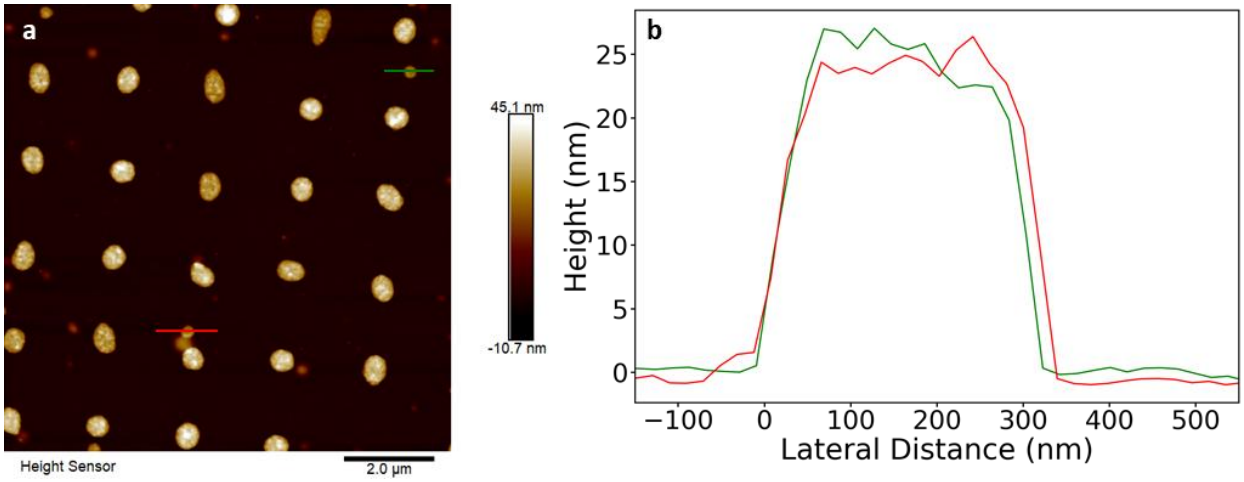

Figure C.5. Large-area AFM characterization. **(a)** Zoomed out AFM image from the print shown in Figure 4.2d of the main text. **(b)** Height profiles from off-target droplets in the AFM image line traces shown in panel a. These droplets have diameters as small as 300 nm.

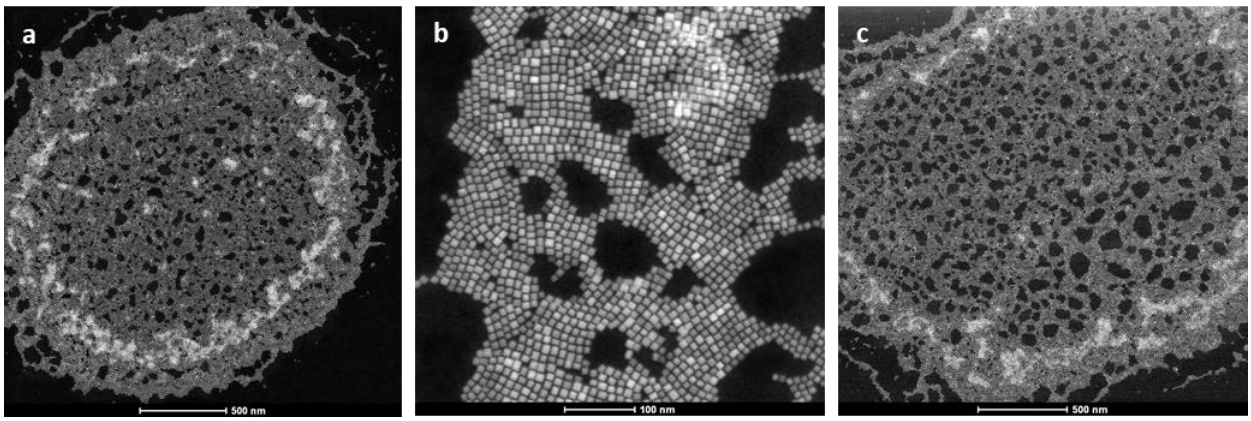

Figure C.6. TEM characterization. **(a-c)** Additional TEM images of EHD inkjet-printed $CsPbBr_3$ NCs. A 'coffee ring' drop shape is visible in panel a,c due to the difference in surface energy between the carbon coated TEM grids used here and the fluorinated SAM coated silicon substrates used elsewhere. Statistics for NC edge length distributions were collected from the image shown in panel b.

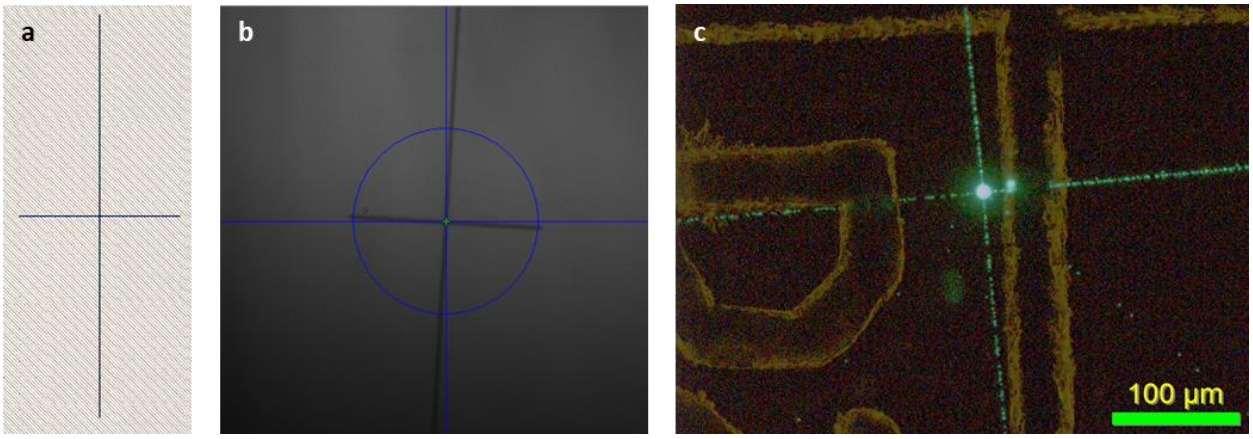

Figure C.7. Demonstration of the EHD printing alignment process. **(a)** Drawing of the alignment marks present at the edges of the nanobeam cavity device substrate. These alignment marks are placed a set distance from the nanobeam cavities, and this distance was used to develop a print pattern to place NCs on the centers of each cavity. **(b)** Alignment camera image of the alignment mark shown in panel a. These marks were used to calibrate the alignment camera location with the substrate. **(c)** PL microscope image of an alignment mark printed with $CsPbBr_3$ NCs. This alignment mark was located with the alignment camera and was used to calibrate the alignment camera location with the location of the nozzle.

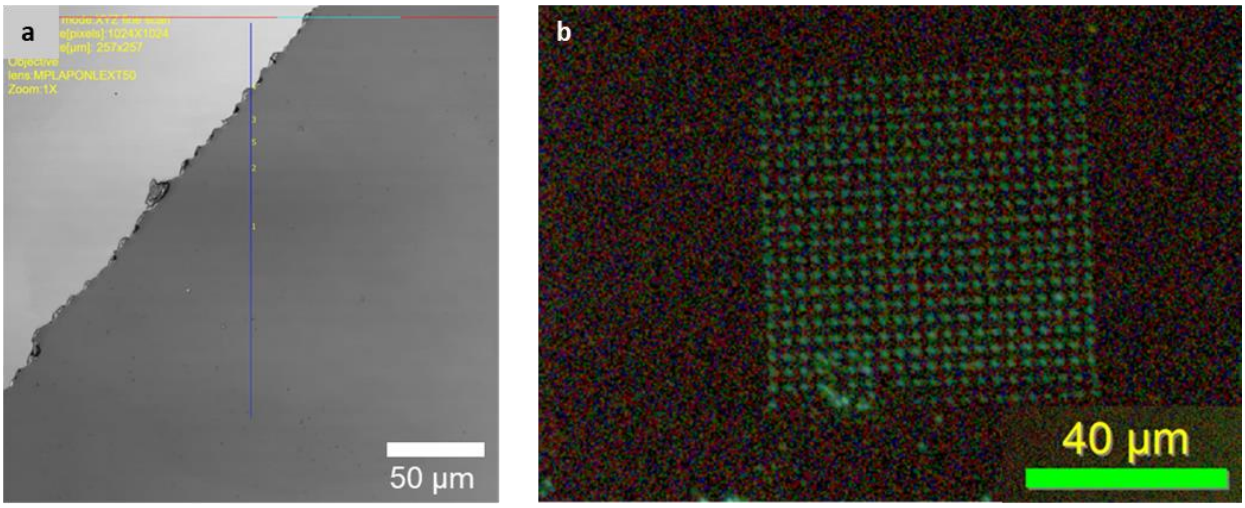

Figure C.8. PMMA coating characterization. **(a)** Confocal microscope image of an EHD inkjet print substrate after coating with PMMA. A scratch was made in the PMMA film, and height profiles taken along that scratch yield a PMMA layer thickness of ~200 nm. **(d)** PL microscope image of an EHD inkjet-printed NC pattern after coating with PMMA and annealing at 70 °C for 10 min. The original print pattern size and feature spacings are largely unchanged after PMMA coating.

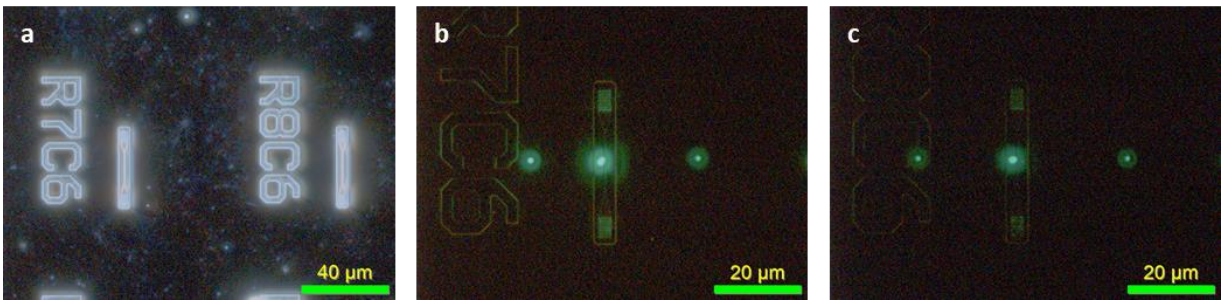

Figure C.9. Additional nanobeam cavity microscope images. **(a)** Dark field microscope image of the EHD inkjet-printed NC nanobeam cavity substrate shown in Figure 4.4a of the main text. **(b-c)** Additional PL microscope images of the nanobeam cavities shown in Figure 4.4b of the main text, imaged with different exposure times.

C.6 References

1. De Roo, J.; Ibáñez, M.; Geiregat, P.; Nedelcu, G.; Walravens, W.; Maes, J.; Martins, J. C.; Van Driessche, I.; Kovalenko, M. V.; Hens, Z., Highly Dynamic Ligand Binding and Light Absorption Coefficient of Cesium Lead Bromide Perovskite Nanocrystals. *ACS Nano* **2016,** *10*, 2071-2081.

2. Chen, Y.; Ryou, A.; Friedfeld, M. R.; Fryett, T.; Whitehead, J.; Cossairt, B. M.; Majumdar, A., Deterministic Positioning of Colloidal Quantum Dots on Silicon Nitride Nanobeam Cavities. *Nano Lett.* **2018,** *18*, 6404-6410.
3. Fong, C. F.; Yin, Y.; Chen, Y.; Rosser, D.; Xing, J.; Majumdar, A.; Xiong, Q., Silicon Nitride Nanobeam Enhanced Emission from All-Inorganic Perovskite Nanocrystals. *Opt. Express, OE* **2019,** *27*, 18673-18682.

VITA

Ted grew up in Tampa, Florida, where he ran cross country and developed a passion for chemistry and mathematics. He did his undergraduate in Chemical Engineering at Washington University in St. Louis and honed his investigatory skills as an undergraduate researcher in the aerosol science research lab of Prof. Pratim Biswas. He enrolled in the Molecular Engineering Ph.D program here at UW and is co-advised by Daniel Gamelin, Christine Luscombe and Devin MacKenzie. Outside of research, Ted has sailed nonstop for over 1,000 miles through various trips and has helped win three duck stickers in the Duck Dodge sailing regattas. He also enjoys ski touring and hiking.